

AD A 109180

NSWC TR 81-156

AERODYNAMIC DESIGN MANUAL FOR TACTICAL WEAPONS

by
LAWRENCE MASON
LEROY DEVAN
FRANK G. MOORE
DONALD McMILLAN
Strategic Systems Department

DTIC
ELECTE
DEC 31 1981
B

JULY 1981

Approved for public release; distribution unlimited.



NAVAL SURFACE WEAPONS CENTER

Dahlgren, Virginia 22448

Silver Spring, Maryland 20910

DTIC FILE COPY

8112 31 017
8112 31 017

NAVAL SURFACE WEAPONS CENTER
Dahlgren, Virginia 22448

UNCLASSIFIED

SECURITY CLASSIFICATION OF THIS PAGE (When Data Entered)

REPORT DOCUMENTATION PAGE		READ INSTRUCTIONS BEFORE COMPLETING FORM
1. REPORT NUMBER	2. GOVT ACCESSION NO.	3. RECIPIENT'S CATALOG NUMBER
NSWC/TR 81-156	AD-A109168	
4. TITLE (and Subtitle)		5. TYPE OF REPORT & PERIOD COVERED
AERODYNAMIC DESIGN MANUAL FOR TACTICAL WEAPONS		
7. AUTHOR(s)		8. PERFORMING ORG. REPORT NUMBER
Lawrence A. Mason Donald McMillan Leroy Devan Frank G. Moore		
9. PERFORMING ORGANIZATION NAME AND ADDRESS		10. PROGRAM ELEMENT, PROJECT, TASK AREA & WORK UNIT NUMBERS
Naval Surface Weapons Center (Code K21) Dahlgren, Virginia 22448		61153N, SR02302; 62332N, SF32392-591
11. CONTROLLING OFFICE NAME AND ADDRESS		12. REPORT DATE
Naval Sea Systems Command Washington, DC 20362		July 1981
14. MONITORING AGENCY NAME & ADDRESS (if different from Controlling Office)		13. NUMBER OF PAGES
		177
		15. SECURITY CLASS. (of this report)
		UNCLASSIFIED
		15a. DECLASSIFICATION/DOWNGRADING SCHEDULE
16. DISTRIBUTION STATEMENT (of this Report)		
Approved for public release; distribution unlimited.		
17. DISTRIBUTION STATEMENT (of the abstract entered in Block 20, if different from Report)		
18. SUPPLEMENTARY NOTES		
19. KEY WORDS (Continue on reverse side if necessary and identify by block number)		
Tactical Weapons	Static Derivatives	Center of Pressure Magnus
Aerodynamics	Drag	Dynamic Derivatives Missile
Missile Aerodynamics	Normal Force	Roll Damping Performance
Projectile Aerodynamics	Lift	Pitch Damping Projectile
Wings	Fins	degree Performance
20. ABSTRACT (Continue on reverse side if necessary and identify by block number)		
<p>The Naval Surface Weapons Center Aeroprediction Code has been extensively applied to the prediction of static and dynamic aerodynamics of missile configurations. Major extensions have recently been made to the Code, extending its capability to $0 < M < 8$ and $0^\circ < \alpha < 180^\circ$ and improving the transonic and dynamic derivative predictions. The theoretical basis for the Code is reviewed. The Code is evaluated through comparisons of computational examples with experiment for body alone, body-tail, and body-tail-canard configurations.</p>		

DD FORM 1473
1 JAN 73EDITION OF 1 NOV 65 IS OBSOLETE
S/N 0102-LF-014-6601UNCLASSIFIED
SECURITY CLASSIFICATION OF THIS PAGE (When Data Entered)

UNCLASSIFIED

SECURITY CLASSIFICATION OF THIS PAGE (When Data Entered)

20. ABSTRACT (Cont'd)

The speed and accuracy of the Code is ideal for use in preliminary design. Representative design charts (generated by the use of the Code) for both the static and dynamic aerodynamic coefficients of a wide variety of configuration components are included. The charts will aid the designer in making preliminary design estimates or for data comparisons.

UNCLASSIFIED

//
SECURITY CLASSIFICATION OF THIS PAGE (When Data Entered)

FOREWORD


This work was undertaken to provide a design tool for use in estimating the aerodynamics of tactical weapons. Rapid estimation of these aerodynamics will then allow one to predict performance or conduct static/dynamic stability analysis in the preliminary and intermediate design stages in an efficient and reasonably accurate manner. Prior to the development of this technology over the past 10 years, aerodynamics were calculated by hand using design charts, wind tunnel data, empirical methods, or just "engineering experience." It is hoped that this methodology has helped to lend an improved process for generating aerodynamics.

Support for the work was provided by the following sponsors: The Naval Sea Systems Command under the Surface-Launched Weapons Aerodynamics and Structures Block Program, the Naval Air Systems Command under the Strike Warfare Weaponry/Aerodynamics/Structures Technology Block, the U.S. Army Missile Command under Project No. 1L162303A214, and the Office of Naval Research under Project No. F41411.

Major procurement contracts from the above funds were let to North Carolina State University, Nielsen Engineering and Research, Inc., and Lockheed Missiles and Space Co., Inc. Minor contracts were let to General Electric, Armament System Dept., Burlington, Vt.; COMPRO of Fredericksburg, Va.; and EG&G of Rockville, Md.

This report was reviewed and approved by Mr. C. A. Fisher, Head, Weapon Dynamics Division (K20).

Released by:


R. T. RYLAND, JR., Head
Strategic Systems Department

Approved for	<input checked="checked" type="checkbox"/>
Special Agent	<input type="checkbox"/>
Investigator	<input type="checkbox"/>
Supervisor	<input type="checkbox"/>
By	
Special Agent	
Investigator	
Supervisor	
A	

DTIC
ELECTE
DEC 31 1981

ACKNOWLEDGMENTS

Since the start of this effort in 1971, there have been several sponsors and numerous technical participants who deserve recognition in addition to the four authors.

The Naval Sea Systems Command and the Naval Surface Weapons Center (NSWC) Independent Research program were the first two sponsors of the original body alone work starting in 1971. Mr. Lionel Pasiuk of the Naval Sea Systems Command has supported this effort from its beginning through the most recent work. He was joined in 1977 by Mr. William Volz of the Naval Air Systems Command. Mr. Volz (as well as Mr. Ray Van Aken and Dr. Lloyd Smith of NWC when Block Programming was developed in 1978) supported the extension of this effort through completion in 1981. Additional support in 1978-79 was given by the Office of Naval Research through Mr. Dave Siegel and in 1978-1980 by Mr. Ray Deep of the Army Missile Command. Without the funds provided by all of these organizations, this work would not have been possible.

The body alone work was performed in 1971-72 by the third author. He was supported in 1973-74 by Mr. William McKerley on the wing-body-tail aerodynamics. Dr. Charles Swanson participated in 1975-76 in the dynamic derivative calculations. Since 1977, there have been several NSWC employees as well as outside contractors who have participated in the extension to higher Mach number and angle-of-attack. Dr. F. R. De Jarnette of North Carolina State University developed the high Mach number static aerodynamics. Dr. Lars Ericsson of Lockheed Missiles and Space Co., Inc. developed a portion of the pitch damping aerodynamics. The improved transonic normal force and drag were developed by Nielsen Engineering and Research. Dr. John Sun was program coordinator for the Extended Code development from 1978-1980 when the first author took over this effort. The second author made many technical and coding modifications required to develop the current comprehensive operational code for the extended Mach number and angle-of-attack computations. Finally, there have been several cooperative students who have assisted in carrying out calculations for the design manual. Most noteworthy were Mark Flenner and Bryan McGraw in addition to the fourth author.

CONTENTS

Paragraph		Page
1	INTRODUCTION	1
2	METHODS OF ANALYSIS	3
2.1	Static Aerodynamics	3
2.1.1	Body Alone Aerodynamics	3
2.1.1.1	Axial Force	4
2.1.1.1.1	Wave or Pressure Axial Force	4
2.1.1.1.2	Friction Axial Force	12
2.1.1.1.3	Rotating Band Axial Force Coefficient	13
2.1.1.1.4	Base Axial Force	13
2.1.1.2	Normal Force and Pitching Moment	14
2.1.1.2.1	Inviscid Normal Force	14
2.1.1.2.2	Viscous Crossflow Model	16
2.1.2	Lifting Surfaces and Interference	
	Aerodynamics	17
2.1.2.1	Axial Force	20
2.1.2.1.1	Wave Axial Force	20
2.1.2.1.2	Skin Friction Axial Force	23
2.1.2.1.3	Trailing Edge Separation Force	23
2.1.2.1.4	Effect of a Fin on the Base	
	Drag of the Body	24
2.1.2.2	Lift and Pitching Moment	24
2.1.2.2.1	Subsonic Flow ($0 < M_\infty < .8$)	24
2.1.2.2.2	Low Supersonic Flow ($1.2 < M_\infty < M_{le}$)	27
2.1.2.2.3	Transonic Flow ($.8 < M_\infty < 1.2$)	31
2.1.2.2.4	High Supersonic Flow ($M_\infty < M_{le}$)	32
2.1.2.3	Interference Lift	32
2.1.2.3.1	Lifting Surface-Body Interference	32
2.1.2.3.2	Wing-Tail Interference	37
2.1.3	High Angle-of-Attack Aerodynamics	38
2.2	Dynamic Derivatives	40
2.2.1	Body Alone	40
2.2.1.1	Roll Damping and Body Magnus Moment	40
2.2.1.2	Pitch Damping Coefficient	41
2.2.2	Lifting Surface Dynamic Derivatives	43
2.2.2.1	Roll Damping	43
2.2.2.1.1	Subsonic Flow ($0 < M_\infty < .8$)	43
2.2.2.1.2	Low Supersonic Flow ($1.2 < M_\infty < M_{le}$)	43
2.2.2.1.3	Transonic Flow ($.8 < M_\infty < 1.2$)	44
2.2.2.1.4	High Supersonic Flow ($M_\infty > M_{le}$)	44
2.2.2.2	Pitch Damping	45
2.2.2.2.1	Subsonic Flow ($M_\infty < .8$)	45
2.2.2.2.2	Low Supersonic Flow ($1.2 < M_\infty < M_{le}$)	46
2.2.2.2.3	Transonic Flow ($.8 < M_\infty < 1.2$)	48

CONTENTS (Cont'd)

Paragraph		<u>Page</u>
2.2.2.2.4	High Supersonic Flow ($M_\infty > M_{le}$)	48
2.2.2.3	Dynamic Derivatives for M_{le}	
	Total Configuration	49
2.2.2.3.1	Subsonic and Low Supersonic Flow	49
2.2.2.3.2	Transonic Flow ($.8 < M_\infty < 1.2$)	50
2.2.2.3.3	LMSC Wing-Body Pitch Damping	50
2.3	Methods of Analysis Summary	52
3	APPLICATIONS TO CURRENT DESIGNS	54
3.1	Tactical Weapons Without Lifting Surfaces (Body Alone Aerodynamics)	54
3.2	Tactical Weapons With Lifting Surfaces	69
4	AIDS TO DESIGN	89
4.1	Body Alone Design	89
4.1.1	Drag	89
4.1.2	Normal Force and Center of Pressure	101
4.1.3	Dynamic Aerodynamics	115
4.2	Lifting Surfaces	120
4.2.1	Drag	120
4.2.2	Lift	130
5	REFERENCES	143
	Appendix--List of Symbols	A-1
	Distribution	

FIGURES

		<u>Page</u>
FIGURE 1.	General Body Geometry	3
2.	Spherically Blunted Nose Geometry	8
3.	Fin Planform Geometry for a Blunted Modified Wedge Cross Section	18
4.	Fin Root Cross Section	18
5.	Supersonic Leading Edge Flat Plate Planform, Case 1 ($M_\infty = 2$)	28
6.	Supersonic Leading Edge Flat Plate Planform, Case 2 ($M_\infty = 1.5$)	29

FIGURES (Cont'd)

		<u>Page</u>
Figure 7.	Supersonic Leading Edge Flat Plate Planform, Case 3 ($M_\infty = 1.2$)	30
8.	Subsonic Leading Edge Flat Plate Planform, ($M_\infty = 1.2$)	30
9.	Triangular Fin and Body Combination	33
10.	Swept Back Trailing Edge Fin and Body Combination	34
11.	Determination of $K_{B(F)}$ for High Aspect-Ratio Range at Supersonic Speeds	36
12.	Roll Angle and Fin Load Definitions (Looking Forward)	39
13.	Methods for Computing Body-Alone Static Aerodynamics	52
14.	Methods for Computing Wing-Alone and Interference Static Aerodynamics	52
15.	Methods for Computing Dynamic Derivatives	53
16.	Comparison of Theory and Experiment for Army/Navy Spinner	55
17.	Comparison of Theory and Test Data for 5 inch RAP Projectile	56
18.	Comparison of Theory and Experiment for 5 inch/54 Improved Projectile	57
19.	Comparison of Theory and Experiment for 175 mm Projectile	59
20.	Comparison of Theory and Experiment for 155 mm Projectile	60
21.	Comparison of Theory and Experiment for Hemisphere-Cylinder	61
22.	NASA Flare Body Data Comparison for Supersonic Mach Numbers	62
23.	30 mm Optimal Projectile Aerodynamics	66
24.	Time of Flight of a 30 mm Optimum Drag Projectile vs. Flight Weight to Slant Ranges of 2.0 km, 3.0 km, and 4.0 km	67
25.	Minimum Time-of-Flight Ballistic Coefficient for a 30 mm Optimum Drag Projectile	68
26.	Comparison of Theory and Experiment for Basic Finner	70
27.	Comparison of Theory and Experiment for Modified Basic Finner at Angles-of-Attack to $\alpha = 45^\circ$ and $M_\infty = 2.5$	71
28.	Comparison of Theory and Experiment for Air Slew at Angles-of-Attack to $\alpha = 45^\circ$ and $M_\infty = 1.3$. . .	72

FIGURES (Cont'd)

		<u>Page</u>
Figure 29.	Comparison of Theory and Experiment for TMX 2774 T-9 Tail in the Supersonic Region	73
30.	Comparison of Theory and Experiment for TMX 1751 for $2.5 < M_{\infty} < 4.5$	75
31.	Comparison of Theory and Experiment for TMX 3070	76
32.	Theoretical Predictions for 3.0 Inch Missile	77
33.	Structural Integrity Study Using the Aeroprediction Code	78
34.	Missile Physical Characteristics	82
35.	Forebody Drag Coefficient vs Boresight Error Slope for Various Shapes and Fineness Ratios	84
36.	Tail Normal Force and Pitching Moment Coefficient vs Taper Ratio	86
37.	Example Missile Design	86
38.	Aerodynamic Coefficients for Example Missile	87
39.	Example Missile Configuration Performance	88
40.	Typical Nose Contours ($L_N = 3.0$ cal)	90
41.	Wave Drag Comparison for Pointed Bodies	91
42.	Wave Drag Comparison for Pointed Bodies (Nose Length = 3.0 cal)	92
43.	Transonic Wave Drag of Tangent Ogives	92
44.	Total Drag for Blunted 7.125° (4 cal) Cones - Truncated to Shorter Length	93
45.	Total Drag for Blunted 10° Cones - Spherically Capped to Shorter Length	93
46.	Separation Pressure Drag on a Cone-Cylinder	95
47.	Wave Drag Coefficient of Conical Boattails at Supersonic Speeds	96
48.	Variance of Boattail Base Diameter on Total Drag vs M_{∞} for a Complete Body Configuration	97
49.	Rotating Band Drag - C_{ARB}	98
50.	Flat Plate Average Skin Friction Coefficient	100
51.	Mean Base Pressure Coefficient ($\alpha = 0^\circ$)	100
52.	Supersonic Normal Force Coefficient Variation for Cone Cylinders	102
53.	Supersonic X_{cp} Variation for Cone Cylinders	102
54.	Supersonic Normal Force Variation for Secant-Ogive Cylinders	103

FIGURES (Cont'd)

		<u>Page</u>
Figure 55.	Supersonic X_{cp} Variation for Secant-Ogive Cylinders	103
56.	Supersonic Normal Force Coefficient Variation for Tangent-Ogive Cylinders	104
57.	Supersonic X_{cp} Variation for Tangent-Ogive Cylinders	104
58.	Variation in $C_{N\alpha}$ and X_{cp} with Afterbody Length for Tangent-Ogive Cylinder Bodies (4 cal Nose) . .	105
59.	Variation in $C_{N\alpha}$ and X_{cp} with Afterbody Length for Conical-Cylinder Bodies (4 cal Nose)	106
60.	Constants to Determine $(C_{N\alpha})_N$ for $M_\infty < 1.2$	108
61.	Increase in $(C_{N\alpha})$ at Subsonic and Transonic Mach Numbers Due to Afterbody	109
62.	Center of Pressure of Afterbody Lift for $M_\infty < 1.2$	109
63.	Decrease in $C_{N\alpha}$ Due to Boattail	110
64.	Normal Force Coefficient Gradient for Boattails (6 cal Afterbody)	111
65.	Center of Pressure for Boattails (6 cal Afterbody)	111
66.	Normal Force for Blunt 10° Cones - Spherically Capped to Shorter Length	113
67.	Center of Pressure for Blunt 10° (2.836 cal) Cones - Spherically Capped to Shorter Length	113
68.	Normal Force for Blunt 7.125° (4 cal) Cones - Truncated to Shorter Length	114
69.	Center of Pressure for Blunt 7.125° (4 cal) Cones - Truncated to Shorter Length	114
70.	Drag Proportionality Factor and Crossflow Drag Coefficient	116
71.	Variation of Magnus Moment for Bodies Without Boattails	118
72.	Magnus Moment Variation for Bodies with Boattails $M_\infty > 2.0$	118
73.	Body Alone Pitch Damping Moment Variation as a Function of Nose Length and Total Body Length . .	119
74.	Transonic Wave Drag Coefficient of a Double-Wedge Fin	121

FIGURES (Cont'd)

		Page
Figure 75.	Wave Drag Coefficient of a Double-Wedge Delta and Rectangular Biconvex Fins at Transonic Speeds . .	123
76.	Supersonic Wave Drag of Wings with Double-Wedge Airfoil Section; $C_t/C_r = 1.0$	124
77.	Supersonic Wave Drag ^t of Wing with Biconvex Airfoil Section	125
78.	Supersonic Wave Drag of Wing with Double-Wedge Airfoil Section, $C_t/C_r = 1.0$	126
79.	Two-dimensional Base ^t Pressure Coefficient	127
80.	Base Pressure Coefficient Change with Fins Located Flush with Base	128
81.	Distance from Base where Fins do not Affect Base Pressure	128
82.	Zero Lift Drag of Wings as a Function of Leading Edge Bluntness; $AR=2$, $\gamma_1 = \gamma_4 = 30^\circ$, $t/c = 0.12$	129
83.	Subsonic Fin Normal-Force Coefficient Gradient . . .	131
84.	Chart for Determining Transonic Lift-Curve Slope at M_a and M_b	132
85.	Normal-Force Coefficient Gradient for Rectangular Fin (Diamond Shape) ($t/C = .025$)	133
86.	Normal-Force Coefficient Gradient for Rectangular Fin (Diamond Shape) ($t/C = .05$)	134
87.	Normal-Force Coefficient Gradient for Rectangular Fin (Diamond Shape) ($t/C = .1$)	135
88.	Normal-Force Coefficient Gradient for Rectangular Fin (Diamond Shape) ($t/C = .15$)	136
89.	Normal-Force Coefficient Gradient for Rectangular Fin (Diamond Shape) ($t/C = .2$)	136
90.	Center of Pressure for Rectangular Fin (Diamond Shape) ($t/C = .025$)	137
91.	Center of Pressure for Rectangular Fin (Diamond Shape) ($t/C = .05$)	138
92.	Center of Pressure for Rectangular Fin (Diamond Shape) ($t/C = .1$)	138
93.	Center of Pressure for Rectangular Fin (Diamond Shape) ($t/C = .15$)	139
94.	Center of Pressure for Rectangular Fin (Diamond Shape) ($t/C = .2$)	139

FIGURES (Cont'd)

		<u>Page</u>
Figure 95.	Normal Force Coefficient Variation for Tapered Double-Wedge Fins	141
96.	Center of Pressure Variation in Supersonic Flow for Tapered Double-Wedge Fins	142

1. INTRODUCTION

In the design of any airframe, there is a need to estimate the aerodynamic characteristics of the body in flight. During the preliminary or conceptual design phase, design changes necessitate the revision of the preliminary estimates each time a change is made. To meet this need, the Navy (Army support in 1977) undertook in 1971 the development of a computer code which would be able to predict the aerodynamic coefficients of a wide variety of configurations rapidly, inexpensively, and with relatively good accuracy. The code was developed in phases with preliminary versions of the code being published in 1972, 1974, and 1977 (see References 1, 2, and 3, respectively). These versions were for the body alone static aerodynamics, wing-body-tail static aerodynamics, and dynamic derivatives, respectively. Applicable Mach number and angle-of-attack ranges were $0 \leq M_\infty \leq 2.5$ and $0 \leq \alpha \leq \text{stall}$, respectively. The final version of this code, simply referred to as the Aeroprediction Code, was completed in late 1981. This version of the code extended the Mach number range to 6 and angle-of-attack to 180° . However, wing-body aerodynamics can only be computed to $\alpha = 45^\circ$. Above $\alpha = 45^\circ$, body alone aerodynamics are generated. Theoretical documentation of this last version of the code is given in Reference 4. The code has been developed to handle a general class of axisymmetric, wing-body-tail configurations (this does not include inlets or base flow). The general approach in the code development has been to combine existing and newly developed computational methods into a single computer program. The basic method, described in more detail in Section 2, is that of component superposition where the body alone, lifting surface alone, and interference contributions are added to obtain the total configuration aerodynamics.

The purpose of this report is twofold: 1) to provide a brief summary of the methods used in the Code, and 2) to provide representative design charts which have been generated by the use of the Aeroprediction Code and which can be used for preliminary design estimates or data comparison. Section 2 provides the summary of the prediction methods. The methods are outlined in sufficient detail so

that one familiar with aerodynamic theory will probably not need to seek further detail in the earlier works. However, many of the intermediate steps and data tables used in the Code are not presented. Section 3 provides a comparison of the theory in the Code and experimental data for a number of representative configurations which will provide the users of both the Code and the design charts a feel for the overall accuracy of the predictions. There are also sections discussing the design of projectiles and missiles to achieve optimum performance. Section 4 presents a limited number of design charts which can be used by the designer to obtain an estimate of the aerodynamic coefficients for a variety of configuration components. The chief purpose of the charts is to show the trends in the coefficients which result from changes in a configuration component. The charts in many cases represent reproductions or extensions of charts provided in earlier works, which are shown both for comparison and to provide new data. The charts presented by no means represent the full range of application of the Aeroprediction Code. Time and funds would not allow a complete examination of the effects of varying geometric parameters. The user may wish to conduct additional parametric analyses within the applicable limits of the Code.

2. METHODS OF ANALYSIS

The basic approach is that of component linear superposition. Body alone, lifting surface alone, and interference aerodynamic contributions are combined into total configuration aerodynamics. No inlet or plume effects are considered.

The general approach has been to combine existing and newly developed approximate computational methods into a single program to compute aerodynamics. Computational times required for the estimate of static and dynamic aerodynamic coefficients for a body-tail-canard configuration, which is the most complex configuration considered, are in Central Processing Unit (CPU) seconds on the CDC 6700 computer as opposed to minutes or hours required for more detailed physical and numerical models. The accuracy obtained, however, is compatible with that required for preliminary or intermediate design estimates.

2.1 STATIC AERODYNAMICS

2.1.1 BODY ALONE AERODYNAMICS

Complete generality of body configuration is not possible. The basic geometry for the most complex configuration considered is shown in Figure 1. The body is axisymmetric.

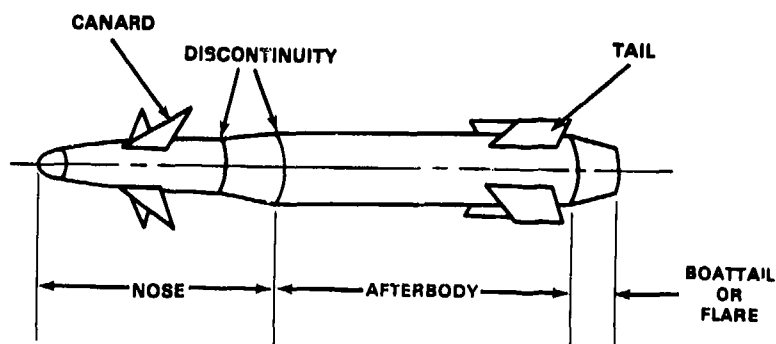


Figure 1. General Body Geometry

The nose may be pointed, spherically blunted, or truncated. For the spherically blunted case, the origin of coordinates is where the spherical cap joins the rest of the nose. Note that \tilde{x} is a coordinate from the nose tip. The nose may also consist of two piecewise continuous sections in addition to a possible spherical cap. At high supersonic Mach numbers, the spherical cap may be generalized to a conic section curve. The afterbody consists of a constant radius section. The boattail or flare may be a conical frustrum or a curved section. A rotating band for a projectile can also be included.

The reference area is associated with a reference body diameter for all aerodynamic coefficients. The diameter must be that at the end of the nose.

2.1.1.1 AXIAL FORCE

Axial force components are broken down into linear superposition of wave or pressure force, friction force, rotating band force, and base force.

2.1.1.1.1 WAVE OR PRESSURE AXIAL FORCE

The wave or pressure axial force is defined as the forebody axial force due to normal stress or pressure. In the subsonic-transonic flow region, the forebody surface pressures are affected by boundary layer separation at the nose-afterbody junctions, at the end of the body, and on a steep boattail.

2.1.1.1.1.1 SUBSONIC AND TRANSONIC FLOW ($M_\infty < 1.2$). Currently the wave axial force is assumed to be contributed by the nose and the boattail in a linear superposition. For bodies with long afterbodies, the nose and boattail drag are essentially uncoupled. In other words, the nose axial force does not depend on boattail parameters and afterbody length (subsonic Mach numbers), and the boattail axial force does not depend on nose parameters and afterbody length. In reality, the boattail axial force and base force are coupled for subsonic Mach numbers, even for long afterbodies.

Complete generality of solution would require a solution of small disturbance potential, full potential, or Euler model equations. Computational times are prohibitive even for the simplest small disturbance model.

For the nose axial force, the approach is to utilize computational axial force coefficient data and experimental data for a nose followed by a long afterbody in a table lookup manner. Reference 5 indicates that the nose axial force coefficient is shape dependent. The family of tangent ogives and conical noses approximate the boundaries of the envelope of shapes of interest.

The nose axial pressure or wave drag force coefficient is given by a linear interpolation between a blunted ogive value and a blunted cone value.

$$C_{AN} = \frac{[C_{ANO}(R_N, L_N, M_\infty)(R'_0 - R'_S) + 2C_{ANC}(\epsilon_S, M_\infty)R'_S]}{(R'_S + R'_0)} \quad (1)$$

Details and evaluation of the prediction are given in Reference 4.

C_{ANO} is the tangent ogive value and C_{ANC} is the sharp cone value. R'_0 is the slope at $x = 0$ and R'_S is the slope at the nose-afterbody junction. When R'_S is zero, the ogive value is obtained, and, when $R'_S = R'_0$, the cone value is obtained. ϵ_S is the cone angle associated with R'_S .

The value for $C_{ANO}(R_N, L_N, M_\infty)$ is obtained from a table lookup interpolation routine for blunted tangent ogive noses with long afterbodies. Tabular values are obtained from solutions of the full potential equation and a model of the Euler equations. The original computational method reported in Reference 6 obtains a solution of the Euler equations model by an implicit time asymptotic method. Computational accuracy from Reference 6 for shorter nose lengths was deemed to be insufficient. Hence, the full potential model of Reference 7 was used to update the table. The potential model data transmitted by G. Kuhn of NEAR, Inc. are unpublished. Discrete values of M_∞ are .8, .95, 1.05, and 1.2. R_N values are spaced in .05 increments from 0 to .5. L_N values range from .75 to 5. For values below $M_\infty = .8$, C_{ANO} is decayed quadratically from the value at $M_\infty = .8$ to 0 at $M_\infty = .5$.

The C_{ANC} tabular values were obtained by integrating pressure data for pointed cone-cylinders from Reference 8 and blending these data with values from the classical Taylor-Maccoll solutions. C_{ANC} values are decayed to a finite value asymptote below $M_\infty = .5$. Reference 9 indicates that the effect of blunting is not significant for bluntness as great as $R_N = .4$ for pointed conical noses

below shock attachment Mach numbers. ϵ_S tabular values are in 5° increments ranging from 0° to 20° . M_∞ tabular values are .5, .7, .8, .95, 1.05, and 1.2.

The boattail axial force model is reported in Reference 1. For supersonic Mach numbers close to 1.0, Reference 10 gives an approximate solution of the small disturbance potential equation on a boattail which follows a long afterbody. For Mach numbers below 1.05, the boattail drag is decayed to 0.0 in a linear manner at $M_\infty = .95$ from the value at $M_\infty = 1.05$.

2.1.1.1.2 LOW SUPERSONIC MACH NUMBERS ($1.2 \leq M_\infty \leq M_\ell$). M_ℓ is a Mach number separating low supersonic inviscid computations from high supersonic computations for the body alone components for static coefficient prediction. M_ℓ is a program input between 2 and 3.5 which is dictated by the limits of the small disturbance models used for the low supersonic Mach number flow region.

Detailed theory and evaluation for this section are given in Reference 1. For pointed bodies, the basic model is the Van Dyke second-order perturbation solution of the potential equation (Reference 11). The full nonlinear potential equation can be separated into an axial flow nonlinear problem and a linear nonconstant coefficient (constants depend on an axial solution) crossflow problem when the angle of attack is small (15° or less).

First-order linear solutions are obtained by neglecting all nonlinear terms for the axial flow and crossflow problems. The first-order axial flow problem is solved by superposing axial source solutions in integral form. The source strength distribution is estimated by a piecewise second-order Taylor series representation. The classical Kármán-Moore source distribution is first-order piecewise linear. Van Dyke estimates the highest order nonlinear terms using the first-order solution. Thus a solution of the nonlinear axial flow problem is obtained by a second-order iteration or perturbation. The second-order partial

differential equation has the same linear terms and is nonhomogeneous. An approximate closed form particular solution was found by Van Dyke to the same order of accuracy as the nonlinear terms retained. The second-order homogeneous solution is solved using a piecewise second-order axial source distribution.

To be consistent, the crossflow solution contributes terms of order $\sin^2 \alpha$ to the axial force coefficient. However, the Code uses the full nonlinear pressure coefficient relation. The crossflow solution contributes a term of order $\sin \alpha$ to the normal force. The crossflow solution will be discussed in the section on normal force or lift at zero angle of attack. Only a first-order linear crossflow solution is considered in the "hybrid" model.

Thus far, the discussion has dealt with a pointed body solution. The origin of the supersonic axial source and doublet distributions coincide with $x = 0$. The perturbation solution is limited by the requirement that the Mach angle be greater than the maximum body slope. In the Code, the requirement is that the maximum body slope be less than .95 of the slope of the Mach angle for pointed bodies.

For a spherically blunted body the slope exceeds the Mach angle slope on part of the sphere. A modified Newtonian pressure distribution is matched with the perturbation theory at some point on the sphere. The modified Newtonian pressure distribution is given as

$$C_p = C_{p0} \sin^2 \delta \quad (2)$$

$$\sin \delta = \sin \epsilon \cos \alpha - \cos \epsilon \cos \theta \sin \alpha \quad (3)$$

where

θ is the azimuthal angle from the leeside,

ϵ is the angle associated with the body slope, and

C_{p0} is the stagnation pressure coefficient behind a normal shock.

The method for matching pressure distribution and for selecting the origin of the source distribution is complex. In order to improve the recompression

predicted at higher Mach numbers in the neighborhood of the sphere-body junction, the nose shape was modified as shown in Figure 2.

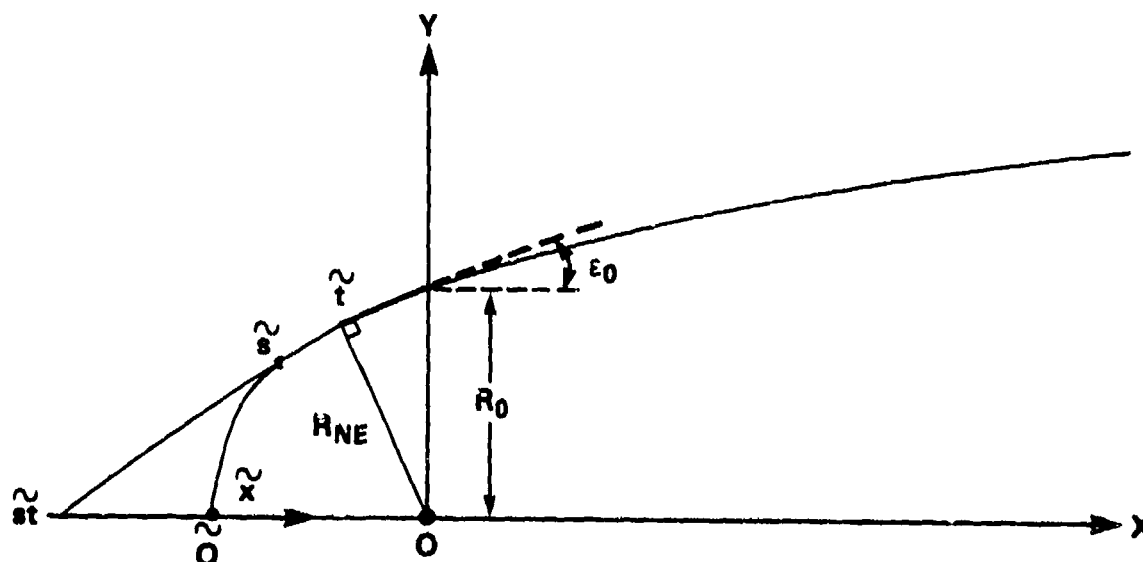


Figure 2. Spherically Blunted Nose Geometry

The tangent to the body at the origin of coordinates is extended, and a perpendicular is dropped from the origin to point \tilde{t} . For low supersonic flow the spherical nose cap is replaced by a sphere and a conical frustrum recompression ramp. The effective sphere radius is then $R_{NE} = R_0 \cos \epsilon_0$ as opposed to the one shown in Figure 1 where $R_N = R_0 / \cos \epsilon_0$.

The perturbation solution starts at point \tilde{s} . The point \tilde{s} initially is chosen where the surface tangent angle is 27.5° . An additional requirement is that

$$F \tan \mu \leq R'_0 \quad (4)$$

where

F is an input to the code of about .95, and

μ is the Mach wave angle.

If Equation (4) is not satisfied, then the effective free stream Mach number is cut back to the point where $F \tan \mu = R'_0$. If $\tan (27.5^\circ) < R'_0$, then \tilde{s} coincides

with \tilde{t} . The origin for the source or doublet distribution, \tilde{st} , is obtained by extending a tangent from \tilde{s} to the axis at \tilde{st} . Thus, the perturbation solution starts as a cone solution and marches from \tilde{s} down the body. The modified Newtonian solution starts at the stagnation point. On seven meridian planes of constant θ (0° , 30° , 60° , ..., 180°), an intersection between the two distributions is sought. If no intersection is obtained, then a pressure discontinuity is allowed at \tilde{s} . However, even if there is an intersection, there is a pressure slope discontinuity. The Newtonian pressure distribution is used upstream of the point of intersection. The perturbation solution is used downstream of the intersection.

For the truncated body case (Figure 1 with a flat nose), a pseudo sphere is used to provide a solution at the spherical cap-body junction. The "hybrid" solution begins at point \tilde{s} and continues down the body. Loads are not integrated on the pseudo sphere. No pressure intersection is required. On the flat face, the mean pressure is assumed to be .9 of the stagnation value.

Once the C_p distribution is obtained from the "hybrid" model, the axial force coefficient is given by

$$C_A = 8/\pi \int_0^L \int_0^\pi C_p(\tilde{x}, \theta) R R' d\theta d\tilde{x} . \quad (5)$$

Dimensions here are in calibers. C_p is given by the full nonlinear isentropic Bernoulli relation.

A lower limit criterion for M_2 is given approximately by

$$.95 \tan \mu > R'_{\max} .$$

For a spherically blunted body, R'_{\max} is for the part of the body downstream of the spherical cap. Numerical stability and accuracy is degraded for blunt bodies as the Mach number increases.

2.1.1.1.1.3 HIGH SUPERSONIC FLOW ($M_\infty > M_2$). Detailed theory and evaluation for this section is given in Reference 4. The method used is based on a modification of that given in Reference 12.

The body in Figure 1 consists of piecewise continuous elements. The first element is a conic section of the form

$$R^2 = 2 C\tilde{x} + B\tilde{x}^2 . \quad (6)$$

The remainder of the body consists of two nose sections, an afterbody, and a boattail or flare. Some of these sections may be omitted. Each piecewise continuous section is divided into n (currently 40) increments. This defines points where the pressure is to be calculated. Tangents are drawn to the body at these points and extended until intersections with neighboring tangents are found. Thus, the body is replaced by a circumscribed body of linear segments. On a pointed or truncated nose the first tangency point is at the origin. On a conic-section blunt nose, the first tangency point is determined by a match with a modified Newtonian pressure distribution. If the first section of the nose is a pointed cone, obviously no subdivision is necessary.

The pressure coefficient distribution is assumed to be represented as

$$C_p = (C_p)_{\alpha=0} - \Lambda \sin 2\alpha \cos \theta + (\Gamma \cos^2 \theta + \Delta \sin^2 \theta) \sin^2 \alpha/2 \quad (7)$$

where Λ , Γ , and Δ can be represented as

$$\Lambda = - \frac{1}{2} \left(\frac{\partial C_p}{\partial \alpha} \right)_{\alpha=0, \theta=0} , \quad (8)$$

$$\Gamma = \left(\frac{\partial^2 C_p}{\partial \alpha^2} \right)_{\alpha=0, \theta=0} , \text{ and} \quad (9)$$

$$\Delta = \left(\frac{\partial^2 C_p}{\partial \alpha^2} \right)_{\alpha=0, \theta=\pi/2} . \quad (10)$$

From second-order shock-expansion theory, which neglects incoming characteristics at the body surface and makes other approximations for the outgoing characteristic equations, one may show that when $(C_p)_{\alpha=0}$, the Λ , Γ , and Δ variations on a straight line segment are given by the same functional form

$$Y = Y_a + (Y_2 - Y_a) e^{-\eta} , \text{ and} \quad (11)$$

$$\eta = \frac{-\left(\frac{\partial C_p}{\partial s}\right)_{\alpha=0} s}{(C_{p2} - C_{pa})_{\alpha=0}} \quad (12)$$

Here s is the distance along the linear segment, subscript 2 refers to the value at the beginning of the segment, and subscript a refers to an asymptotic value.

Slopes are discontinuous across a segment junction. Jump conditions across a slope discontinuity are obtained from Prandtl-Meyer isentropic relations and higher derivatives thereof. Pressure coefficient values just after a corner can thus be related to values just before a corner (indicated by the subscript 1). Asymptotic values are given by an approximate cone solution for positive values of local ε and free stream Mach number. The pressure gradient jump at a corner is given by a relation from Reference 12.

For negative values of ε , $(C_{pa})_{\alpha=0}$ is assumed to be zero and the remaining asymptotic values of the pressure functions are given by a blend of slender body and hypersonic approximations at free stream Mach numbers.

For a blunt body, the initial values of the pressure coefficients are obtained by evaluation of Equation (2) and its derivatives at the match point. The match point is where the local Mach number is 1.1 as determined by a combination of Equation (2), evaluated at $\alpha = 0$, and the isentropic pressure relation. For a pointed body or truncated body the initial values of the pressure functions are obtained from the approximate cone solution evaluated at ε_0 at the free stream Mach number. For the truncated flat face, the average pressure is again assumed to be .9 of the stagnation value. Values at the tangency point and at the end of the segment are obtained from Equations (11) and (12) for the pressure functions.

Once the pressure distribution is determined, C_A is obtained from

$$C_A = 8 \int_0^L RR' \left[(C_p)_{\alpha=0} + \frac{\Gamma+\Delta}{4} \sin^2 \alpha \right] d\tilde{x} \quad (13)$$

2.1.1.1.2 FRICTION AXIAL FORCE

The boundary layer on the surface of an open-end cylinder is analogous to that on a flat plate of the same length. The model used here is that of Van Driest (Reference 13) and is given in detail in Reference 1. A portion of the forward part of the plate is assumed to be laminar. A critical Reynolds number based on body length is chosen as 10^6 (Reference 1).

The friction axial force coefficient is given as

$$C_{AF} = \frac{4S_b}{\pi} \left[C_F + \frac{R_{NC}}{R_{NL}} \left(\frac{1.328}{\sqrt{R_{NC}}} - C_{FC} \right) \right], \quad R_{NL} \geq R_{NC} \quad (14)$$

where

S_b is the body surface area in calibers, and

R_{NL} and R_{NC} are Reynolds number and critical Reynolds number, respectively, based on body length.

For $R_{NL} < R_{NC}$,

$$C_{AF} = \frac{4}{\pi} S_b \frac{1.328}{\sqrt{R_{NL}}} \quad (15)$$

from the well-known Blasius flat plate solution. C_F and C_{FC} are friction coefficients obtained at the Reynolds number and critical Reynolds number, respectively. In general, C_F is given by

$$d_1 / \sqrt{C_F} - \log C_F = d_2 \quad (16)$$

where

$$d_1 = .55723 [\sin^{-1}(C_1) + \sin^{-1}(C_2)] / \sqrt{T_w/T_\infty},$$

$$d_2 = \log R_{NL} - 1.26 \log (T_w/T_\infty),$$

$$C_1 = \frac{2A^2 - B}{(B^2 + 4A^2)^{1/2}},$$

$$C_2 = \frac{B}{(B^2 + 4A^2)^{1/2}},$$

$$A = \left(\frac{\gamma-1}{2} \frac{M_\infty^2}{T_w/T_\infty} \right)^{\frac{1}{2}},$$

$$B = \frac{1 + \frac{\gamma-1}{2} M_\infty^2}{T_w/T_\infty} - 1, \text{ and}$$

$$T_w/T_\infty = 1 + .9 \frac{\gamma-1}{2} M_\infty^2.$$

Equation (16) is solved twice by a Newton-Raphson iteration algorithm for the input R_{NL} and $R_{NL} = R_{NC}$.

2.1.1.1.3 ROTATING BAND AXIAL FORCE COEFFICIENT

The band height, H , is assumed to be much less than the band width. The band is also assumed to be far back on a constant cross section afterbody in fully developed turbulent flow.

Then

$$C_{ARB} = \Delta C_A (M_\infty) H / .01 \quad (17)$$

where H is the band height in calibers and $\Delta C_A (M_\infty)$ is a table lookup axial force coefficient for a band .01 caliber in height.

2.1.1.1.4 BASE AXIAL FORCE

It is assumed that the boattail or flare is located after a relatively long afterbody so that the approaching external flow is at free stream conditions.

The mean base pressure, then, is a function of boattail length, shape, and final diameter. The model adapted in Reference 1 is

$$C_{AB} = -C_{P_{AB}} (M_\infty, 1) (R_B/R_{ref})^3 \quad (18)$$

where $C_{P_{AB}} (M_\infty, 1)$ is the axial pressure coefficient for a cylinder without a boattail.

For a flare, the model used is

$$C_{AB} = -C_{P_{AB}} (\theta_B, M_\infty) (R_B/R_{ref})^2. \quad (19)$$

Here, R_{ref} is the constant radius of the afterbody and R_B is the base radius.

$C_{AB}(\theta_B, M_\infty)$ is the average base force coefficient from experimental data for a constant flare angle ($0 < \theta_B < 15^\circ$). Analysis of the available data leads to the conclusion that Equation (18) is approximately valid at higher supersonic Mach numbers and invalid at other Mach numbers except for very small boattail angles.

At angle-of-attack, an incremental value is added. The expression is based on data from Reference 14.

$$\Delta C_{ABA} = (.6493\alpha - .002833M_\infty) (R_B/R_{ref})^2 \quad (20)$$

Here α is the angle-of-attack in radians. Note that the equation has been revised from that given in Reference 1 to fit the data more accurately. For flares, $(R_B/R_{ref})^2$ is used in Equation (20). Equation (20) is valid for the body alone case. In the section on lifting surface and interference aerodynamics, Equation (20) is replaced by a different expression. The total base axial force coefficient is given by $C_{AB} + \Delta C_{ABA}$.

2.1.1.2 NORMAL FORCE AND PITCHING MOMENT

The body normal force is broken down into inviscid and viscous crossflow contributions. Moment centers are defined with respect to the nose. Reference length is the body reference diameter. The final moment is about the moment center.

2.1.1.2.1 INVISCID NORMAL FORCE

2.1.1.2.1.1 SUBSONIC AND TRANSONIC FLOW ($M_\infty < 1.2$). In Reference 1, $C_{N\alpha}$ and $C_{m\alpha}$ are assumed to be contributed by a linear superposition of component parts of the body. Each component is assumed to be independent of the other. The nose normal force is predicted from a fit of the cone alone data of Reference 9. The center of pressure prediction is given by slender body theory. The afterbody $C_{N\alpha}$ is given as a table lookup function of afterbody length and free stream Mach number.

Both C_N and x_{cp} are given by the transonic small disturbance theory of Reference 15.^α For low Mach numbers, C_N is predicted from a limited data correlation. For low Mach numbers, the x_{cp} prediction is assumed to be the same as for transonic flow.

The boattail C_N is based on limited data correlation where $C_N/[1 - (R_B/R_{ref})^2]$ is fitted as a function of $\sqrt{|M_\infty^2 - 1|}$. x_{cp} is also given by a slender body theory estimate. The correlation functional form is based on slender body theory.

This combination of methods is necessitated by the lack of a theoretical and experimental data base.

The approach of Reference 16, which was evaluated in some detail in Reference 4, was intended to improve the predictive capability in transonic flow. Complete generality obviously is not possible. The nose was assumed to be a blunted tangent ogive. The boattail was assumed to be conical.

The individual body part contributions are superimposed linearly. However, the individual contributions are assumed to be functions of all body parameters such as nose spherical radius, nose length, afterbody length, and boattail angle. The data base for C_N and C_m is generated by solving the Euler equations at 1° angle of attack. Unfortunately, the size of the data base was not large enough to properly represent this limited model. Parts of the data base were also suspect as to accuracy, in particular the boattail contribution at all Mach numbers and the C_N prediction at supersonic Mach numbers.

For each individual part, C_N or C_m are fitted to a quadratic Taylor series functional form for four Mach numbers (.75, .9, .95, 1.2). 15-fit coefficients are involved in the Taylor series in four geometric parameters. For each Mach number, the Taylor series for the nose, the afterbody, and .5, 1., and 1.5 caliber boattail lengths are used. The zero length (zero contribution), .5, 1., and 1.5 caliber estimates are used to provide data for a four-point Lagrange fit for the boattail contribution. At $M_\infty = .6$, the individual body part contributions are given by the model from Reference 1. A five-point Lagrange fit in M_∞ yields the final component part contributions in the range $.6 < M_\infty < 1.2$. For $M_\infty \leq .6$,

the prediction is given by the older model. The data at $M_\infty = 1.2$ have been replaced by a fit to a large set of data generated by the supersonic small disturbance Van Dyke potential model of Reference 17.

Currently either of the two models is an input option. For afterbody lengths of more than 5.0 calibers, the older model is used since the data base for the more recent model is limited to an afterbody of 5.0 calibers.

2.1.1.2.1.2 LOW SUPERSONIC FLOW ($1.2 \leq M_\infty \leq M_\ell$). A line doublet distribution on the axis permits a solution of the first-order linear crossflow equation. A boundary layer thickness based on flat plate theory is added to the original body before the crossflow equation is solved. As indicated in the section on axial force prediction, C_p is based on a "hybrid" combination of first-order crossflow velocity and second-order axial flow velocity. The pitching moment about the nose and the normal force are then given by

$$C_N = - \frac{8}{\pi} \int_0^L \int_0^\pi C_p(\tilde{x}, \theta) R \cos\theta \, d\theta \, d\tilde{x} \text{ and,} \quad (21)$$

$$C_m = \frac{8}{\pi} \int_0^L \int_0^\pi \tilde{x} C_p(\tilde{x}, \theta) R \cos\theta \, d\theta \, d\tilde{x}. \quad (22)$$

2.1.1.2.1.3 HIGH SUPERSONIC FLOW ($M_\infty > M_\ell$). The basic model has been given in the corresponding section on axial force prediction where C_N and C_m may be given in terms of the pressure coefficient as

$$C_N = 4 \sin 2\alpha \int_0^L R \Lambda \, d\tilde{x} \text{ and} \quad (23)$$

$$C_m = - 4 \sin 2\alpha \int_0^L \tilde{x} R \Lambda \, d\tilde{x}. \quad (24)$$

2.1.1.2.2 VISCOUS CROSSFLOW MODEL

The model of Allen and Perkins (Reference 18) is used and is given in condensed form in Reference 1. The theory is analogous to slender body theory in

that the normal force loading is assumed to be given for a local two-dimensional cylinder exposed to the crossflow velocity, $V_\infty \sin \alpha$.

An incremental normal force coefficient is then given as

$$\begin{aligned}\Delta C_N &= \frac{4\eta(L)}{\pi} \left[2 \int_0^L R C_{dc} (M_\infty \sin \alpha) d\tilde{x} \right] \sin^2 \alpha \\ &= \frac{4\eta(L)}{\pi} C_{dc} (M_\infty \sin \alpha) S_p \sin^2 \alpha.\end{aligned}\quad (25)$$

where C_{dc} is an infinite cylinder crossflow drag coefficient given by a table lookup interpolation. Fully developed turbulence independent of crossflow Reynolds number is assumed. η is a finite length correction factor which is given by a table lookup interpolation, and S_p is the planform area in calibers.

Similarly the incremental moment about the nose is given as

$$\Delta C_m = - \frac{4}{\pi} \eta C_{dc} x_p \sin^2 \alpha \quad (26)$$

where x_p is the center of the planform area.

2.1.2 LIFTING SURFACES AND INTERFERENCE AERODYNAMICS

Again, complete generality of geometry is not possible. The basic fin planform is assumed to be a trapezoid with root and tip edges parallel to the free stream. No camber is considered. Either planar or cruciform combinations of fins are considered. Two sets of inline lifting surfaces are considered in the most general case. Longitudinal control deflections of all movable surfaces are assumed. In addition to the individual fin geometry, the location of the fin apex and a mean body diameter are given as input data.

The fin cross section can be a modified double wedge or biconvex. Leading and trailing edges may be blunted cylindrically and independently normal to the edges. Each piecewise continuous segment of a fin cross section is assumed to be similar. Figure 3 shows a typical fin planform.

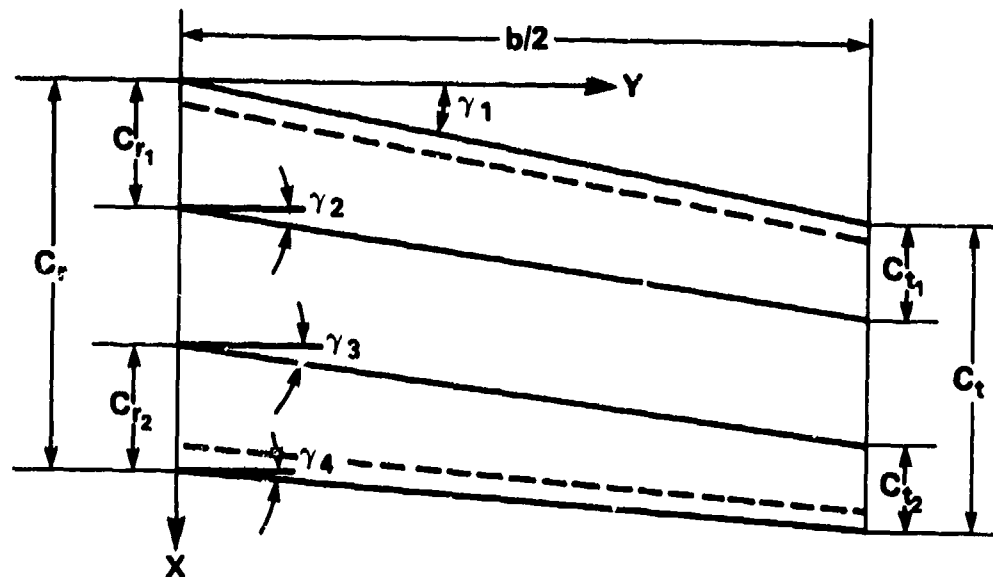


Figure 3. Fin Planform Geometry for a Blunted Modified Wedge Cross Section

Planform parameters shown which are needed to describe the modified wedge are γ_1 , b , C_r , C_t , C_{r1} , and C_{r2} . For a blunted biconvex section, C_{r1} and C_{r2} are not needed. All dimensions are in feet. The x and y are local coordinates.

From the geometry,

$$\tan \gamma_4 = \frac{b/2 \tan \gamma_1 + C_t - C_r}{b/2} \quad (27)$$

The values of γ_2 and γ_3 depend on the cross-section parameters. The dashed lines are the traces where the cylindrical bluntings meet inclined planes of the wedge. A root cross section for a modified wedge is shown in Figure 4. The slope is continuous where the cylindrical blunting meets the inclined plane.

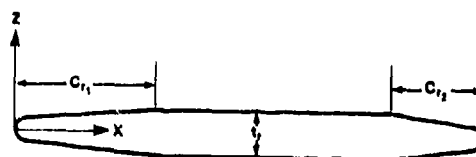


Figure 4. Fin Root Cross Section

Each of the five segments shown is piecewise similar with linear taper in y . In Figure 4, the radii appear as segments of ellipses. The required cross section geometry inputs are t_r , t_t , ρ_{lr} , ρ_{tr} , ρ_{lt} , and ρ_{tt} where t_t is the tip thickness, ρ_{lr} is the root leading edge radius, ρ_{tr} is root trailing edge thickness, and ρ_{lt} and ρ_{tt} are similar parameters for the tip. For a biconvex cross section t_t , ρ_{lt} , and ρ_{tt} are computed.

From the planform geometry,

$$\tan \gamma_2 = \frac{b/2 \tan \gamma_1 + C_{t_1} - C_{r_1}}{b/2} \quad (28)$$

Here, C_{t_1} is obtained from geometry of a plane perpendicular to the leading edge at the tip and the assumption of piecewise similarity.

$$C_{t_1} = [t_t/2 \cos \delta_1 - \rho_{lt} (1 - \sin \delta_1)]/(\sin \delta_1 \cos \gamma_1) \quad (29)$$

The angle δ_1 is the angle of inclination of the forward plane in a cross section perpendicular to the leading edge and is given by

$$\sin \delta_1 = -B + \sqrt{B^2 + C} \quad (30)$$

where

$$B = \frac{\rho_{lr} (C_{r_1} \cos \gamma_1 - t_r)}{\frac{t_r^2}{4} + (C_{r_1} \cos \gamma_1 - \rho_{lr})^2}, \text{ and} \quad (31)$$

and

$$C = \frac{\frac{t_r^2}{4} - \rho_{lr}^2}{\frac{t_r^2}{4} + (C_{r_1} \cos \gamma_1 - \rho_{lr})^2} \quad (32)$$

Using a similar analysis,

$$\tan \gamma_3 = \frac{b/2 \tan \gamma_2 + C_{r_2} - C_{t_2}}{b/2} \quad (33)$$

where C_{t_2} is given by equations similar to Equations (29) through (32) using the subscript "2".

For the biconvex case,

$$\rho_{lt} = \rho_{lr} C_t/C_r, \quad (34)$$

$$t_t = t_r C_t/C_r, \text{ and} \quad (35)$$

$$\rho_{tt} = \rho_{tr} C_t/C_r. \quad (36)$$

Equations (34) through (36) follow from the requirement of piecewise similarity.

2.1.2.1 AXIAL FORCE

Axial force components are broken down into a linear superposition of wave friction and base components for each fin. In addition, the tail affects the incremental base axial force given by Equation (20). The total axial force for fins is given by the sum of the forces per fin times the number of fins (2 or 4 assumed per set). The canard and tail fin set forces are added. The only interference is the incremental base force due to the tail (four fins only). In addition, the fin normal forces in the presence of a body in the case of a fin deflection have component $C_{NF(B)} \sin \delta_F$ contributions to the axial force. The angle δ_F is the fin control deflection.

2.1.2.1.1 WAVE AXIAL FORCE

2.1.2.1.1.1 LOW SUPERSONIC FLOW ($1.05 \leq M_\infty \leq M_\ell$). The transonic wave axial force is a simple linear decay to zero from the value at $M_\infty = 1.05$ given by the model presented here.

The basic model equation is the first order linear potential model which was applied to the first order lift and drag problem for the body-alone case.

$$\beta^2 \phi_{xx} - \phi_{yy} - \phi_{zz} = 0 \quad (37)$$

where

ϕ is the disturbance potential,

x, y lie in the plane of the free stream velocity vector, and

z is up.

The boundary conditions are applied at $z = 0$ and the spanwise contributions are neglected. A source distribution in the x, y plane is used to satisfy the differential equation. Application of the limit as $z = \pm 0$ determines the source distribution strength as a local solution in analogy with slender body theory. Thus, for the lift or drag problem,

$$\phi(x, y, \pm 0) = \mp \frac{1}{\pi} \int_{\sigma} \int \frac{w(\xi, \eta) d\xi d\eta}{\sqrt{(x-\xi)^2 - \beta^2(y-\eta)^2}} \quad (38)$$

where σ , the hyperbolic influence region upstream, is defined by

$$(x-\xi)^2 - \beta^2 (y-\eta)^2 = 0.$$

For the drag problem,

$$w(\xi, \eta) = \pm \frac{1}{2} \frac{\partial t}{\partial \xi}(\xi, \eta)$$

where t is the thickness distribution. From similarity, the slope distribution is the same in every chord plane for every piecewise continuous part of the cross section. For the biconvex case, $\frac{\partial t}{\partial x}(x/c)$ is continuous. For the modified wedge, $\frac{\partial t}{\partial x}$ is discontinuous. The integration region is bounded by the projection of the upstream Mach cone onto the x, y plane and its intersection with the leading edge and side edges of the planform consisting of two fins placed together. No intersection of the opposite side is considered. The numerical method of Reference 2 superimposes basic solutions for constant slope regions.

The $C_p(x, y)$ distribution is given by

$$C_p(x, y) = -2 \frac{\partial \phi}{\partial x}. \quad (39)$$

Note that this is the pressure coefficient for $\alpha = 0$, $\delta_F = 0$. For a subsonic generator (lines associated with angles $\gamma_1, \gamma_2, \gamma_3, \gamma_4$), C_p has an integrable singularity.

For the blunted leading edge case, a modified Newtonian distribution is assumed to apply from the stagnation point to the end of the cylindrical section. The pressure coefficient, C_p , is then discontinuous at this "match" point. The thin wing theory is used from the forward junction to any similar junction with a

trailing edge radius. It is assumed that separation occurs after the rear cylinder-airfoil junction and that no contribution to wave axial force occurs past this junction. The fin base force is considered later.

Once C_p is obtained, the wave axial force coefficient for a single fin is given by

$$C_{AW} = \frac{1}{S_{ref}} \int_0^{b/2} \int_{y \tan \gamma_1}^{y \tan \gamma_1 + C(y)} C_p(x, y) \frac{\partial t}{\partial x} dx dy \quad (40)$$

Here $C(y)$ is the local chord. For the wing alone case S_{ref} is the planform area for two fins. Otherwise,

$$S_{ref} = \frac{\pi D^2}{4}.$$

Note that, for $\gamma_3 < 0$ or $\gamma_4 < 0$, the planform is modified so that $\gamma_3 = 1^\circ$ or $\gamma_4 = 1^\circ$. For such a planform, the resultant axial force is higher than for the given planform. For greater detail, see Reference 2.

2.1.2.1.1.2 TRANSONIC FLOW ($M_\infty < 1.05$). A linear decay from the value at $M_\infty = 1.05$ to zero at $M_\infty = .85$ is assumed such that

$$C_{AW} = 5 C_{AW(M_\infty=1.05)} (M_\infty - .85), \quad .85 < M_\infty < 1.05 \quad (41)$$

$$C_{AW} = 0 \text{ for } M_\infty \leq .85.$$

2.1.2.1.1.3 HIGH SUPERSONIC FLOW ($M_\infty > M_2$). The theory used to determine the lifting surface properties is given and evaluated in Reference 4. The theory used to determine the pressure is based on two-dimensional supersonic flow properties. At a given point on the surface, the slope of the surface relative to the undisturbed free stream is determined first. If this angle makes a compression surface, the pressure is calculated from oblique shock theory using the inclination angle. If the angle indicates an expansion surface, the pressure is calculated from Prandtl-Meyer theory. There is no spanwise variation of the pressure distribution. For blunt leading or trailing edges, a Newtonian distribution is assumed as before.

The axial force is given by an equation similar to Equation (40). However, in this case the lift and drag problems are solved simultaneously. The single fin axial force is given by

$$C_{Aw} = \frac{1}{2S_{ref}} \int_0^{b/2} \int_{y \tan \gamma_1}^{C(y) + y \tan \gamma_1} \left(C_{pU} + C_{pL} \right) \frac{\partial t}{\partial x} dx dy \quad (42)$$

where U and L refer to upper and lower surface values, respectively.

2.1.2.1.2 SKIN FRICTION AXIAL FORCE

The model here is essentially the same as for the body alone case. For a single fin,

$$C_{AF} = \frac{S_w}{S_{ref}} \left[C_F + \frac{R_{NC}}{R_{NL}} \left(\frac{1.328}{\sqrt{R_{NC}}} - C_{FC} \right) \right] \quad (43)$$

where

$S_w = b(C_r + C_t)/2$ and is the wetted area for a single fin.

Here, R_{NC} is 5×10^5 and R_{NL} is based on the mean aerodynamic chord

$$\bar{C} = 2/3 \frac{(C_t^3 - C_r^3)}{(C_t^2 - C_r^2)} \quad (44)$$

From flat plate subsonic strip theory, the fin x_{cp} lies on the quarter chord where $C = \bar{C}$.

2.1.2.1.3 TRAILING EDGE SEPARATION FORCE

The model is based on the base pressure for flow over a two-dimensional or semi-infinite (in spanwise direction) flat plate. This pressure is given by a table lookup interpolation function of Mach number. For a single fin,

$$C_{AB} = \frac{b C_{pB}(M_\infty)}{2S_{ref}} [\rho_{tr} + \rho_{tt}] \quad (45)$$

2.1.2.1.4 EFFECT OF A FIN ON THE BASE DRAG OF THE BODY

In this case, Equation (20) is replaced by

$$\Delta C_{ABA} = [\alpha (.0035 - .01 x_{AFT}) + C_{PB} (M_\infty) (t_r/C_r - .1x_{AFT})] (R_B/R_{ref})^3 \quad (46)$$

The last part of Equation (46) is dropped for $t_r/C_r \leq .1x_{AFT}$ where x_{AFT} is the distance from the base to the root trailing edge divided by the root chord. For flares, $(R_B/R_{ref})^2$ is used in Equation (46).

2.1.2.2 LIFT AND PITCHING MOMENT

Lift contributions are broken down by the component superposition principal. Here, for the wing alone, which consists of two fins placed together, wing loading is considered first. Subsequently, interference effects are considered.

2.1.2.2.1 SUBSONIC FLOW ($0 < M_\infty \leq .8$)

Equation (37) applies again. The well-known Göthert rule transforms the equation to Laplace's equation for subsonic Mach numbers. From the well-known solution for two-dimensional incompressible flow over a cylinder, a bound circulation may be added to the solution. The circulation contributes the lift. An integral representation of the three-dimensional vector may be obtained by defining a vector potential. The vector potential satisfies a vector Poisson equation. This leads to the well-known analogy with the Biot-Savart law for electromagnetic theory. A Kutta condition is applied at the trailing edge to remove the indeterminacy. After much manipulation and application of boundary conditions, it may be shown (References 19 and 20) that

$$\bar{\beta} \tan \alpha \approx \bar{\beta} \alpha = \frac{1}{8\pi} \int_{-b/2}^{b/2} \int_{x_{LE_0}(y)}^{x_{TE_0}(y)} \frac{\Delta C_{p0}(X_0, Y)}{(y-Y)^2} \left[1 + \frac{x_0 - X_0}{(x_0 - X_0)^2 + (y - Y)^2} \right] dX_0 dY \quad (47)$$

where

$$\Delta C_{p0} = C_{pL0} - C_{pU0} = 2\gamma_0, \quad \bar{\beta} = \sqrt{1 - M_\infty^2} \quad (48)$$

and

ΔC_{p0} is the differential pressure coefficient loading, and

γ_0 is the streamwise circulation per unit length.

The outer integral requires a Mangler principal-value treatment (Reference 20). Here, x_0 and X_0 are the stretched dimensions $x/\bar{\beta}$, $X/\bar{\beta}$. The pressure coefficient differential is given by

$$\Delta C_{p0} = \bar{\beta} \Delta C_p$$

where the subscript 0 refers to the analogous $M_\infty = 0$ case. The compressibility parameter $\bar{\beta}$ cancels when ΔC_{p0} is substituted into Equation (47).

Equation (47) is first transformed to dimensionless variables

$$\chi = \frac{x_0 - x_{LE0}(y)}{x_{TE0}(y) - x_{LE0}(y)}, \quad \xi = \frac{X_0 - x_{LE0}(Y)}{x_{TE0}(Y) - x_{LE0}(Y)}, \quad \text{and} \quad (49)$$

$$\zeta = \frac{y}{b/2}, \quad \eta = \frac{Y}{b/2}. \quad (50)$$

Substituting Equations (49) and (50) into Equation (47) yields

$$\alpha(x, y) = \frac{1}{4\pi b} \oint_{-1}^1 \frac{C(\eta)}{(\xi - \eta)^2} \left[\int_0^1 \Delta C_p(\xi, \eta) K(\xi, \eta) d\xi \right] d\eta \quad (51)$$

where

$$C(\eta) = x_{TE0}(Y) - x_{LE0}(Y), \quad \text{and} \quad (52)$$

$$K(\xi, \eta) = 1 + \frac{x_0 - X_0}{(x_0 - X_0)^2 + (y - Y)^2}. \quad (53)$$

Equation (53) is discontinuous in X_0 at x_0 when $Y = y$. When $X_0 < x_0$, $K = 2$. When $X_0 > x_0$, $K = 0$. $\alpha(x, y) = \alpha$ for the static lifting problem. ΔC_p is given by an approximating function with undetermined coefficients. Equation (51) is evaluated once for each of the coefficients (method of collocation). The coefficients are obtained by matrix inversion.

An assumed functional form (see Reference 21) is given as

$$\Delta C_p(\xi, \eta) = \sum_{j=1}^n \sum_{i=1}^m \Delta C_p(\xi_i, \eta_j) h_i(\xi) g_j(\eta) \quad (54)$$

where

$$h_i(\xi) = \sqrt{\frac{\xi_i}{1-\xi_i}} \sqrt{\frac{1-\xi}{\xi}} \frac{\prod_{k \neq i}^m (\xi - \xi_k)}{\prod_{k \neq i}^m (\xi_i - \xi_k)}, \text{ and} \quad (55)$$

$$g_j(\eta) = \sqrt{\frac{1-|\eta|}{1-|\eta_j|}} \frac{\prod_{\ell \neq j}^n (|\eta| - |\eta_\ell|)}{\prod_{\ell \neq j}^n (|\eta_j| - |\eta_\ell|)} \quad (56)$$

The interpolation pivot points, (ξ_i, ξ_k) , are given by

$$\xi_i = \frac{1}{2} \left\{ 1 - \cos \left[\frac{\pi(2i-1)}{2m-1} \right] \right\}, \quad i = 1, 2, \dots, m. \quad (57)$$

Values of χ_r , chordwise location where the boundary conditions are applied, are

$$\chi_r = 1 - \xi_i, \quad r = 1, 2, \dots, m, \quad i = m - r + 1. \quad (58)$$

The interpolation points, η_j , are given by the n zeros of the Jacobi polynomial

$$\mu(\eta_j) = 0 = \sum_{\ell=0}^n \frac{(-1)^\ell}{2^{2\ell}} \left\{ \frac{m!}{\ell!} \right\}^2 \frac{(2m+2\ell+1)! \eta_j^\ell}{(m-\ell)! (m+\ell)! (2m+1)!} \quad (59)$$

The boundary condition points ξ_s , $s = 1, 2, \dots, n$ are the same as the η_j . The boundary conditions are thus evaluated at a set of $n \times m$ points (χ_r, ξ_s) $r = 1, 2, \dots, m$; $s = 1, 2, \dots, n$. The functional form for ΔC_p contains the leading edge singularity for a two-dimensional flat plate, satisfies the Kutta condition ($\Delta C_p = 0$) at the trailing edge, and satisfies the tip loading condition ($\Delta C_p = 0$). The program is coded effectively as $m = 3$ and $n = 8$. However, four η points are chosen for $\eta > 0$ and four points are chosen for $\eta < 0$. Two functions are thus needed for ΔC_p , one for $\eta > 0$ and one for $\eta < 0$. For the lifting problem, $\Delta C_p(\xi_i, \eta_j)$ is even valued in η .

The normal force and pitching moment ($x_{cg} = 0$) coefficients are given by

$$C_N = \frac{2}{S_{ref}} \int_0^{b/2} \int_{y \tan \gamma_1}^{y \tan \gamma_1 + C(y)} \Delta C_p(x, y) dx dy, \text{ and} \quad (60)$$

$$C_m = - \frac{2}{S_{ref} C_{ref}} \int_0^{b/2} \int_{y \tan \gamma_1}^{y \tan \gamma_1 + C(y)} (x + \bar{x} C_{ref}) \Delta C_p dx dy \quad (61)$$

where \bar{x} is the location of the wing apex from the origin in calibers. For the wing alone case, $\bar{x} = 0$ and $C_{ref} = \bar{C}$ as given in Equation (44), and S_{ref} is the planform area for two fins.

2.1.2.2.2 LOW SUPERSONIC FLOW ($1.2 \leq M_\infty \leq M_{\ell_e}$)

The Mach number, M_{ℓ_e} , separates low supersonic computations from high supersonic computations for the wing static and dynamic lifting and interference aerodynamics. M_{ℓ_e} is a program input chosen as high as practical for the thin wing theory application (usually $4.0 < M_{\ell_e} < 5.0$) as this provides a better comparison with inviscid lift and moment coefficient data than the strip theory.

The basic solution of Equation (37) for a thin wing is given by

$$\phi = \mp \frac{1}{\pi} \int_{\sigma} \int \frac{w(\xi, \eta) d\xi d\eta}{\sqrt{(x-\xi)^2 - \beta^2(y-\eta)^2}} \quad (62)$$

where

$w(\xi, \eta) = -\alpha$ on the wing only.

In this case, the area of influence, σ , contains points which are not on the wing. For points off the wing, $w(\xi, \eta)$ is not zero as was the case for the symmetric axial force problem.

The leading edge may be supersonic or subsonic. The trailing edge is restricted to the supersonic case. If the trailing edge is subsonic, the input Mach number is increased so that the trailing edge is slightly supersonic. The swept-forward trailing edge case presents no problems. Again no influence of an opposite half wing tip is assumed; the Mach number is increased

for those low-aspect ratio planforms where this occurs. For a more detailed explanation and evaluation, see Reference 2.

The supersonic leading edge case is the simplest. Three subcases are delineated.

Figure 5 indicates Case 1 when the Mach lines from the apex and leading edge at the tip do not intersect. For this case, three zones bounded by the x axis, right Mach line from the root apex, and left Mach line from the tip apex are defined. The regions are designated as 1, 2, and 3. Typical σ areas of integration are bounded by corresponding numerals 1, 2, and 3. For region 3, the σ area of influence is determined by the method of Evvard and Krasilchikova (Reference 20). For explicit ΔC_p relations, see Reference 2.

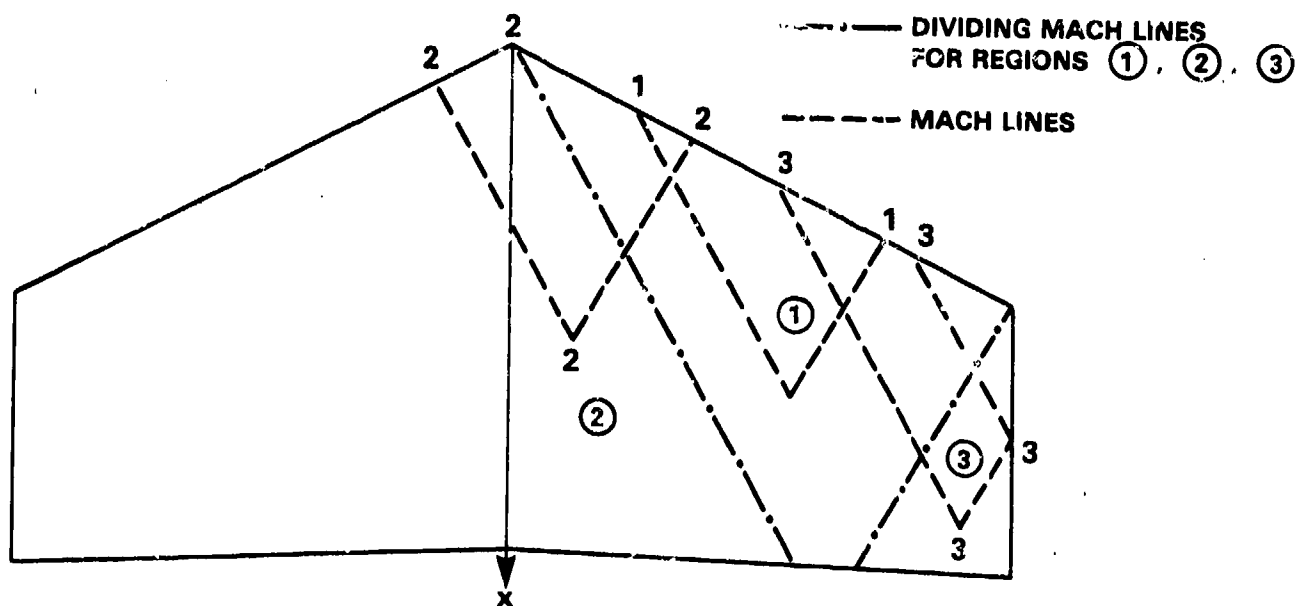


Figure 5. Supersonic Leading Edge Flat Plate Planform, Case 1
($M_\infty = 2$)

A second supersonic leading edge situation, Case 2, is shown in Figure 6. Here the two Mach lines intersect and the root chord apex Mach line intersects the trailing edge. M_∞ is lower for this case.

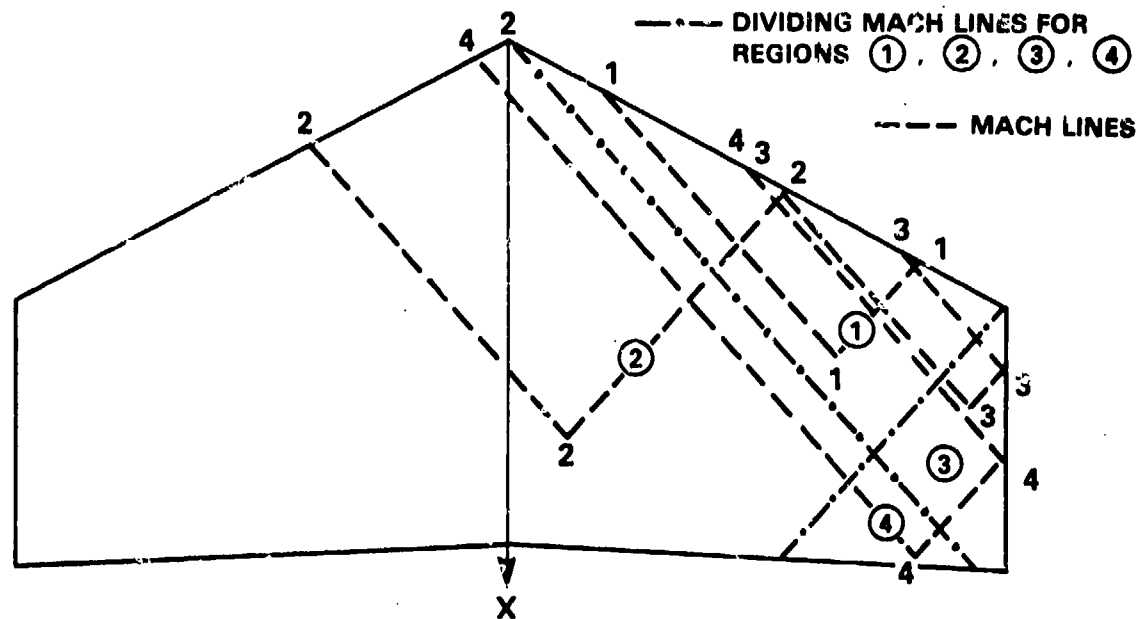


Figure 6. Supersonic Leading Edge Flat Plate Planform,
Case 2 ($M_\infty = 1.5$)

Four zones are obtained this time, as indicated in Figure 6.

In Figure 7 (Case 3), the apex Mach line intersects the side edge. Only the integration area for zone 5 is shown this time. In this case,

$$\Delta C_p = (\Delta C_p)_2 - (\Delta C_p)_5.$$

$(\Delta C_p)_5$ refers to an equivalent integration tip region contribution. The approach taken in Reference 2 seems to be more complex.

The approach for the subsonic leading edge case is much more complex than the supersonic leading edge case. Figure 8 indicates the regions of interest and integration influence region.

For the case of Figure 8, no part of the side or leading edge is supersonic. Here, w is unknown between the planform and the apex Mach lines. For region 1, the solution is given by transforming Equation (37) in conical flow variables to a two-dimensional Laplace equation in a cross section perpendicular to the Mach

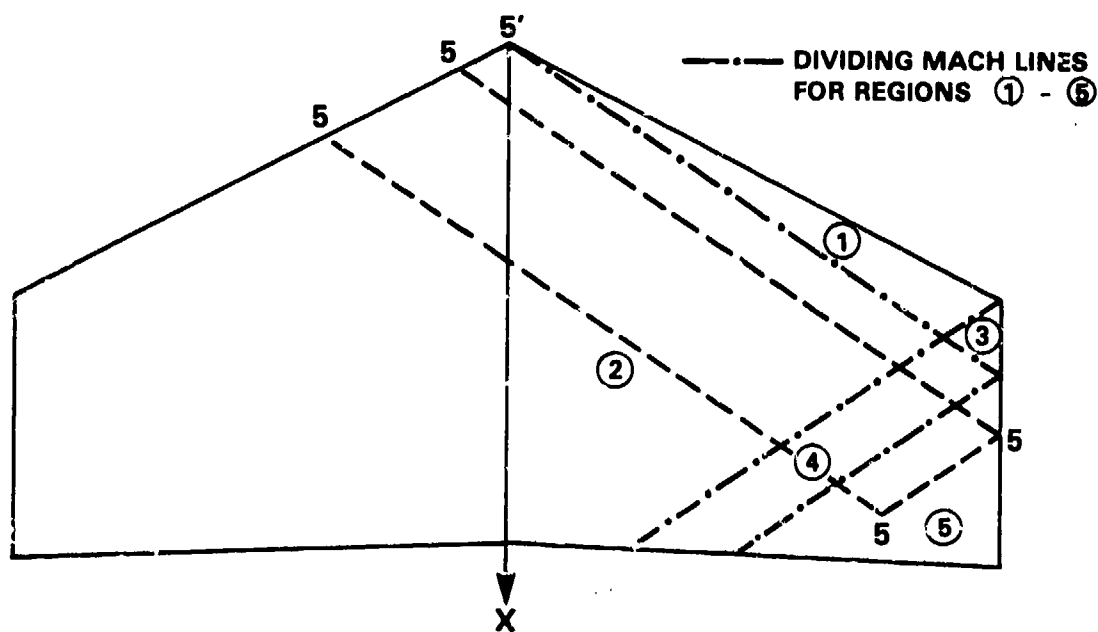


Figure 7. Supersonic Leading Edge Flat Plate Planform,
Case 3 ($M_\infty = 1.2$)

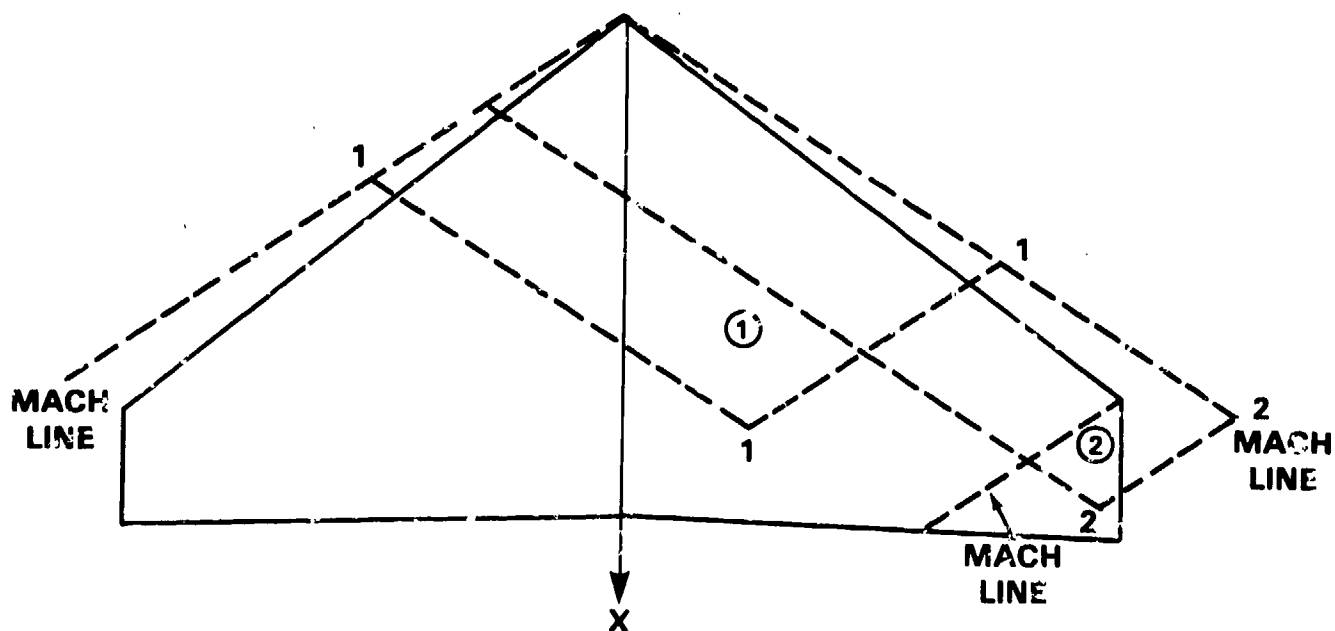


Figure 8 Subsonic Leading Edge Flat Plate Planform
($M_\infty = 1.2$)

cone from the apex. For points in region 2, an additional tip solution must be added to cancel lift off the wing. The ΔC_p relations are given in Reference 2.

2.1.2.2.3 TRANSONIC FLOW ($.8 < M_\infty < 1.2$)

Thickness effects are neglected for the subsonic and supersonic flow regimes. The approach taken in transonic flow is the same as that in DATCOM (Reference 22). Details are also given in Reference 2.

A linear interpolation in a table of C_{N_α} values is used. At $M_\infty = .8$ and $M_\infty = 1.2$, C_{N_α} is computed using the subsonic and low supersonic models. Three additional Mach numbers are then computed: M_{fb} , $M_a = M_{fb} + .07$, and $M_b = M_{fb} + .14$ where M_{fb} , the force break Mach number, is obtained by a table lookup interpolation. First, a force break Mach number, $(M_{fb})_0$, for an equivalent rectangular planform is obtained as a table lookup function of \bar{t}/\bar{C} and aspect ratio. The thickness \bar{t} is taken at the mean aerodynamic chord \bar{C} given by Equation (44). Then, M_{fb} is obtained as a table lookup function of $(M_{fb})_0$ and the sweep of the mid-chord line, $\gamma_{1/2}$. Next, C_{N_α} at M_{fb} , M_a , and M_b are computed where the theoretical value of C_{N_α} at M_{fb} is first given from lifting line theory as

$$(C_{N_\alpha})_{fbt} = \frac{2\pi(AR)}{2 + [AR^2(\bar{\beta}^2 + \tan^2 \gamma_{1/2}) + 4]^{1/2}} \quad (63)$$

where

AR is the aspect ratio, and

$$\bar{\beta} = \sqrt{|1 - M_\infty^2|}.$$

Then,

$$(C_{N_\alpha})_{fb} = (C_{N_\alpha})_{fbt} \frac{(C_{N_\alpha})_{fb}}{(C_{N_\alpha})_{fbt}} \quad (64)$$

The ratio in Equation (64) is given as a table lookup function of \bar{t}/\bar{C} and aspect ratio. Then $(C_{N_\alpha})_a$ and $(C_{N_\alpha})_b$ are given as

$$(C_{N_\alpha})_a = (1 - K_a) (C_{N_\alpha})_{fb}, \text{ and} \quad (65)$$

$$(C_{N_\alpha})_b = (1 - K_b) (C_{N_\alpha})_{fb} \quad (66)$$

where K_a is given as a table lookup function of \bar{t}/\bar{c} and AR and K_b is given as a table lookup function of \bar{t}/\bar{c} . The final value of C_{N_α} is obtained by a linear interpolation in a table of the five values which have been computed.

The x_{cp} is given by a linear interpolation between the value at $M_\infty = .8$ and the value at $M_\infty = 1.2$.

2.1.2.2.4 HIGH SUPERSONIC FLOW ($M_\infty > M_{\ell_e}$)

The tangent wedge method has been previously outlined in connection with the wing wave axial force. For lifting properties, defined in terms of C_{pU} and C_{pL} , one obtains:

$$C_N = \frac{2}{S_{ref}} \int_0^{b/2} \int_{y \tan \gamma_1}^{y \tan \gamma_1 + C(y)} (C_{pL} - C_{pU}) dx dy, \text{ and} \quad (67)$$

$$C_m = - \frac{2}{S_{ref} C_{ref}} \int_0^{b/2} \int_{y \tan \gamma_1}^{y \tan \gamma_1 + C(y)} (x + \bar{x} C_{ref}) (C_{pL} - C_{pU}) dx dy. \quad (68)$$

2.1.2.3 INTERFERENCE LIFT

The total lift as given by component buildup is discussed rather extensively in Reference 2. For $M_\infty > M_{\ell_e}$, interference is not considered. For $M_\infty \leq M_{\ell_e}$, interference factors are obtained from slender body with certain correction factors taking into account canard and body vortex wakes as well as lifting surface proximity to the body base. Compressibility corrections are also made.

2.1.2.3.1 LIFTING SURFACE-BODY INTERFERENCE

The first problem to be considered is that of an undeflected lifting surface-body combination at angle-of-attack. For the combination, the lift is given by

$$L_C = K_C L_F \quad (69)$$

where

$$K_C = K_{B(F)} + K_{F(B)} + K_B, \quad (70)$$

$$K_{B(F)} = L_{B(F)} / L_F, \quad (71)$$

$$K_{F(B)} = L_{F(B)} / L_F, \text{ and} \quad (72)$$

$$K_B = L_B / L_F \quad (73)$$

and where

L_F is the lift of the fin alone (2 fins placed together),

$L_{B(F)}$ is lift on the body due to the presence of the fins,

$L_{F(B)}$ is the lift on the fin in the presence of a body,

L_B is the body alone lift,

L_B and L_F are predicted from the theories already described, and

$K_{B(F)}$ and $K_{F(B)}$ are given by slender body theory (see Reference 23).

Figure 9 shows a triangular fin and body combination planform view.

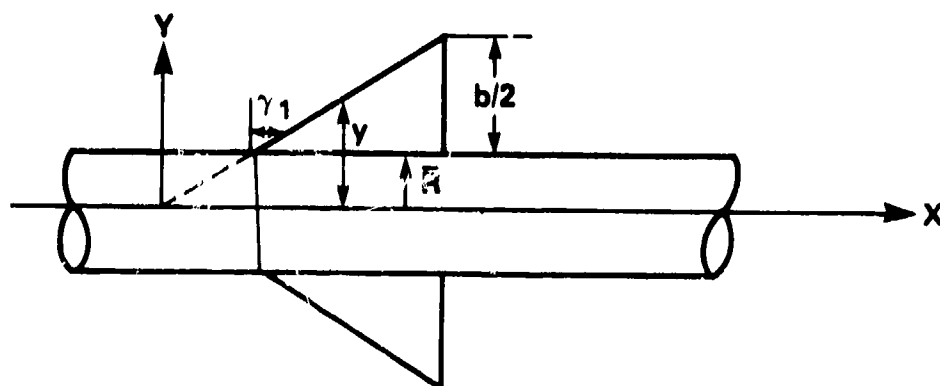


Figure 9. Triangular Fin and Body Combination

Slender fin-body theory (radial distance small from the axis) shows that the lift problem solution is given by a local solution of Laplace's equation in the cross flow plane. Solution of Laplace's equation is readily obtained with the

aid of the Joukowski and Swartz-Christoffel transformations. \bar{R} is a mean local radius.

The resulting vertical loading coefficients are given in terms of $\frac{dR}{dx}$, $\frac{dy}{dx}$, R , Y , and y . Integration over the individual wing and body planform areas gives

$$K_{F(B)} = \frac{4}{\pi(\Lambda-1)^2} \left[\frac{(\Lambda^2 + \frac{1}{\Lambda^2})}{2} \pi/2 - \frac{(\Lambda + \frac{1}{\Lambda})^2}{4} \sin^{-1}\left(\frac{2\Lambda}{\Lambda^2 + 1}\right) - \frac{(\Lambda - \frac{1}{\Lambda})}{2} \right] = W(\Lambda), \text{ and} \quad (74)$$

$$K_{B(F)} = \left(1 + \frac{1}{\Lambda}\right)^2 - K_{F(B)} = B(\Lambda) \quad (75)$$

where

$$\Lambda = \frac{b/2 + \bar{R}}{\bar{R}}$$

If the trailing edge remains straight or swept forward, the results in Equations (74) and (75) apply. However, for the swept forward trailing edges, $K_{F(B)}$ and $K_{B(F)}$ are zero if the pressure loading is integrated to the trailing edge. The argument given in Reference 23 is that the planform beyond where y is a maximum contributes nothing to the loading since the forward downwash cancels the angle-of-attack loading on the rear. Therefore, the triangular planform results are assumed to hold for the trapezoidal planform.

For the swept back trailing edge in Figure 10, the solid boundaries for the cross section are different downstream from the root trailing edge. In

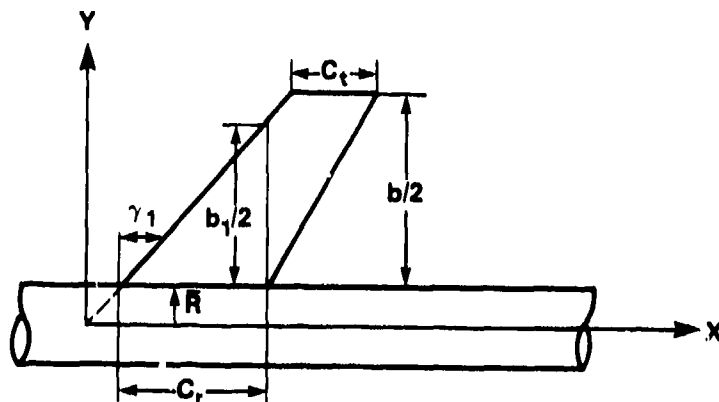


Figure 10. Swept Back Trailing Edge Fin and Body Combination

Reference 2 the following modifications are made:

$$K_{B(F)} = B(\Lambda) G, \text{ and} \quad (76)$$

$$K_{F(B)} = 1 + (W(\Lambda) - 1)G \quad (77)$$

where

$$G = \frac{C_r}{b/2 \tan \gamma_1 + C_t} \quad (78)$$

When $B(\Lambda) = 0$, $W(\Lambda) = 1$, the large aspect ratio limits are obtained. The $G = 1$ limit corresponds to straight or swept forward trailing edges. The case when $b/2 \tan \gamma_1 < C_r < b/2 \tan \gamma_1 + C_t$ needs additional investigation. For this case, the cross sections are the same up to the root trailing edge as that for which Equations (74) and (75) were derived. The forward downwash would then cancel the rear planform loading. For the case when $C_r < b/2 \tan \gamma_1$, G might be replaced by

$$G = \frac{(b_1)/2 + \bar{R}}{b/2 + \bar{R}}.$$

In addition, there is a lift contribution by a finite control deflection

$$C_{NF(B)} = k_{F(B)} (C_{N_\alpha})_F \delta_F \quad (79)$$

The potential problem in the crossflow plane ($\alpha = 0$) consists of a uniform downwash on the lifting surface in an undisturbed far-flow field (see Reference 23). In addition,

$$\begin{aligned} C_{NB(F)} &= (k_{F(B)} - k_{F(B)}) (C_{N_\alpha})_F \delta_F \\ &= (W(\Lambda) - \Delta(\Lambda)) (C_{N_\alpha})_F \delta_F \end{aligned} \quad (80)$$

An explicit relationship for $k_{F(B)}$ is given in Reference 2. For a swept trailing edge a correction is made as before:

$$k_{F(B)} = 1 + [\Delta(\Lambda) - 1] G, \text{ and} \quad (81)$$

$$k_{B(F)} = [W(\Lambda) - \Delta(\Lambda)] G. \quad (82)$$

Equation (75) for B is used for subsonic Mach numbers and Mach numbers up to when the Mach line from the leading edge of the tip does not intersect the body section perpendicular to the root chord. Figure 11 illustrates three possible

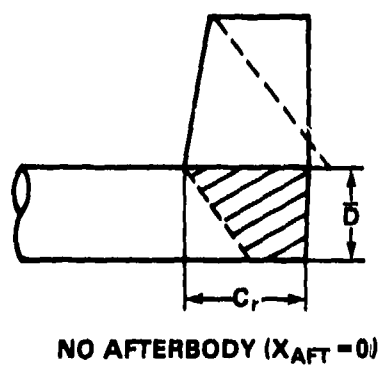
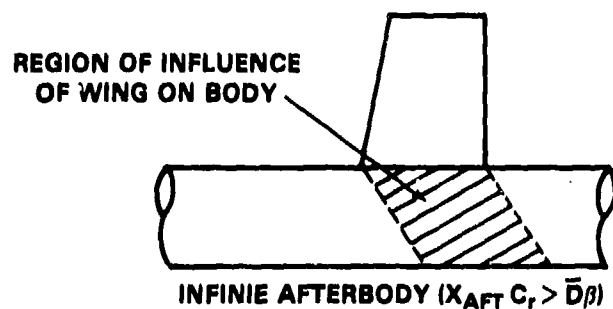
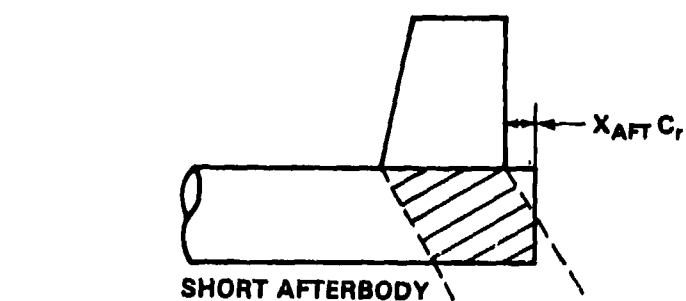


Figure 11. Determination of $K_{B(F)}$ for High Aspect-Ratio
Range at Supersonic Speeds

subcases. In this case, the body loading area is redefined by the crosshatching. The criteria for this case is given by

$$\beta > \frac{2C_r}{b} - \tan \gamma_1 . \quad (83)$$

For the no-afterbody case, B_{NA} is a function of C_r/β . For $\beta \bar{D} \geq C_r$ (the Mach line from the root chord leading edge intersects the end of the body), C_r/β is set equal to \bar{D} . Subcases for the no after body case are subsonic and supersonic leading edges. Subsonic leading edge values of B_{IA} are given for the infinite afterbody value case of x_{AFT} . The short afterbody computation of B_{SA} is given by the linear interpolation where ($x_{AFT} C_r < \bar{D}\beta$):

$$B_{SA} = \frac{[B_{IA} - B_{NA}]}{\bar{D}\beta} x_{AFT} C_r + B_{NA} . \quad (84)$$

2.1.2.3.2 WING-TAIL INTERFERENCE

Thus far only body-lifting surface interferences have been considered. An additional interference is given by vortex effects of the canard or wing on the tail. A single-line vortex is assumed to be shed from each canard panel. The vortex strength relationship and effective lateral location are obtained from the wing loading distribution given by slender wing-body theory. The vortices are assumed to be aligned with the free stream velocity. The canard hinge is assumed to be at the quarter chord. This is enough information to adequately define the vortex locations at the tail. The negative lift coefficient due to the downwash of the canard shed vortex on the tail is given by

$$C_{NT(V)} = (C_{N_\alpha})_W (C_{N_\alpha})_T [K_{W(B)} \sin \alpha + k_{W(B)} \sin \delta_W] \frac{i_T (b'_T - \bar{R}_T)}{2\pi AR_T (f_W - \bar{R}_W)} \left(\frac{S_W}{S_{ref}} \right) . \quad (85)$$

Here, the W subscript refers to the wing or canard, the T subscript refers to the tail, f_W is the span location of the panel vortex obtained from slender

body theory, and i_T is the tail interference factor also obtained from slender body theory. The crossflow potential problem for the tail-body combination consists of the solution for two point vortices of a given strength and location in an undisturbed flow field. b'_T is the tail half-span (including the body radius).

In Reference 2 an expression is given for a negative lift on the tail due to body shed vorticity. This is neglected in the current version of the program.

The normal force coefficient can now be written as

$$\begin{aligned} C_N &= C_{NB} + \left\{ \left[K_{W(B)} + K_{B(W)} \right] \alpha + \left[k_{W(B)} + k_{B(W)} \right] \delta_W \right\} (C_{N_\alpha})_W \\ &\quad + \left\{ \left[K_{T(B)} + K_{B(T)} \right] \alpha + \left[k_{T(B)} + k_{B(T)} \right] \delta_T \right\} (C_{N_\alpha})_T \\ &\quad + C_{NT(V)} \\ &= C_{NB} + C_{NW(B)} + C_{NB(W)} + C_{NT(B)} + C_{NB(T)} + C_{NT(V)} . \end{aligned} \quad (86)$$

At subsonic Mach numbers ($M_\infty \leq .8$), the center of pressure for $C_{NW(B)}$, and $C_{NB(W)}$ are assumed to be at the wing alone center of pressure. For $C_{NT(V)}$, $C_{NT(B)}$, and $C_{NB(T)}$, the x_{cp} are assumed to coincide with the tail alone x_{cp} .

For supersonic flow $C_{NB(W)}$ and $C_{NB(T)}$, the x_{cp} values are assumed to be given by the centroid of the areas in Figure 11. At transonic speeds the center of pressure values are given by linear interpolation between the values at $M_\infty = 1.2$ and $M_\infty = M_{fb}$.

2.1.3 HIGH ANGLE-OF-ATTACK AERODYNAMICS

The current approach is empirically based on, and is an adaption of, the method described in Reference 24.

The range of input parameters for a cruciform configuration is limited to:

1. $.8 < M_\infty < 3.0$;
2. Angle-of-attack 0° to 180° for isolated components (roll angle 0°) and 0° to 45° for body-tail combinations at arbitrary roll angles from 0° to 180° ;

3. Tail: trapezoidal planform, side edges parallel to the body centerline;
 - A. Leading edge sweep angle: 0° to 70° ;
 - B. Taper ratio: 0 to 1;
 - C. Aspect ratio (two panels): .5 to 2.0;
 - D. Trailing edge straight and parallel to end of body;
4. Nose length (pointed tangent ogive): 1.5 to 3.5 calibers;
5. Cylindrical afterbody: 6 to 18 calibers;
6. Total span-to-diameter ratio (two fins): 1 to 3.33.

The roll definition and positive fin load orientation are shown in Figure 12. Note that θ is measured from the windward side.

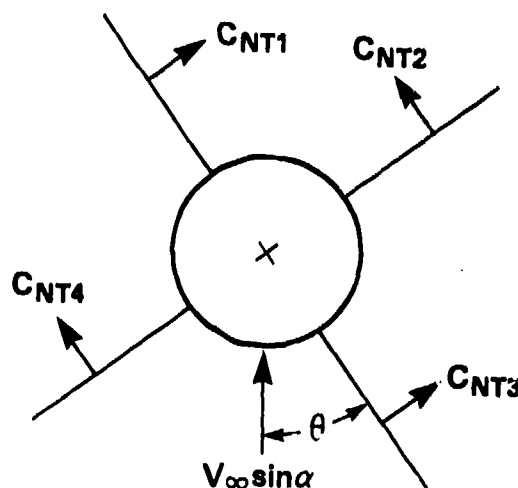


Figure 12. Roll Angle and Fin Load Definitions (Looking Forward)

The axial force coefficient is assumed to be contributed entirely by the body.

The total normal force coefficient is given by

$$C_N = C_{NB} + [(C_{NT1} + C_{NT3}) \sin \theta + (C_{NT2} + C_{NT4}) \cos \theta] S_T / S_{ref} + I_{BT} \quad (87)$$

where C_{NTi} are the individual fin loads in the presence of the body and other fins, and I_{BT} is the tail-to-body carryover normal force coefficient (i.e., $C_{NB(T)}$).

The longitudinal center of pressure from the nose for the entire configuration is given by

$$x_{cp} = \left\{ x_{cpB} C_{NB} + [\sin \theta (x_{cpT1} C_{NT1} + x_{cpT3} C_{NT3}) + \cos \theta (x_{cpT2} C_{NT2} + x_{cpT4} C_{NT4})] S_T/S_{ref} + I_{BT} x_{cpi} \right\} / C_N \quad (88)$$

where

x_{cp} values are given in calibers,

x_{cpB} is the body alone x_{cp} ,

x_{cpTi} are the individual tail x_{cp} values in the presence of the body and other fins, and

x_{cpi} is the center of pressure for the carryover load.

If one neglects the small body frictional roll coefficient and the tail carryover onto the body, one can estimate the static roll coefficient as

$$C_{\ell} = \frac{1}{2} S_T/S_{ref} \sum_{i=1}^4 C_{NTi} \sin [(i^2 - i + 1) \pi/2] [1 + b/D (y_{rpi} / b/2)] \quad (89)$$

Details of the functional forms are given in Reference 24.

2.2 DYNAMIC DERIVATIVES

Dynamic derivative prediction is for small angles-of-attack ($\alpha = 0$) only.

2.2.1 BODY ALONE

2.2.1.1 ROLL DAMPING AND BODY MAGNUS MOMENT

These coefficients are given empirically. The data base is configuration limited. Coefficient Mach number dependence was $0 < M_{\infty} < 5$. An asymptote is

assumed at $M_\infty = 5$. Geometric parameters entering the empirical functional form are the total length, center of moments location, and boattail length, all in calibers. The boattail length is limited to 1.5 calibers for the Magnus moment coefficient computation. The Magnus moment coefficient $C_{m\dot{\alpha}}$ is computed at 1° and 5° angles-of-attack. Magnus moment coefficients are not estimated for bodies with lifting surfaces.

2.2.1.2 PITCH DAMPING COEFFICIENT

The original prediction used the empirical prediction. The method described in References 25 and 26 was intended to improve the $C_{mq} + C_{m\dot{\alpha}}$ prediction. Evaluation of the method is given in Reference 4. Restrictions are:

(1) Initial cylindrical radius for a spherically blunted or truncated body is limited to less than .25 calibers.

(2) Contribution of afterbody and boattail or flare are neglected at higher Mach numbers.

In subsonic flow, $C_{mq} + C_{m\dot{\alpha}}$ is given by a relation based on slender body theory:

$$C_{mq} + C_{m\dot{\alpha}} = -4 (.77 + .23 M_\infty^2) (L \sqrt{.77 + .23 M_\infty^2} - x_{cg})^2. \quad (90)$$

Here, L is the total length in calibers, and x_{cg} is the center of moment location from the nose in calibers.

Hypersonic (embedded Newtonian) flow approximations are applied above a certain Mach number $M_\infty = M^*$ associated with an effective hypersonic velocity parameter of .4 such that

$$M^* = .4 \csc \theta^* \quad (91)$$

$$\theta^* = \tan^{-1} \left(\frac{1}{2L_N} \right). \quad (92)$$

If $M^* < 1.5$, then $M^* = 1.5$ is chosen. For $1 < M_\infty < M^*$ a linear interpolation is used where

$$C_{mq} + C_{m\dot{\alpha}} = \frac{M^* - M_\infty}{M^* - 1} (C_{mq} + C_{m\dot{\alpha}})_{M_\infty = 1} + \frac{M_\infty - 1}{M^* - 1} (C_{mq} + C_{m\dot{\alpha}})_{M_\infty = M^*} \quad (93)$$

For $M_\infty \geq M^*$, a direct application of a modified Newtonian pressure distribution at $\alpha = 0$ for the pitching motion gives

$$C_{mq} + C_{m\dot{\alpha}} = -16 \int_0^{L_N} \frac{C_{po} C_Y (x - x_{cg} + RR')^2 RR'}{1 + R'^2} dx \quad (94)$$

Note that for a spherically blunted body the contribution of the spherical cap is neglected. The stagnation pressure coefficient, C_{po} , behind a bow shock is approximated for large Mach numbers as

$$C_{po} = \frac{\gamma + 3}{\gamma + 1} \left[1 + \frac{1.5}{\gamma + 3} \frac{1}{M_\infty^2} \right] \quad (95)$$

and C_Y is given as

$$C_Y = \begin{cases} 1.01 + 1.31 [\log (10 M_\infty \sin \epsilon)]^{-7/3} & M_\infty \sin \epsilon \geq .4 \\ 1.625 & M_\infty \sin \epsilon < .4 \end{cases} \quad (96)$$

The Lockheed Missiles and Space Company (LMSC) model was assumed to be able to replace the empirical method for the body-alone pitch damping coefficient. Since the LMSC prediction neglects the effects of afterbody and boattail at supersonic Mach numbers, the empirical method often predicts better values for pitch damping. For this reason and because of other limitations for bodies with lifting surfaces, the pitch damping prediction method is currently an input option to the code.

The LMSC body-alone algorithm was extensively evaluated by R. Whyte in Reference 27. A conclusion reached in Reference 27 is that the LMSC algorithm is adequate for most applications. For certain nose-afterbody configurations with the x_{cg} located forward, poor results were obtained when compared with data at

supersonic Mach numbers. The code was modified for these cases. When the value of C_{mq} predicted is less negative than that predicted by the empirical method and not within 75 percent of the empirical value, the empirical value is chosen.

2.2.2 LIFTING SURFACE DYNAMIC DERIVATIVES

The rolling rate is assumed small and, hence, Magnus moment is neglected.

2.2.2.1 ROLL DAMPING

2.2.2.1.1 SUBSONIC FLOW ($0 < M_\infty \leq 0.8$)

Equation 51 is again applicable. The effective angle-of-attack is given by $\alpha(x,y) = \frac{pY}{V}$. In this case, the resultant $(\Delta C_p)_p$ obtained by matrix inversion is odd-valued in η .

With $(\Delta C_p)_p = (\overline{\Delta C_p})_p p/V_\infty$, C_{lp} is given as

$$C_{lp} = C_l / -\frac{pC_{refp}}{2V_\infty} \quad (97)$$

where C_{refp} is b for the wing-alone case. Using the definition in Equation (97) one obtains

$$C_{lp} = -\frac{2N}{S_{ref} C_{refp}^2} \int_0^{b'} \int_{y \tan \gamma_1}^{y \tan \gamma + C(y)} y (\overline{\Delta C_p})_p dx dy \quad (98)$$

Note that the planform considered is that obtained by extending the leading and trailing edges to the body centerline. b' is the total span.

2.2.2.1.2 LOW SUPERSONIC FLOW ($1.2 \leq M_\infty \leq M_{le}$)

The approach used for the static lift problem is applicable here. In this case, $w(\xi, \eta) = -\frac{p\eta}{V_\infty}$ is not a constant.

The approach for subsonic and supersonic leading edges is similar to that used for the static lift problem. Specific relationships for $(\Delta C_p)_p = p/V_\infty (\overline{\Delta C_p})_p$

are given in Reference 3. The modified planform considered for subsonic flow is used again.

2.2.2.1.3 TRANSONIC FLOW ($.9 < M_\infty < 1.2$)

An empirical approach is taken here. It is assumed that the C_{lp} variation is similar to that for C_{N_α} such that

$$(C_{lp})_{M_\infty} = (C_{lp})_{M_{ref}} \frac{(C_{N_\alpha})_{M_\infty}}{(C_{N_\alpha})_{M_{ref}}} \quad (99)$$

This is somewhat similar to the approach of Reference 28. Equation (99) is used with $M_{ref} = .8$ to establish C_{lp} at $M_\infty = .933$. Equation (99) is then used again to establish C_{lp} at $M_\infty = 1.067$ with $M_{ref} = 1.2$. Interference corrections are made for each fin at $M_\infty = .8, .933, 1.067$, and 1.2 as explained later. The C_{lp} for the body is added to the lifting surface contributions for the above Mach numbers. The final total C_{lp} value at M_∞ is given by a four-point Lagrange interpolation.

2.2.2.1.4 HIGH SUPERSONIC FLOW ($M_\infty > M_{le}$)

At higher Mach numbers, where $M_\infty > M_{le}$, the potential model for determining the lifting surface roll damping is assumed^e to be invalid.

In analogy with the static prediction for $M_\infty > M_{le}$, the strip loading is assumed to be proportional to the local chord and distance^e from the centerline. The loading is forced to zero at the tip in an elliptical manner. With these assumptions,

$$\begin{aligned} C_{lp} &= \frac{-N(C_{N_\alpha})_F \left(\frac{b}{C_{refp}}\right)^2}{4I_1} \int_0^1 \left(\eta + \frac{\bar{D}}{b}\right)^2 \frac{C(\eta)}{C_r} \sqrt{1 - \eta^2} d\eta \\ &= \frac{-N(C_{N_\alpha})_F}{4I_1} \left(\frac{b}{C_{refp}}\right)^2 \left[I_1 \left(\frac{\bar{D}}{b}\right)^2 + 2 I_2 \left(\frac{\bar{D}}{b}\right) + I_3 \right] \end{aligned} \quad (100)$$

where

$$I_1 = \pi/4 - (1 - \lambda)/3,$$

$$I_2 = 1/3 - (1 - \lambda) \pi/16,$$

$$I_3 = \pi/16 - 2(1 - \lambda)/15,$$

and $(C_N)_F^\alpha$ is the strip theory value for two fins. This approach was evaluated in Reference 4.

2.2.2.2 PITCH DAMPING

The total pitch damping coefficient, $C_{mq} + C_{m\dot{\alpha}}$, is made up of two terms. The first term, C_{mq} , is due to the rotational rate about the moment reference axis. The second term is due to a downward translational acceleration, \dot{w}/V_∞ , perpendicular to the body centerline.

The original method for low Mach numbers was based upon small disturbance lifting theory (Reference 3). The method developed by LMSC as presented in References 25 and 26 was intended to apply over the entire Mach number range at $\alpha = 0$. However, it is limited in lifting surface aspect ratio for low supersonic flows and to one lifting surface. For this and other reasons, the choice of method for pitch damping, as earlier indicated for body pitch damping, is a program input. The LMSC method is based on slender wing-body methods in the subsonic and low supersonic flow regime. At high Mach numbers, it is based upon Newtonian embedded strip theory.

Even if the LMSC option is chosen, the older computational estimate is obtained first in the program flow and the newer estimate subsequently. The LMSC model will be presented in the section on interference.

2.2.2.2.1 SUBSONIC FLOW ($M_\infty \leq .8$)

Rotation about the moment center induces the following angle-of-attack on the wing

$$\alpha(x,y) = \frac{q}{V_\infty} [x + C_{ref} (\bar{x} - x_{cg})] \quad (101)$$

For the wing alone case, $\bar{x} = 0$, $C_{ref} = \bar{C}$, and x_{cg} is given \bar{C} units. Otherwise, \bar{x} and x_{cg} are in caliber units and $C_{ref} = D$.

$(\Delta C_p)_q = (\overline{\Delta C_p})_q q/V_\infty$, obtained by matrix inversion for the collocation approach of Equation (51), is an even-valued distribution in y . Note that the second term in Equation (101) contributes an equivalent constant angle-of-attack lift.

The pitch damping coefficient, C_{mq} , is defined as

$$C_{mq} = \frac{C_m}{\frac{qC_{ref}}{2V_\infty}} \quad (102)$$

Using the definition of Equation (102) one obtains for C_{mq} :

$$C_{mq} = -4 \int_0^{\frac{b'}{2}} \int_{y \tan \gamma_1}^{y \tan \gamma_1 + C(y)} [x + C_{ref} (\bar{x} - x_{cg})] (\overline{\Delta C_p})_q dx dy \quad (103)$$

$$\frac{S_{ref} C_{ref}^2}{}$$

The planform is again extended through to the body centerline. Here, $C_{m\dot{\alpha}}$ is assumed to be zero. A review of Reference 3 indicates that various methods are available for estimating $C_{m\dot{\alpha}}$. However, the computational cost is incompatible with the rapid estimates desired here and the additional accuracy unwarranted.

2.2.2.2.2 LOW SUPERSONIC FLOW ($1.2 \leq M_\infty \leq M_{\lambda_e}$)

The C_{mq} problem proceeds as before:

$$w(\xi, \eta) = -\frac{q}{V_\infty} [\xi + C_{ref} (\bar{x} - x_{cg})] \quad (104)$$

Specific relations for $(\Delta C_p)_q = (q/V_\infty) (\overline{\Delta C_p})_q$ are given in Reference 3 for the variable part of $w(\xi, \eta)$.

The vertical acceleration problem for $\dot{\alpha}$ is an unsteady potential problem which obeys the following equation for the perturbation potential:

$$\frac{\partial^2 \phi}{\partial y^2} - (M_\infty^2 - 1) \frac{\partial^2 \phi}{\partial x^2} = \frac{1}{a_\infty^2} \frac{\partial^2 \phi}{\partial t^2} + \frac{2M_\infty}{a_\infty} \frac{\partial^2 \phi}{\partial x \partial t} \quad (105)$$

where a_∞ is the free stream value of the speed of sound. The boundary condition for the dimensionless vertical velocity is

$$w(\xi, \eta) = -\dot{\alpha} t. \quad (106)$$

Equation (106) may be rewritten as

$$w(\xi, \eta) = -\dot{\alpha} \left(\frac{M_\infty^2}{\beta^2} \frac{\xi}{V_\infty} + t - \frac{M_\infty^2 \xi}{\beta^2 V_\infty} \right). \quad (107)$$

The first term of Equation (107) has the form of the variable part of equation (106). The form of Equation (107) suggests a solution of the form

$$\phi = \dot{\alpha} \left(t - \frac{M_\infty^2}{\beta^2} \frac{x}{V_\infty} \right) \phi_1 + \dot{\alpha} \frac{M_\infty^2}{\beta^2} \phi_2. \quad (108)$$

On the surface $\phi_{1z} = -1$, $\phi_{2z} = -x/V_\infty$. The first term of Equation (108) satisfies the differential Equation (105) and leads to the equation

$$\frac{\partial^2 \phi_1}{\partial y^2} = \beta^2 \frac{\partial^2 \phi_1}{\partial x^2}. \quad (109)$$

Thus it is seen that ϕ_1 is the lifting potential with $\alpha = 1$. It is also seen that ϕ_2 is the potential corresponding to the variable part of C_{mq} with $q = 1$. Equation (108) may be rewritten as

$$\phi = \dot{\alpha} \left(t - \frac{M_\infty^2 x}{\beta^2 V_\infty} \right) \phi_{(\alpha=1)} + \dot{\alpha} \frac{M_\infty^2}{\beta^2} \phi_{(q=1)}. \quad (110)$$

The equivalent of the Bernoulli relationship for the time dependent case is

$$V_\infty \phi_t + \frac{(V_\infty \vec{i} + \vec{\nabla} \phi) \cdot (V_\infty \vec{i} + \vec{\nabla} \phi)}{2} + \frac{a^2}{\gamma-1} = V_\infty^2 + \frac{a_\infty^2}{\gamma-1}. \quad (111)$$

Equation (111), evaluated at $t = 0$ from Equation (110) with the usual small terms of $O(\vec{\nabla} \phi \cdot \vec{\nabla} \phi)$ neglected, yields an estimate of $(\Delta C_p)_\alpha$ as

$$(\Delta C_p)_\alpha = \dot{\alpha} \left[\frac{M_\infty^2}{\beta^2} (\Delta C_p)_{q=1} - \frac{4(\phi)_{\alpha=1}}{\beta^2 V_\infty} - \frac{M_\infty^2 x}{\beta^2 V_\infty} (\Delta C_p)_{\alpha=1} \right]. \quad (112)$$

Explicit relations for $(\Delta C_p)_{\dot{\alpha}} = \frac{\dot{\alpha}}{V_{\infty}} (\overline{\Delta C_p})_{\dot{\alpha}}$ are given in Reference 3. Then, $C_{m\dot{\alpha}}$ is

$$C_{m\dot{\alpha}} = \frac{C_m}{\frac{\dot{\alpha}}{V_{\infty}} \frac{C_{ref}}{2}} = -4 \frac{\int_0^{b/2} \int_{y \tan \gamma_1}^{y \tan \gamma_1 + C(y)} [x + C_{ref} (\bar{x} - x_{cg})] (\overline{\Delta C_p})_{\dot{\alpha}} dx dy}{S_{ref} C_{ref}^2} \quad (113)$$

2.2.2.2.3 TRANSONIC FLOW ($.8 < M_{\infty} < 1.2$)

The approach taken is exactly the same as for C_{lp} .

$$(C_{mq} + C_{m\dot{\alpha}})_{M_{\infty}} = (C_{mq} + C_{m\dot{\alpha}})_{M_{ref}} \frac{(C_{N_{\alpha}})_{M_{\infty}}}{(C_{N_{\alpha}})_{M_{ref}}} \quad (114)$$

Note that at $M_{\infty} = .8$, $C_{m\dot{\alpha}} = 0$. At $M_{\infty} = 1.2$, $C_{m\dot{\alpha}} \neq 0$. The total $C_{mq} + C_{m\dot{\alpha}}$ for the complete configuration includes a canard downwash onto the tail term, $(C_{m\dot{\alpha}})_{T(V)}$, for $M_{\infty} < 1.2$.

2.2.2.2.4 HIGH SUPERSONIC FLOW ($M_{\infty} > M_{le}$)

A simple strip theory model is considered here. $C_{m\dot{\alpha}}$ is not considered.

$$\begin{aligned} C_{mq} &= - \frac{8(C_{N_{\alpha}})_F}{C_{ref}^2 C_r b (1+\lambda)} \int_0^{b/2} \int_{y \tan \gamma_1}^{y \tan \gamma_1 + C(y)} [x + (\bar{x} - x_{cg}) C_{ref}]^2 dx dy \\ &= - \frac{2}{3} \frac{(C_{N_{\alpha}})_F C_{ref}^2}{C_r b (1+\lambda) \tan \gamma_1} \left\{ (\bar{x} - x_{cg})^4 - \left(\frac{b \tan \gamma_1}{2 C_{ref}} + \bar{x} - x_{cg} \right)^4 \right. \\ &\quad - \frac{1}{1 - \frac{b \tan \gamma_1}{2 C_r (1-\lambda)}} \left[\left(\frac{C_r}{C_{ref}} + \bar{x} - x_{cg} \right)^4 - \left(\frac{(b/2) \tan \gamma_1 + C_r \lambda}{C_{ref}} \right. \right. \\ &\quad \left. \left. + \bar{x} - x_{cg} \right)^4 \right] \left. \right\}. \quad (115) \end{aligned}$$

2.2.2.3 DYNAMIC DERIVATIVES FOR TOTAL CONFIGURATION

For roll and pitch damping, no interference is assumed for the high Mach number range. The LMSC pitch damping will be presented separately here.

2.2.2.3.1 SUBSONIC AND LOW SUPERSONIC FLOW

It has already been noted that the lifting surface contribution was obtained for a planform consisting of an extension of the leading and trailing edges to the body centerline.

An additional lifting surface interference is based on slender body theory (see Reference 29). The lifting surface contribution in the presence of the body is given in terms of a span to diameter ratio for C_{lp} :

$$\frac{(C_{lp})_{FB}}{(C_{lp})_{\bar{D}=0}} = f\left(\frac{\bar{D}}{2y}\right). \quad (116)$$

Here, however, $(C_{lp})_{\bar{D}=0}$ is based on the modified planform. For a complete configuration,

$$C_{lp} = (C_{lp})_B + (C_{lp})_{WB} + (C_{lp})_{TB}. \quad (117)$$

A similar fin-body interference term for $C_{mq} + C_{m\dot{\alpha}}$ is given as

$$\frac{(C_{mq} + C_{m\dot{\alpha}})_{FB}}{(C_{mq} + C_{m\dot{\alpha}})_{\bar{D}=0}} = g\left(\frac{\bar{D}}{2y}\right). \quad (118)$$

At Mach numbers below 1.2 an additional $C_{m\dot{\alpha}}$ term due to downwash lag from the canard onto the tail (see Reference 23) is given as

$$(C_{m\dot{\alpha}})_{T(V)} = \frac{2(x_{cpT} - x_{cpw})(x_{cpT} - x_{cgD})}{D^2} \frac{\partial C_{Nl(V)}}{\partial \alpha}. \quad (119)$$

For $M_\infty \geq 1.2$, $(C_{m\dot{\alpha}})_{T(V)} = 0$.

For a complete configuration $C_{mq} + C_{m\dot{\alpha}}$ is given by

$$\begin{aligned} C_{mq} + C_{m\dot{\alpha}} = & (C_{mq} + C_{m\dot{\alpha}})_B + (C_{mq} + C_{m\dot{\alpha}})_{WB} + (C_{mq} + C_{m\dot{\alpha}})_{TB} \\ & + (C_{m\dot{\alpha}})_{T(V)}. \end{aligned} \quad (120)$$

2.2.2.3.2 TRANSONIC FLOW (.8 < M_∞ < 1.2)

The approach for C_{lp} and C_{mq} + C_{mα̇} is the same. Values at M_∞ = .8, .933, 1.067, and 1.2 for the complete configuration are used in a 4-point Lagrange interpolation to obtain total C_{lp} and C_{mq} + C_{mα̇} at a given M_∞.

2.2.2.3.3 LMSC WING-BODY PITCH DAMPING

For M_∞ ≤ 1, slender wing-body theory is used where

$$(C_{mq} + C_{m\dot{\alpha}})_T = (C_{mq} + C_{m\dot{\alpha}})_{TB} - (C_{mq} + C_{m\dot{\alpha}})_B \quad (121)$$

Note that this theory is for a body-tail configuration only.

$$\begin{aligned} (C_{mq} + C_{m\dot{\alpha}})_{TB} = & -4 \left(\frac{\bar{D}_T}{D} \right)^2 (1 - .23 \bar{\beta}^2) \left\{ \left[\bar{x}_T \sqrt{1 - .23 \bar{\beta}^2} - x_{cg} \right]^2 \right. \\ & - \left[\frac{\bar{x}_T D + C_{rT}}{D} - x_{cg} - \bar{C}/D \left(1 - \sqrt{K_{ma}} \right) \right]^2 \left. \right\} \\ & - 4 \left(\frac{b_T}{D} \right)^2 K_{ma} \left[\frac{x_{te}}{D} - x_{cg} - \bar{C}/D \left(1 - \sqrt{K_{ma}} \right) \right]^2 \end{aligned} \quad (122)$$

where

$$\bar{C}/D = \frac{C_{rT}}{D} \left\{ 1 - \left[(1 - \lambda_T) - \frac{b_T}{2C_{rT}} \tan \gamma_1 \right] \bar{\eta} \right\}, \quad (123)$$

$$\bar{\eta} = \frac{1 + 2\lambda_T}{3(1 + \lambda_T)}, \quad (124)$$

$$x_{te}/D = \frac{\bar{x}_T D + C_{rt}}{D} - \frac{C_{rt}}{D} + \bar{C}/D, \quad (125)$$

$$K_{ma} = 2 / \left[1 + \overline{AR} \bar{\beta} / 4 + \sqrt{1 + \left(\frac{\overline{AR} \bar{\beta}}{4} \right)^2} \right], \quad (126)$$

$$\overline{AR} = AR_T \frac{(1 + \bar{D}_T/b_T)}{\left(1 + \frac{\bar{D}_T}{b_T} \frac{1 - \lambda_T}{1 + \lambda_T} \right)}, \quad (127)$$

and \overline{AR} is the modified planform aspect ratio obtained by extending the leading and trailing edges to the body centerline.

For supersonic flow, $1 < M_\infty \leq \sqrt{1 + (AR_T/4)^2}$, Equation (121) applies again.

$$(C_{mq} + C_{m\dot{\alpha}})_{TB} = -4 \left(\frac{b_T}{D} \right)^2 K_{ma} \left[\frac{x_{te}}{D} - x_{cg} - \bar{C}/D \left(1 - \sqrt{K_{ma}} \right) \right]^2 + \left[1 - \left(\frac{\bar{x}_T D + C_{rT}}{D} - x_{cg} \right)^{-2} \right] (C_{mq} + C_{m\dot{\alpha}})_B \quad (128)$$

A maximum AR_T corresponds to $\sqrt{1 + (AR_T/4)^2} = 2$ or $AR_T < 2.31$. For larger aspect ratio planforms the code reverts to the older theory.

For hypersonic flow, $M_\infty > \sqrt{1 + (AR_T/4)^2}$,

$$(C_{mq} + C_{m\dot{\alpha}})_{TB} = -8/\pi \frac{C_{rT}}{D} \frac{b_T}{D} \frac{f^*}{\beta} \left[\frac{1 + \lambda_T}{6} + 4 \xi^* (\xi^* - a^*) + 4/3 a^{*2} - (1 - \lambda_T) (2\xi^{*2} - 8/3 \xi^* a^* + a^{*2}) \right] \quad (129)$$

where

$$\xi^* = \frac{\bar{x}_T D + C_{rT}}{D} - x_{cg} - \frac{1}{2} \frac{C_{rT}}{D}, \quad (130)$$

$$a^* = \frac{1}{2} \frac{C_{rT}}{D} \left(1 - \lambda_T + \frac{b_T}{2C_{rT}} \tan \gamma_1 \right), \quad (131)$$

and f^* is the dynamic pressure ratio across the bow shock and is defined as

$$f^* = \begin{cases} 1.0 & K_N \leq 1.25 \\ -\frac{K_N - 1.25}{12.669724} & 1.25 < K_N \leq 11 \\ .17 & K_N > 11 \end{cases} \quad (132)$$

2.3 METHODS OF ANALYSIS SUMMARY

The body-alone static analysis methods are summarized in Figure 13. The Mach number region division points are nominally at $M_\infty = .8$, 1.2, and M_∞ or $M_{\infty e}$.

Methods for computing the wing-alone and interference static aerodynamics are given in Figure 14.

COMPONENT \ MACH NUMBER REGION	SUBSONIC	TRANSONIC	LOW SUPERSONIC	HIGH SUPERSONIC
NOSE WAVE DRAG	—	EULER PLUS EMPIRICAL	SECOND-ORDER VAN DYKE PLUS MODIFIED NEWTONIAN	SECOND-ORDER SHOCK-EXPANSION PLUS MODIFIED NEWTONIAN
BOATTAIL WAVE DRAG	—	WU AND AOYOMA	SECOND-ORDER VAN DYKE	SECOND-ORDER SHOCK-EXPANSION
SKIN FRICTION DRAG	VAN DRIEST II			
BASE DRAG	EMPIRICAL			
INVISCID LIFT AND PITCHING MOMENT	EMPIRICAL	EULER OR WU AND AOYOMA PLUS EMPIRICAL	TSIEN FIRST-ORDER CROSSFLOW	SECOND-ORDER SHOCK-EXPANSION
VISCOUS LIFT AND PITCHING MOMENT	ALLEN AND PERKINS CROSSFLOW			

Figure 13. Methods for Computing Body-Alone Static Aerodynamics

COMPONENT \ MACH NUMBER REGION	SUBSONIC	TRANSONIC	LOW SUPERSONIC	HIGH SUPERSONIC
INVISCID LIFT AND PITCHING MOMENT	LIFTING SURFACE THEORY	EMPIRICAL	LINEAR THEORY	SHOCK-EXPANSION STRIP THEORY
WING-BODY INTERFERENCE	SLENDER BODY THEORY AND EMPIRICAL		LINEAR THEORY, SLENDER BODY THEORY AND EMPIRICAL	—
WING-TAIL INTERFERENCE	LINE VORTEX THEORY			—
WAVE DRAG	—	EMPIRICAL	LINEAR THEORY + MODIFIED NEWTONIAN	SHOCK-EXPANSION + MODIFIED NEWTONIAN STRIP THEORY
SKIN FRICTION DRAG	VAN DRIEST			
TRAILING EDGE SEPARATION DRAG	EMPIRICAL			
BODY BASE PRESSURE DRAG CAUSED BY TAIL FINS	EMPIRICAL			

Figure 14. Methods for Computing Wing-Alone and Interference Static Aerodynamics

Finally, the methods to compute the dynamic derivatives are summarized in Figure 15. Input option refers to use of LMSC or other prediction methods for $C_{mq} + C_{m\dot{\alpha}}$ for body-alone or body-tail configurations.

COMPONENT \ MACH NUMBER REGION	SUBSONIC	TRANSONIC	LOW SUPERSONIC	HIGH SUPERSONIC
BODY-ALONE PITCH DAMPING MOMENT	EMPIRICAL			
	(OR)	(OR)	(OR)	(OR)
	MODIFIED SLENDER-BODY THEORY	LINEAR INTERPOLATION	EMBEDDED NEWTONIAN THEORY	
WING AND INTERFERENCE ROLL DAMPING	LIFTING SURFACE THEORY	EMPIRICAL	LINEAR THIN-WING THEORY	STRIP THEORY
BODY-ALONE MAGNUS MOMENT	EMPIRICAL			
WING AND INTERFERENCE MAGNUS MOMENT	ASSUMED ZERO			
BODY-ALONE ROLL DAMPING MOMENT	EMPIRICAL			
WING AND INTERFERENCE PITCH DAMPING MOMENT	SLENDER-WING THEORY	SUPERSONIC SLENDER-WING THEORY	EMBEDDED NEWTONIAN STRIP THEORY	
	(OR)	(OR)	(OR)	(OR)
	LIFTING SURFACE THEORY	EMPIRICAL	LINEAR THIN-WING THEORY	STRIP THEORY

* INPUT OPTION. MACH DIVISION POINTS ARE AT $M_\infty = 1$ AND $M_\infty = \bar{M}^*$.
 \bar{M}^* IS VARIABLE, BUT $\bar{M}^* \geq 1.5$.

** INPUT OPTION. MACH DIVISIONS AT $M_\infty = 1$ AND A MACH NUMBER DEPENDENT ON ASPECT RATIO, $M_\infty = \sqrt{1 + (AR_w/4)}$.

Figure 15. Methods for Computing Dynamic Derivatives

At high angles-of-attack, the body-alone or body-tail computations are based on the empiricism of Reference 24. Only static derivatives are determined.

Computation times depend on configuration, code option, and Mach number. A computation time can range from less than a second to between 30 seconds and a minute per Mach number on the CDC 6700 computer.

3. APPLICATIONS TO CURRENT DESIGNS

In this section, data are presented for a variety of complete configurations of current interest. In most cases, experimental data are shown for comparison with the theoretical predictions and an estimation made of the accuracy of the predictions. Both the static and dynamic coefficients are presented in many cases.

3.1 TACTICAL WEAPONS WITHOUT LIFTING SURFACES (BODY ALONE AERODYNAMICS)

Since the aerodynamic coefficients of the individual body components and many of the nose-afterbody shapes are presented in Section 4, the data presented here are limited to complete configurations. In Figures 16 through 20, the static and dynamic aerodynamic coefficients are presented for several spin-stabilized projectiles. In Figure 16, the predicted characteristics of the basic Army/Navy Spinner are shown. In general, the static aerodynamics are predicted reasonably well with the errors generally staying less than 10 percent throughout the Mach number range. The dynamic derivative predictions, utilizing the empirical method (see Section 2.2.1), are generally poor and are of the right order-of-magnitude only.

Figures 17 and 18 give the estimated aerodynamic coefficients for a 5 inch Rocket Assisted Projectile (RAP) and an Improved 5 inch/54 Projectile (Reference 30), respectively. The 5 inch RAP has a nose length of 2.5 calibers, a 2.2 caliber afterbody, a .5 caliber boattail, and a rotating band near the end of the afterbody. The Improved round has a 2.75 caliber nose, a 1.45 caliber afterbody, and a 1.0 caliber boattail. The Improved round employs a discarding rotating band and therefore has no such protrusions in flight. In both of these cases, there is good agreement with experimental data obtained for the drag coefficient throughout the Mach number range where data are available. Fair agreement was achieved for the normal force and center-of-pressure location. For the 5 inch RAP C_N prediction, the agreement approaching $M_\infty = 2.5$ is very good, whereas at lower Mach numbers the theory is consistently about 10 percent low. This is due in

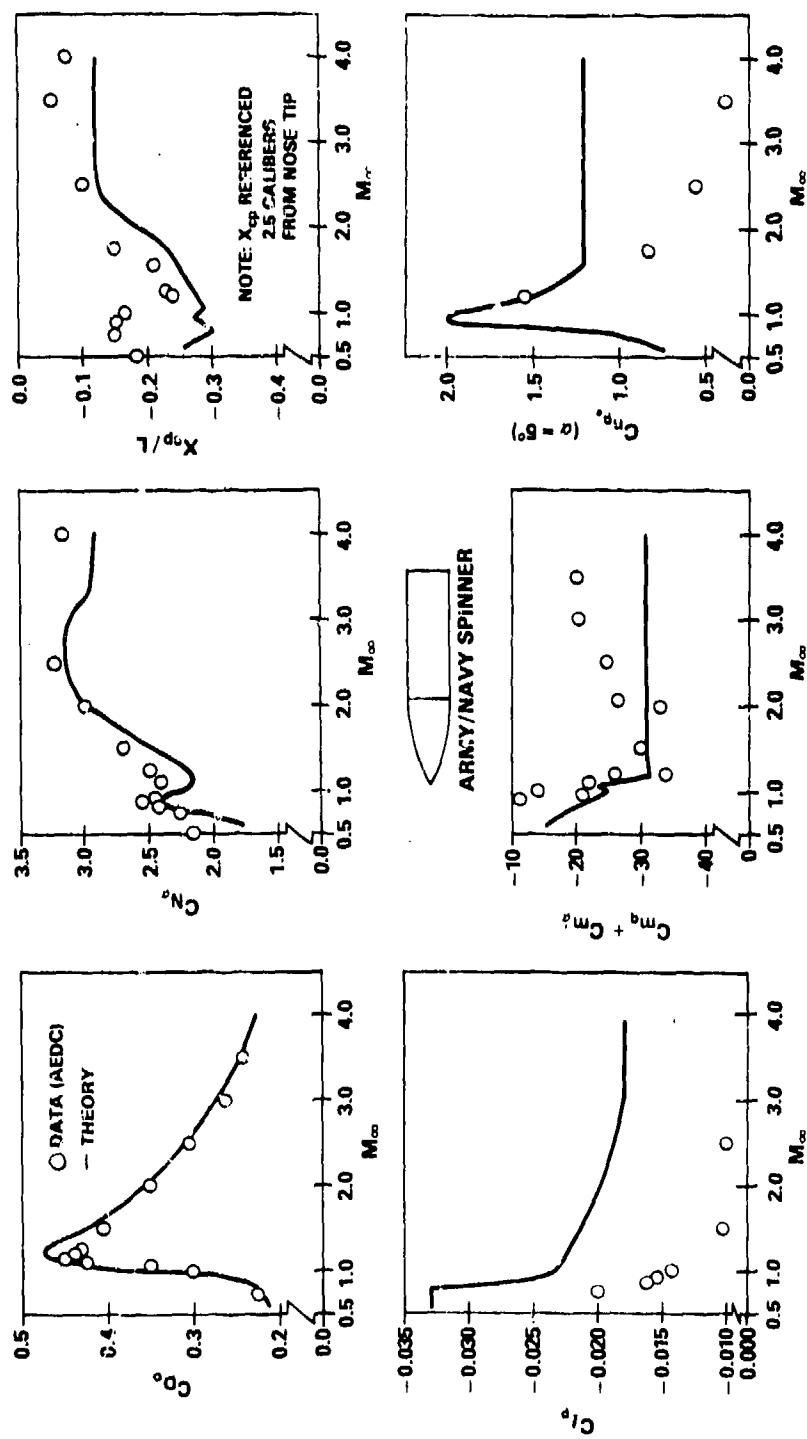


Figure 16. Comparison of Theory and Experiment for Army/Navy Spinner

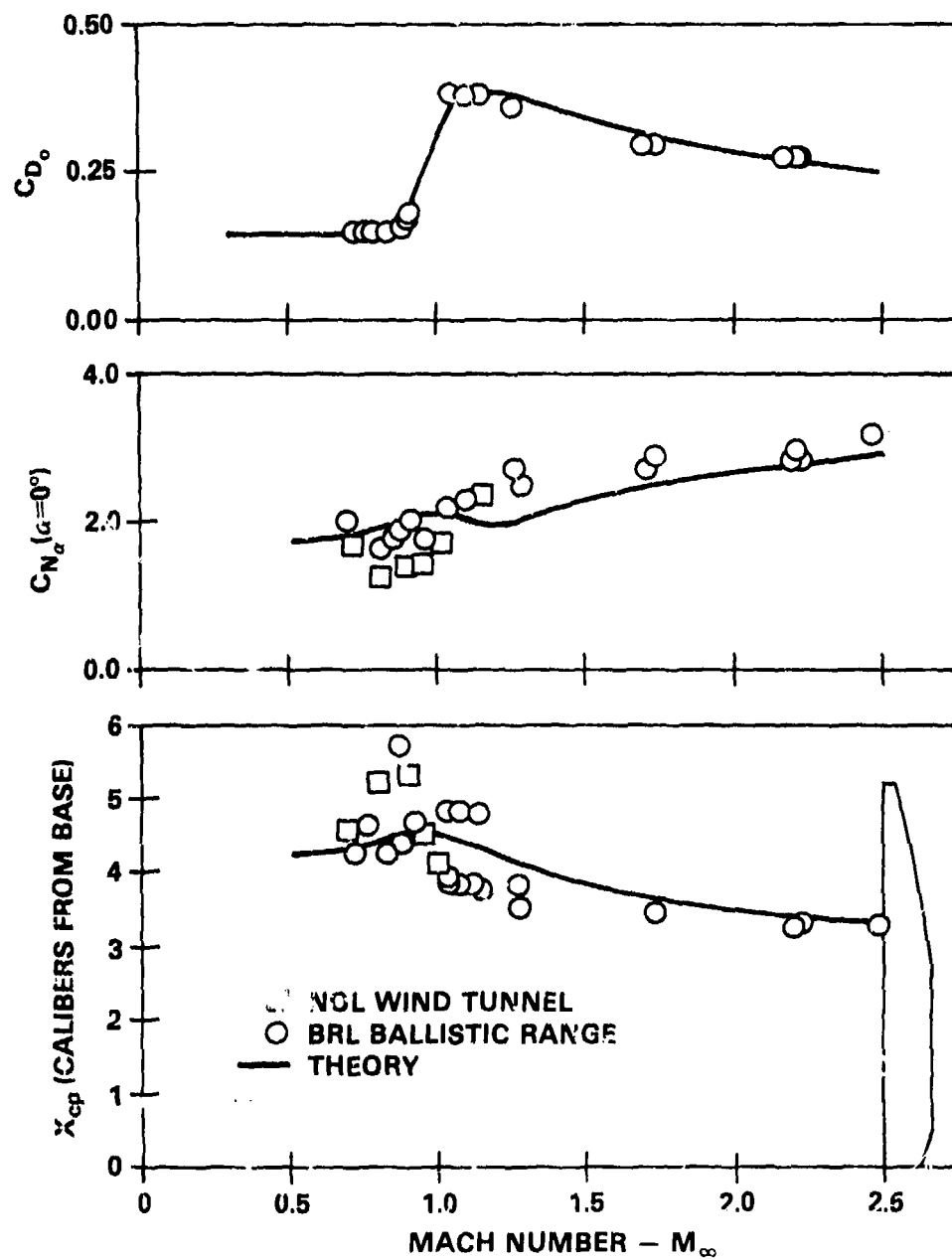


Figure 17. Comparison of Theory and Test Data for 5 inch RAP Projectile

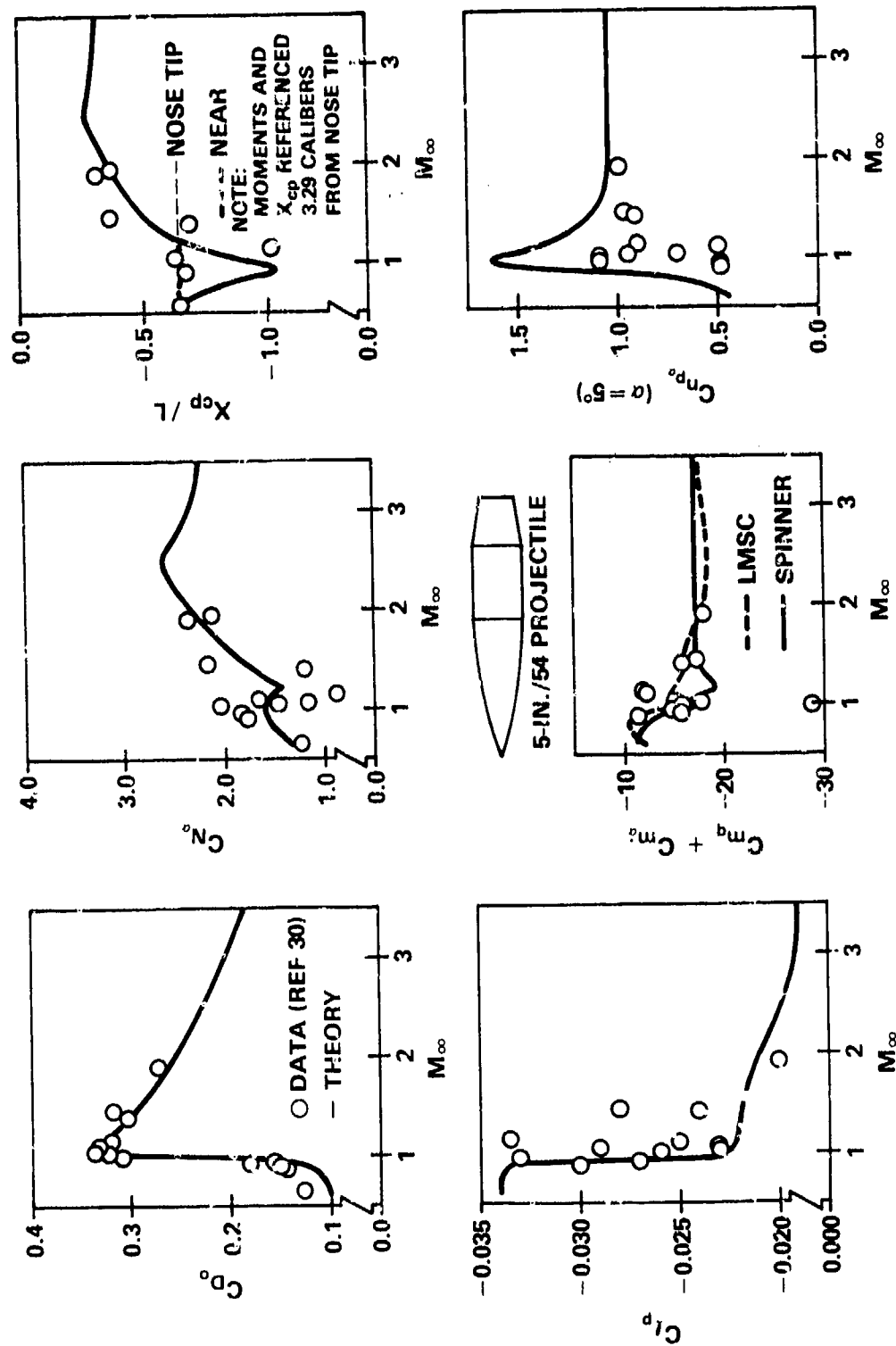


Figure 18. Comparison of Theory and Experiment for 5 inch/54 Improved Projectile

part to the inability of the inviscid theory to predict the afterbody lift correctly at low supersonic Mach numbers. For the Improved round, the dynamic derivatives' predictions are, in general, good. The LMSC methodology (Reference 25) and the empirical predictions (both of which are available in the Aeroprediction Code at the user's option) show good agreement for $C_{mq} + C_{m\dot{\alpha}}$ except in the high transonic flow region, where the agreement is fair.

In these cases, M_0 was generally set at $M_\infty = 2.0$ resulting in the use of the potential theory rather than the second-order shock expansion theory for $M_\infty = 2.0$. If M_0 had been set at $M_\infty = 2.5$, the potential theory would have been applied at this Mach number also, and the predictions at $M_\infty = 2.5$ for C_D and $C_{N\alpha}$ would have been considerably lower. This is a result of the Mach wave angle ^{α} lying too close to the initial body slope.

Figures 19 and 20 present the aerodynamic coefficients for two Army shells, the 175 mm M437 (Reference 31) and the 155 mm projectiles. Again, good agreement is obtained for the drag coefficient, and fair agreement is achieved for the normal force and center-of-pressure location.

Figures 21 and 22 illustrate the Code's capability to predict the aerodynamics for blunt bodies and bodies with flares. In each case, it was necessary to modify the body geometry to be compatible with the second-order perturbation theory used for low supersonic Mach number calculations. The hemispherical nose on the 5.5 caliber hemisphere-cylinder body was modified to include a 0.1 caliber conical frustrum with $\Delta R = .01$ at the aft end (L_N remained constant). The remainder of the body was described directly. The NASA flared-body nose was replaced by a sphere-cone-flare body. The spherical cap was allowable in this case because of the slight slope of the afterbody prior to the flare. For the hemisphere-cylinder, the drag predictions compare favorably with data (Reference 32) but the $C_{N\alpha}$ and x_{cp} predictions are "hit and miss," as shown in Figure 21. In the case of the flared body, a slight increase in the bluntness resulted when the nose was changed to the spherical cap. As shown in Figure 22, the effect of this change is particularly noticeable in the C_A and $C_{N\alpha}$ predictions. The drag and normal force are overpredicted by as much as 15 percent in the low supersonic region compared to data (Reference 33). The x_{cp} predictions are within one-half

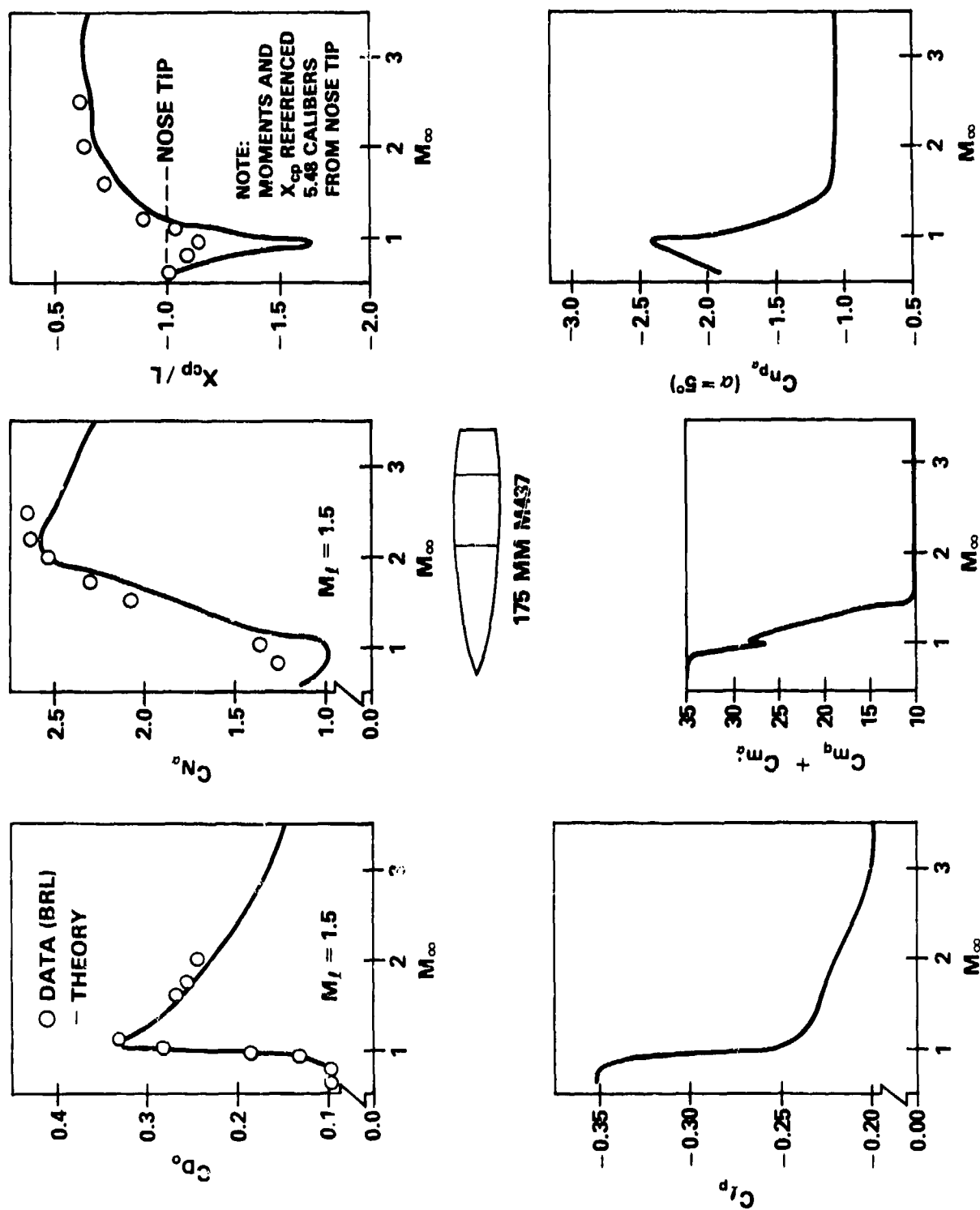


Figure 19. Comparison of Theory and Experiment for 175 mm Projectile

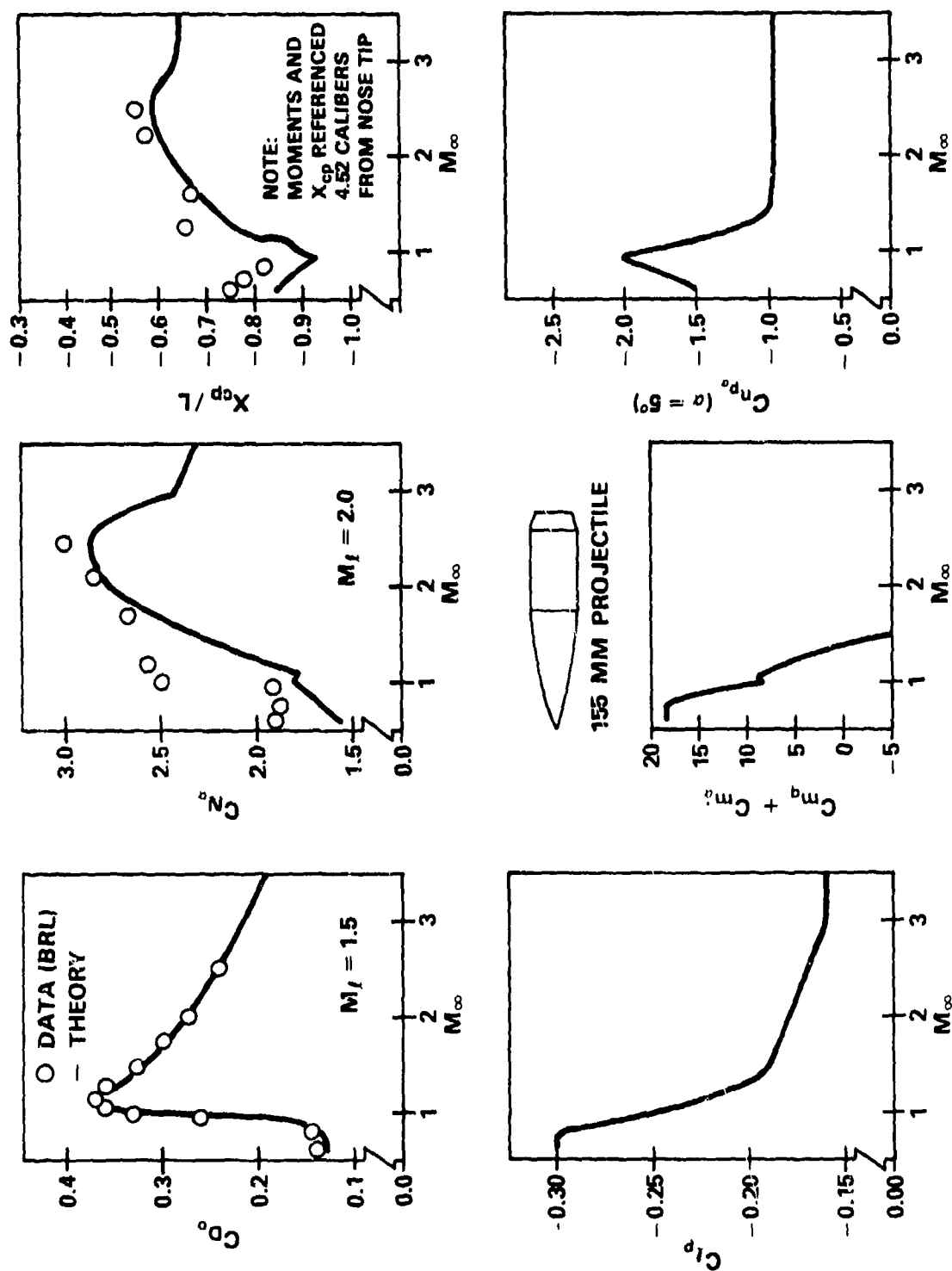


Figure 20. Comparison of Theory and Experiment for 155 mm Projectile

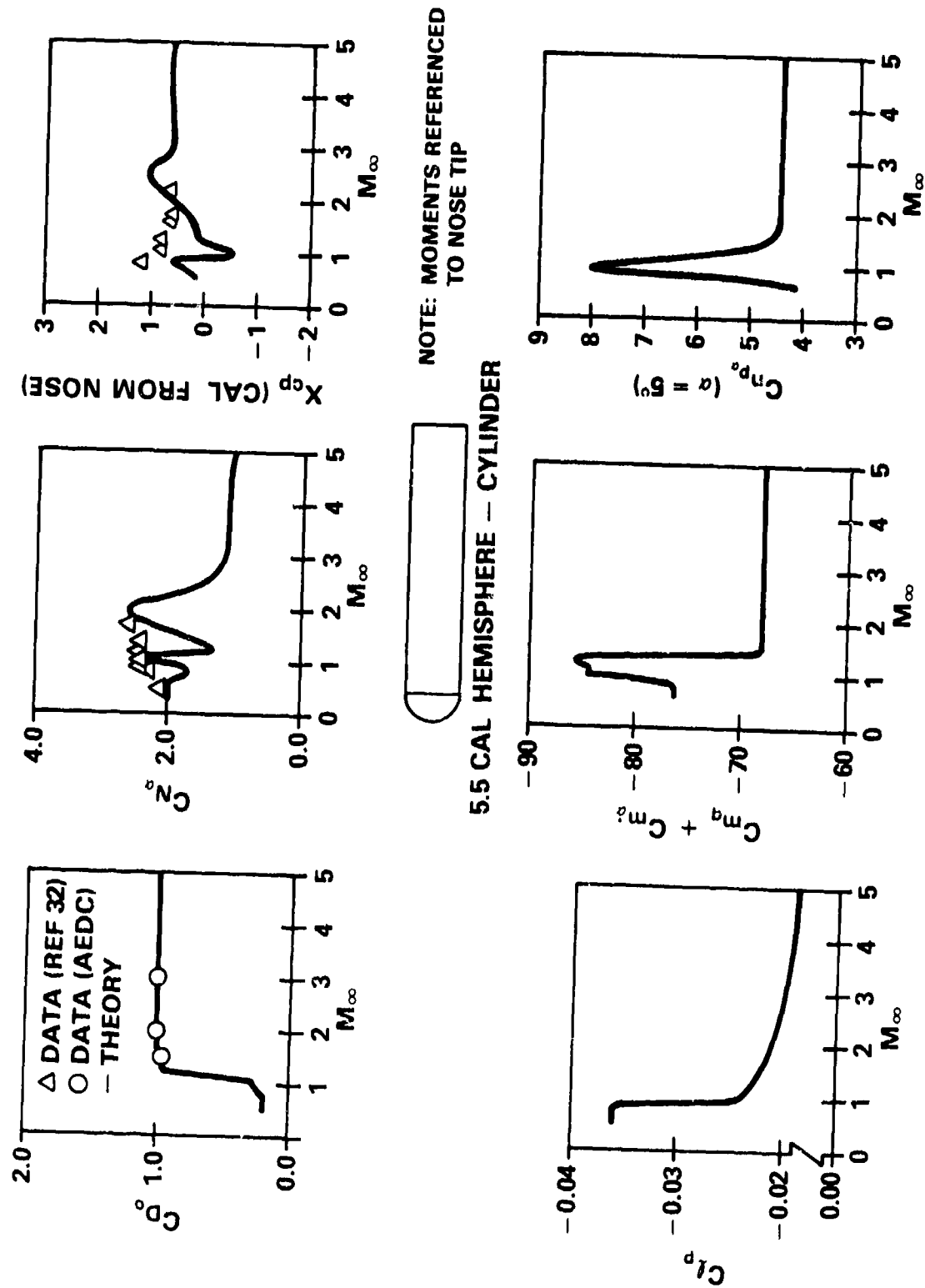


Figure 21. Comparison of Theory and Experiment for Hemisphere-Cylinder

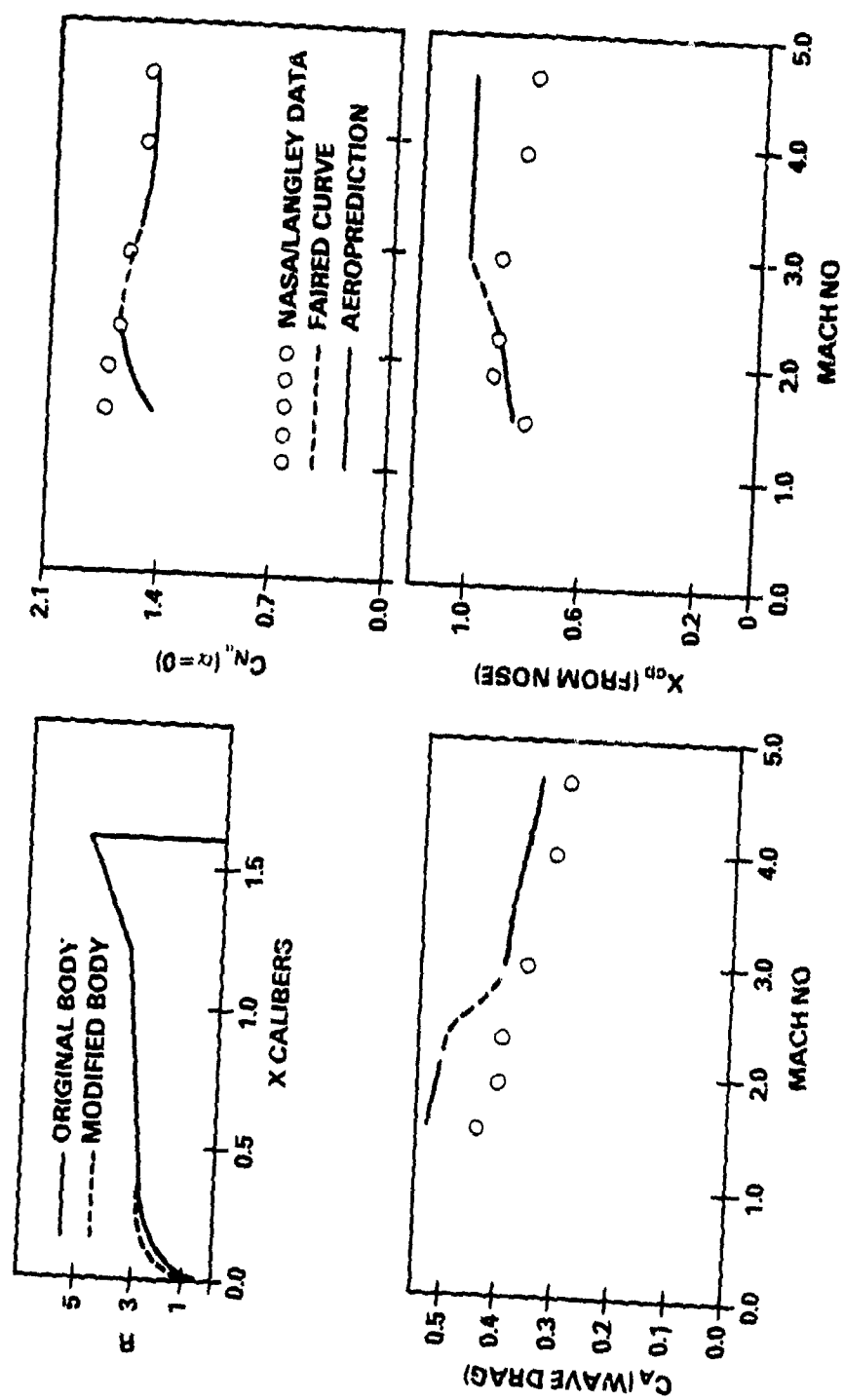


Figure 22. NASA Flare Body Data Comparison for Supersonic Mach Numbers

caliber. Note the faired portion in the predictions in the range $2.0 < M_\infty < 3.0$. This "blending" region is a result of differences in the predictions between the small perturbation theory and the second-order shock expansion theory. It is well known that above $M_\infty = 2.0$ the perturbation theory begins to weaken. For the blunt bodies, the theory does not hold at all. The second-order shock expansion theory, on the other hand, is best applied in the high supersonic region. In the majority of cases, its accuracy degrades rapidly below $M_\infty = 3.0$. To account for this difficulty and to eliminate the discontinuity in the predictions, a weighted fairing was used in this region.

Projectile Performance. In recent years, there has been a renewed emphasis on improving the design of projectiles. For the A/A defense role, the major considerations are time of flight and accuracy. For surface-to-surface applications, the usual concern is maximum range as well as accuracy.

In minimizing the time of flight, it is necessary to optimize the ballistic coefficient, $\beta = W/C_D S_{ref}$ (Reference 34). The importance of this parameter is recognized in the following equations for the velocity and time of flight as a function of range:

$$V = V_o \exp \left[-\frac{\rho g}{2\beta} R_x \right] \quad (133)$$

and

$$t_f = \frac{2\beta}{V_o \rho g} \exp \left[\frac{\rho g}{2\beta} R_x - 1 \right] \quad (134)$$

The drag coefficient, C_D , is assumed to be constant over the range of interest. For increasing values of β , the velocity increases and the time decreases (both exponentially) for a given range, R_x . One would at first feel that a maximum value of β would provide the best performance. However, when designing a round for a given gun system, the muzzle velocity depends directly on the projectile

weight. Usually the new design is replacing an old one. If the new weight is less than the previous standard weight, the muzzle velocity for the new design can be estimated by relating it to the muzzle energy.

$$m V_o^2 = m_{std} V_{o_{std}}^2$$

or

$$V_o = V_{o_{std}} \left(\frac{m_{std}}{m} \right)^{\frac{1}{2}} = V_{o_{std}} \left(\frac{W_{std}}{W} \right)^{\frac{1}{2}} \quad (135)$$

Equation (135) provides reasonably good estimates as long as the weight difference is not large. Further examination of Equations (133) and (134) reveals that increasing the projectile weight may increase β but it also decreases V_o . The result is that for a given range and gun energy, an optimum value for β exists which will result in the maximum velocity, V , at range, R_x , and a minimum time of flight.

So far the discussion has centered on the projectile weight. Obviously, if the drag is minimized, the velocity retardation is minimized and the performance is optimized further. Therefore, a good approach to optimizing the projectile performance is to first minimize the drag, then to determine the optimum β for the range of interest. In the case of intercepting an air target, the range selected might be the median range over which intercept is desirable or it may be the range at which maximum accuracy or advantage is required.

The above procedure was used to optimize the performance of a 30 mm projectile. The range of interest was 3.0 km. The performance and physical characteristics of the standard projectile were known. Sample trajectory calculations indicated the median Mach number to be about 3.0. An L/D ratio of 5.0 was selected due to the total round length constraints and also to provide good stability. Generally, the higher the fineness ratio (L/D), the more difficult it is to spin-stabilize the body. With these inputs, the optimum shape for minimum drag could be determined. The Aeroprediction Code was then used to obtain the

initial estimates of the aerodynamic coefficients for the design. Figure 23 shows the profile of the body and the predicted coefficients. The optimum shape indicated has a 3.2 caliber nose and a 1.8 caliber boattail with a base diameter of $.7D_{ref}$. It should be noted that the actual theoretical shape had a slight curvature in the boattail near the afterbody-boattail juncture. Later, when these projectiles were fabricated, the profile was approximated by a conical boattail for ease in manufacturing. Comparison of the theory with the ballistic range data obtained later showed good agreement in each case. As a result, the predicted values could be used with greater confidence throughout the Mach number range to conduct a stability analysis.

Having determined the minimum drag profile, it was necessary to find the optimum ballistic coefficient. Figure 24 shows the variation of t_f with projectile weight for several ranges. The weight at which t_f is a minimum suggests the optimum value for β . Note that the optimum weight (and therefore β) varies with the range. The variation in β with the range can be visualized in Figure 25. Having determined the desired weight, it is then left to the designer to determine the fuze weight (if any) and the interior cavity which would provide the center-of-gravity location, polar (spin axis) inertia, and the transverse (pitch axis) inertia for that weight which are necessary for the stability analysis. The benefits achieved through shape optimization can be substantial. In our sample case, reductions in the drag and time of flight were 34 percent and 32 percent, respectively, as compared to the standard design.

The stability requirements for projectile design are discussed in detail in Reference 34. Basically, the main concerns are the gyroscopic stability factor

$$S_g = \frac{I_x^2 p^2}{2I_y \rho V^2 SDC_{m\alpha}} \quad (136)$$

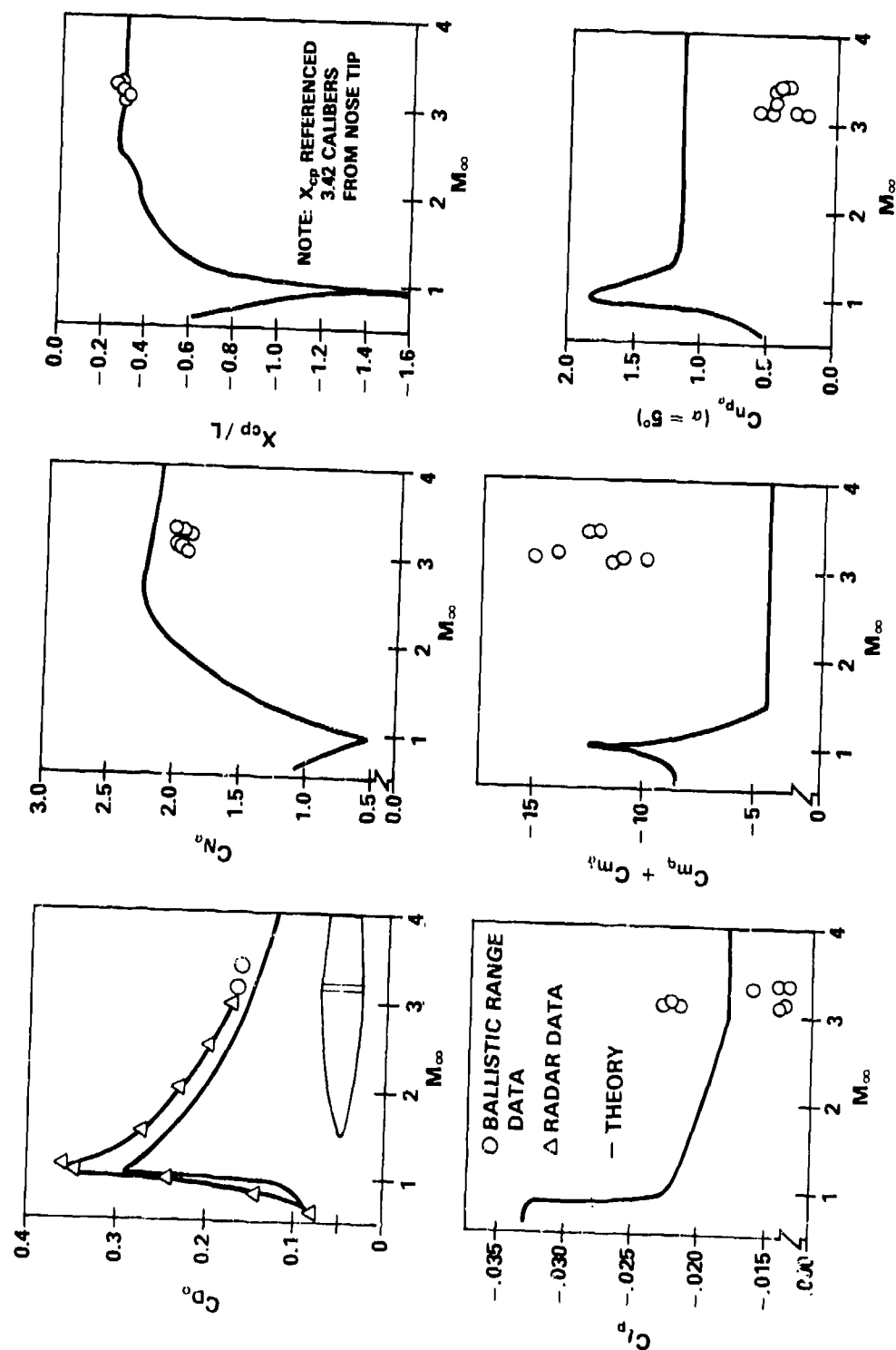


Figure 23. 30 mm Optimal Projectile Aerodynamics

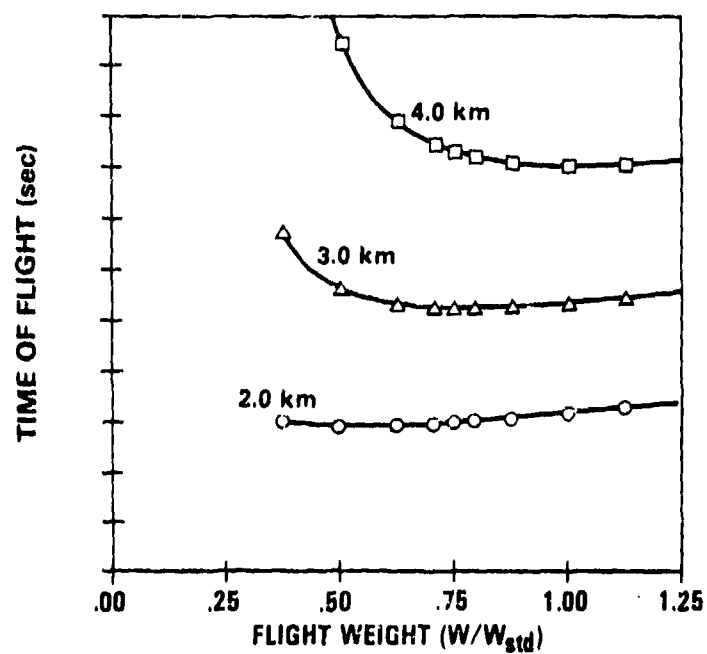


Figure 24. Time of Flight of an Optimum Drag Projectile vs Flight Weight to Slant Ranges of 2.0 km, 3.0 km, and 4.0 km

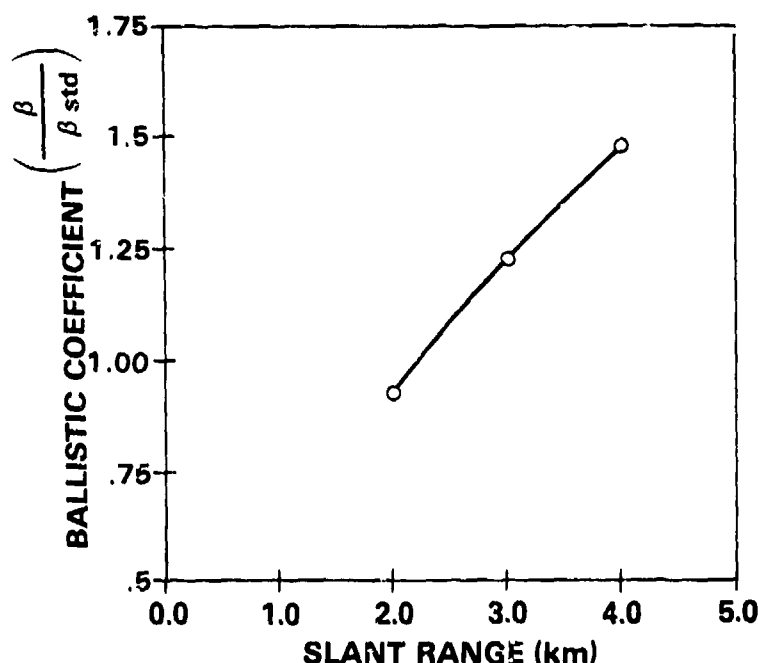


Figure 25. Minimum Time-of-Flight Ballistic Coefficient for a 30 mm Optimum Drag Projectile

and the dynamic stability factor

$$S_d = \frac{2 \left(C_{N_\alpha} - C_D + \frac{mD^2}{2I_y} C_{n_{p\alpha}} \right)}{C_{N_\alpha} - C_D - \frac{mD^2}{2I_y} (C_{m_q} + C_{m_\alpha}) + \frac{mD^2}{2I_x} C_{\ell_p}} \quad (137)$$

For dynamic flight stability, $S_g \geq 1.0$ and $0 < S_d < 2.0$. In practice, good projectile designs have, for standard atmosphere conditions at launch, $S_g > 1.3$ and $S_d \approx 1.0$. If the values of S_g and S_d are determined for a particular design to be outside of these ranges, it is generally easier from an aerodynamic standpoint to look at ways to vary the I_x/I_y ratio and the center-of-gravity location first to correct the problem. If the physical limitations render this approach unsuccessful, then the basic exterior design must be changed, usually through increasing the length of the cylindrical section of the body with corresponding reductions in the boattail length or nose length. The gyroscopic stability of a spin-stabilized projectile usually increases after muzzle exit (at least until apogee). Therefore, it is most critical that adequate stability be obtained near

the muzzle. However, both S_g and S_d vary during the flight and should be examined throughout the trajectory to ensure the projectile will fulfill its mission. The values for these parameters for the 30 mm Optimal Projectile sample case were $S_g = 2.23$ and $S_d = 0.96$ for standard atmospheric conditions at the muzzle. The value for S_d was determined based on the ballistic range data since the theory predicted $C_{mq} + C_{m\dot{\alpha}}$ and $C_{n p\alpha}$ poorly in this case.

3.2 TACTICAL WEAPONS WITH LIFTING SURFACES

Figures 27 through 33 give the aerodynamic coefficients for several missile configurations with one or two sets of lifting surfaces. In each case, a fin set is comprised of four fins in a cruciform arrangement.

In Figures 26 through 29, the aerodynamics for configurations with only one set of lifting surfaces are shown. The first, Figure 26, is the Basic Finner model, which has a 2.84 caliber conical nose and a total length of 10.0 calibers. The triangular airfoil, rectangular planform fins have $AR = 2.0$ and $t/C = .08$, where $C = D_{ref}$ and $AR = \text{Aspect Ratio}$. The geometry is representative of the data base and can be modelled precisely in the Aeroprediction Code with the exception of the blunt trailing edge for the fins. In the computer model, the trailing edge was given a radius of $t/2$. As expected, the theoretical predictions match the data (Reference 35) quite well, including the dynamic derivatives except in the transonic region where the fin effects are underpredicted.

The next three examples can be classed as variations of the Basic Finner configuration. Each has a tangent ogive nose, the Modified Basic Finner and the Air Slew configurations having a 2.5 caliber nose and the TMX-2774 having a 3.0 caliber nose. The Modified Basic Finner (Reference 36) and Air Slew (AEDC) have an overall length of 10.0 calibers and a modified double-wedge airfoil section fin of $AR = 1.0$, $t/C = .036$, $C_r = 1.33D$, $\lambda = .5$, and $\gamma_1 = 53^\circ$. The leading edge (LE) and trailing edge (TE) bluntnesses are small. The Air Slew is a scaled version of the Modified Basic Finner except for the fin bluntnesses. For the Air Slew, the leading and trailing edges are sharp. The data for the Modified Basic Finner at $M_\infty = 2.5$ and the Air Slew at $M_\infty = 1.3$ illustrate the capabilities of the adapted Martin High Alpha empirical algorithm. Noting the

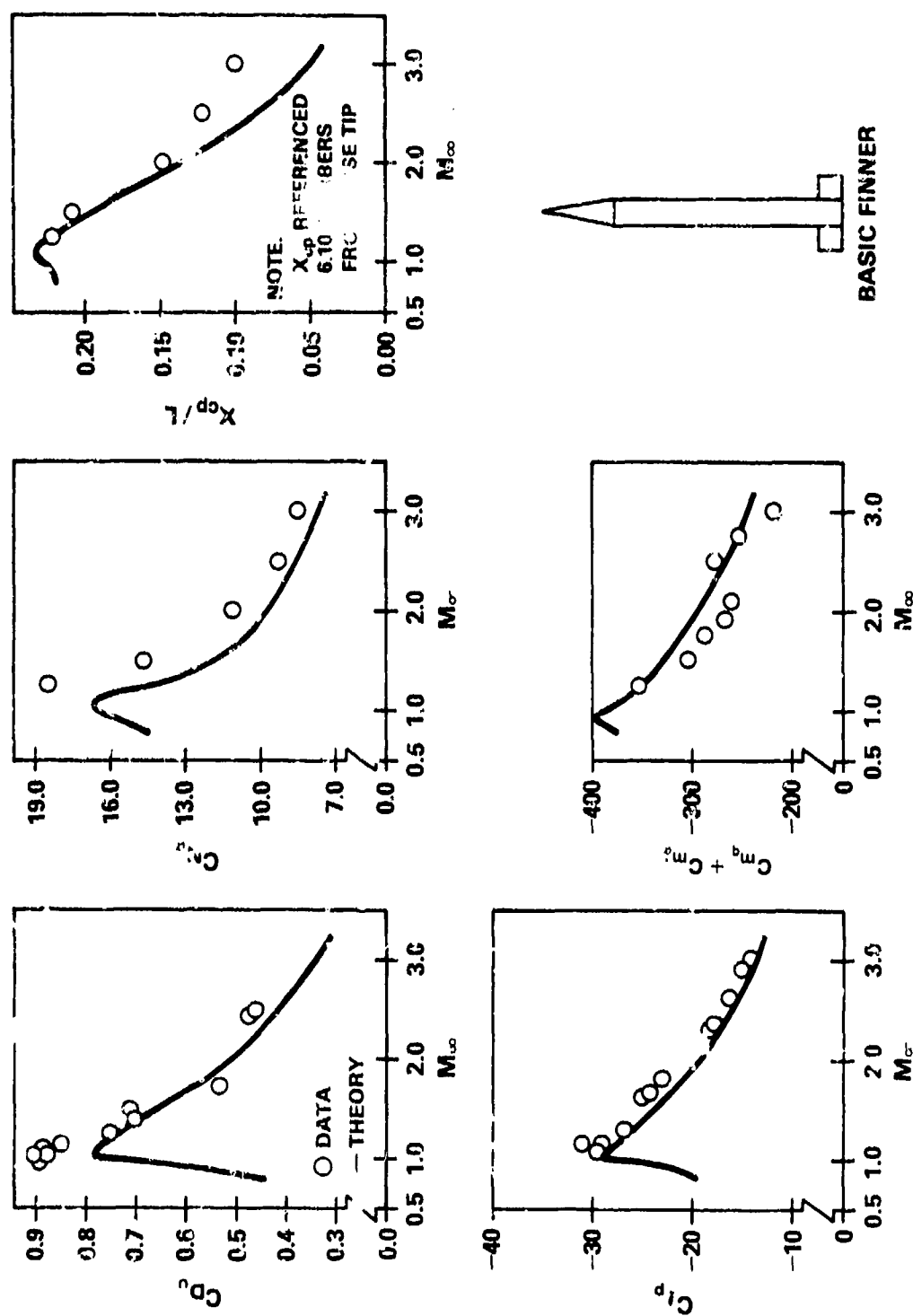


Figure 26. Comparison of Theory and Experiment for Basic Finner

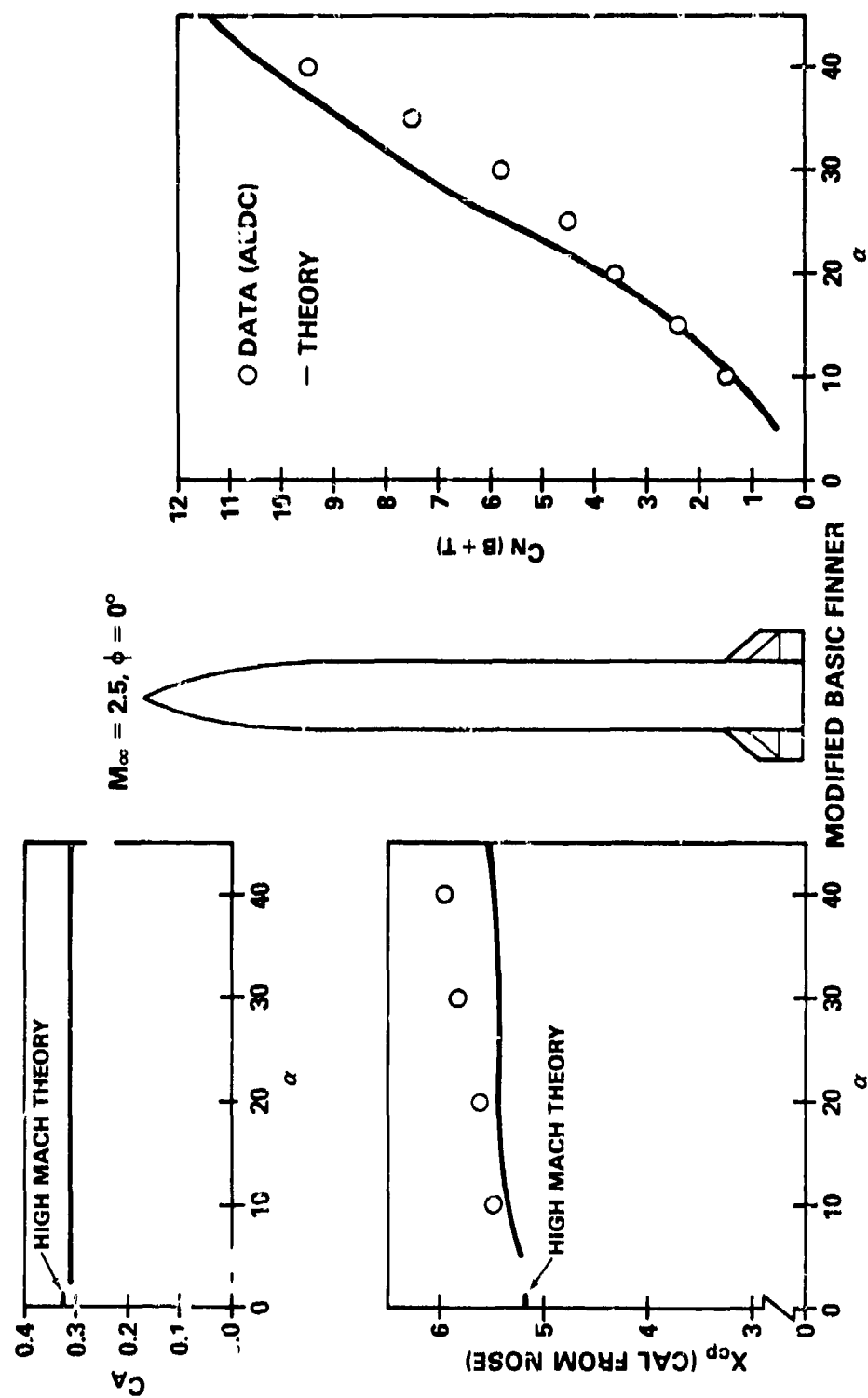


Figure 27. Comparison of Theory and Experiment for Modified Basic Finner at Angles-of-Attack to $\alpha = 45^\circ$ and $M_\infty = 2.5$

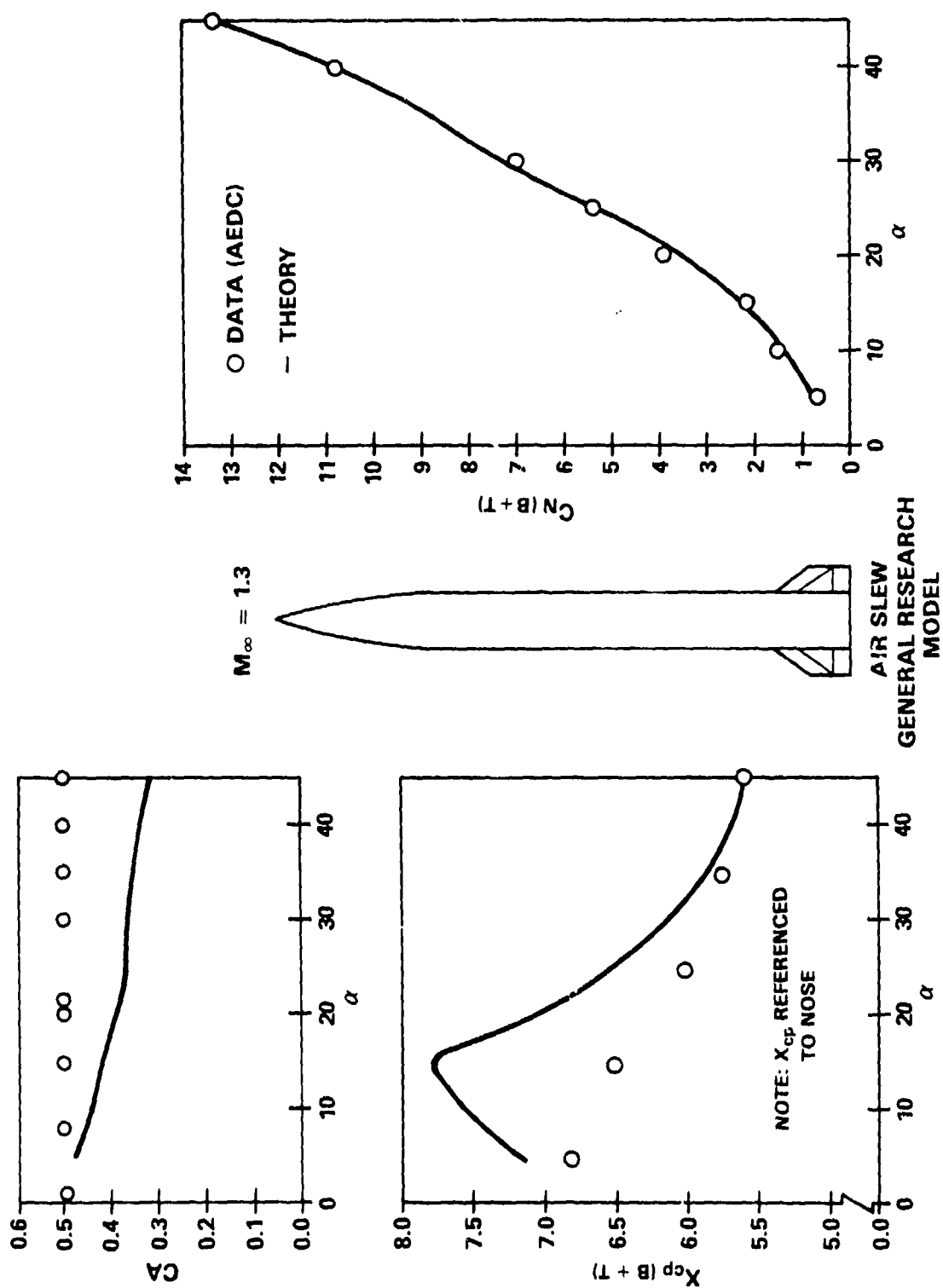


Figure 28. Comparison of Theory and Experiment for Air Slew at Angles-of-Attack to $\alpha = 45^\circ$ and $M_\infty = 1.3$

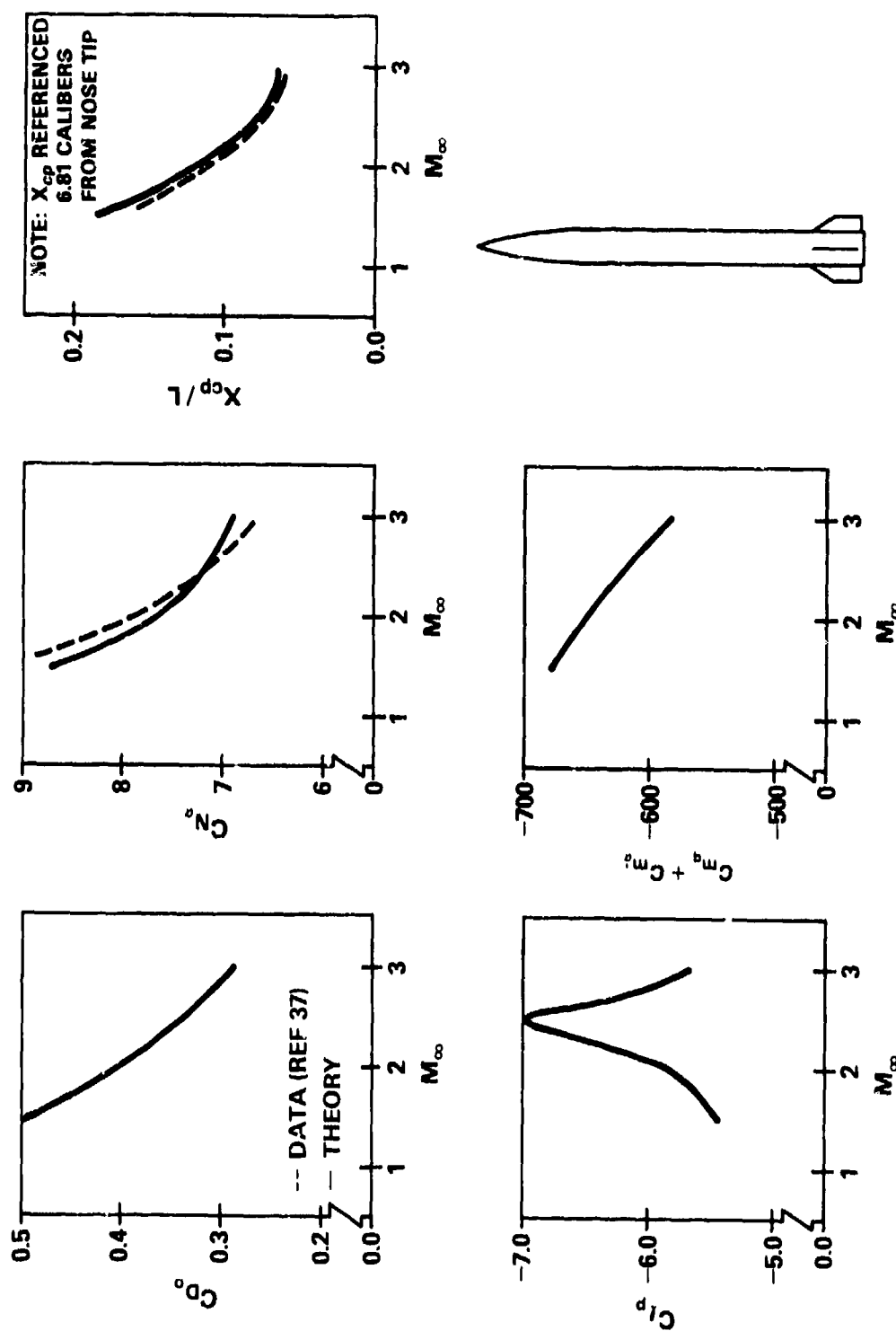
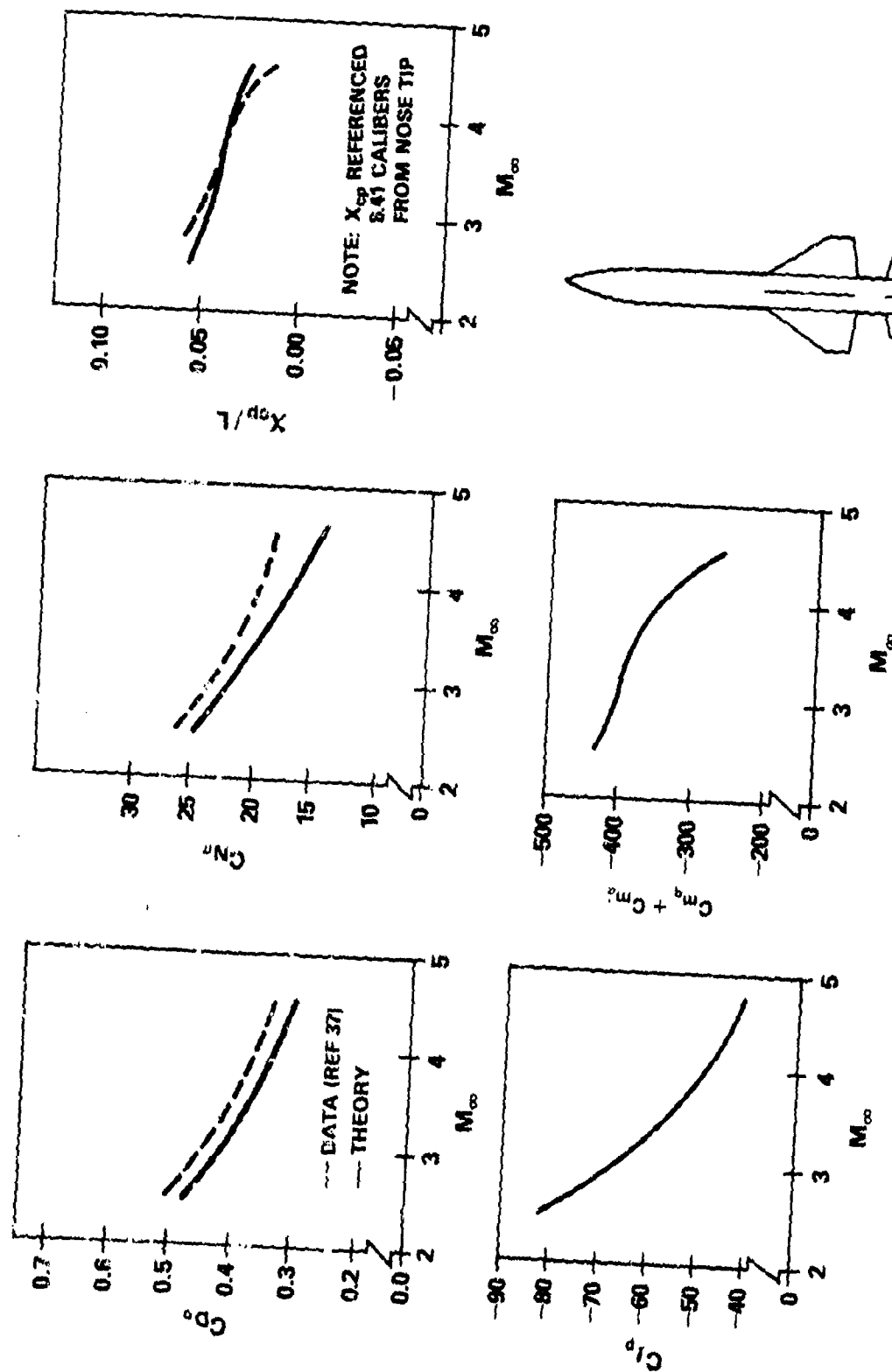


Figure 29. Comparison of Theory and Experiment for TMX 2774 T-9 Tail in the Supersonic Region

small differences in the configurations, the Code predicts the respective trends very well. The slope and magnitude of the C_N predictions compare quite well except at the higher Mach number and $20^\circ < \alpha < 40^\circ$. In this region, the errors range from 5 to 30 percent, reaching a maximum at $\alpha = 30^\circ$. The x_{cp} predictions show similar trends and are of the right order of magnitude only at $M_\infty = 2.5$. The negative trend in the C_A prediction with increasing α is not supported by the data.

The last of the body-tail configurations is the NASA TMX-2774 body (Figure 29) which is 13.06 calibers long with a .53 caliber, 4.2° boattail, and fins of $AR = .84$, $t/C = .07$, $C_x = 1.9$, $\lambda = .42$, and $\gamma_1 = 62.9^\circ$ (Reference 37). The LE and TE are sharp. The data include the effect of two strakes, 180° apart, which were not included in the model due to limits on the number of lifting surfaces and the small aspect ratio. In this case, the C_N and x_{cp} predictions compare well. Again, it should be pointed out that for small aspect ratios the influence on the opposite half wing tip is neglected. Also, no interference effects are considered at high supersonic Mach numbers. As a result, C_{lp} and $C_{mq} + C_{m\dot{\alpha}}$ predictions for small AR often behave erratically. The peak in the curve for C_{lp} is representative of the problem and can be seen elsewhere.

Figures 30 through 32 present data for configurations having two sets of lifting surfaces. The large-winged ($AR = 1.52$) TMX-1751 configuration (Figure 30) incorporated body strakes which were included in the data but, as before, were not included in the model (Reference 37). This partially accounts for the differences in C_N and x_{cp} . The agreement with data for the TMX-3070 (Figure 31) is very good for C_D and C_N in spite of protrusions on the actual model, including a fin assembly sleeve (Reference 37). The prediction for x_{cp} is fair to poor, however, with errors ranging from .15 calibers (1.0 percent of the distance from the nose) to 4.9 calibers (35 percent). This is probably caused by an underprediction of the lift for the highly swept canards and errors in the predicted pressure distributions on the hemispherical nose noted earlier. Note again the fluctuation in C_{lp} due to the lower AR tail. The next example, in Figure 32, is an illustration of probably the most complex configuration which can be handled by the Aeroprediction Code. The body is comprised of a spherically blunted 2.1 caliber nose, a cylindrical afterbody, and an 8.9° boattail. The



NASA TMX-1751

Figure 30. Comparison of Theory and Experiment for TMX 1751 for $2.5 < M_\infty < 4.5$

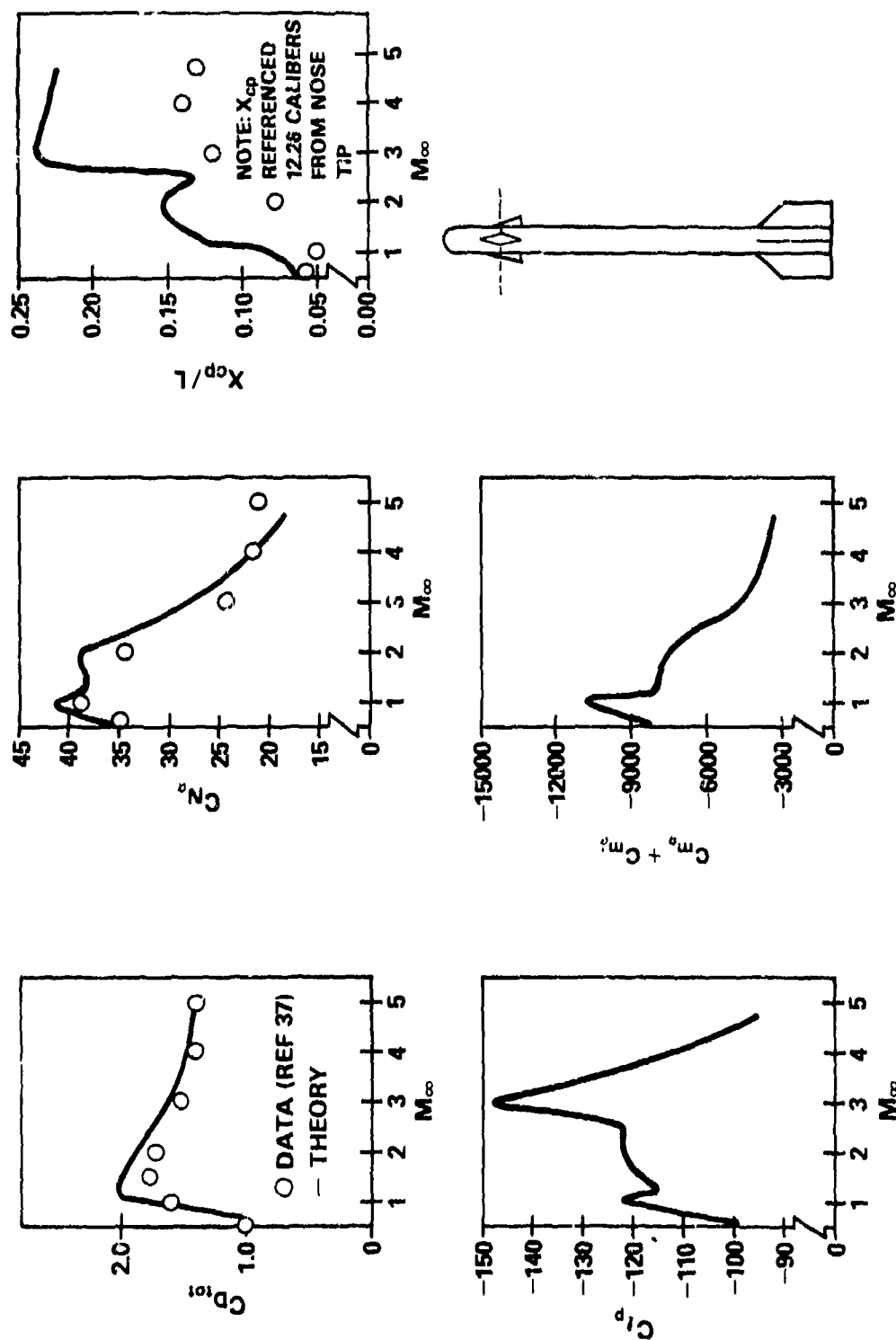


Figure 31. Comparison of Theory and Experiment for IMX 3070

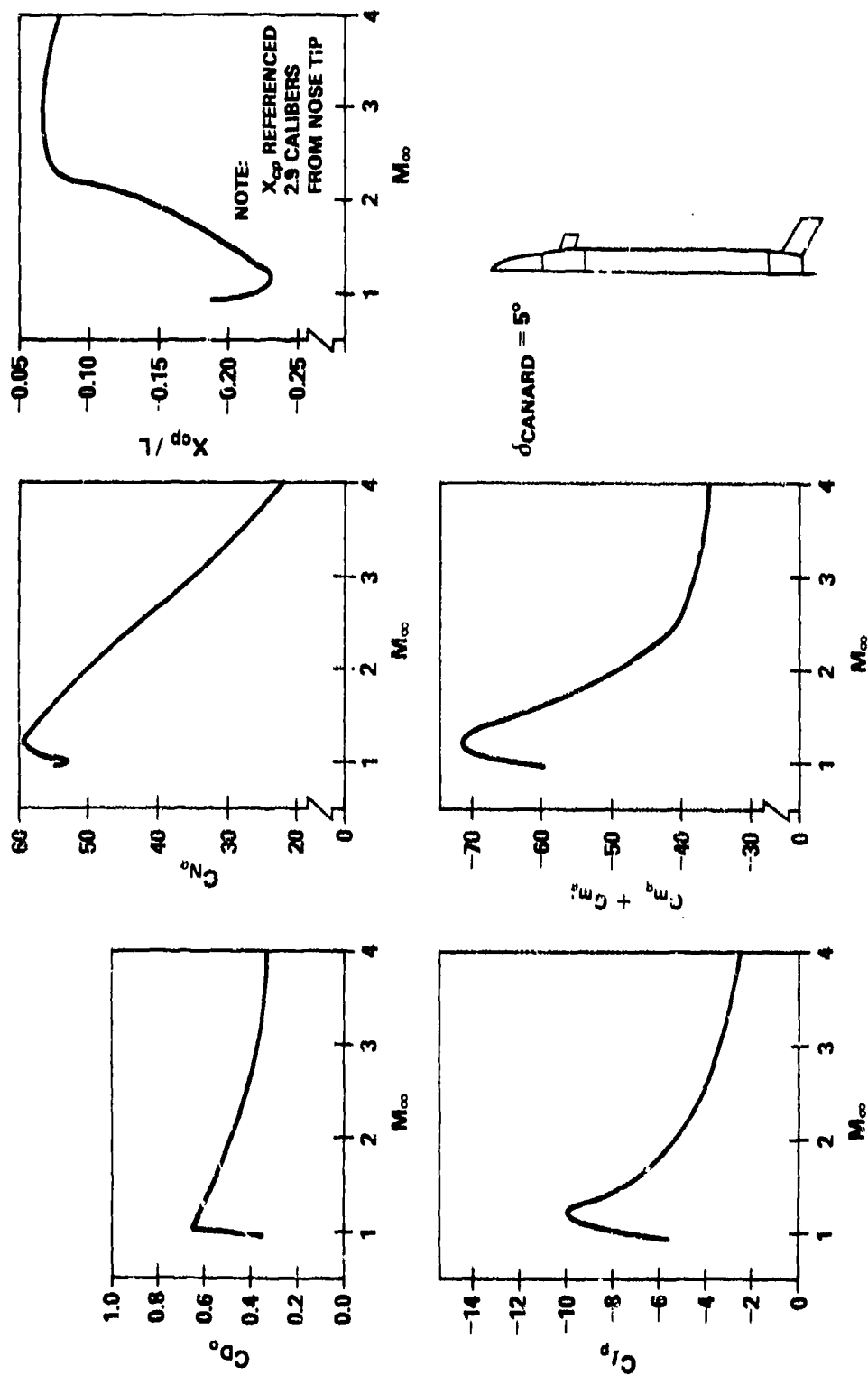


Figure 32. Theoretical Predictions for 3.0 Inch Missile

nose is divided into two distinct ogival nose sections. There are two sets of swept lifting surfaces, each having different fin geometries and deflections. The Aeroprediction Code provides data for the individual body components. The data shown in the example are for the total configuration with a 5° canard deflection.

One capability of the Code which has not yet been mentioned is illustrated in the following example. In this case, the Aeroprediction Code was modified to compute the total sectional normal force coefficients along a missile body as a function of Mach number and angle-of-attack. The results of the aerodynamic analysis were then used in a finite element structural analysis to predict structural integrity. The results of the analyses, shown in Figure 33, indicate that structural failure of the two configurations examined can occur during maneuvering flight due to the large aerodynamic bending moment. Unpublished flight test results confirmed the predictions.

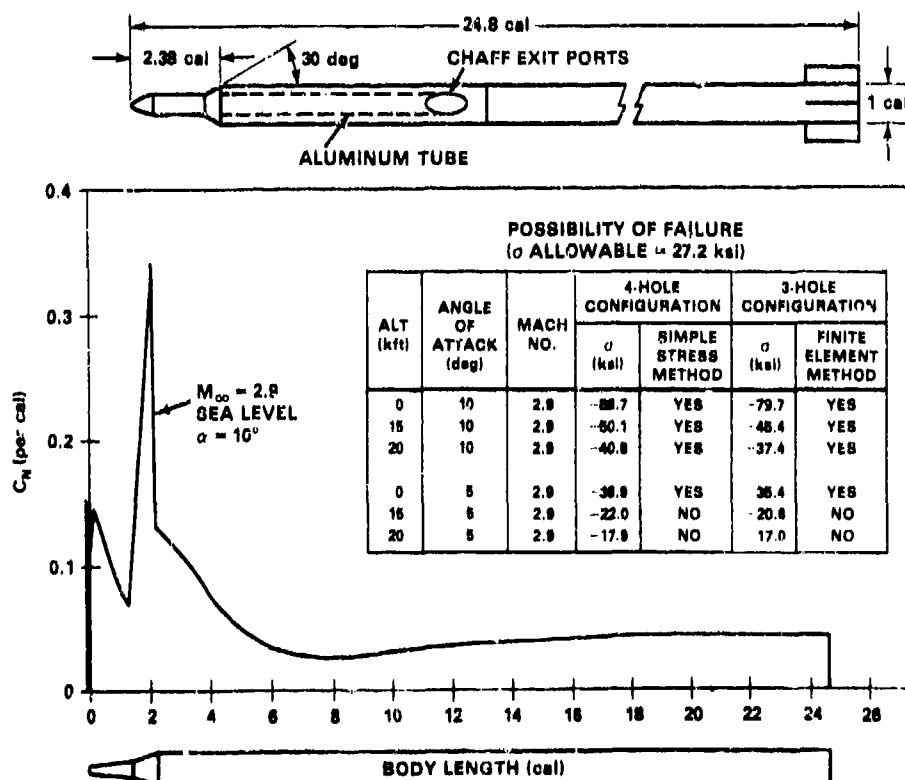


Figure 33. Structural Integrity Study Using the Aeroprediction Code

Missile Performance. Designing a missile for optimum performance is a very complex procedure with a number of tradeoffs and considerations. A few factors which are considered include the velocity, range, time of flight, altitude, launch angle, payload, maneuverability, responsiveness, lift-to-drag ratio, and performance of the propulsion system. In contrast to the projectile performance optimization where the ballistic coefficient plays an important role, a missile design is typically optimized for one or more of the factors listed. Moreover, there are more options available to the aerodynamicist in achieving the performance goals due to the lifting surfaces. The Aeroprediction Code is ideal to parametrically examine the aerodynamic factors affecting performance as a result of its relative low cost and accuracy.

To illustrate, a typical design approach is outlined which can be used to arrive at a preliminary surface launched missile design which satisfies the desired performance objectives.

Initially the missile performance requirements must be established. The specified requirements should include maximum and minimum range, missile velocity, altitude ceiling, maneuverability (g's) required, and airframe time constant. These requirements will usually be driven by the threat spectrum to be engaged. The launch and payload weight and volume constraints may also be specified due to the given launching tube or canister envelope. The maximum range requirement can be driven by several factors including the fire control radar detection range and the firing doctrine to be utilized. The minimum range (must-kill range) is usually established by doctrine. In this example, the missile is assumed to be launched from a square canister of specified length, L . The payload is assumed to include the guidance electronics, radome, warhead, and fuze. The average missile velocity is assumed to be in the $M_\infty = 3.0$ range.

The maximum flight range for the missile is a function of the time history of the missile velocity which in turn is the integral of the thrust and drag along the flight path.

The configuration sizing, therefore, involves design tradeoffs of the airframe drag and weight and the propulsion system thrust required to deliver the payload to the maximum range with adequate intercept velocity and maneuver capability. Since additional missile weight adversely impacts the propulsion system, flight performance, and packaging requirements, the designer generally desires to determine the minimum launch weight to meet stated requirements.

The missile intercept speed affects several aspects of guidance, including: the maximum allowable target crossing angle, which is a function of the target speed; the seekers maximum look angle and the airframe angle-of-attack; the miss distance, which tends to increase as the closing velocity increases due to receiver and seeker servo noise; and the missile guidance time constant, τ_g . The total missile guidance time constant is defined as the time from the initial tracking loop input upon target acquisition to the time it takes the missile to achieve approximately 63 percent of the desired rate-of-change of the flight path angle, $\dot{\gamma}$. The missile guidance time constant can be approximated to first order using the relation

$$\tau_g = \tau_1 + \tau_F + \tau_{AF} + N \frac{V_c}{V_m} \left(\frac{\alpha}{\dot{\gamma}} \right) R_{be} \quad (138)$$

where

τ_1 is the tracking loop time constant,

τ_F is the guidance filter time log,

τ_{AF} is the airframe time constant,

N is the effective navigation ratio,

V_c is the missile closing velocity,

V_m is the missile average velocity,

$\alpha/\dot{\gamma}$ is the turning rate time constant, and

R_{be} is the radome boresight error slope.

A low value of τ_g is desirable in order to reduce miss distance sensitivity to target maneuver and provide adequate terminal accuracy under adverse conditions. The adverse conditions such as electronic countermeasures or weather result in a reduction in the range available for guidance. A useful criterion for seeker end game performance is to allow a minimum of $10 \tau_g$ (10 guidance time constants) to correct terminal heading error. It can be seen from the above relation that decreases in $\frac{V_c}{V_m}$ and $\frac{\alpha}{\dot{y}}$, both of which decrease with increasing missile velocity, decrease the total time constant. Also, limitations due to the battlespace, which is the distance between the maximum and minimum ranges, and the firing doctrine (such as a shoot-look-shoot doctrine) encourage the selection of as high a missile velocity as possible. However, the increase in the miss distance as the closing velocity increases forces a compromise on the selection of the desired missile velocity. In our example, an $M_\infty = 3$ missile velocity appears to meet these restraints.

The sizing of the missile is a function of the propulsion type and capability, the type of aerodynamic control (or thrust control if used), and the maneuverability (g's) required. The propulsion system selection is based on altitude, thrust, and burn time requirements. Both simple boost and boost-sustain motors should be examined and correlated with the missile weight to provide the required average or sustain velocity over the desired range.

The choice of the type of aerodynamic control is largely a tradeoff involving the location of the controlling surfaces on the body. Canards offer advantages in obtaining a quick response from the missile. However, canards are angle-of-attack limited and often lead to pitch and roll control problems due to the interference of the shed vortices on the rear stabilizing surfaces. Wings, which must be larger to produce the same moment due to their closeness to the center of gravity, have similar advantages and disadvantages as canards. Tail alone control has the advantages of lower overall weight and better pitch/roll control due to the elimination of vortex interaction with vortices shed from lifting surfaces located forward of the tail. It has the disadvantages of longer missile response time because the control force to rotate the missile is opposite

to the desired direction of travel and actuator packaging must be accomplished around the rocket motor. In this case, tail control is selected for the conceptual missile design. A jettisonable set of jet vane controls may be added in order to implement the quick turn maneuver from the vertical when a vertical launch system is utilized.

Having made the above choices, the missile diameter and fineness ratio can be determined. Using an average overall packing density of .062 lb/in³, relationships between the missile length, diameter, and weight for the body-tail type configuration can be obtained as shown in Figure 34. Based on these curves, an 8-inch diameter configuration apparently would best meet the length and weight constraints shown.

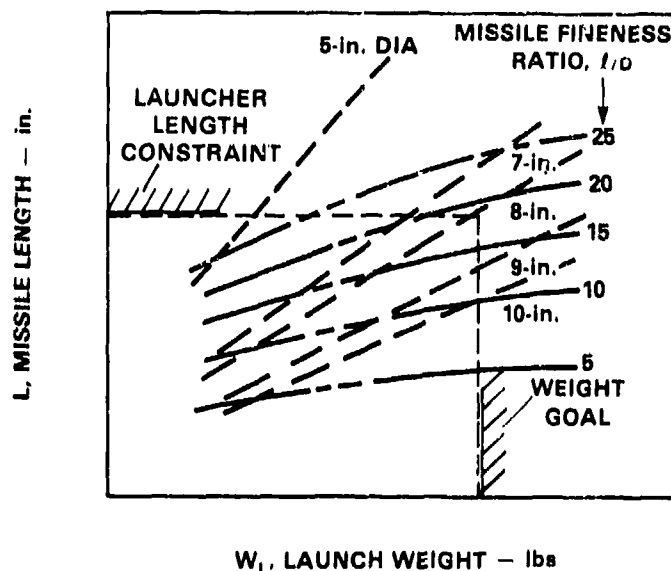


Figure 34. Missile Physical Characteristics

Sufficient missile maneuverability is required in the terminal phase of flight to compensate for guidance errors, heading error, and target maneuvers. An estimate of the missile maneuverability, a_m , required to correct for guidance errors due to noise and target maneuvers is provided by the relation

$$a_m \geq (3a_T + 8) g \quad (139)$$

where a_T is the maneuvering target acceleration.

The miss distance due to initial heading error, HE_0 , is based on an average missile acceleration, a_m , applied over time, t_f , and is given by

$$m_{HE} = V_m t_o (1 - t_f/t_o)^N HE_0 \quad (140)$$

where $t_o \approx 10 \tau_g$ and the initial missile acceleration (assuming no g saturation) is:

$$a_m = \frac{N V_m}{t_f g} HE_0 \text{ (g's)}. \quad (141)$$

For a 2.0 second guidance time, $\tau_g = .2$, and $N = 3$, an initial HE of 10° can be corrected and the miss distance eliminated provided the missile can achieve a 27 g maneuver.

Figure 35 shows the radome boresight error slope variation versus nose drag coefficient for several nose shapes and fineness ratios. To minimize the boresight error while achieving relatively low drag, a 2.25 caliber Von Kármán nose contour is selected.

It is now possible to define the overall missile fineness ratio. For the trimmed condition, it is necessary that the summation of the moments be zero such that

$$C_{m\alpha} \alpha_{Trim} + C_{m\delta} \delta_F = 0 \quad (142a)$$

or

$$\alpha_{Trim} = -\left(\frac{C_{m\delta}}{C_{m\alpha}}\right) \delta_f \quad (142b)$$

Therefore, to obtain maximum maneuverability, it is desired to minimize the total untrimmed pitching moment coefficient, $C_{m\alpha}$. Similarly, the normal force for the trimmed condition is

$$C_{N_{Trim}} = C_{N_\alpha} \alpha_{Trim} + C_{N_\delta} \delta_F \quad (142c)$$

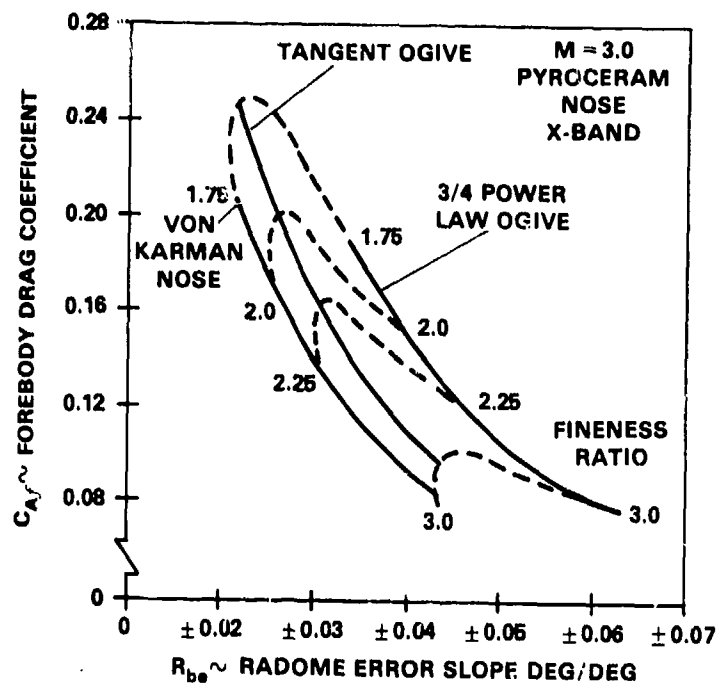


Figure 35. Forebody Drag Coefficient vs Boresight Error Slope for Various Shapes and Fineness Ratios

Since deflection of the tail surfaces produces a negative normal force to achieve the desired angle-of-attack, it can be seen that the body untrimmed C_N required is greater than the trimmed condition. With this in mind, several tail sizes and planforms were examined to obtain a first approximation of the tail size and to estimate the negative normal force effect. Figure 36 shows the variation of the tail normal force due to deflection, $C_{N\delta}$, and the total configuration pitching moment, $C_{m\alpha}$, for a hypothetical body versus taper ratio assuming a diamond airfoil cross section. The optimum tail for maneuverability is that which produces the least negative force with deflection and the minimum total pitching moment. For this example, the optimum tail was that having a $C_t/C_r = .364$ resulting in a $C_{N\delta} = -0.67$ (deg^{-1} , based on the planform area, S_T). If the center of gravity of the total missile configuration after burnout is assumed to be .54L from the nose tip, the normal force required versus angle-of-attack

for configurations of varying L/D ratios can be determined. In this case, the total trimmed C_N required for the required maneuver is 3.4 for a maximum angle-of-attack of 18° . This indicates that a body alone normal force coefficient of 4.0 must be obtained. This is possible with a $L/D = 18$ which was shown earlier to also meet the length and weight constraints.

The resulting preliminary missile configuration and the estimated aerodynamic coefficients are shown in Figure 37 and 38. Using these data and the propulsion data, the missile performance can be predicted for various conditions. A typical trajectory is shown in Figure 39.

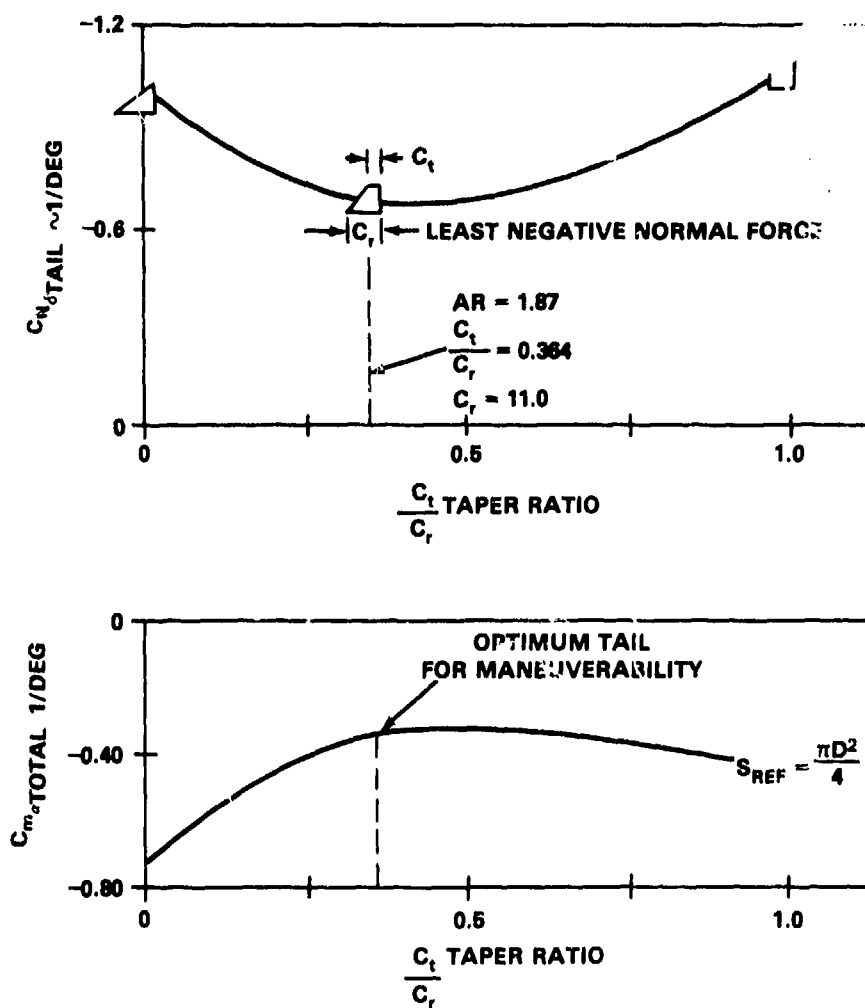


Figure 36. Tail Normal Force and Pitching Moment Coefficient vs Taper Ratio

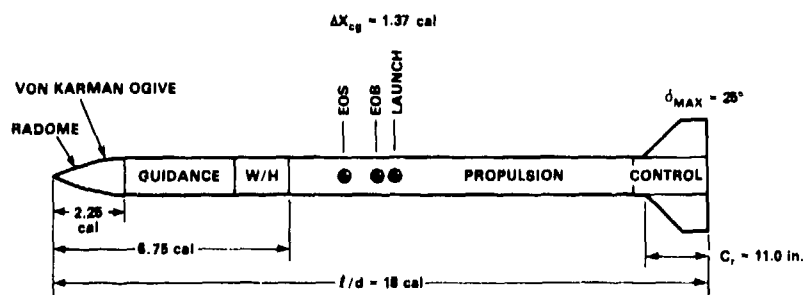


Figure 37. Example Missile Design

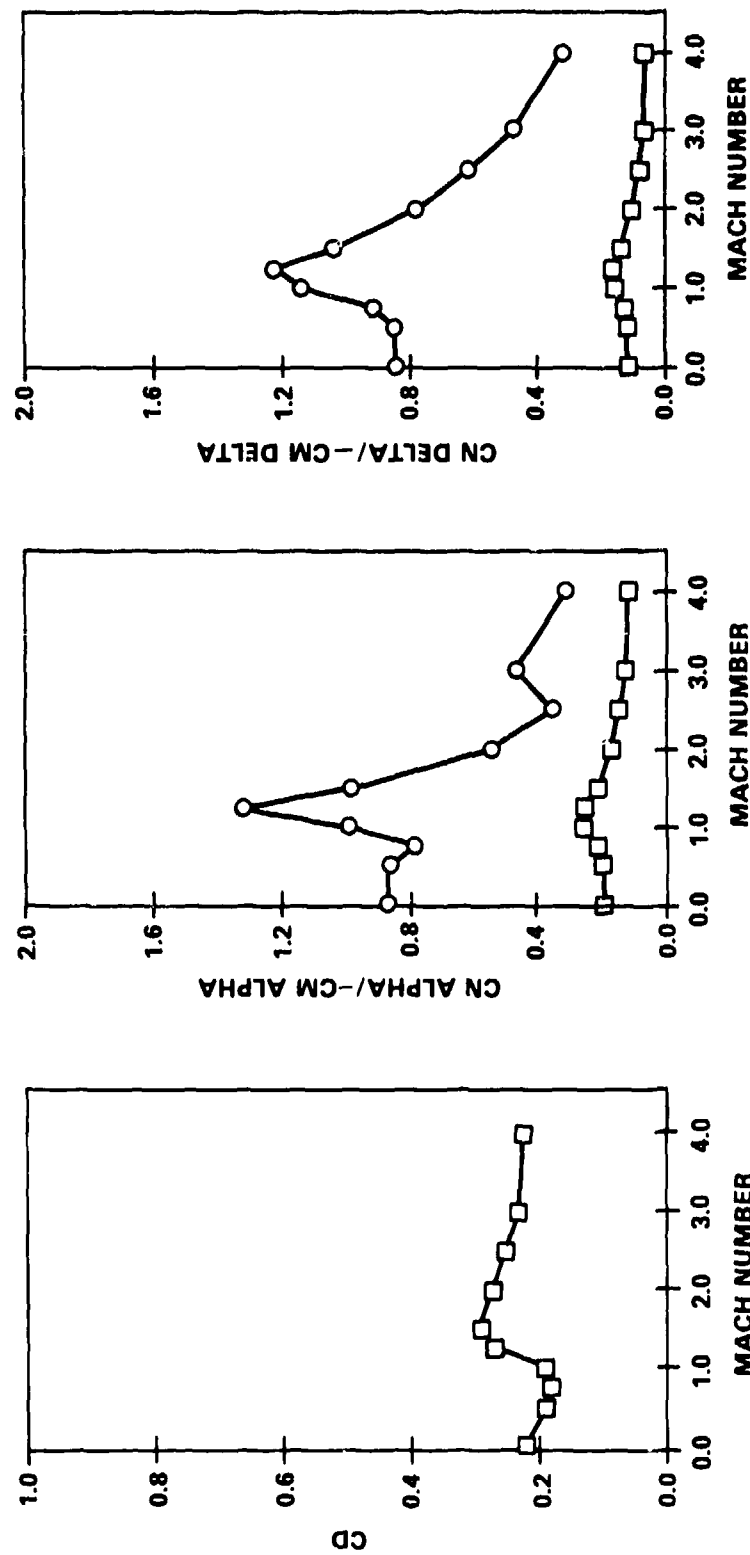


Figure 38. Aerodynamic Coefficients for Example Missile

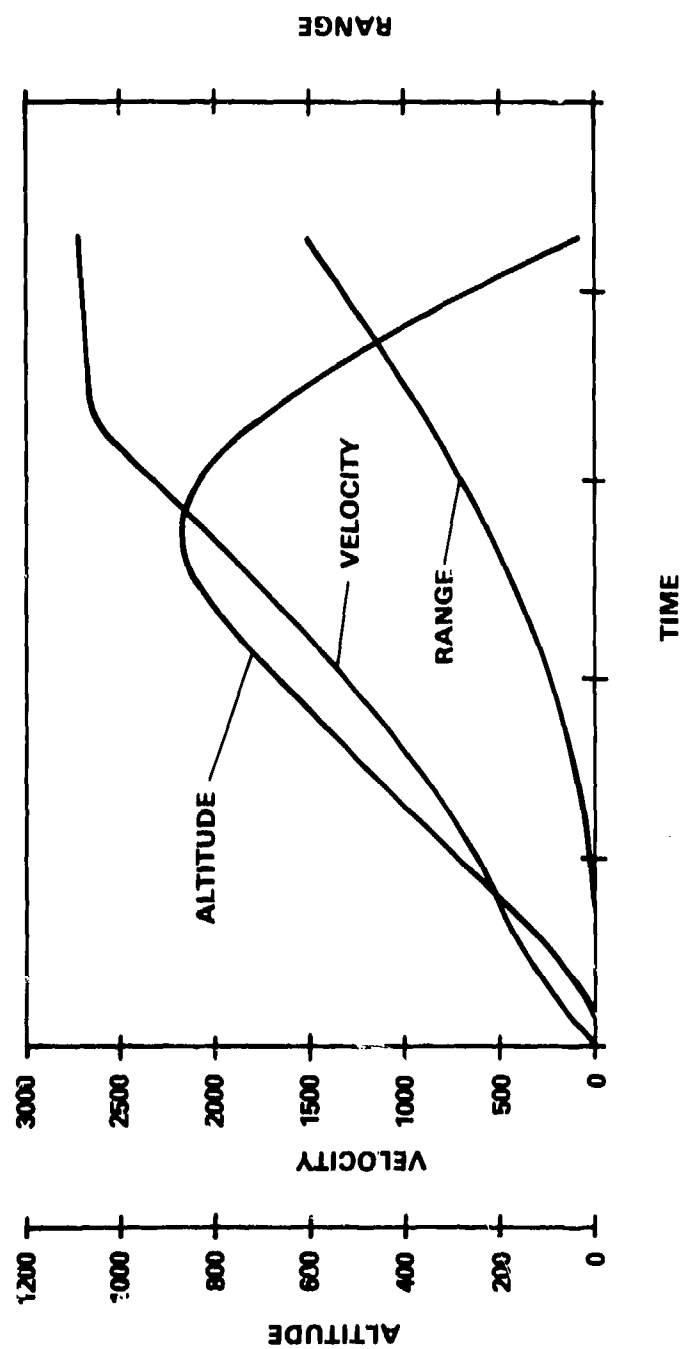


Figure 39. Example Missile Configuration Performance

4. AIDS TO DESIGN

As can be readily seen in the material of Section 2, a large number of methods and data have been brought together into one computer program. The resulting configurational generality possible allows one to examine the effects of design modifications of various configuration components on the total configuration aerodynamics and stability. Handbooks have been previously published (References 5, 22, and 32) which have provided aids to the missile designer for certain classes of configurations. In this section, a number of design charts are presented which were generated using the Aeroprediction Code for various configuration components of both pointed and blunt bodies. These charts represent portions, reproductions, and extensions of the charts presented in these earlier handbooks. The user is encouraged to compare the data presented with that of the earlier works where possible. The basic desire of the authors is to show the trends due to modifications in the design components which will guide the designer in the preliminary design process. For body component parameters within the limits of the charts presented here, the reader can use the method of component superposition (i.e., to add up the various effects of each component) to obtain the aerodynamics of the complete configuration.

4.1 BODY ALONE DESIGN

The aerodynamic coefficients were determined for a large number of body alone, axisymmetric shapes throughout the Mach number range. The characteristics of the body components were varied systematically to establish the trends in the aerodynamic coefficients. Particular attention was given to bodies with conical, tangent-ogive, and secant-ogive nose contours as shown in Figure 40 because of their primary interest to missile designers.

4.1.1 DRAG

As indicated in Section 2, the total drag of the body is the sum of the nose wave drag, the skin-friction drag, the boattail wave drag, the base drag, and the drag of protrusions, plus the crossflow contribution. In this section, data are

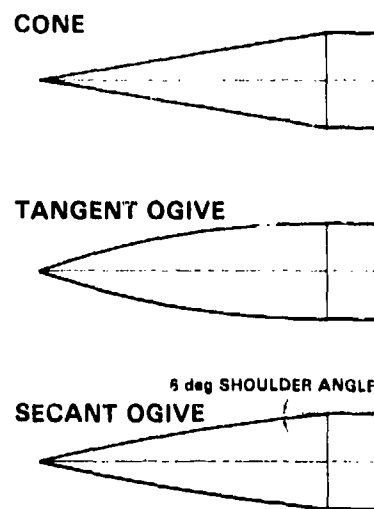


Figure 40. Typical Nose Contours ($L_N = 3.0$ cal)

presented for $\alpha = 0^\circ$. For moderate angles-of-attack, a crossflow drag correction is presented.

The nose wave drag is influenced primarily by nose shape, fineness ratio (L_N/D), and Mach number. The effect of these parameters on the wave drag in supersonic flow is illustrated in Figure 41 for pointed bodies. In general, the wave drag decreases for increasing nose fineness ratio and Mach number. Of the nose contours shown, the secant ogive is shown to provide the lowest wave drag within the Mach number range $1.0 < M_\infty < 6.0$. Earlier studies (References 5 and 38) have shown that the minimum wave drag for secant ogives for low supersonic Mach numbers ($M_\infty < 2.5$) is obtained by using a radius of curvature twice that used for a tangent ogive of the same length. In this comparison, all of the secant ogive profiles had a constant shoulder angle of 6.0° . For low supersonic Mach numbers ($M_\infty < 2.0$) slender body theory predicts the minimum drag profile to be the well-known Von Karman ogive. Newtonian theory predicts that the conical nose shape would become the minimum drag profile as $M_\infty \rightarrow \infty$. Therefore, in general, the expected trend in supersonic flow is that for a given nose length and diameter the minimum drag profile would vary slowly from the Von Karman ogive to the secant ogive (with radius twice that of a tangent ogive) and then to a conical nose shape as the Mach number increases. Although not shown, the

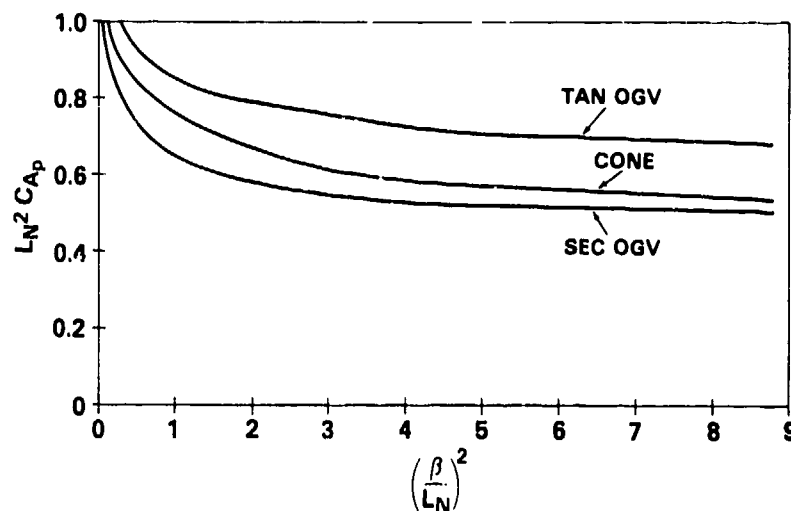


Figure 41. Wave Drag Comparison for Pointed Bodies

power-law nose contours also closely follow these trends and may in some instances exhibit lower drag than the secant ogive due to nose bluntness. For example, the 6.0° (shoulder angle) secant ogive can be approximated by the two-thirds power-law nose. As the Mach number increases, the power used to obtain the low drag shape increases to a value of 1 which corresponds to the conical shape.

For a nose of fineness ratio of 3.0, the variation in the wave drag with nose shape is shown in Figure 42. In this case, the more blunted tangent ogive is shown to have the lower wave drag for $M_\infty = 1.0$. For subsonic Mach numbers, the wave drag contribution is assumed to be zero for $M_\infty < .5$. The exact point at which the wave drag disappears depends on the nose fineness ratio. This is illustrated in Figure 43 which shows the transonic wave drag for various tangent ogives.

The nose wave drag is also influenced by bluntness as shown in Figures 44 and 45 for cones. The data presented are for a 7.125° semi-angle truncated cone with fineness ratio 4.0 when not blunted and for a 10° semi-angle spherically capped cone. When adding the spherical cap or truncating the nose, the nose length was reduced back to the point where the proper value for R_N (the radius

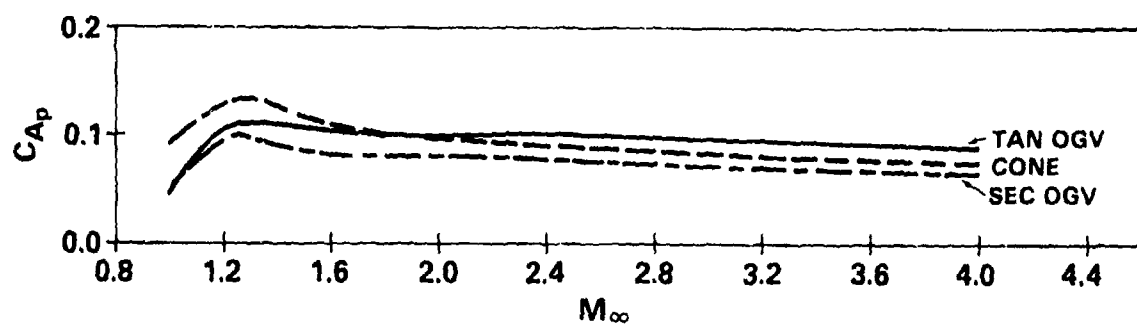


Figure 42. Wave Drag Comparison for Pointed Bodies (Nose Length ≈ 3.0 cal)

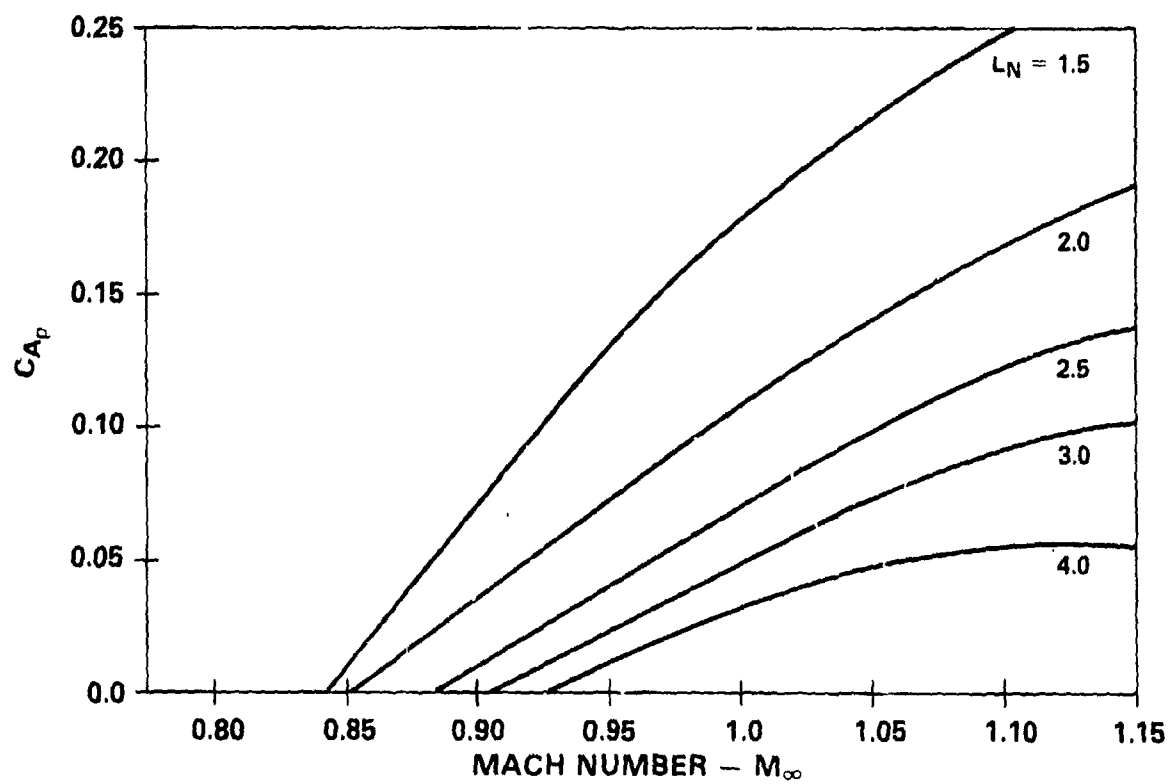


Figure 43. Transonic Wave Drag of Tangent Ogives

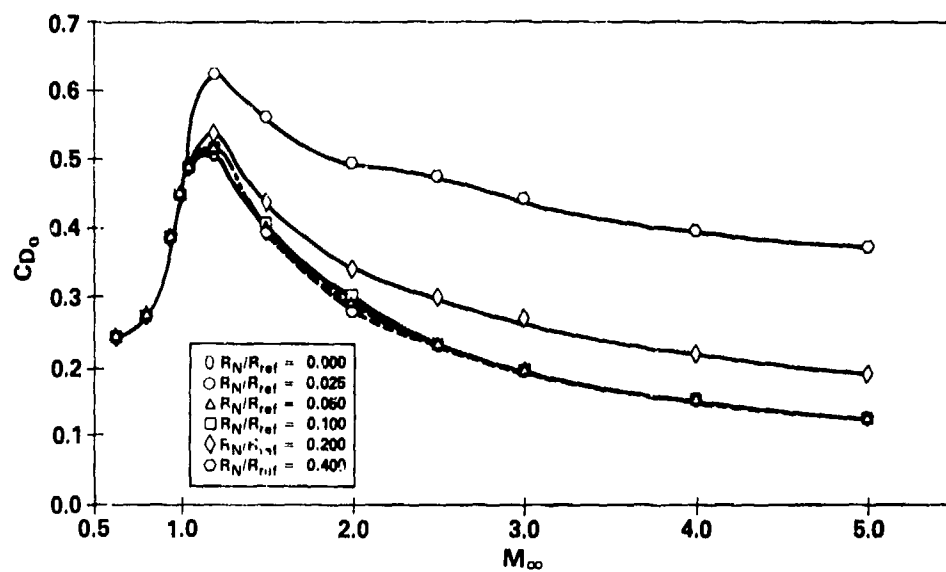


Figure 44. Total Drag for Blunted 7.125° (4 cal) Cones - Truncated to Shorter Length

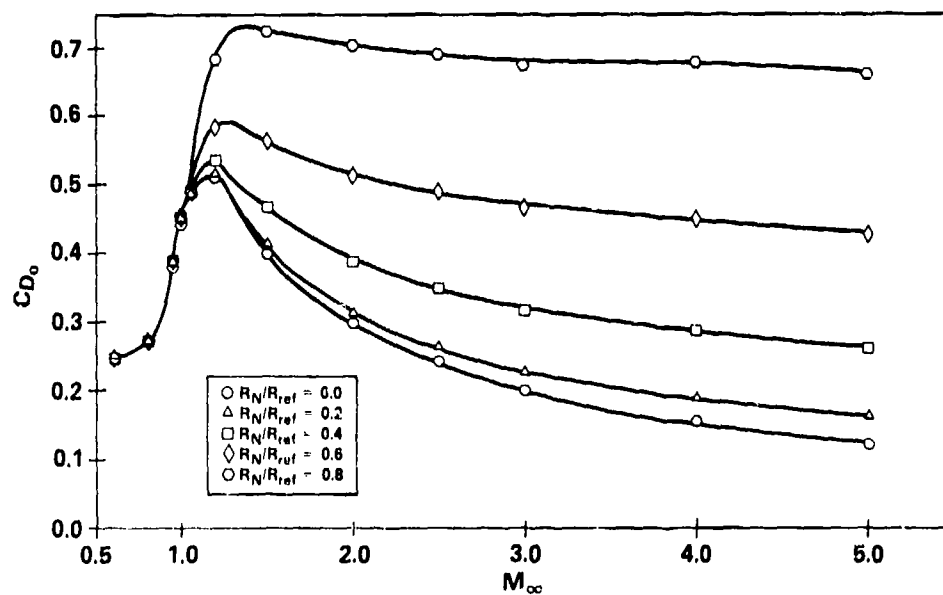


Figure 45. Total Drag for Blunted 10° - Spherically Capped to Shorter Length

of the cap for the spherically capped cones) would be obtained while keeping the slope of the conical frustrum constant. As can be seen, truncation alone has a slightly greater effect than truncation with a spherical cap. Note, however, that a portion of the difference can be attributed to the slightly different nose lengths obtained in the two cases for the same bluntness ratio. The different nose length results from both the different slopes and the smaller body radius at the point of tangency of the spherical cap. In either case, bluntness of the nose up to $R_N/R_{ref} = .1$ has a negligible effect on the wave drag (or on the other aerodynamic coefficients, as shown in the following subsections). Further increases in the bluntness ratio results in pronounced increases in the drag.

On very low fineness ratio pointed noses with little or no curvature, the high body slope may result in a viscous separation drag at subsonic and transonic Mach numbers. This drag results from a separation bubble formed by flow detachment at the nose tip due to strong adverse pressure gradients and reattachment downstream. The phenomenon is somewhat Mach number dependent and is clearly noticeable for $M_\infty < .8$. Its presence is apparent up to $M_\infty \sim .95$ or so depending on the cone angle. Figure 46 shows the magnitude of the nose separation drag for cones with and without afterbodies at subsonic speeds. The effect of the nose separation bubble is noticeably reduced by the influence of the afterbody. The effect of nose curvature is to eliminate the adverse pressure gradients and therefore the phenomenon does not occur.

For angles-of-attack near zero, the contribution of cylindrical afterbodies to the wave drag is assumed to be zero and thus no additional contribution to the wave drag occurs. Flares and boattails contribute positively to the wave drag. Wave drag data for flares are presented in References 5 and 22, and the reader is referred to these publications in these instances.

The wave drag of the boattail is primarily influenced by the boattail slope or angle, the boattail length, Mach number, and the length of the preceding afterbody as this affects the degree of pressure recovery on the afterbody and subsequent expansion at the afterbody-boattail juncture. For short afterbodies ($L_A < 4.0$ calibers), the pressure recovery and thus the boattail wave drag are

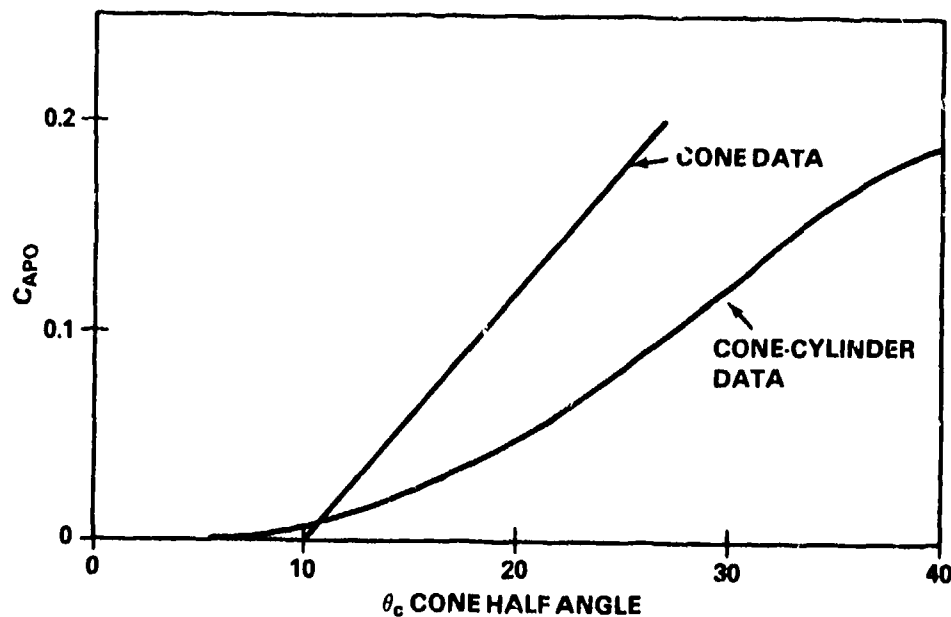


Figure 46. Separation Pressure Drag on a Cone-Cylinder

also influenced by the nose shape (Reference 14), the influence generally becoming stronger as the nose shoulder angle increases. In this study, the effects of nose shape and afterbody length on the boattail were not examined. However, it should be noted that the numerical marching technique used in the Aeroprediction Code would allow one to examine these parameters, at least to the end of the afterbody.

The wave drag coefficient for conical boattails in supersonic flow is given in Figure 47. For a given boattail length, decreasing the base diameter increases the boattail wave drag. However, as can be seen from Equation (136), decreasing the base diameter also results in a lower base pressure. Therefore, an optimum configuration with respect to drag would balance these drag contributions. The overall decrease in total drag of a configuration can be strongly influenced by the boattail design. This is illustrated clearly in Figure 48 which shows the variation in the total drag of a 10.5 caliber body having a 3.0 caliber tangent-ogive nose, a 6.0 caliber cylindrical afterbody, and a 1.5 caliber conical boattail with various base diameters. In subsonic flow, decreasing

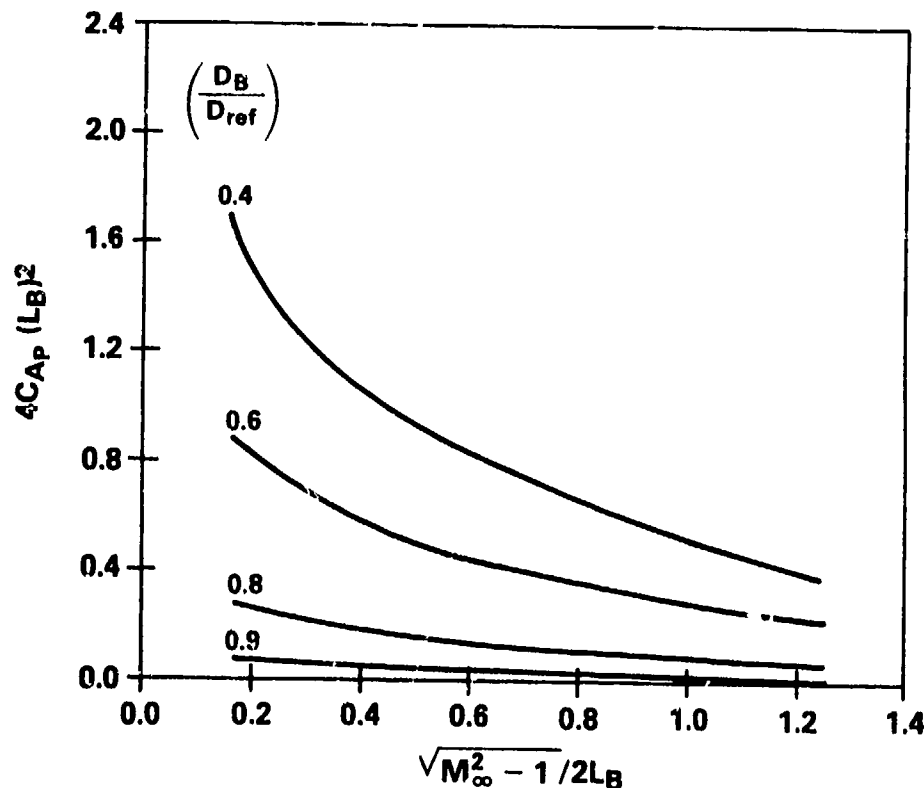


Figure 47. Wave Drag Coefficient of Conical Boattails at Supersonic Speeds

base diameter continues to decrease the total drag. In transonic and supersonic flows, however, decreasing the base diameter to a ratio of $D_B/D_{ref} = .4$ or lower results in an increase in the total drag. In supersonic flow, as the Mach number increases, the influence of the base drag decreases rapidly, thus allowing larger base diameters to achieve a minimum drag boattail design.

Many projectiles also retain rotating bands in flight. In the absence of fraying, the drag increment due to a rotating band has been functionalized (Reference 1) and can be obtained by using Equation (17) and the curve shown in Figure 49. More recently, rotating bands have been designed for full-bore projectiles which discard upon muzzle exit, thus eliminating this drag contribution and allowing for a cleaner shape.

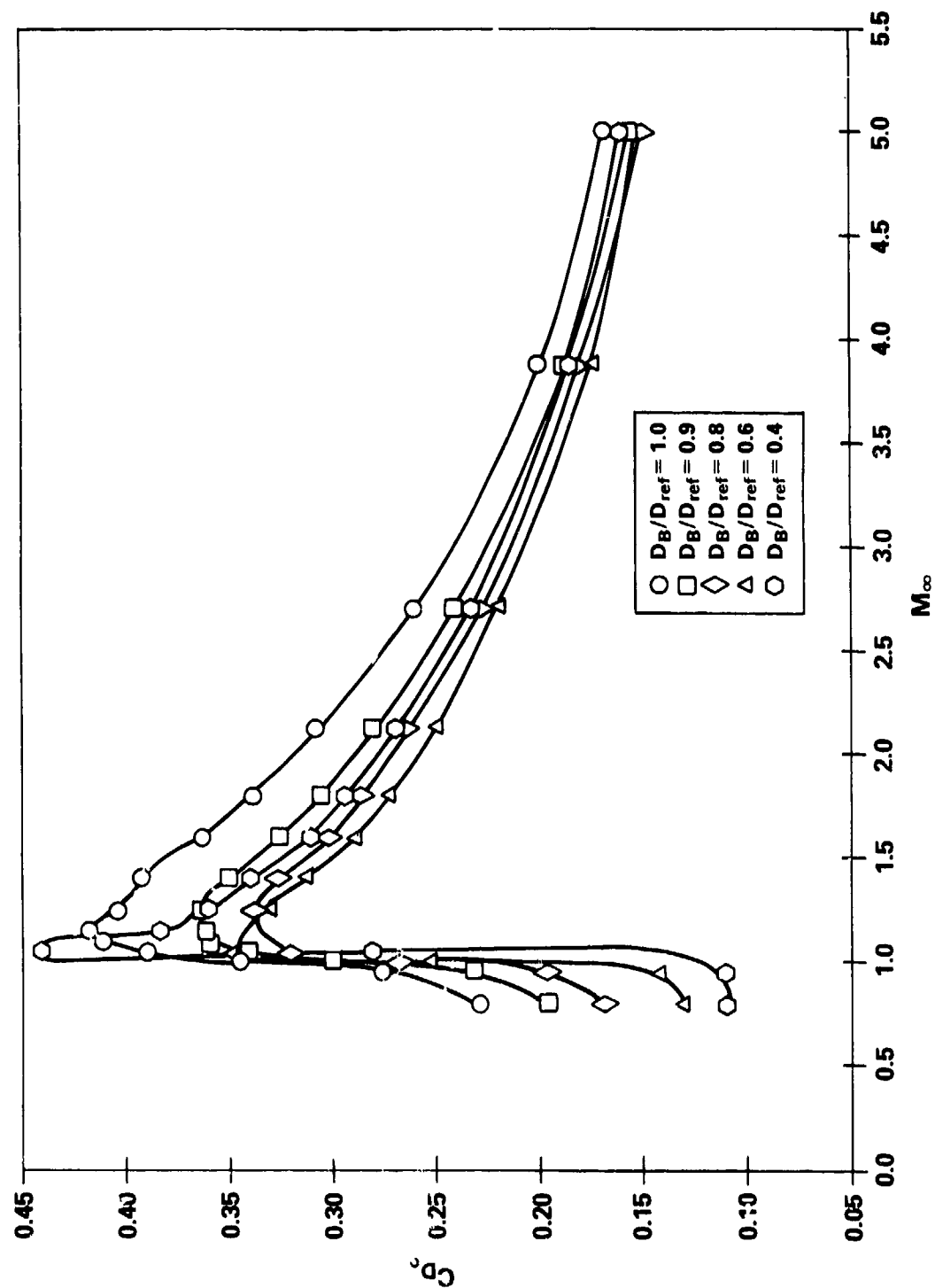


Figure 48. Variance of Boattail Base Diameter on Total Drag vs M_∞ for a Complete Body Configuration

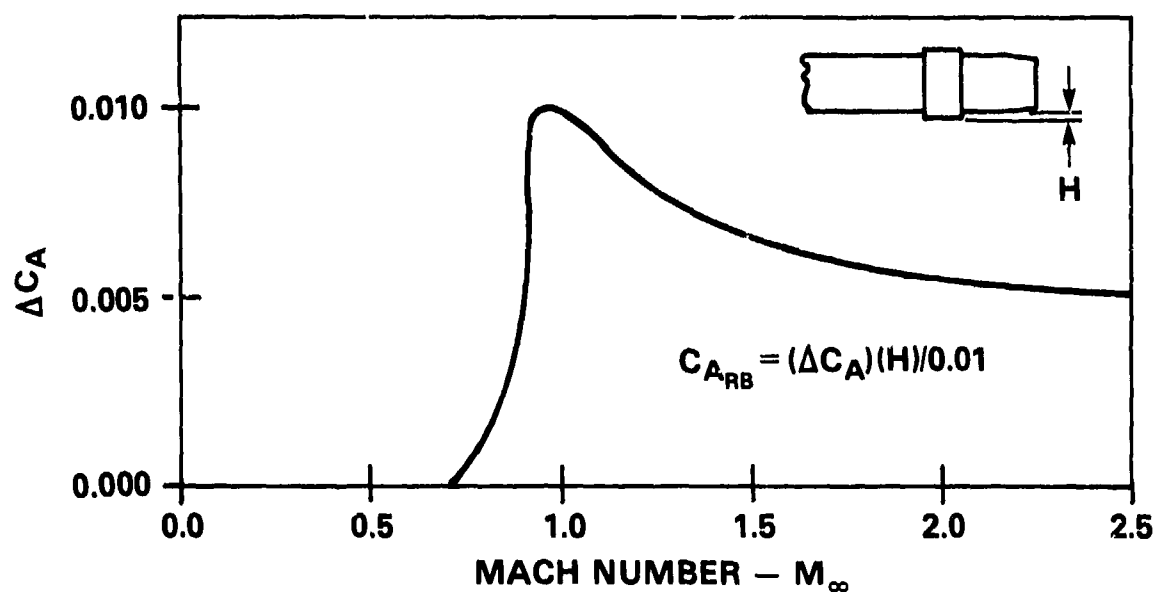


Figure 49. Rotating Band Drag - $C_{A_{RB}}$

For $\alpha > 0$, additional drag results from the viscous crossflow velocity ($V = V \sin \alpha$). For moderate angles-of-attack, one needs first to determine the total normal force (as outlined in the following section beginning on page 98). Then, the total drag is

$$C_D = C_A \cos \alpha + C_N \sin \alpha \quad (143)$$

where

$$C_A = C_{D_0} \cos^2 \alpha. \quad (144)$$

The skin friction component of the total drag is computed using Van Driest's method as outlined in Section 2. The skin friction drag is influenced primarily by the Reynolds number, the heat transfer, the Mach number, and the point on the body at which the boundary layer transitions from laminar to turbulent flow. For the body alone, the boundary layer will generally be turbulent over roughly 90 percent of the body, depending on flow conditions and overall body length. For very short bodies and for fins, the percentage will likely be much less.

The calculation of the skin friction coefficient using Van Driest's method is somewhat cumbersome. A rough approximation can be obtained by using the simple formulation (from Reference 5):

$$C_{A_F} = C_F \frac{S_w}{S_{ref}} \quad (145)$$

where

S_w is the wetted surface area,

S_{ref} is the reference arc, and

C_F is the skin friction coefficient determined from Figure 50 multiplied by the factor 1.15 for a body of revolution.

No attempt is made here to examine the trends for the base drag or the various parameters affecting base drag in detail. Deviations in the base drag could occur with variations in the nose shape, afterbody length, angle-of-attack, Reynolds number (if sufficiently low), surface temperature, and boattail shape. However, the most common method to determine the base drag in the absence of any mass base flow (such as base bleed or rocket exhaust) is an empirical method based on data for a long cylindrical afterbody and a fully turbulent boundary layer ahead of the base (Reference 1) and adjusting for the presence of a boat-tail. The relation for determining the base drag in this situation [using Equations (18) and (20) from Section 2)] is

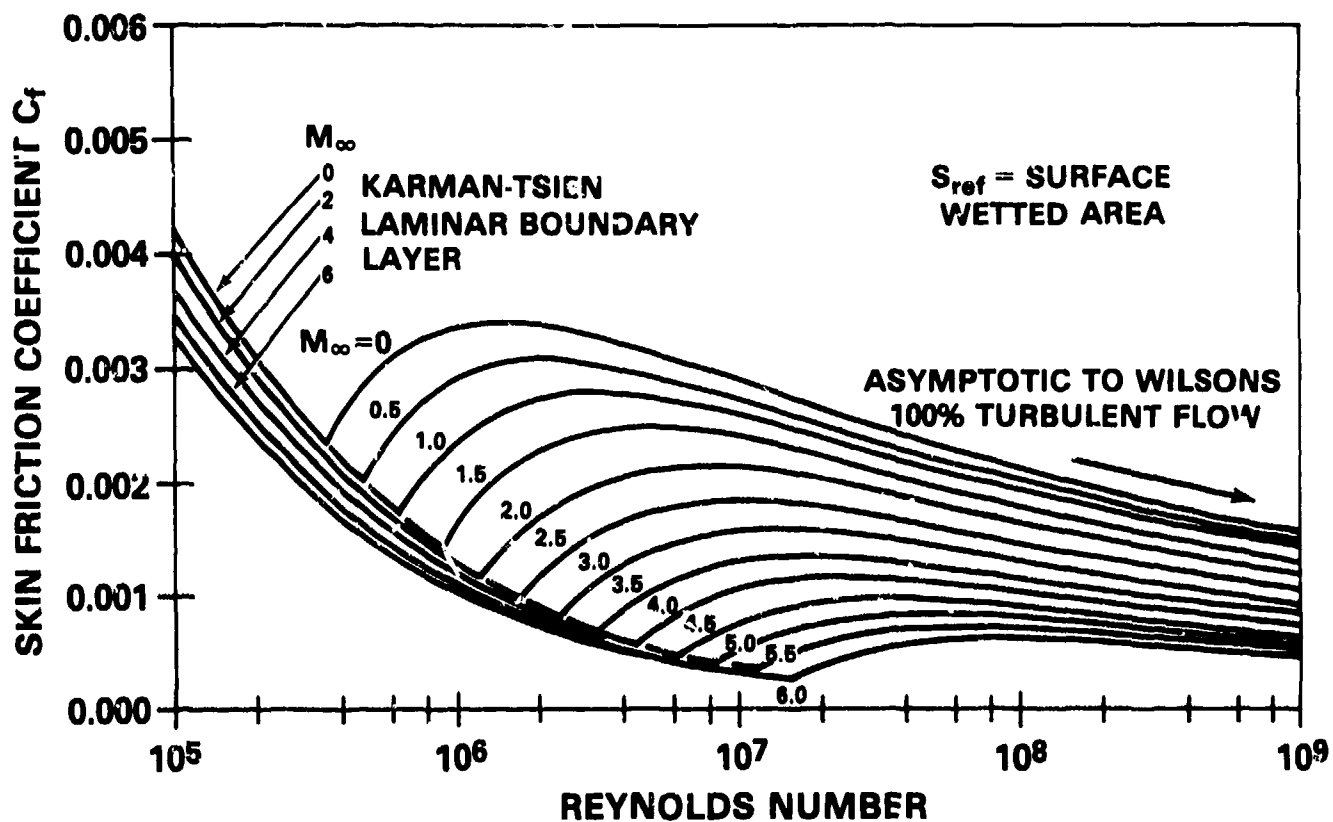
$$C_{AB} = -C_{P_{BA}} (R_B/R_{ref})^3 \quad (18)$$

where $C_{P_{BA}}$ is determined from Figure 51.

For small angles-of-attack and low supersonic Mach numbers, the relation

$$\Delta C_{ABA} = (-.6493\alpha - .002833M_\infty)(R_B/R_{ref})^3 \quad (20)$$

can be used to adjust the base axial force.



* NOTE: LINEAR vs. 4 CYCLE LOG PAPER

Figure 50. Flat Plate Average Skin Friction Coefficient

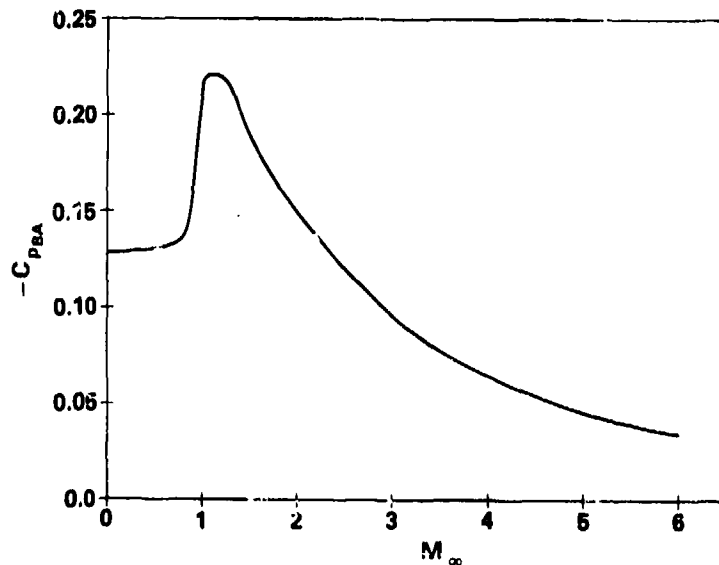


Figure 51. Mean Base Pressure Coefficient ($\alpha = 0^\circ$)

4.1.2 NORMAL FORCE AND CENTER OF PRESSURE

At zero angle-of-attack, an axisymmetric body exhibits no normal force. However, with even small increases in the angle-of-attack, the normal force increases rapidly. The slope of the normal force curve ($C_{N\alpha}$ versus α), expressed as the coefficient $C_{N\alpha}$ and its location of action (center of pressure, x_{cp}) relative to the body center of gravity is of primary concern in assessing the stability of a flight vehicle. Projectiles without lifting surfaces are generally statically unstable and must be stabilized through gyroscopic means. For a statically stable body, the x_{cp} must be rearward of the x_{cg} . This is often achieved by placing lifting surfaces on the rearward portion of the body. The x_{cp} location is more or less positioned depending on flight conditions and the degree of maneuverability desired.

The normal force derivative, $C_{N\alpha}$, and the x_{cp} for various nose-afterbody combinations at zero angle-of-attack are given in Figures 52 through 57. The data presented are for bodies with tangent-ogive, secant-ogive, and conical nose shapes. The effect of nose length, afterbody length, and Mach number can be readily assessed from these graphs. For $\beta/L_N > .9$ (high supersonic flow), the trends for the values of $C_{N\alpha}$ and x_{cp} are quite consistent. Generally, for a given L_N and Mach number, increasing afterbody length results in a corresponding increase in $C_{N\alpha}$ and a decrease in the x_{cp} distance from the nose (in terms of the percentage of the total body length). Note that the data presented are for $\alpha = 0^\circ$. As a result, for a tangent ogive-cylinder body and, to a lesser degree, for the secant ogive-cylinder body, the data indicate that an increase in the afterbody length beyond $L_A/L_N = 3.0$ does not significantly increase $C_{N\alpha}$. This would not necessarily be the case for higher angles-of-attack. The effects of afterbody length and Mach number are more easily visualized in Figures 58 and 59 for $L_N = 4.0$ caliber tangent ogive-cylinder and cone-cylinder bodies.

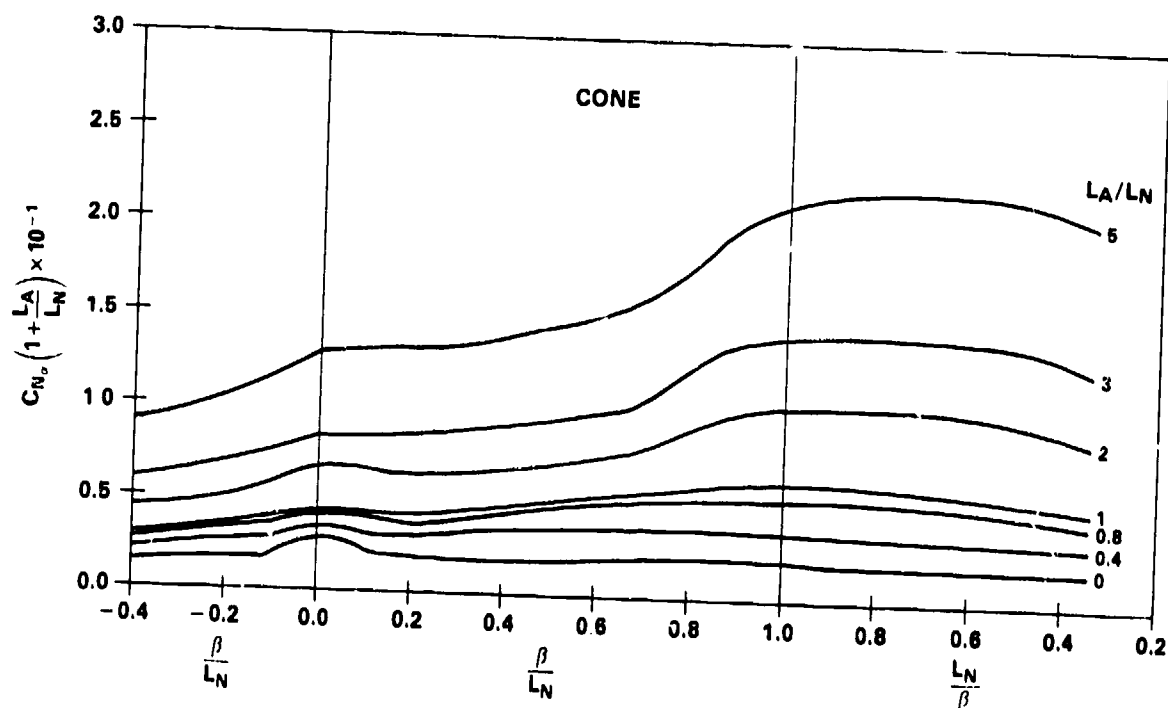


Figure 52. Supersonic Normal Force Coefficient Variation for Cone Cylinders

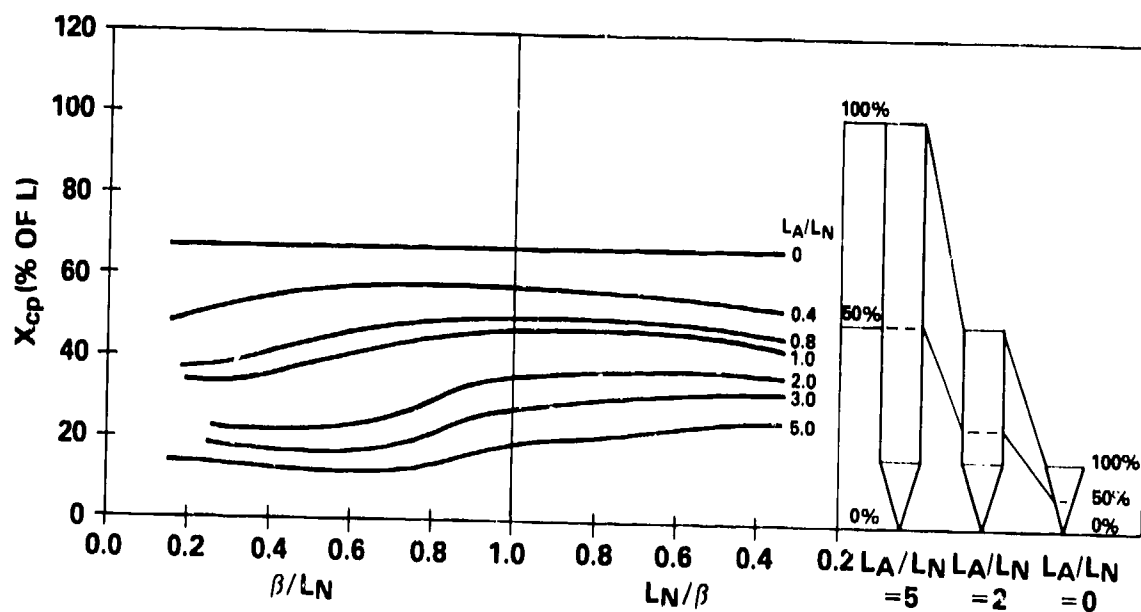


Figure 53. Supersonic X_{cp} Variation for Cone Cylinders

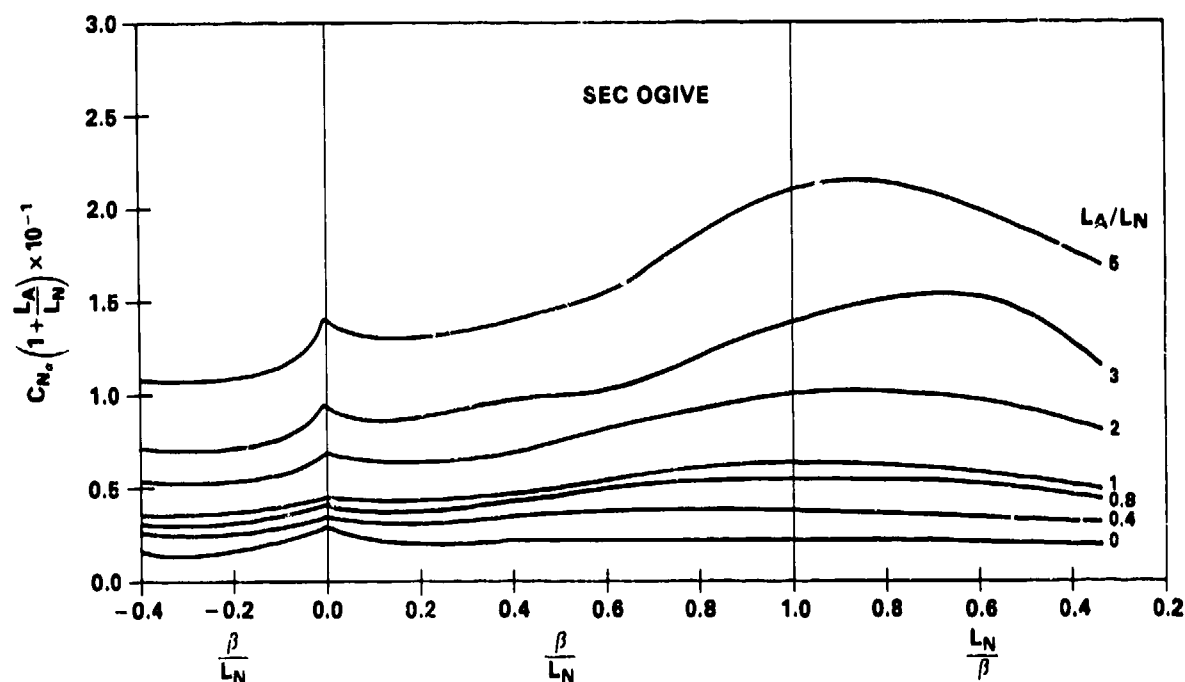


Figure 54. Supersonic Normal Force Variation for Secant-Ogive Cylinders

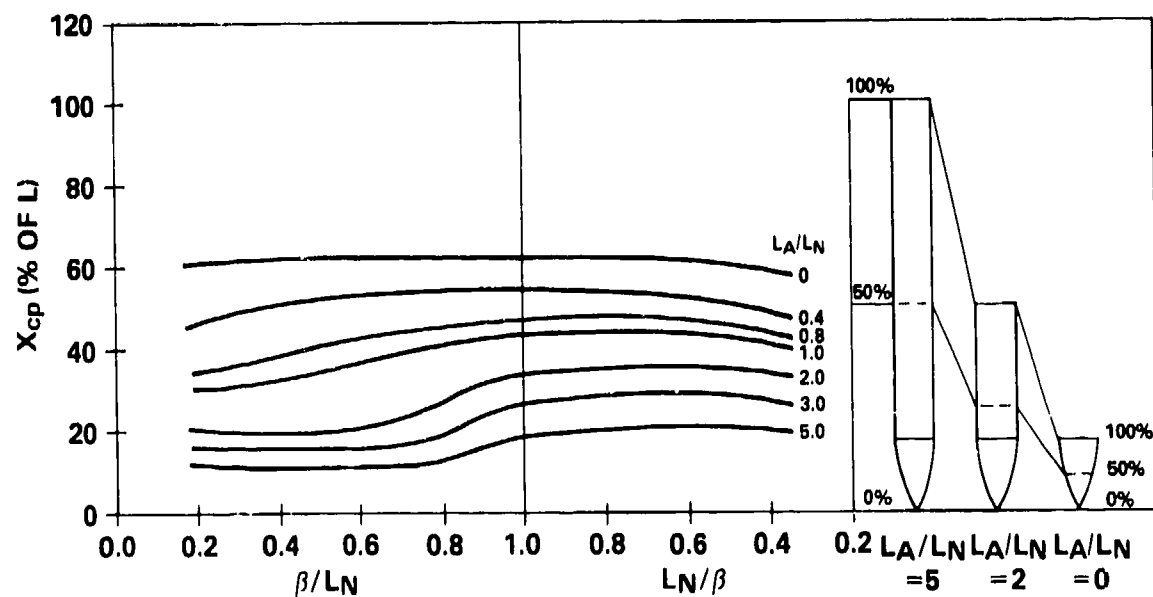


Figure 55. Supersonic X_{cp} Variation for Secant-Ogive Cylinders

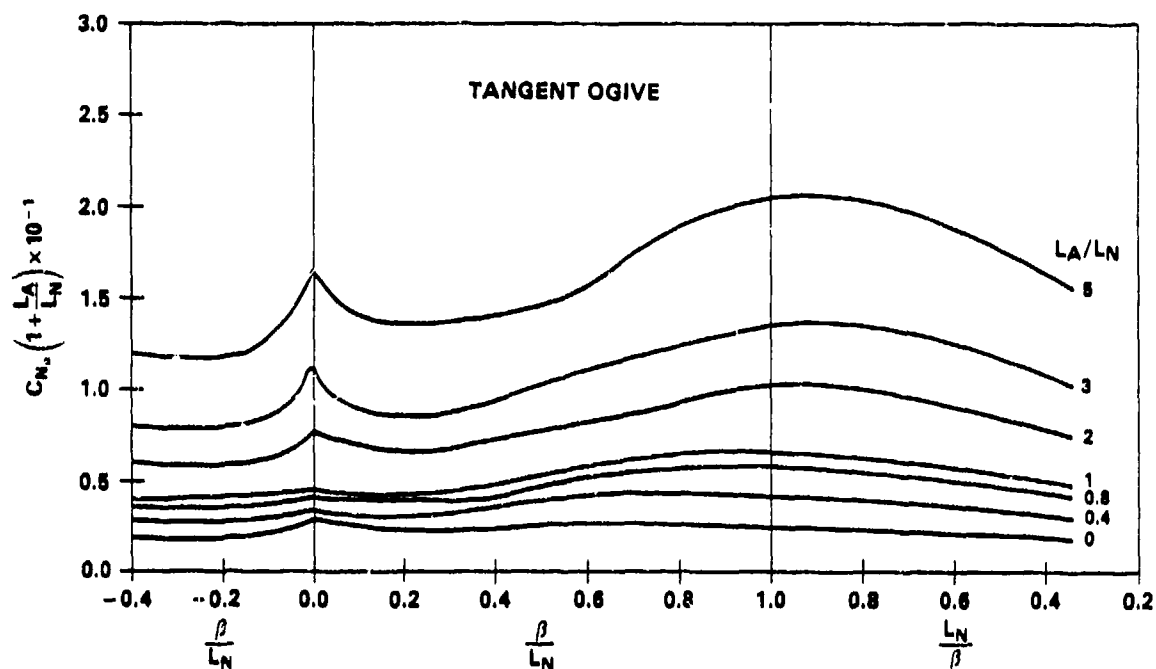


Figure 56. Supersonic Normal Force Coefficient Variation for Tangent-Ogive Cylinders

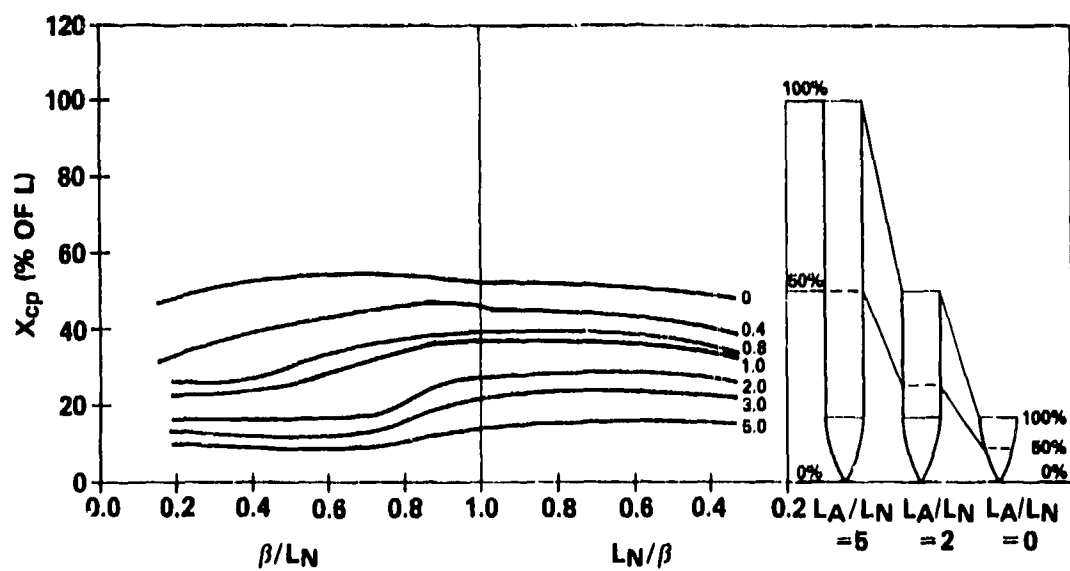


Figure 57. Supersonic X_{cp} Variation for Tangent-Ogive Cylinders

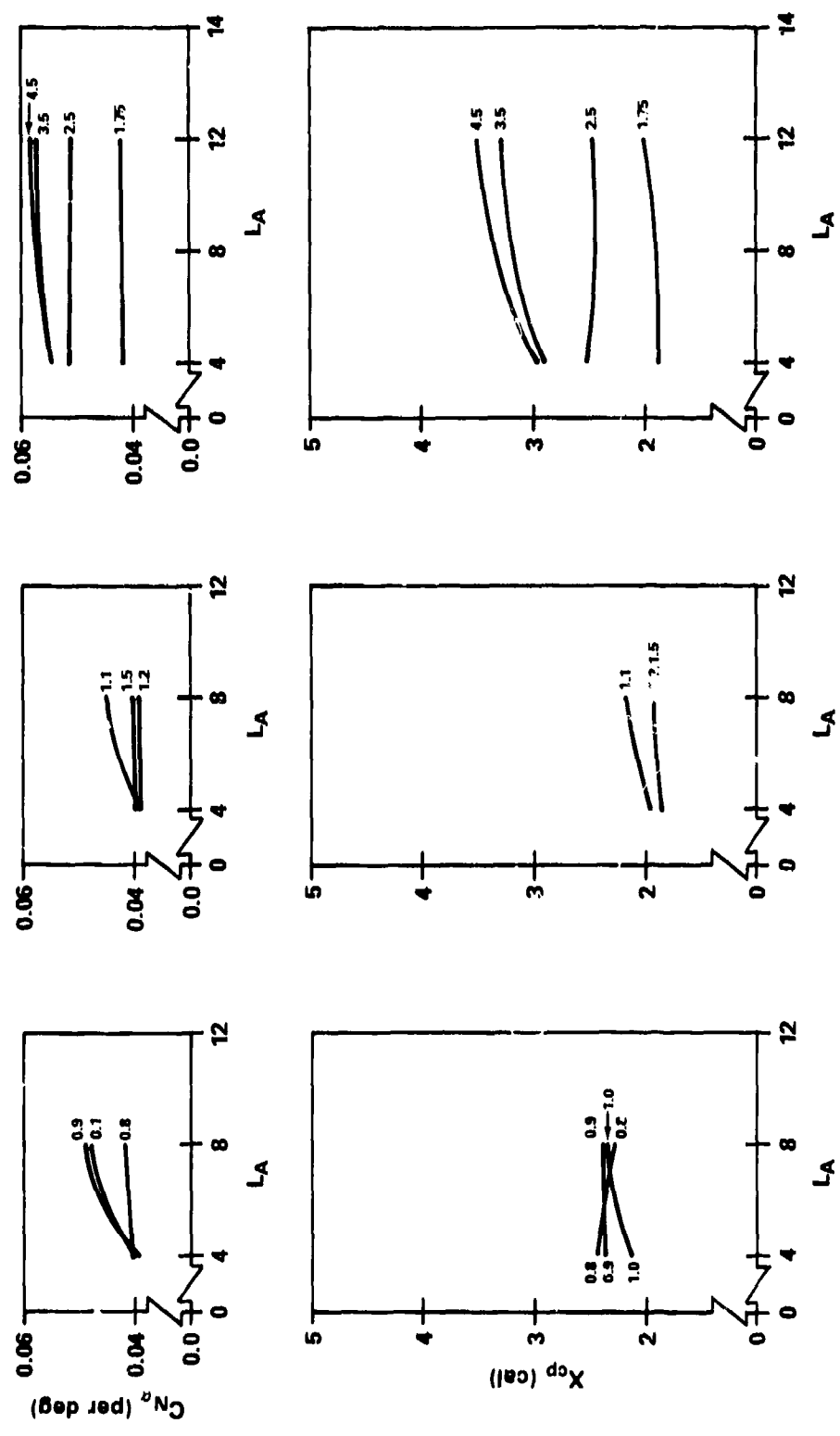


Figure 58. Variation in $C_{N\alpha}$ and X_{cp} with Afterbody Length for Tangent-Ogive Cylinder Bodies (4 cal Nose)

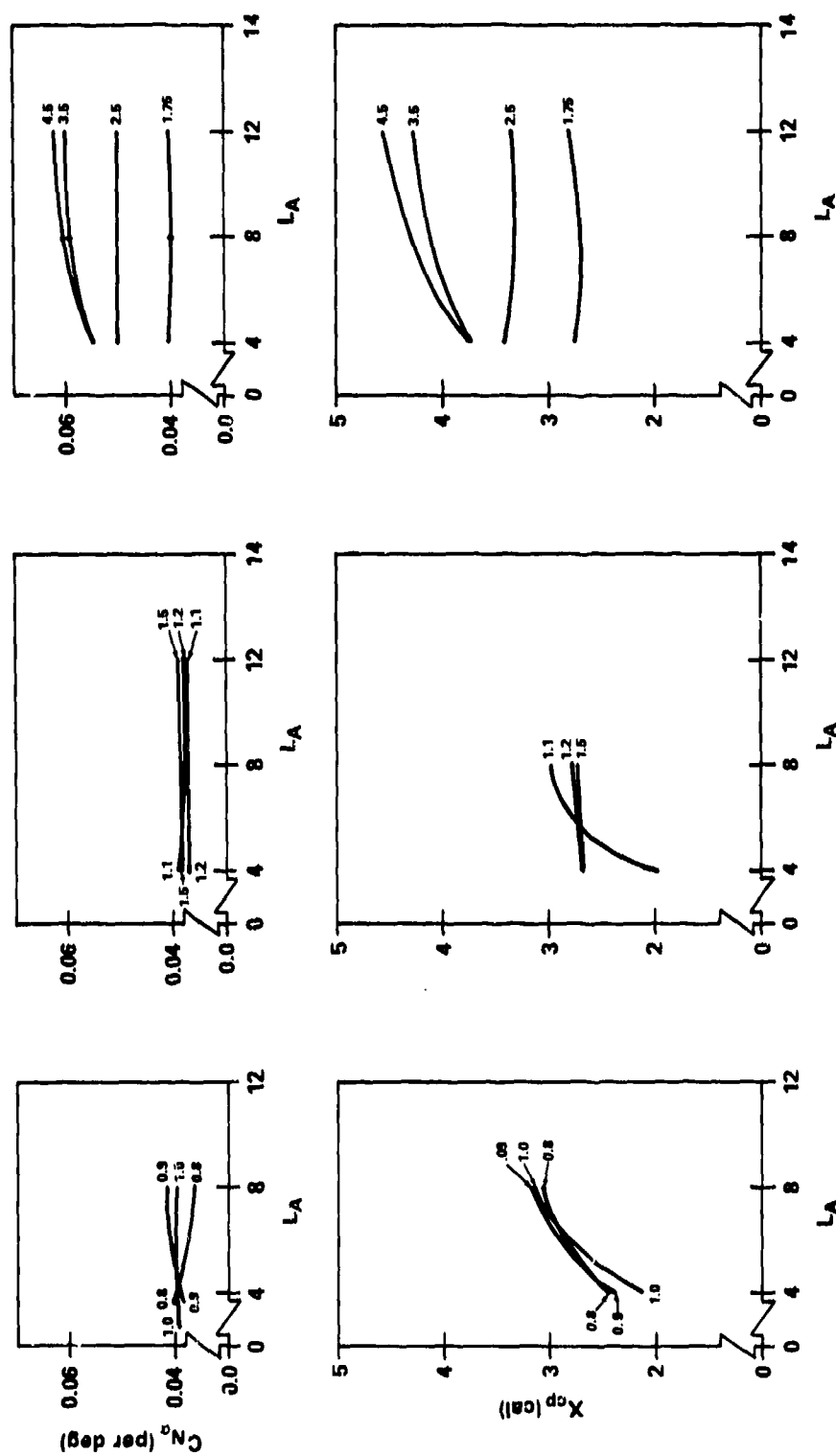


Figure 59. Variation in C_N and X_{cp} with Afterbody Length for Conical-Cylinder Bodies (4 cal Nose)

For increasing nose length or decreasing Mach number (β/L_N decreasing), C_{N_α} increases gradually to a maximum before falling off.

In the region $\beta/L_N > .9$, the results shown compare favorably with those of Reference 22. In the transonic and subsonic regions, the β/L_N correlation does not continue to hold. (This portion of the graph is shown for illustrative purposes only and should not be used for data extraction.) Note that the predicted trend for C_{N_α} , although not well defined, is for C_{N_α} to decrease in each case, as β/L_N decreases below a value of 1.0, to a value of α 2.2, which is about 10.0 percent above the slender body value.

For subsonic flow, the total inviscid normal force for a nose-cylinder body is simply

$$C_{N_\alpha} = (C_{N_\alpha})_N + (C_{N_\alpha})_A \quad (146)$$

where the nose contribution is

$$(C_{N_\alpha})_N = C_1 \tan \delta^* + C_2 \quad (147)$$

and $(C_{N_\alpha})_A$ is the afterbody contribution (Reference 1). The values for C_1 and C_2 are given in Figure 60 and $(C_{N_\alpha})_A$ is found from Figure 61. The angle δ^* is the nose shoulder angle at the nose-afterbody juncture. Slender body theory yields the x_{cp} location for the nose in subsonic flow as

$$(x_{cp})_N = L_N - \frac{(Vol)_N}{S_{ref}} \quad (148)$$

For the afterbody, it is suggested that one use Figure 62 taken from Reference 1. A simplified expression for the x_{cp} for the total body is then

$$x_{cp} = [(x_{cp})_N (C_{N_\alpha})_N + (x_{cp})_A (C_{N_\alpha})_A] / C_{N_\alpha} \quad (149)$$

The effect of a boattail is to reduce the normal force and to shift the total body x_{cp} forward (Reference 5). The degree of effect is a function of the same parameters which were mentioned in regard to the drag. The general behavior of the boattail normal force is illustrated in Figure 63 (Reference 39). For

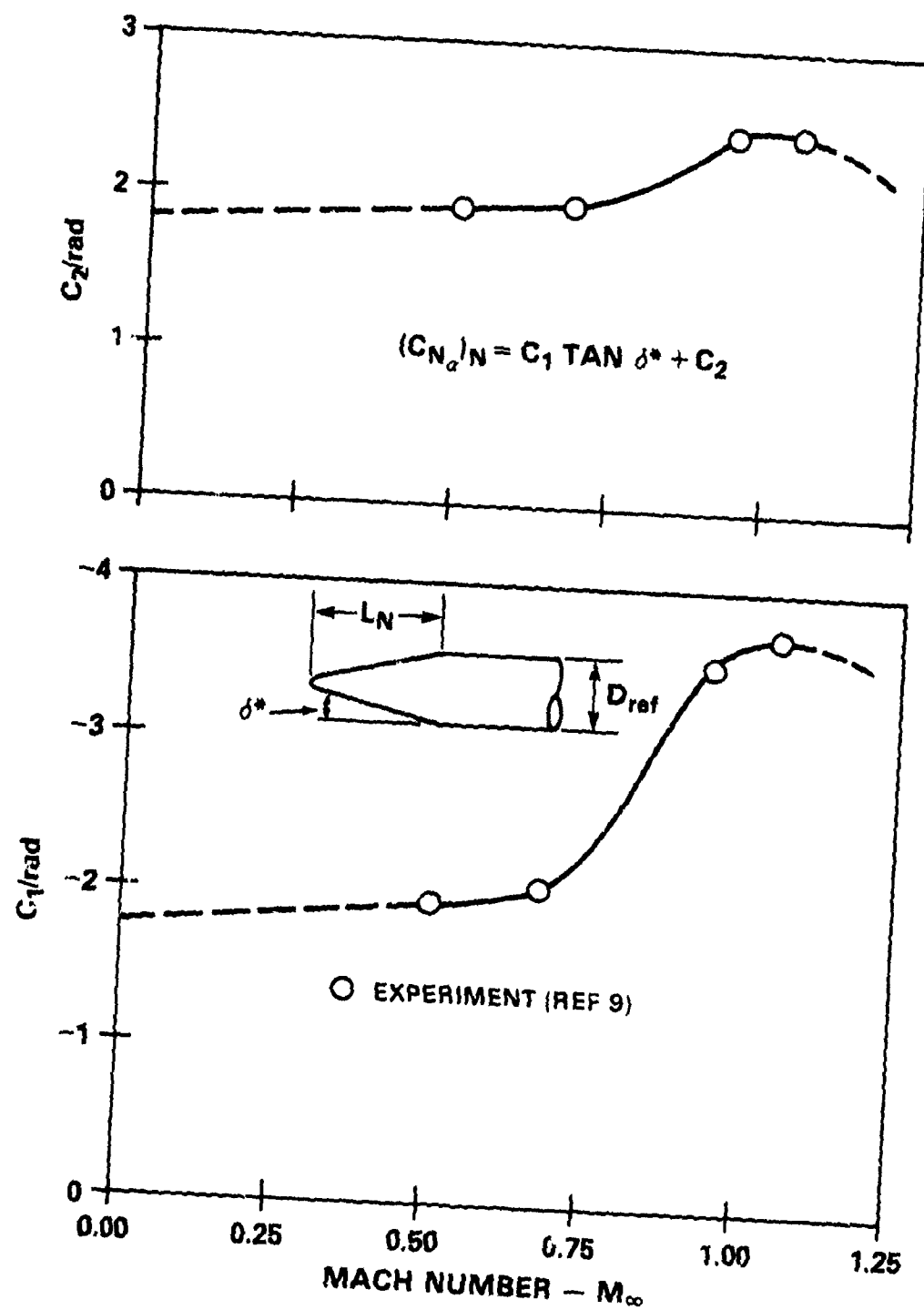


Figure 60. Constants to Determine $(C_{N_\alpha})_N$ for $M_\infty < 1.2$

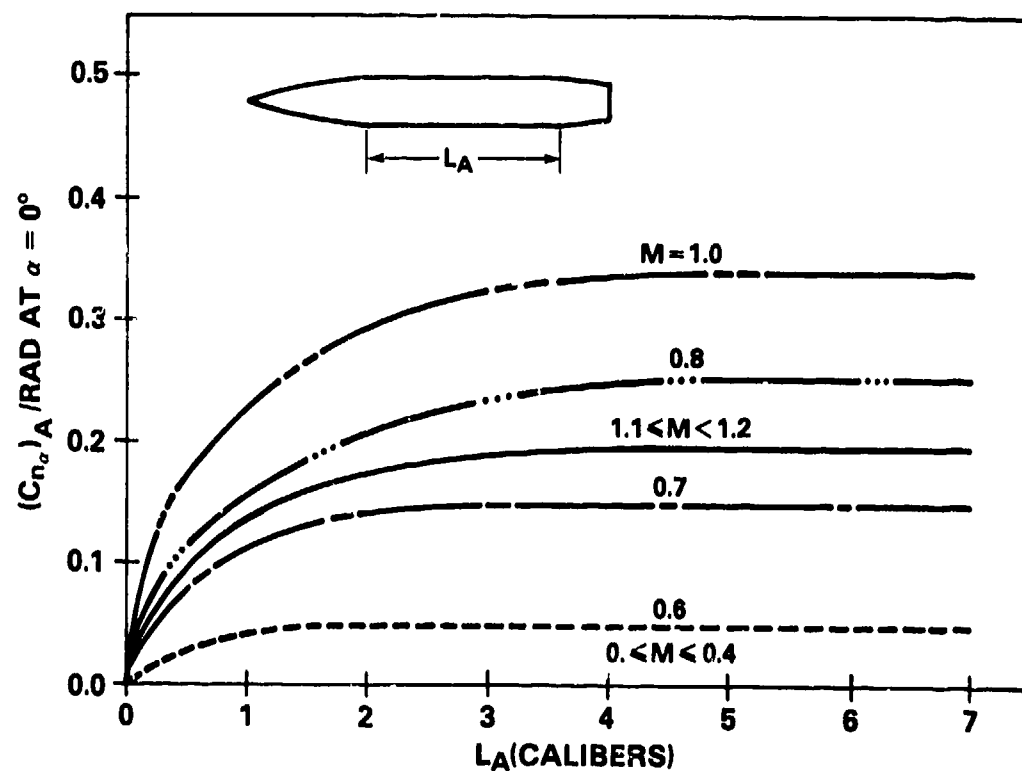


Figure 61. Increase in $(C_{N_\alpha})_A$ at Subsonic and Transonic Mach Numbers Due to Afterbody

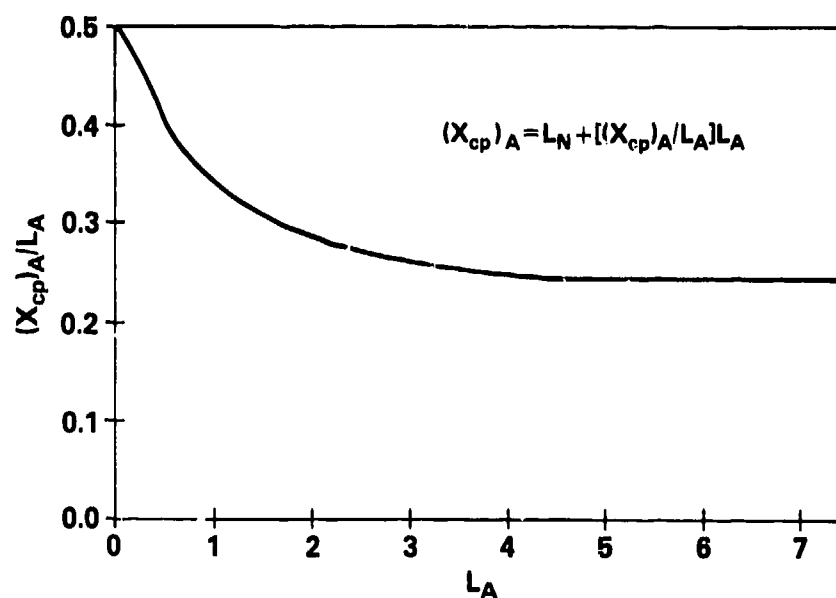


Figure 62. Center of Pressure of Afterbody Lift for $M_\infty < 1.2$

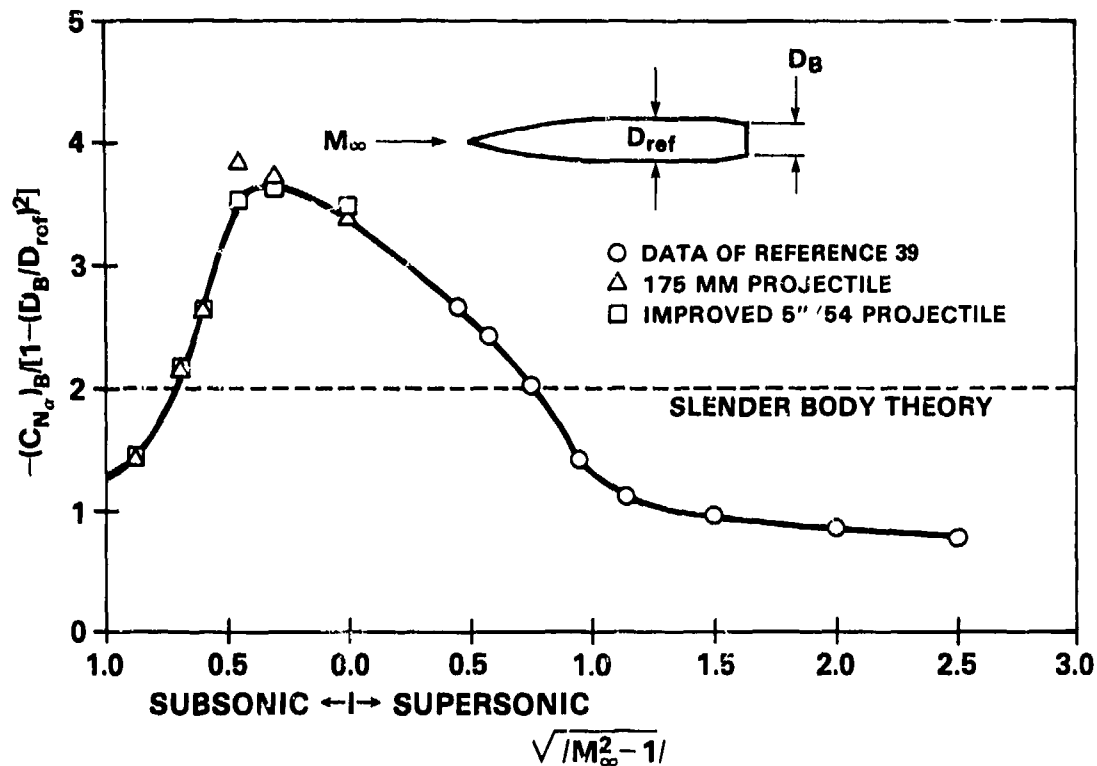


Figure 63. Decrease in C_{N_α} Due to Boattail

supersonic flow, the trend is more easily seen in Figure 64. For a given Mach number and base diameter, increasing the boattail length results in increasing normal force losses. Increasing the base diameter or increasing the Mach number has the opposite effect, resulting in a restoration of the normal force. Note again that the Aeroprediction Code varies from the slender body theory value. In this case, the boattail effect is underestimated by roughly 15 percent. Neither theory has been verified by a detailed comparison with experimental data. Thus, the accuracy of these theories could not be determined. The location of the center of pressure on a boattail is presented in Figure 65. Again, increasing the boattail length for a given base diameter and Mach number reduces the value of x_{cp}/L_B even though the x_{cp} location relative to the afterbody-boattail shoulder is moving rearward. If the nose-afterbody length is held constant, the

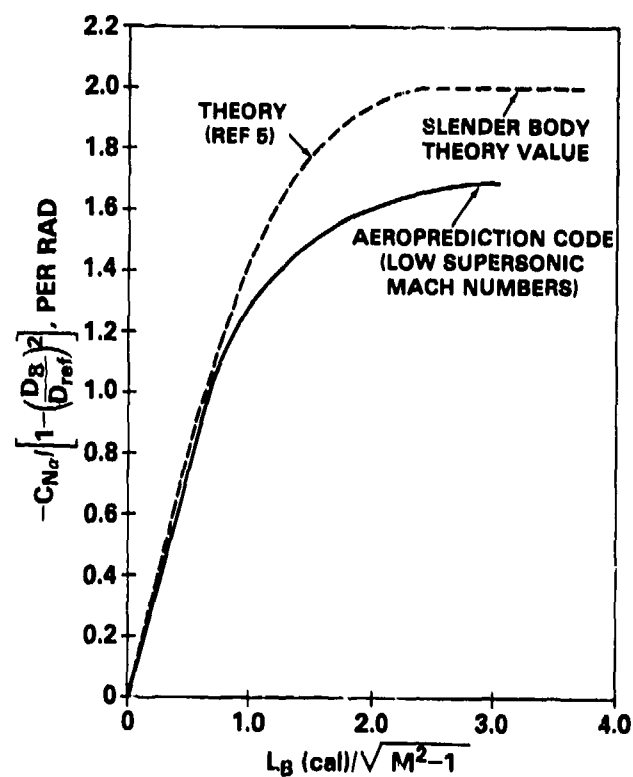


Figure 64. Normal Force Coefficient Gradient for Boattails (6 cal Afterbody)

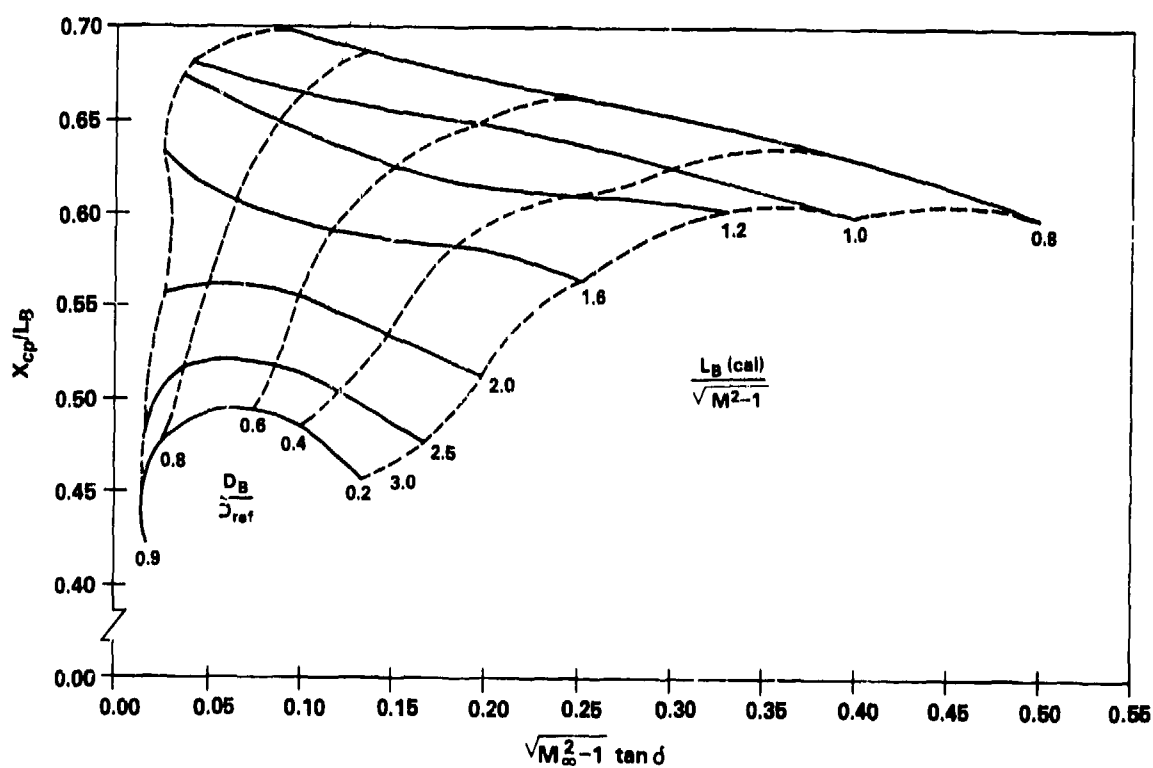


Figure 65. Center of Pressure for Boattails (6 cal Afterbody)

increasing boattail length therefore causes a strong destabilizing trend. However, if the total body length is held constant, this destabilizing effect is greatly reduced and in some cases eliminated.

When designing a boattail, one must avoid boattail angles sufficiently large to cause flow separation at the shoulder. This is particularly the case for conical boattails, whereas for ogival shapes a slightly greater boattail angle (as determined by the local slope) can sometimes be tolerated. The angle at which flow separation occurs can vary considerably, again depending on the local flow conditions. For projectiles and other short bodies, separation appears generally to occur for shoulder angles of 6° to 10° or greater. However, on boattails following long afterbodies, the flow has been known to remain attached for shoulder angles up to 15° .

For spinning bodies such as projectiles, one should also examine the effect of boattail design on the Magnus force and Magnus moment. More is said concerning these effects in the following paragraphs. For now, suffice it to say that flight tests have shown that boattail design is important as far as the Magnus force and moment are concerned, particularly in transonic flow.

The effects of nose bluntness on the normal force and center of pressure are shown in Figures 66 and 67 for spherically capped and truncated conical noses. The data presented are for truncated 7.125° semi-vertex angle cones with a fineness ratio of 4.0 calibers for no blunting ($R_N/R_B = 0$) and 10° spherically capped cones. When adding the spherical cap or truncating the nose, the nose length was reduced as previously described in the drag paragraph. Overall, blunting the nose up to a bluntness ratio of $R_N/R_{ref} = .1$ has a negligible effect on $C_{N\alpha}$ (see Figure 68) and a small effect on the x_{cp} location. Theoretically, the x_{cp} location experiences an abrupt shift forward with initial blunting due to truncation (as shown in Figure 69) which does not occur when the spherical cap is added. This phenomenon has not been verified experimentally.

At $\alpha > 0$, there is a nonlinear contribution to the normal force due to the viscous crossflow velocity. The correction for angle-of-attack as given in Reference 18 [and using Equations (25) and (26) from Section 2] is

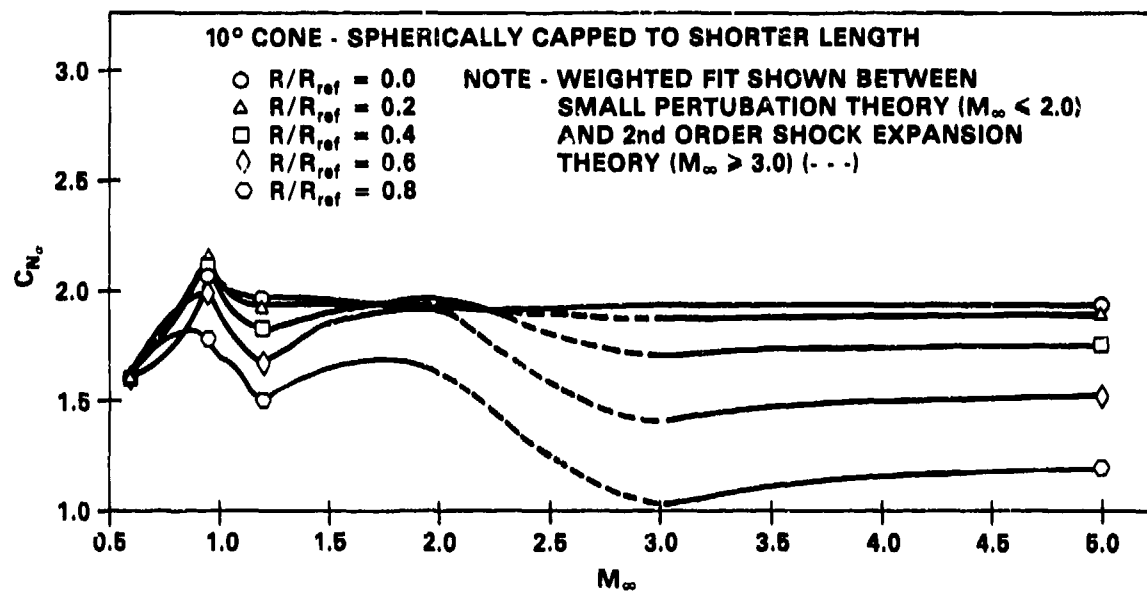


Figure 66. Normal Force for Blunt 10° Cones - Spherically Capped to Shorter Length

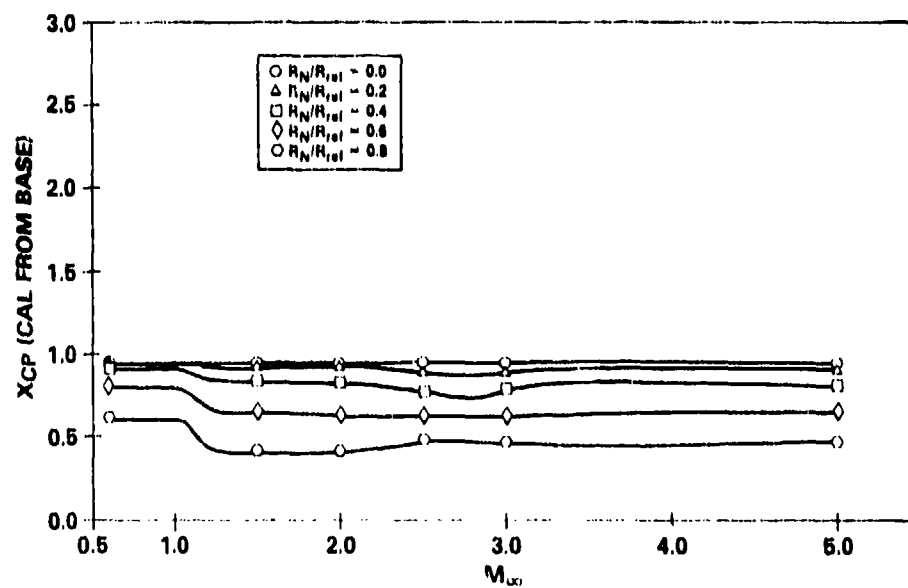


Figure 67. Center of Pressure for Blunt 10° (2.836 cal) Cones - Spherically Capped to Shorter Length

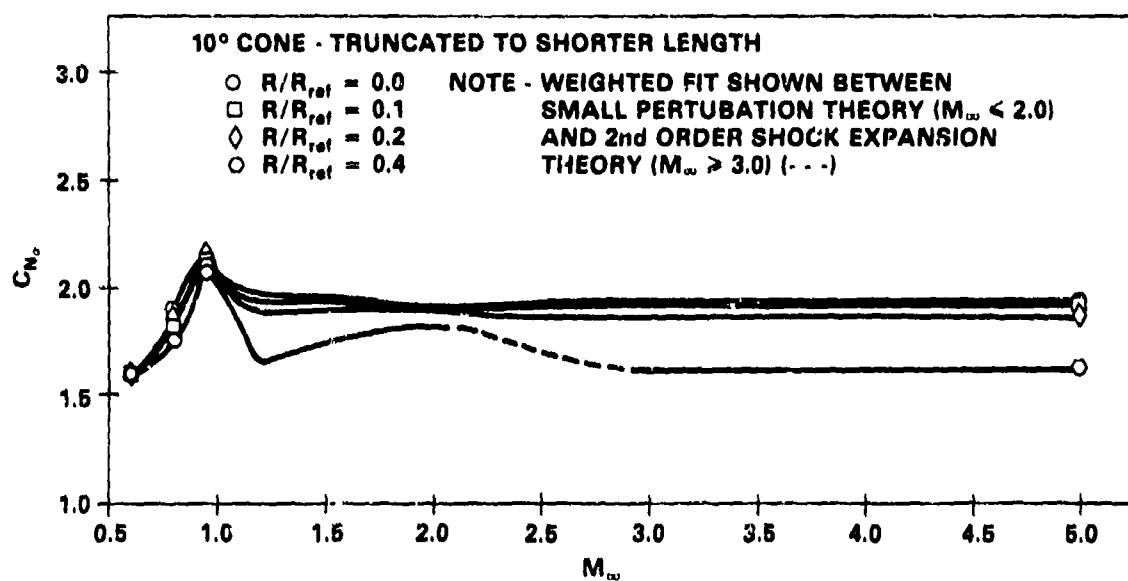


Figure 68. Normal Force for Blunt 7.125° (4 cal) Cones - Truncated to Shorter Length

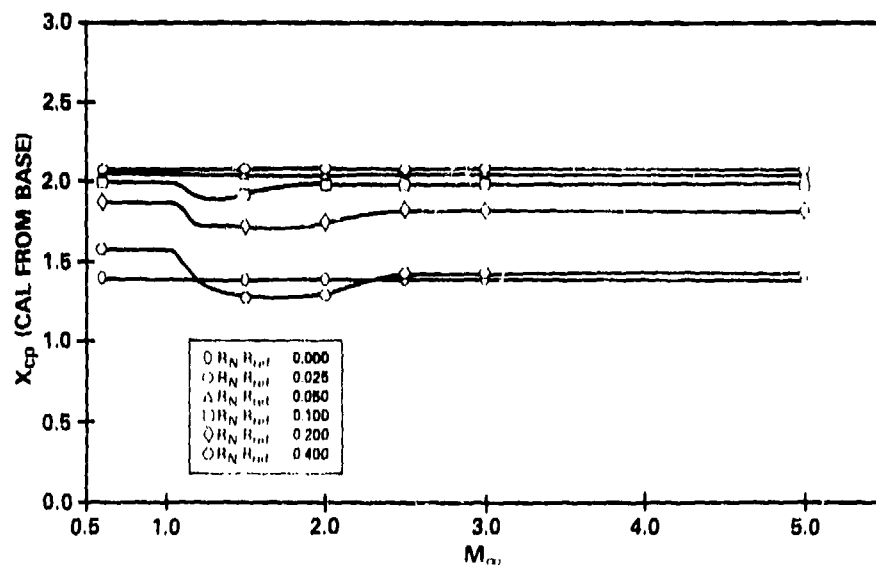


Figure 69. Center of Pressure for Blunt 7.125° (4 cal) Cones - Truncated to Shorter Length

$$\Delta C_N = \frac{4\eta(L)}{\pi} C_{dc} (M_\infty \sin \alpha) S_p \sin^2 \alpha \quad (25)$$

and

$$\Delta C_m = - \frac{4}{\pi} \eta C_{dc} x_p \sin^2 \alpha \quad (26)$$

where η and C_{dc} are given in Figure 70,

S_p is the planform area of the body in the plane of the body's longitudinal axis, and

S_{ref} is the reference area.

The center of pressure for the entire body is then

$$x_{cp} = - \frac{C_m + \Delta C_m}{C_N + \Delta C_N} \quad (150)$$

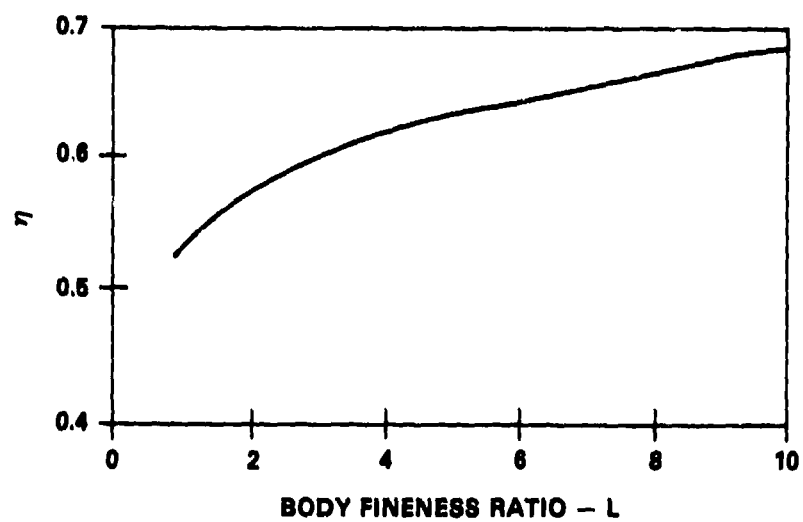
Equations 25, 26 and 145 do not account for any crossflow Reynolds number dependence. A more detailed presentation on the effects of incidence is given in Reference 18.

4.1.3 DYNAMIC AERODYNAMICS

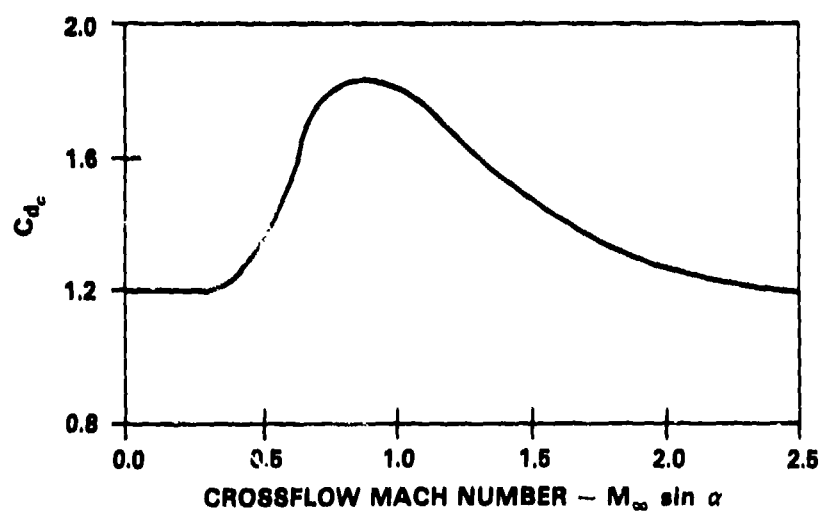
The Roll Damping Coefficient for an axisymmetric body is the result of the skin friction force tangential to the rolling axis. As indicated in Section 2, this coefficient has been accurately predicted using the known values for a given configuration and adjusting these values through the relation

$$C_{lp} = (C_{lp})_1 L/L_1. \quad (151)$$

The data presented in Section 3 were thus obtained and can be similarly used if desired to estimate the C_{lp} values for additional configurations so long as the comparison design is approximately the same length.



Drag Proportionality Factor - η



Crossflow Drag Coefficient

Figure 70. Drag Proportionality Factor and Crossflow Drag Coefficient

The Magnus force and Magnus moment are the results of boundary layer distortion on a spinning body at angle-of-attack. Usually, empirical methods are used to predict the magnitude of the Magnus coefficients. The Aeroprediction Code does not take into account any variations in the nose shape or length, only the total body length. It is assumed that the Magnus moment is also independent of the boattail slope. Sample variations of the Magnus moment for bodies with and without boattails are shown in Figures 71 and 72 which indicate that increasing the body length and/or adding a boattail increases the Magnus moment. The Magnus moment is not determined for bodies with lifting surfaces. For missiles, this is not significant. For bombs, fin Magnus is important.

The pitch damping coefficient, $C_{mq} + C_{m\dot{\alpha}}$, indicates the pitching moment produced by rotational motion about the pitching axis and can be determined theoretically as shown in Section 2 (Equations 90-96). Examples are given in Section 3. The reader is referred to these sections for more information on these methods.

The theory found in Reference 25 indicates that the pitch damping coefficient is strongly influenced by the nose length where the afterbody length is less than 1.0 caliber in length. For afterbody lengths greater than 1.0 caliber, the main parameter is the total body length. The influence of the boattail is negligible as long as the length of the boattail is included in the total body length when determining $C_{mq} + C_{m\dot{\alpha}}$. In general, increasing the nose length in conjunction with very small afterbodies or increasing the total body length increases C_{mq} . The adaptation of the slender body theory in Reference 22 also indicates that the increase in $C_{mq} + C_{m\dot{\alpha}}$ is proportional to the increase in the magnitude of the pitching moment, C_m , and that, for configurations with very long afterbodies ($L_A \rightarrow \infty$), the value $^{\alpha}$ of $C_{mq} + C_{m\dot{\alpha}}$ approaches the value of $-C_{m\dot{\alpha}}$. Figure 73 illustrates the variation in $C_{mq} + C_{m\dot{\alpha}}$ with body length as predicted by the method discussed in Reference 25.

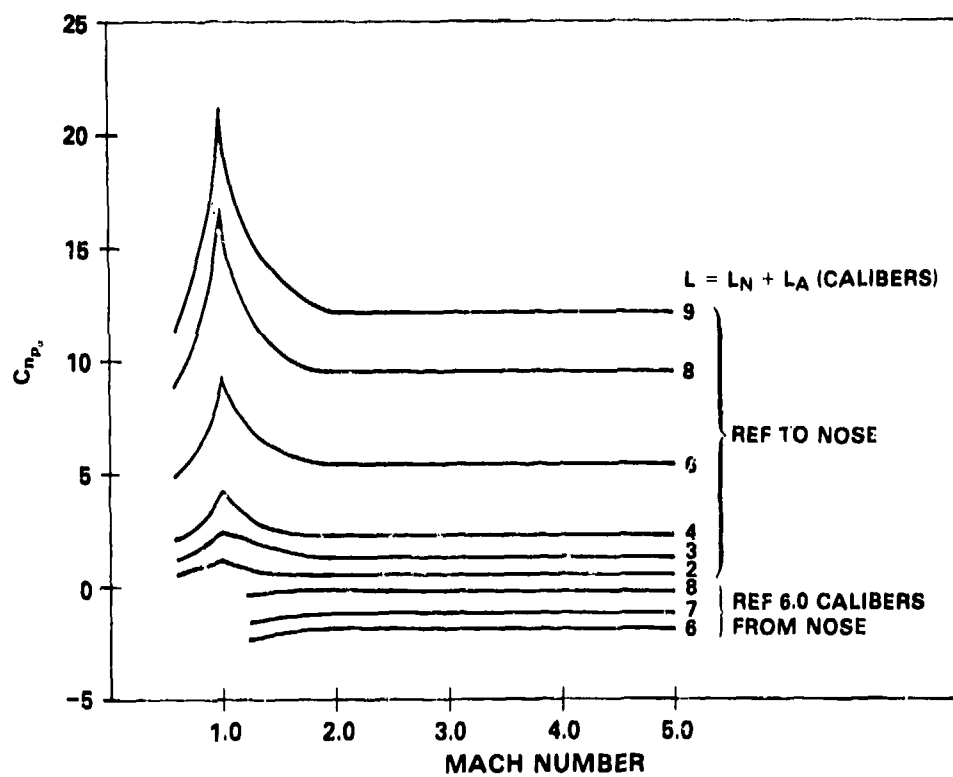


Figure 71. Variation of Magnus Moment for Bodies Without Boattails

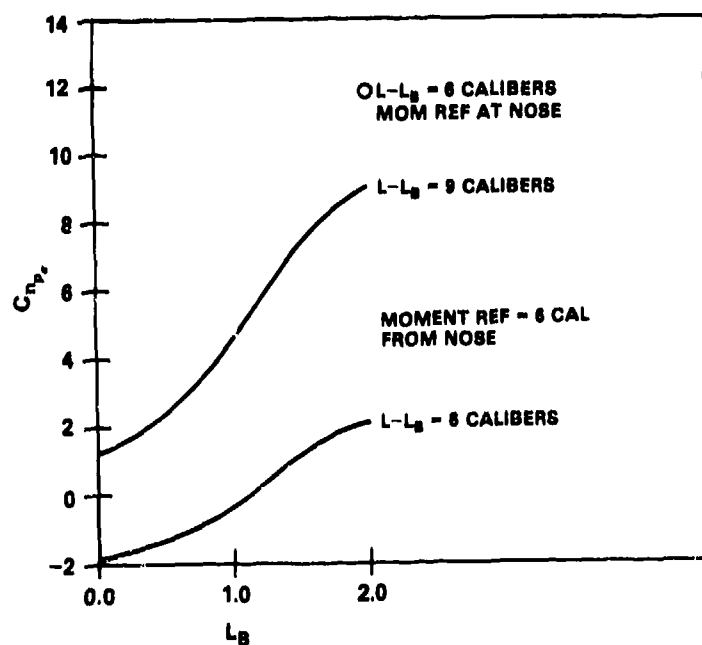


Figure 72. Magnus Moment Variation for Bodies with Boattails $M_{\infty} > 2.0$

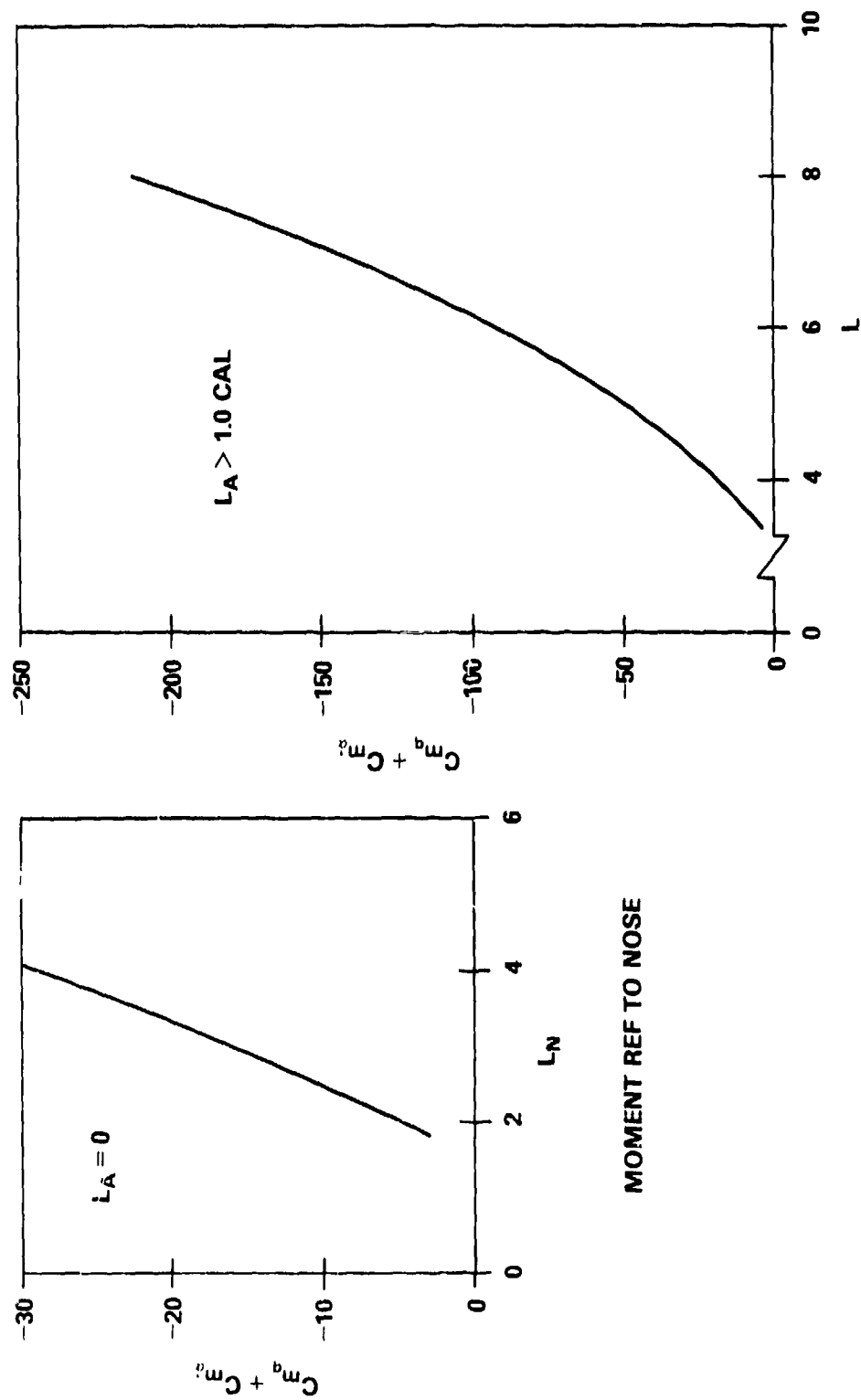


Figure 73. Body Alone Pitch Damping Moment Variation as a Function of Nose Length and Total Body Length

4.2 LIFTING SURFACES

A large number of wing alone cases (two fins together with total span, b , no body present) were considered using the Aeroprediction Code. The majority of cases represented rather simple planform shapes; i.e., diamond or biconvex airfoil sections with a constant shape and thickness ratio along the span and sharp leading and trailing edges. Exact linear theory is applicable in these cases. The results of the numerical solutions obtained by the Code are compared with the analytical predictions of the linear theory. The numerical method used in the Code can be applied over a wide range of airfoil shapes and planforms. Modified double wedge and biconvex airfoils with blunt leading and trailing edges and tapered, swept fins with variable (but similar) airfoil sections and variable thickness with span are also possible. However, no camber or twist is considered. Because of the large number of variations in geometry possible, the examples which follow are generally limited to the simple planform shapes. The reader is referred to Section 1 of this report and to Reference 2 for more details on the theory utilized in the Code.

4.2.1 DRAG

The drag of a single fin is generally small compared to that of the total configuration. As the number of fins increases, the drag contribution of the lifting surfaces can become quite significant, although rarely dominant. Geometrical factors which are predominant in affecting the drag are aspect ratio, thickness ratio, bluntness of leading and trailing edges, leading edge sweep angle, and airfoil shape.

Reference 2 contains several examples which compare the numerical results for the two-dimensional pressure coefficient with that of the exact linear theory. The comparisons verify the accuracy of the numerical method for both the chordwise and spanwise distributions.

Figures 74 and 75 show the wave drag coefficients for rectangular and delta planform fins with sharp LE and TE for transonic speeds. The wave drag is assumed to decay linearly from $M_\infty = 1.05$ to zero at $M_\infty = 0.85$. In general, for

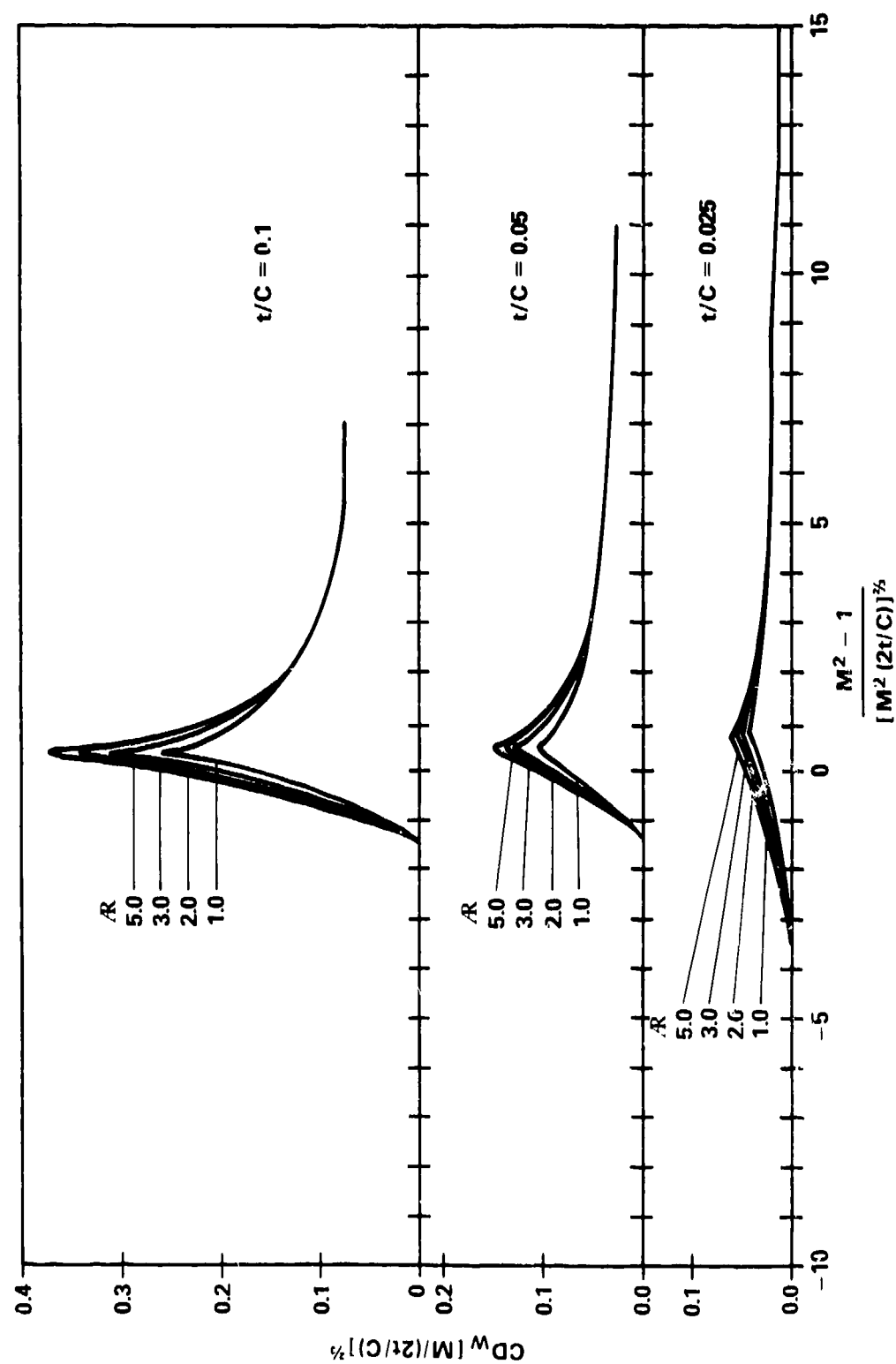


Figure 74. Transonic Wave Drag Coefficient of a Double-Wedge Fin

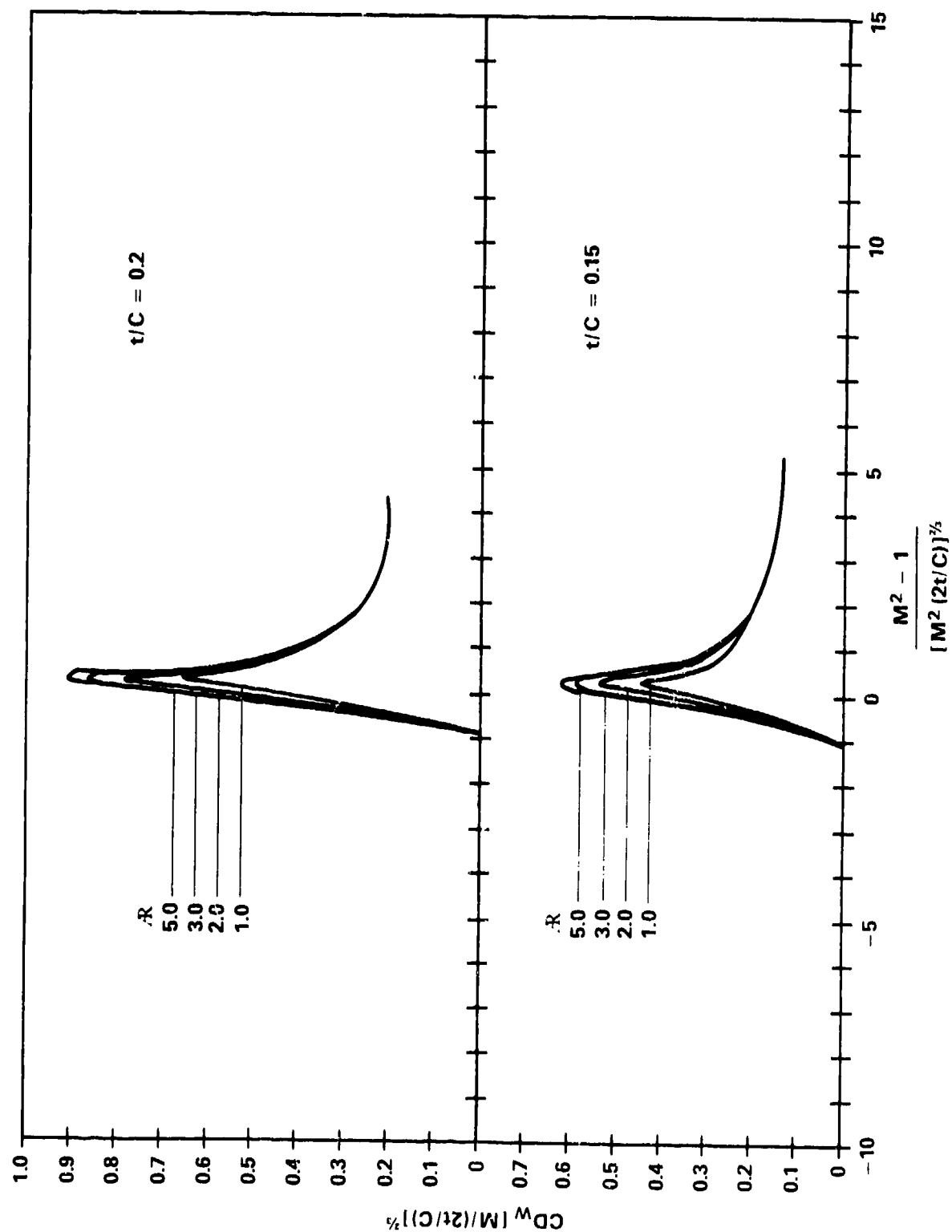


Figure 74. Transonic Wave Drag Coefficient of a Double-Wedge Fin (Cont'd)

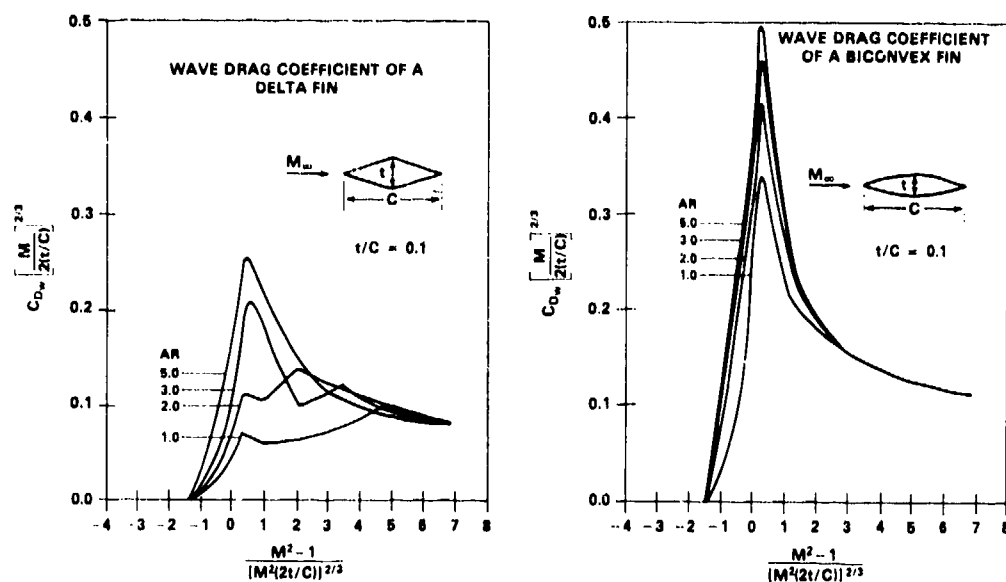


Figure 75. Wave Drag Coefficient of a Double-Wedge Delta and Rectangular Biconvex Fins at Transonic Speeds

constant thickness with span, which is the case here, and zero sweep angle, the wave drag coefficient based on the planform area does not change with increasing span. The area which is an exception to this rule is $1.0 < M_\infty < 1.2$. In this flow region, the effect of increasing the aspect ratio is to increase the wave drag coefficient. Thickness effects are also shown to be present.

Figures 76 and 77 compare the supersonic wave drag predictions of the two theories for modified double-wedge and biconvex-planform fins, respectively, with various sweep angles, γ , and constant chord length. The agreement is very favorable. It can be seen that the wave drag increases with thickness but decreases with an increasing sweep angle. Figures 76 and 77 apply for fins of moderate aspect ratios and moderate supersonic Mach numbers. For higher values of these parameters for rectangular fins with diamond airfoil sections, one can use Figure 78, which is an extension of the curve for $AR \tan \gamma = 0$ in Figure 76. One should note that the drag can change significantly with sweep depending on whether the leading edge is subsonic (lies forward of the Mach wave line) or supersonic (lies entirely rearward of the Mach wave line). Reference 5 shows supersonic wave drag predictions using the linear theory for fins with various taper ratios. Also shown in Reference 5 are form factors which can be applied to a variety of airfoil shapes to adjust the drag prediction of the diamond airfoil

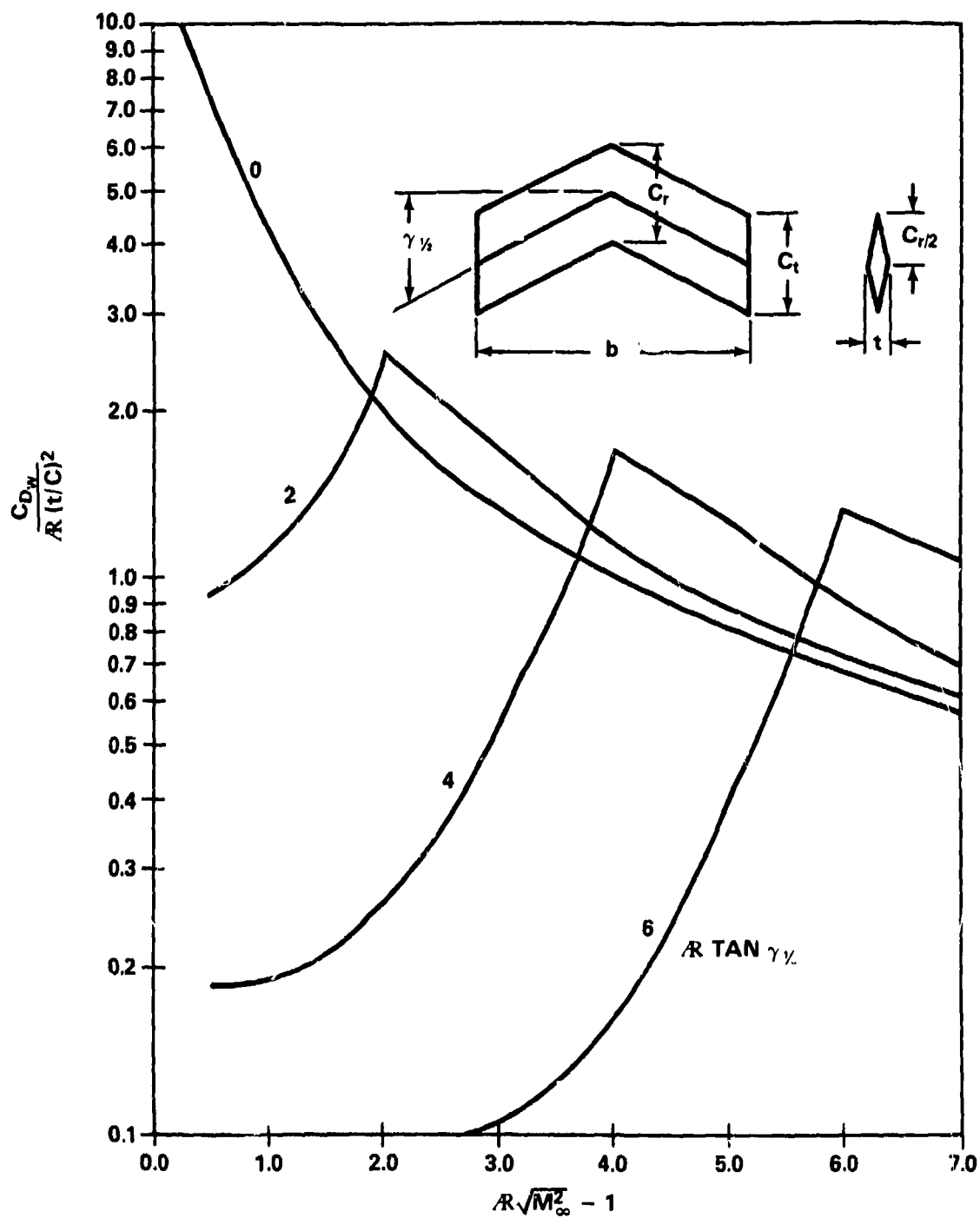


Figure 76. Supersonic Wave Drag of Wings with Double-Wedge Airfoil Section; $C_t/C_r = 1.0$

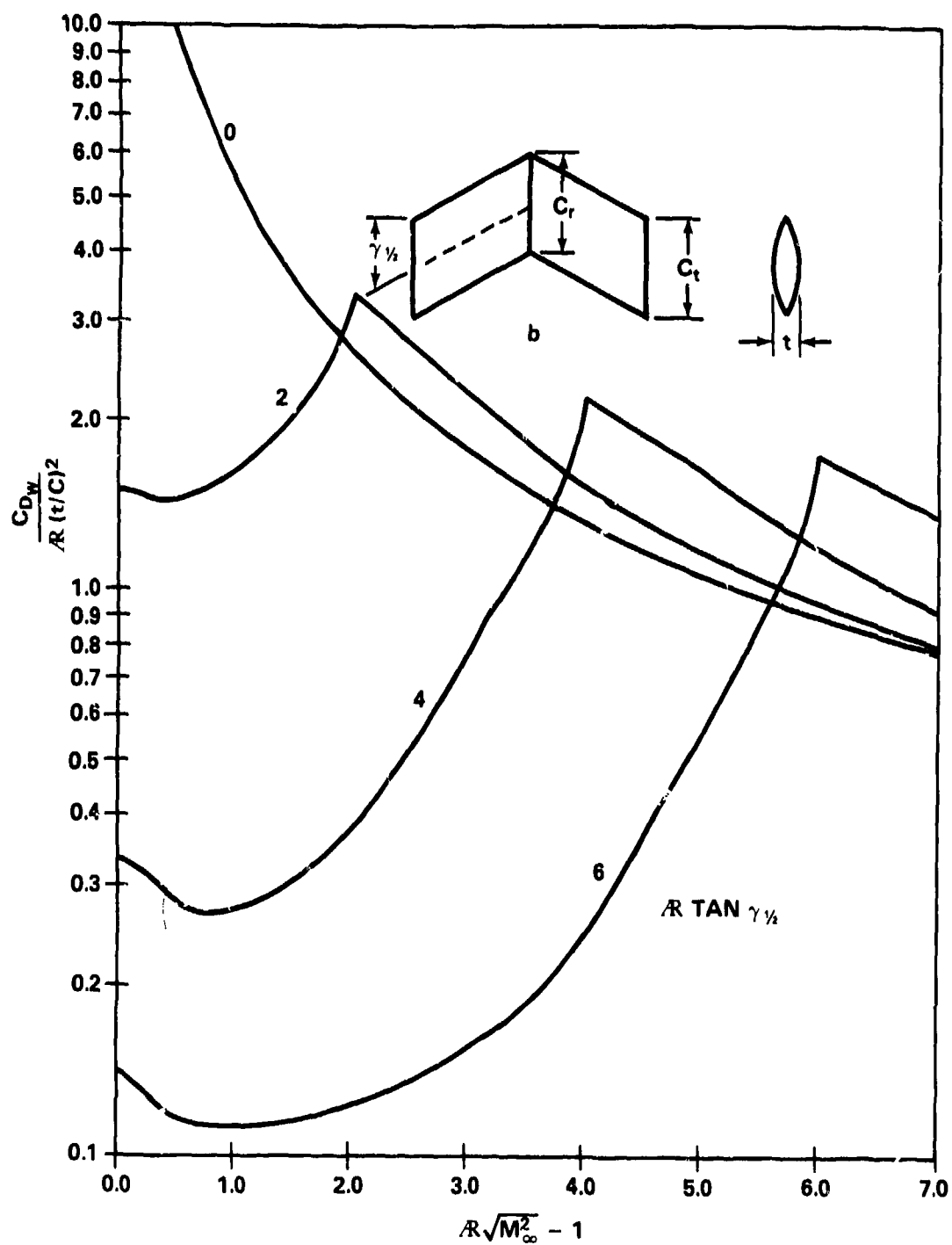


Figure 77. Supersonic Wave Drag of Wing with Biconvex Airfoil Section

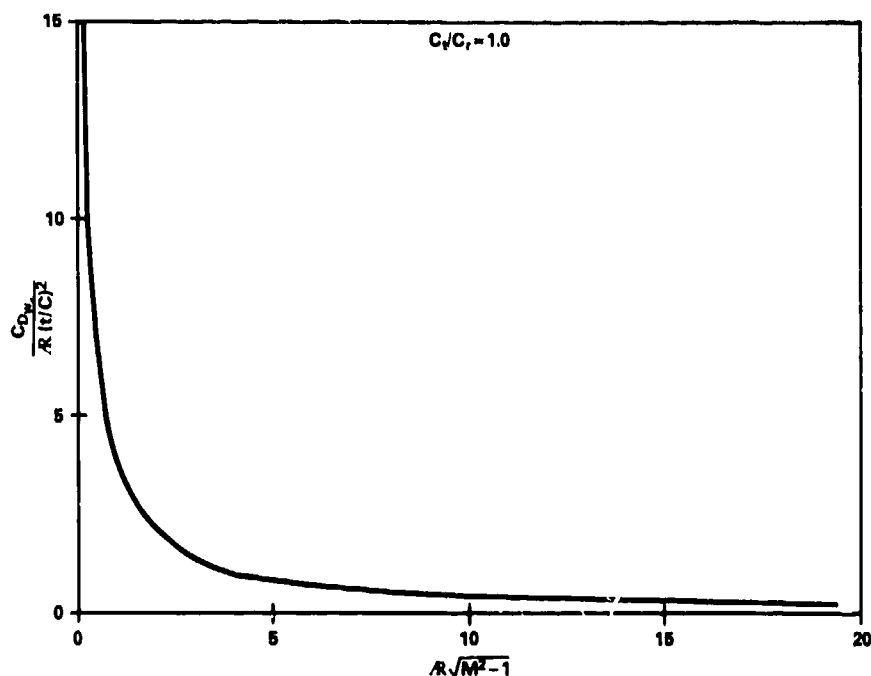


Figure 78. Supersonic Wave Drag of Wing with Double-Wedge Airfoil Section, $C_t/C_r = 1.0$

to obtain the drag for a fin with a similar aspect ratio, chord length, and Mach number. As one would expect, in general, the greater the initial slope on the airfoil for a given thickness ratio, the greater the wave drag contribution.

The base pressure of the fin, referred to as the trailing edge separation drag, is similar to the three-dimensional phenomenon which occurs on the body. The pressure in the rear of the fin is that of a two-dimensional rearward facing step. Experimental results (Reference 40) for fins with no TE slope are shown in Figure 79. The data have been extrapolated for $M_\infty < 1.1$ based on the general shape of the three-dimensional base pressure curve. The base pressure on one fin can be adjusted for TE taper (varying bluntness) by Equation (44) in Section 2.

The position of the fin with respect to the base on the body can also affect the base pressure (of the body). Also, the geometric fin parameters which determine the extent of this effect are the aspect ratio, thickness ratio, profile

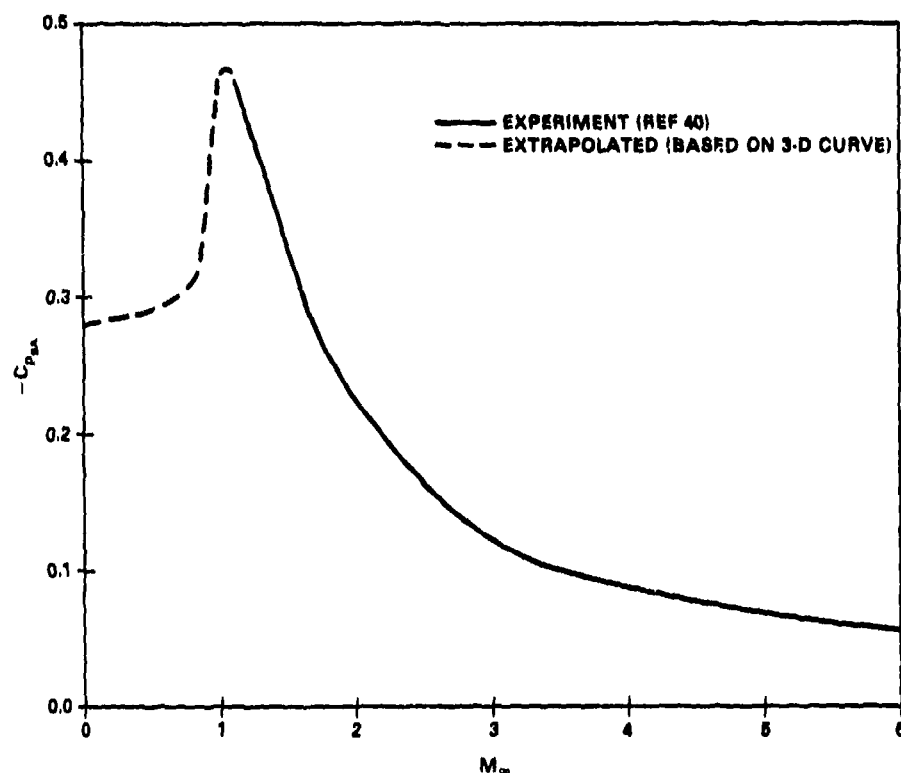


Figure 79. Two-dimensional Base Pressure Coefficient

or shape, sweepback angle, and number of fins. The effect of thickness is shown in Figure 80 which indicates that the effect increases with an increasing thickness ratio for a given Mach number. The other geometric parameters were not examined. The distance or location of the fin upstream from the base at which the fins no longer affect the base pressure varies linearly with t/C , as shown in Figure 81 (Reference 41). The change in base pressure is assumed to vary linearly from a maximum when the TE of the fin is flush with the base to zero at the distance indicated. Fins extending downstream of the base are assumed to have the same effect as those that are flush with the base.

The LE bluntness effect on the drag was also examined. The trends for several Mach numbers are shown in Figure 82 for a biconvex airfoil. Bluntness is seen to have a larger effect at the high supersonic Mach numbers. However, the

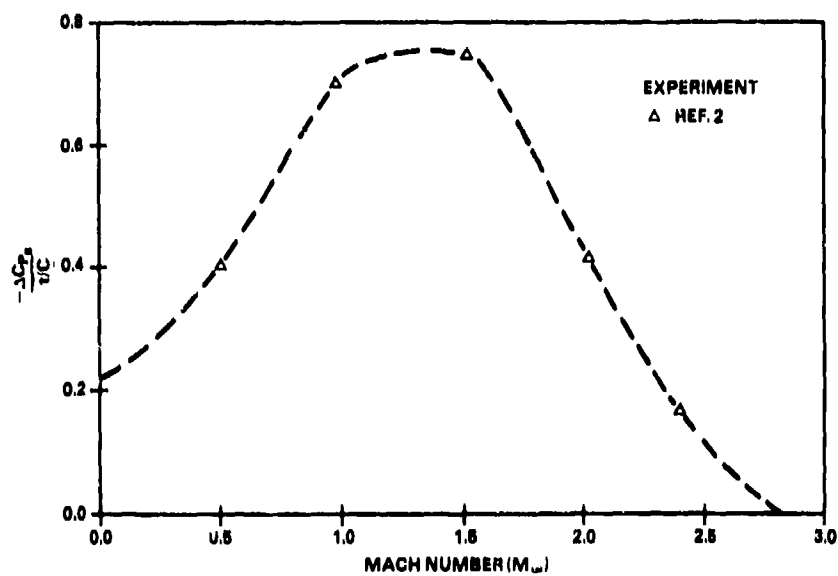


Figure 80. Base Pressure Coefficient Change with Fins Located Flush with Base

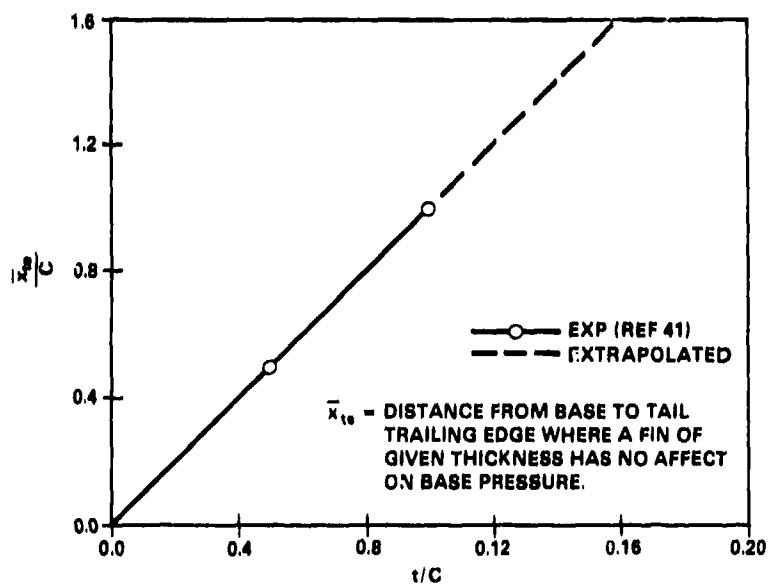


Figure 81. Distance from Base where Fins do not Affect Base Pressure

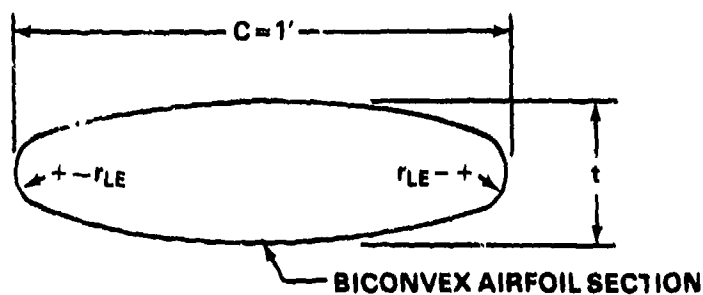
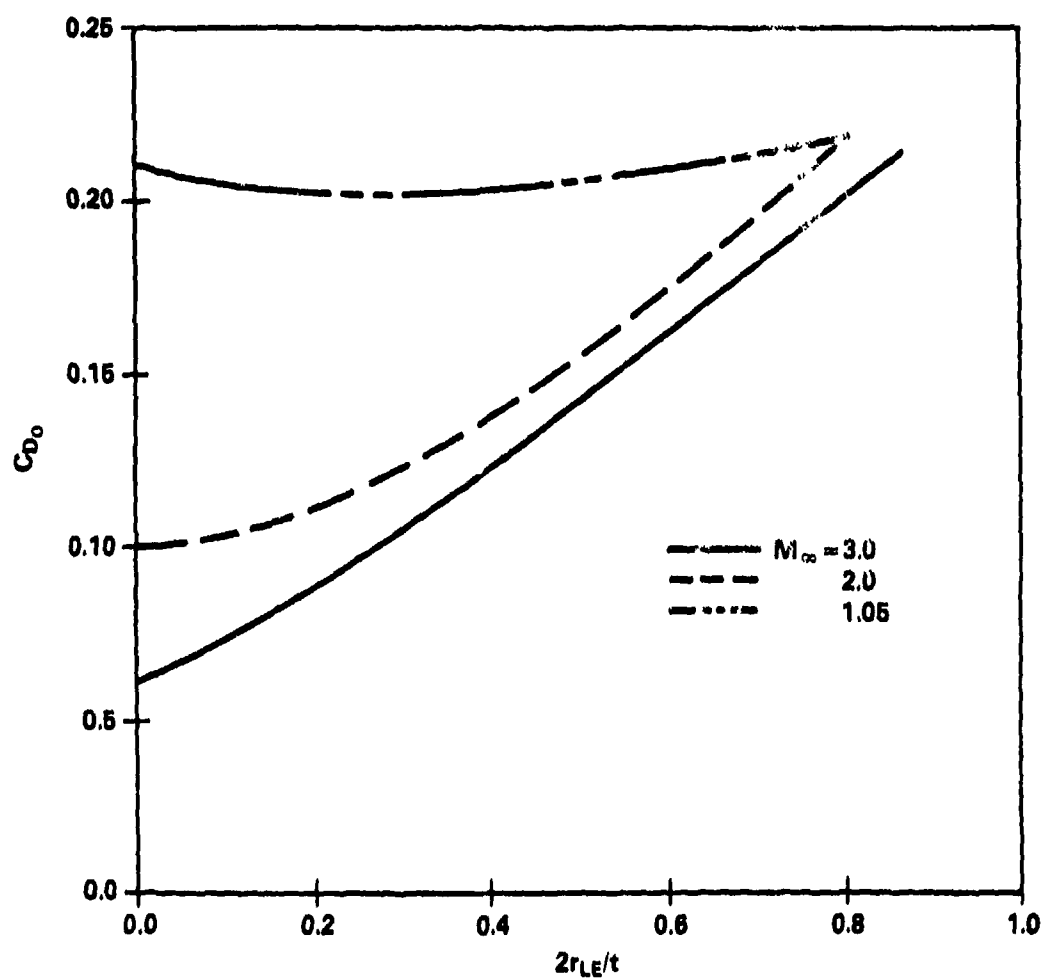


Figure 82. Zero Lift Drag of Wings as a Function of Leading Edge Bluntness; $AR=2$, $\gamma_1 = \gamma_4 = 30^\circ$, $t/C = 0.12$

effect at the lower supersonic Mach numbers is shown to indicate a stronger dependence on the LE radius. The exact linear theory does not hold in these cases.

The reader is referred to Section 2 for a discussion of the skin friction drag component.

4.2.2 LIFT

For subsonic speeds, the only contribution to the lift or normal force is assumed to be due to the angle-of-attack. The procedure in this instance (as shown in Section 2) is to determine the normal force and x_{cp} for a similar wing of aspect ratio βAR at Mach number zero and angle-of-attack, $\beta \alpha$. The variation of $C_{N\alpha}$ for a diamond airfoil in subsonic flow is given in Figure 83. For transonic flow, the relation

$$\left(C_{N\alpha} \right)_{fb} = \frac{(1-ac) 2\pi AR}{2 + [AR^2 (\beta^2 + \tan^2 \gamma_b) + 4]^{1/2}} \quad (152)$$

is used to compute the lift curve slope at the force break Mach number and at intermediate Mach numbers, M_a and M_b (defined in Section 2). The force break Mach number is assumed to represent the point at which the flow transitions from subsonic to transonic flow. The force break Mach number varies with aspect ratio and thickness as shown in Figure 84-A. The factor, ac , is a correction factor to the lifting line theory to account for the decrease in the lift curve slope for thick fins as a function of thickness. The variation of this factor is shown in Figure 84-B at $M_\infty = M_a$ and Figure 84-C at $M_\infty = M_b$. The further determination of $C_{N\alpha}$ in transonic flow is outlined in Section 2.

Figures 85 through 94 show the variation in $C_{N\alpha}$ and x_{cp} as a function of AR , t/C , and Mach number for a rectangular fin with sharp LE and TE for transonic and supersonic flows. Although shown as a function of the transonic similarity parameters, these curves were extended to show the decreasing effect of the aspect ratio. For the rectangular fin, the effect of AR is not considered for high supersonic Mach numbers where strip theory is used, although some small effect is noticed in the x_{cp} location. The effect of fin thickness in this region is thus more clearly seen. For $M_\infty > 3.0$, increased thickness is shown to

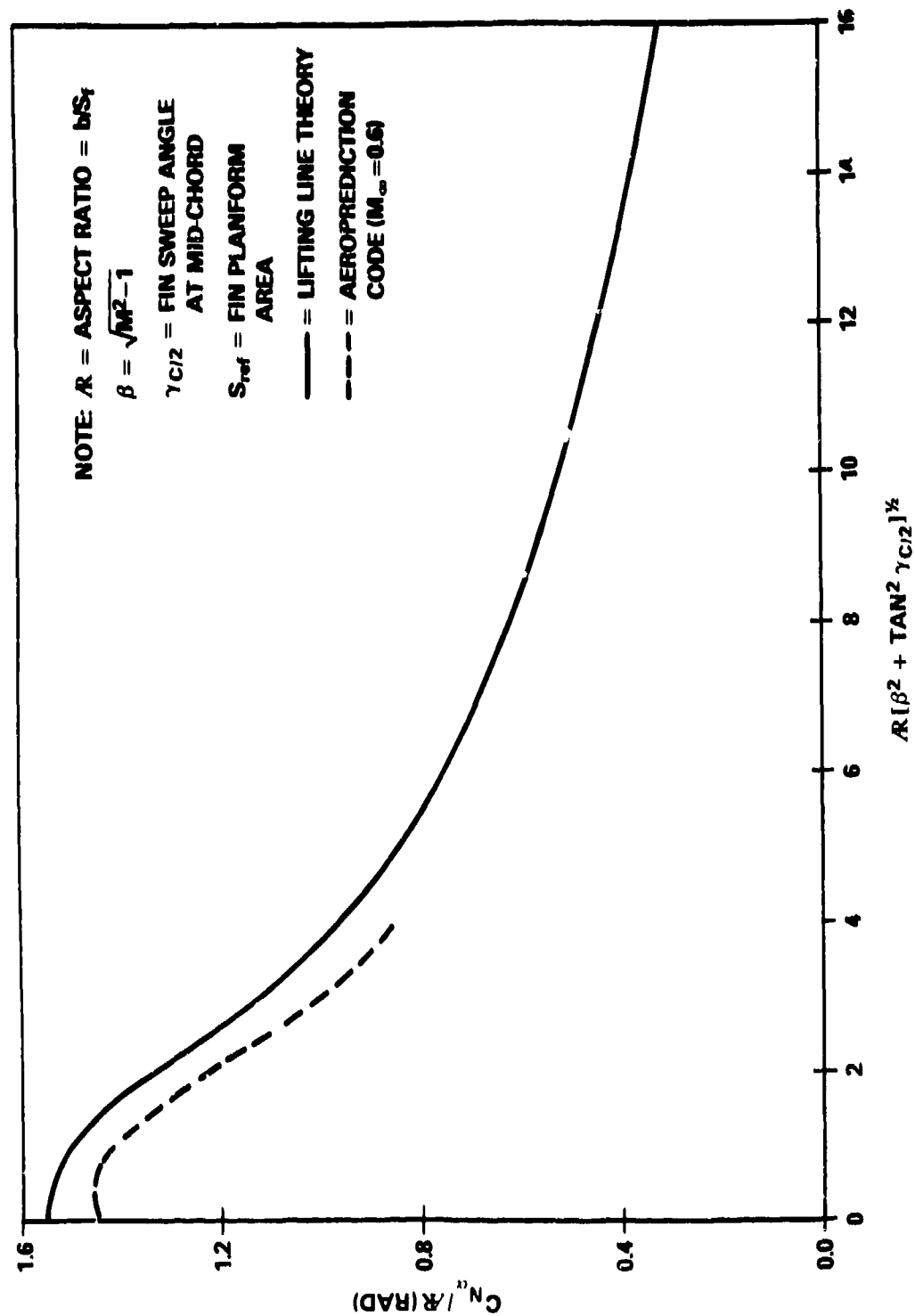


Figure 83. Subsonic Fin Normal-Force Coefficient Gradient

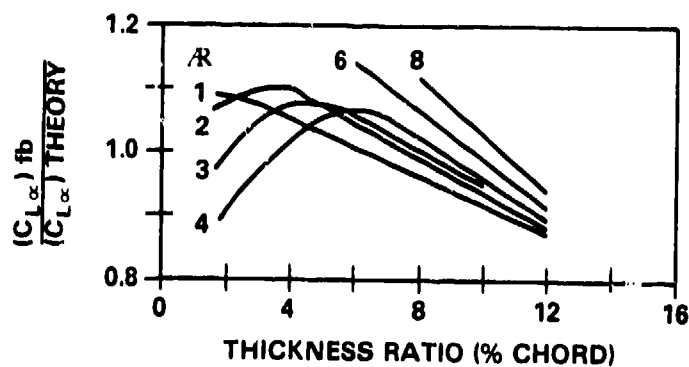


Figure 84-A. Correction to Lift-Curve Slope at Force-Break Mach Number

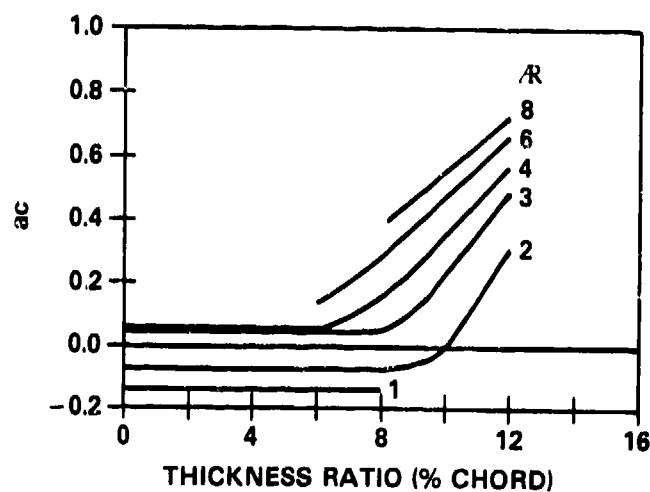


Figure 84-B. Chart for Determining Lift-Curve Slope Correction Factor at M_a

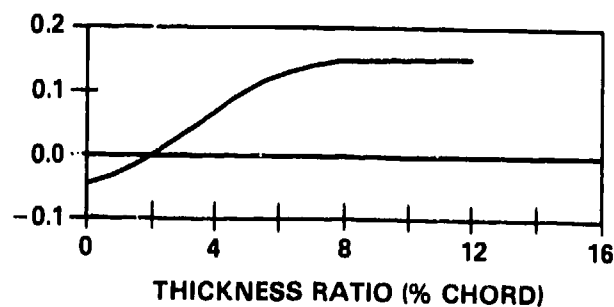


Figure 84-C. Chart for Determining Lift-Curve Slope Correction Factor at M_b

Figure 84. Chart for Determining Transonic Lift-Curve Slope at M_a and M_b

NOTE: $C_t = \text{CONST}$, $\alpha = 0^\circ$, SHARP L.E.

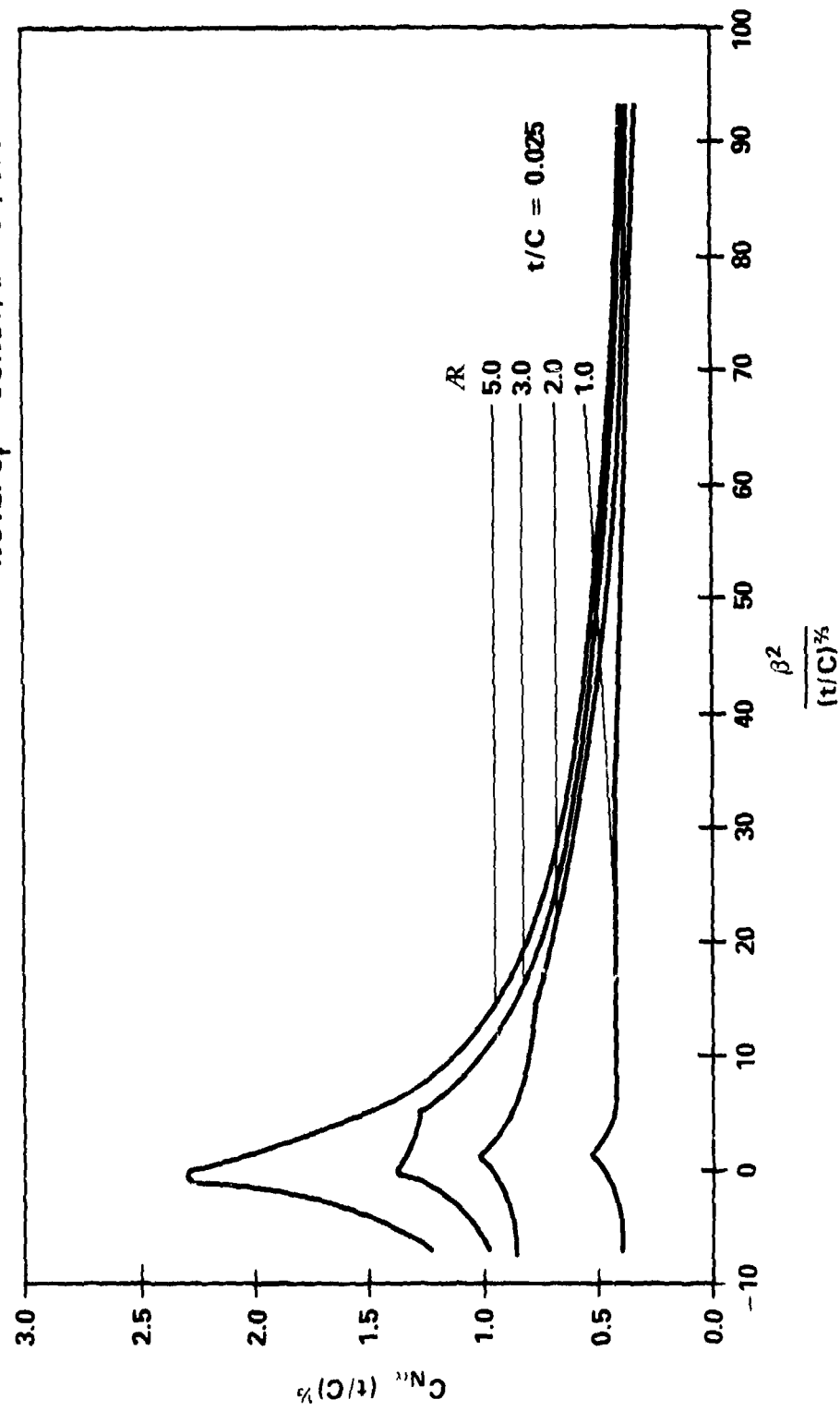


Figure 85. Normal-Force Coefficient Gradient for Rectangular Fin (Diamond Shape) ($t/C = .025$)

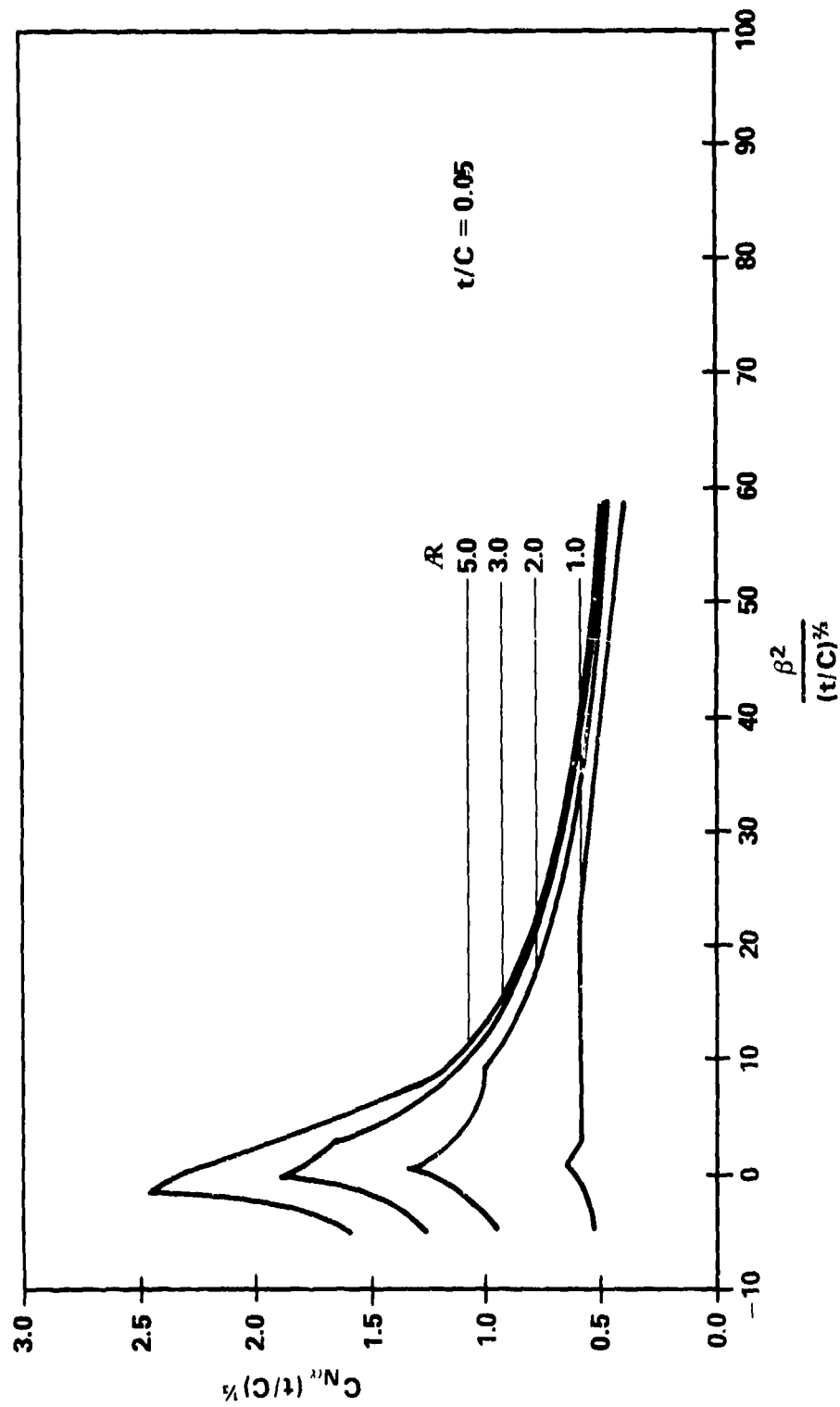


Figure 86. Normal Force Coefficient Gradient for Rectangular Fin
(Diamond Shape) ($t/C = .05$)

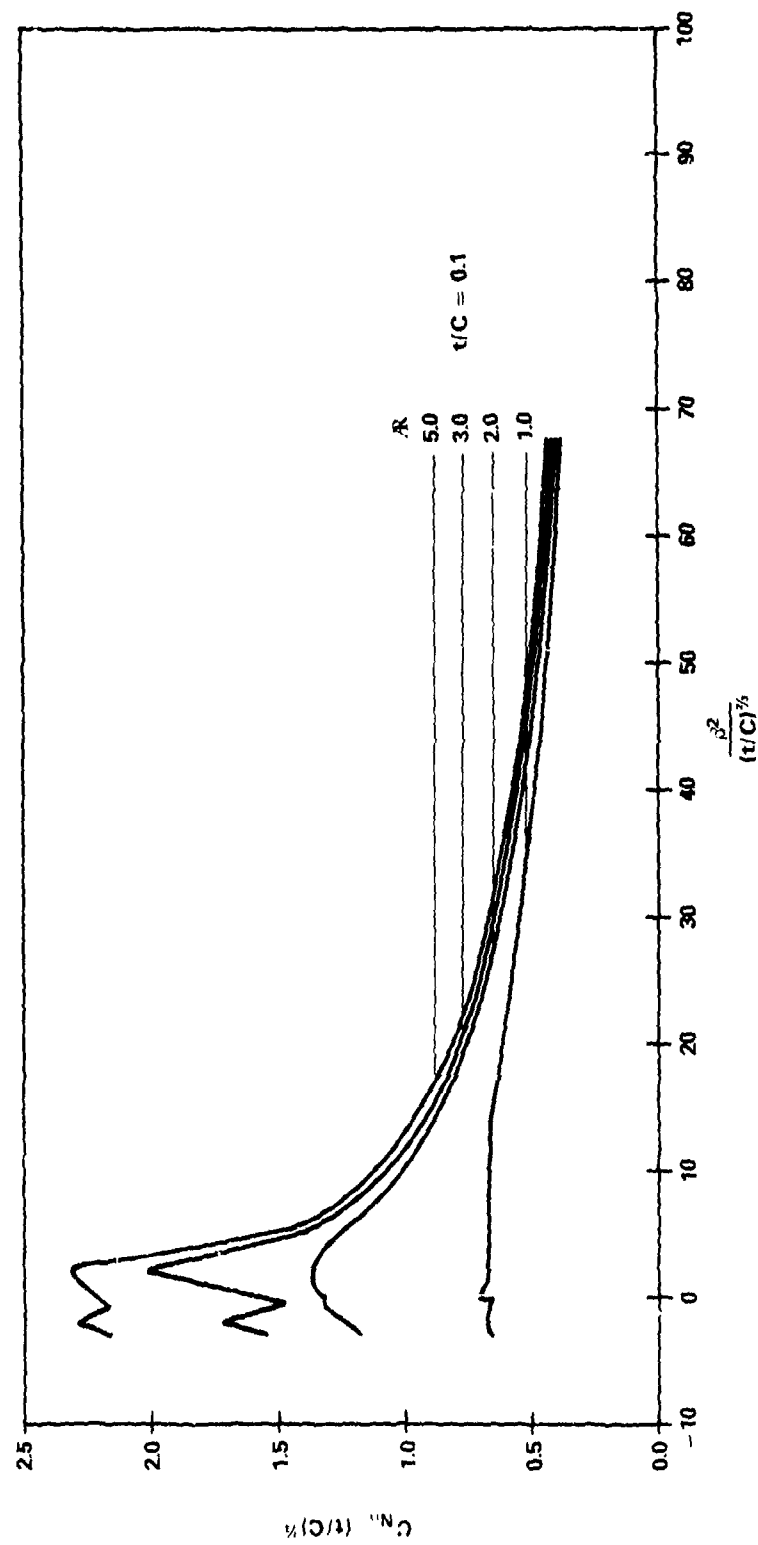


Figure 87. Normal-Force Coefficient Gradient for Rectangular Fin
(Diamond Shape) ($t/c = .1$)

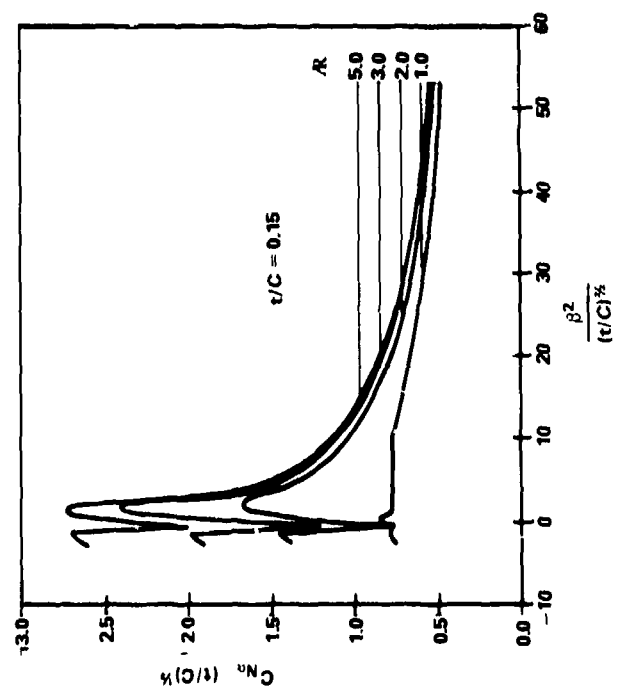


Figure 88. Normal-Force Coefficient Gradient
for Rectangular Fin (Diamond Shape)
($t/C = .15$)

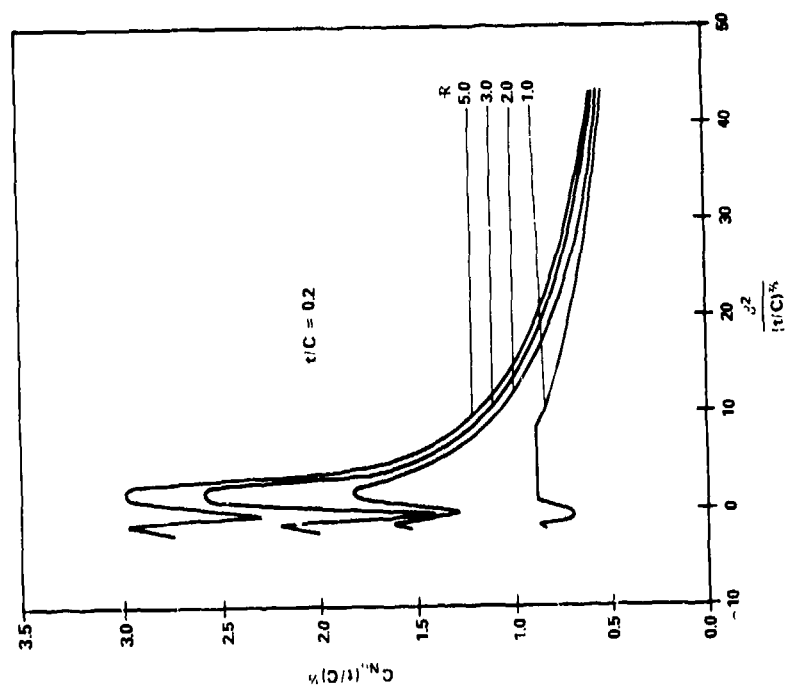


Figure 89. Normal-Force Coefficient Gradient
for Rectangular Fin (Diamond Shape)
($t/C = .2$)

NOTE: $C_r = \text{CONST}$, $\alpha = 0^\circ$, SHARP L.E.

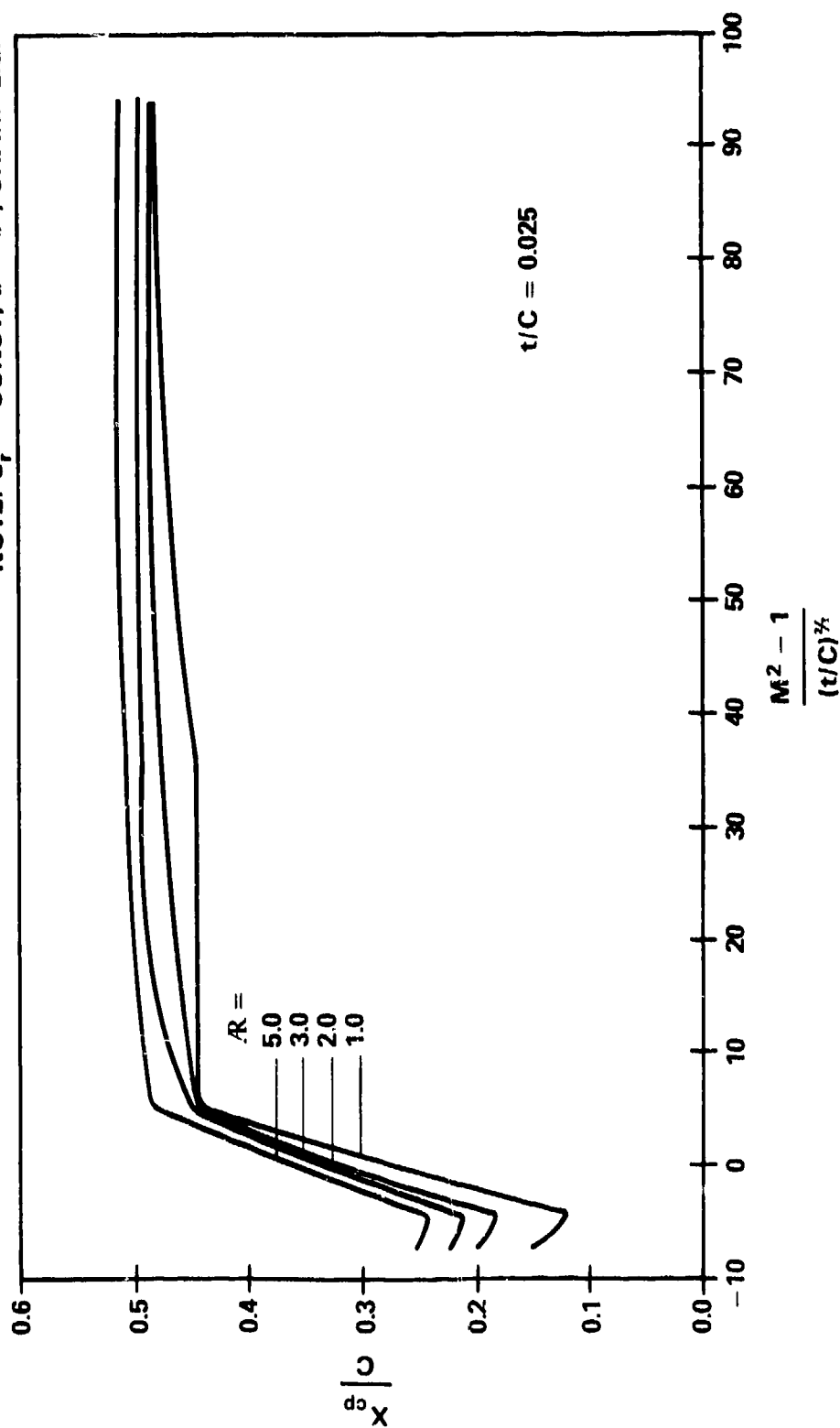


Figure 90. Center of Pressure for Rectangular Fin (Diamond Shape) ($t/C = .025$)

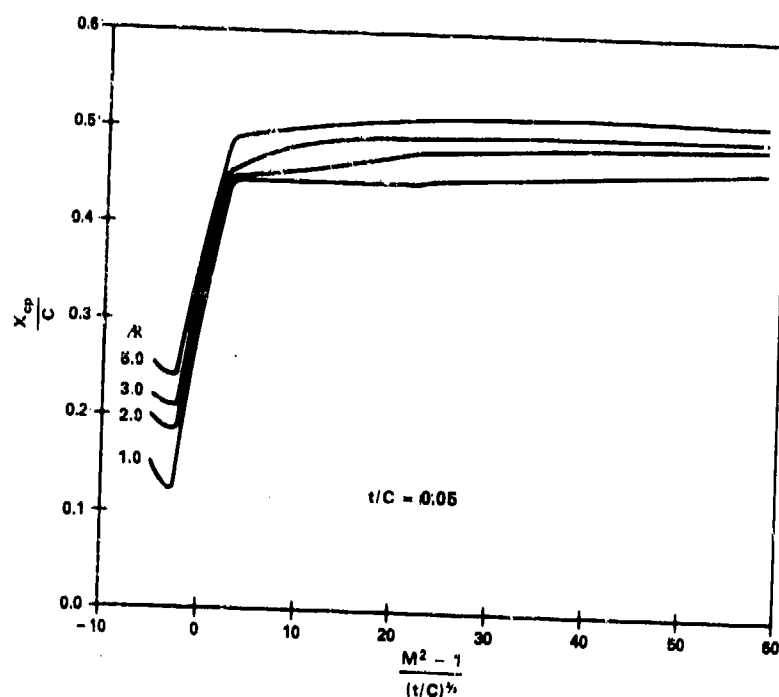


Figure 91. Center of Pressure for Rectangular Fin (Diamond Shape) ($t/C = .05$)

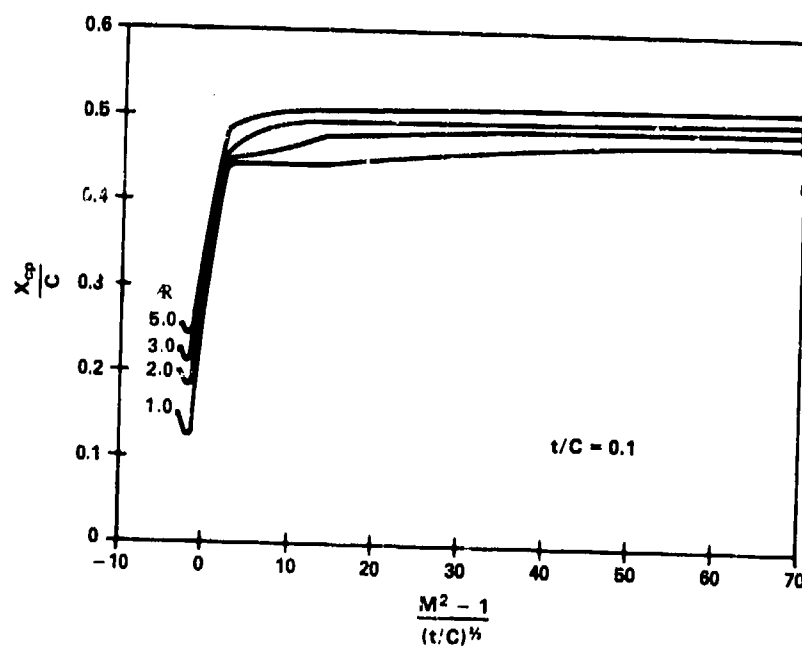


Figure 92. Center of Pressure for Rectangular Fin (Diamond Shape) ($t/C = .1$)

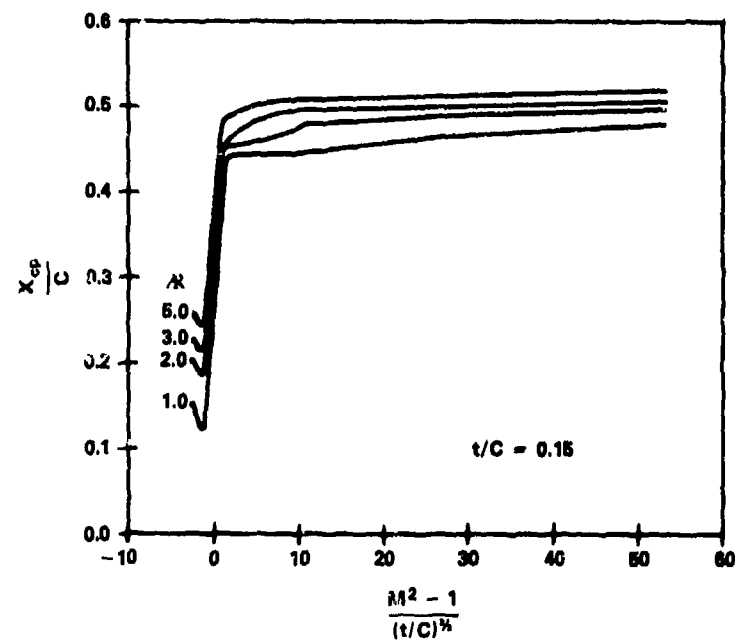


Figure 93. Center of Pressure for Rectangular Fin (Diamond Shape) ($t/C = .15$)

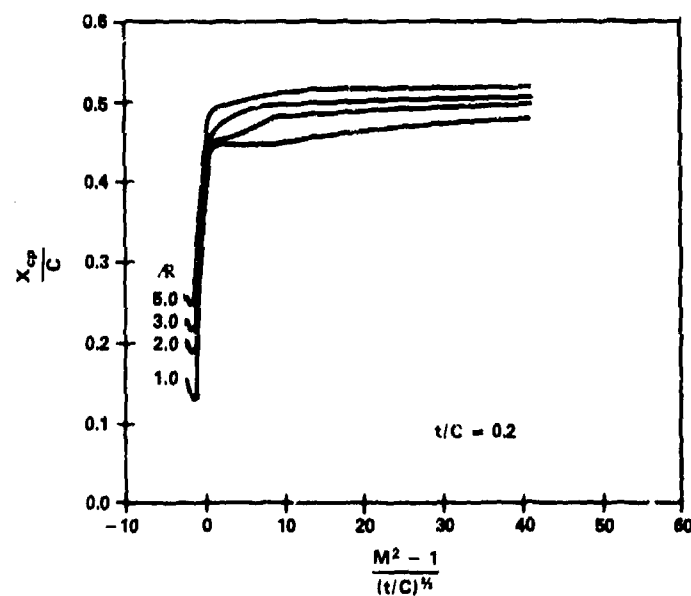


Figure 94. Center of Pressure for Rectangular Fin (Diamond Shape) ($t/C = .2$)

result in increased $C_{N\alpha}$ and a forward shift in the x_{cp} location. For low supersonic Mach numbers, the effects of AR and γ_{LE} are assumed to dominate the variation in $C_{N\alpha}$ and x_{cp} and thus the effect of thickness on lift is not considered. The transonic predictions compare well with the experimental data correlations given in Reference 5.

Variations in the $C_{N\alpha}$ and x_{cp} with LE sweep angle, γ_{LE} , and taper are shown in Figures 95 and 96, respectively. Generally, the lift curve slope effect is more noticeable in the low supersonic flow region for the subsonic LE case ($\gamma_{LE} < \mu$) than when the LE is supersonic ($\gamma_{LE} \geq \mu$). (The cases shown here are for unswept TE. The Code can also be used for cases with TE sweep but, as these trends are similar, the reader is referred to Reference 5 for more detailed charts produced using exact linear theory.) Generally, the lift curve slope is reduced with increasing γ_{LE} for a given taper ratio, λ , (increasing AR), and decreased with increasing λ for a given γ_{LE} (decreasing AR). In supersonic flow, changes in γ_{LE} for a given λ and Mach number have very little effect on the x_{cp} location as a function of the root chord, while increasing λ results in a forward movement in x_{cp} . The effect of thickness was discussed in the rectangular fin case and that discussion also applies here.

For complete configurations, the presence of a body with the fin causes interference effects on both the lift and the center of pressure. The interference lift is composed of three parts: the lift of the fin due to the presence of the body, the lift of the body due to the presence of the fin, and the vortex lift on the tail due to vortices shed by a wing or other forward-located lifting surface. The methods to determine these effects are discussed in detail in Section 2. The equations for summarizing the coefficients for the individual body components to obtain the coefficients for the total configuration including the interference effects are also given in Section 2.

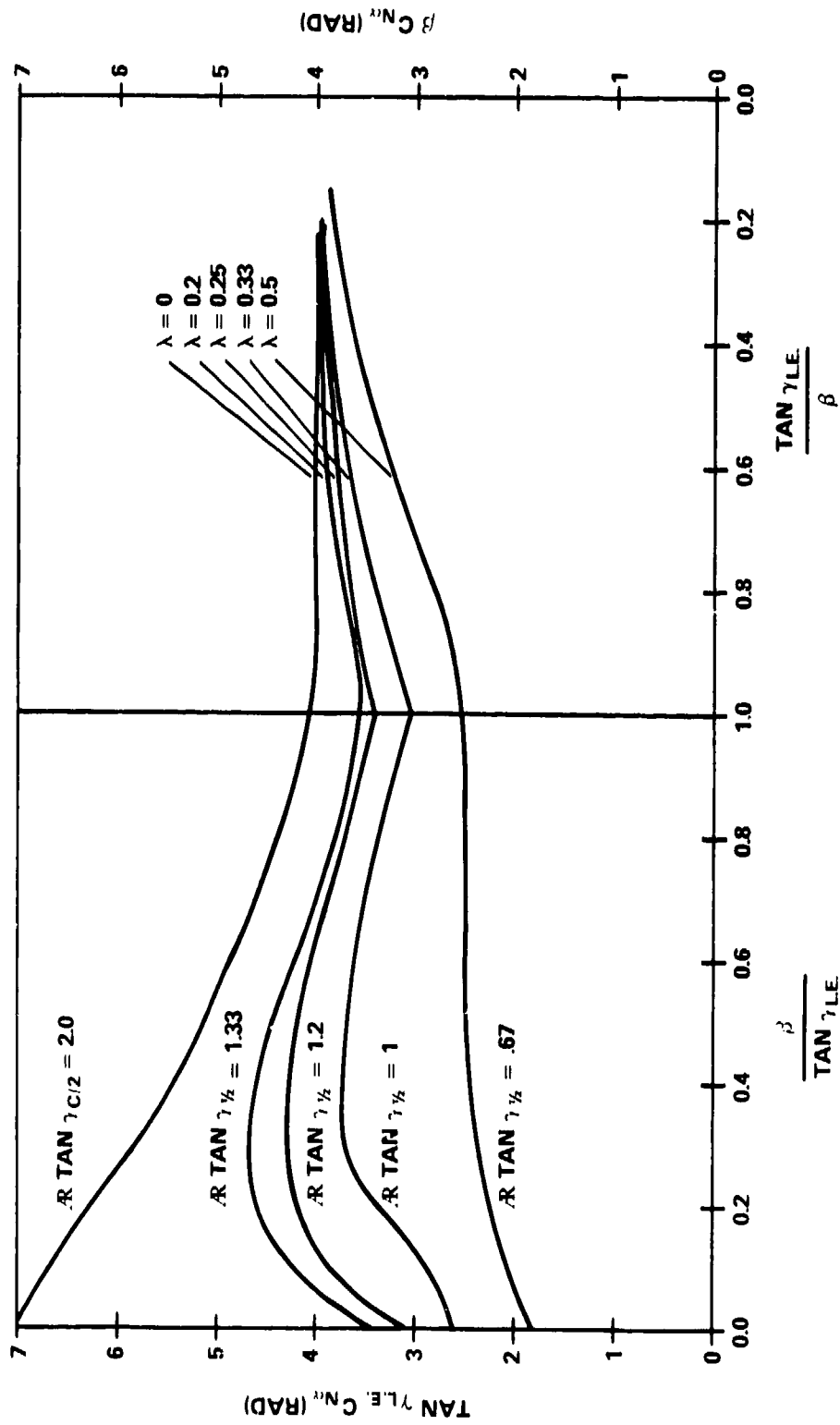


Figure 95. Normal Force Coefficient Variation for Tapered Double-Wedge Fins

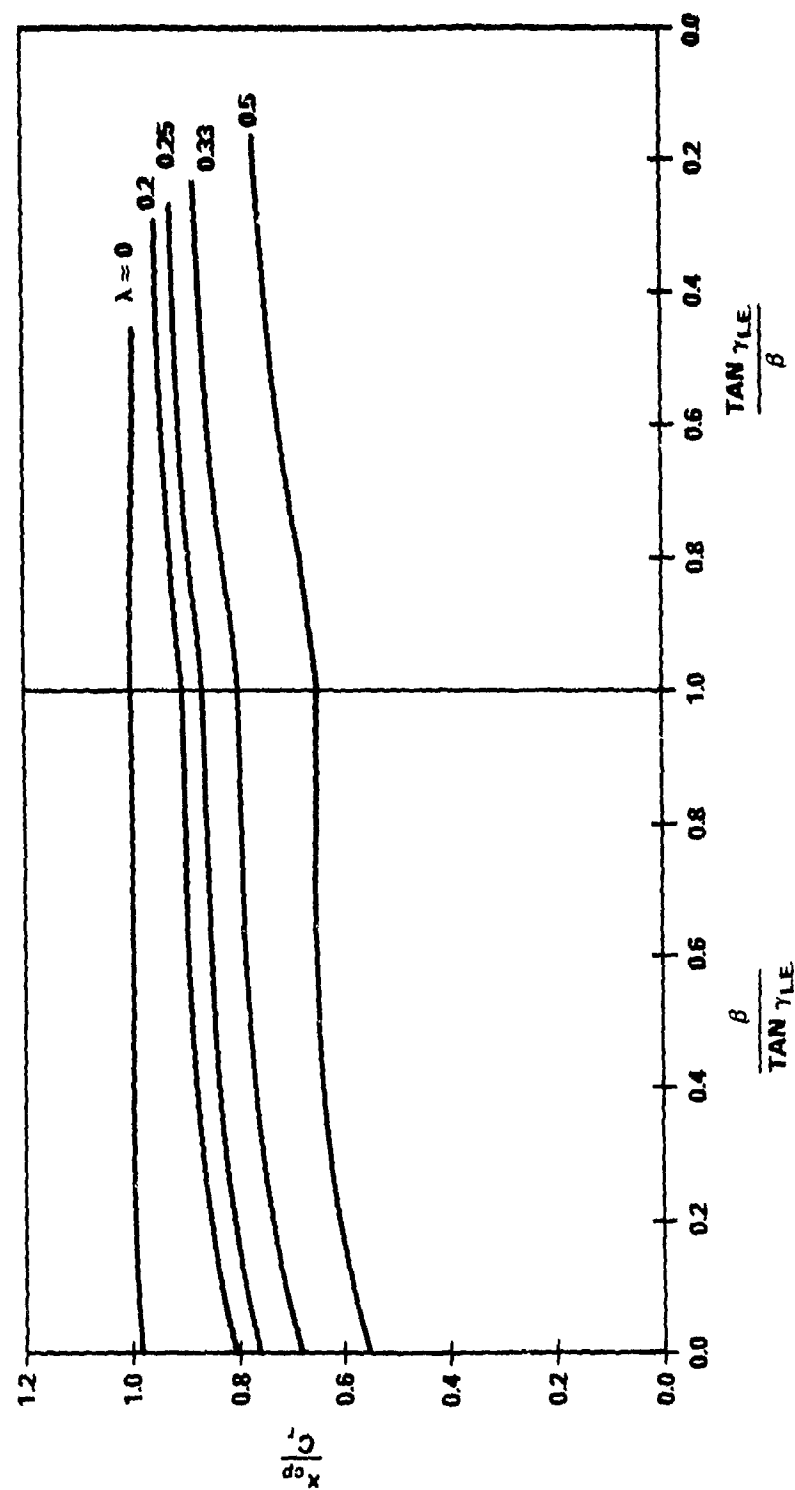


Figure 96. Center of Pressure Variation in Supersonic Flow
for Tapered Double-Wedge Fins

5. REFERENCES

1. F. G. Moore, Body Alone Aerodynamics of Guided and Unguided Projectiles at Subsonic, Transonic and Supersonic Mach Numbers, NWL Technical Report TR-2796, (Dahlgren, Va., November 1972).
2. F. G. Moore, Aerodynamics of Guided and Unguided Weapons, Part I, Theory and Application, NWL TR-3018, (Dahlgren, Va., December 1973).
3. F. G. Moore and R. C. Swanson, Aerodynamics of Tactical Weapons to Mach Numbers 3 and Angle 15°. Part I - Theory and Application, NSWC/DL TR-3584, (Dahlgren, Va., February 1977).
4. L. Devan, Aerodynamics of Tactical Weapons to Mach Number 8 and Angle-of-Attack 180° - Part I, Theory and Application, NSWC TR 80-346, (Dahlgren, Va., October 1980).
5. U.S. Army Material Command, Engineering Design Handbook - Design of Aerodynamically Stabilized Free Rockets, AMCP 706-280, (Washington, D.C., July 1968).
6. D. Chaussee, Improved Transonic Nose Wave Drag Estimates for the NSWC Missile Aerodynamic Computer Program, NSWC/DL TR-3830, (Dahlgren, Va., April 1978).
7. J. O. Keller and J. C. South, RAXBOD: A FORTRAN Program for Inviscid Transonic Flow over Axisymmetric Bodies, NASA TMX-72331, (Langley, Va., February 1976).
8. R. L. Hamner and A. D. Leff, Linear Aerodynamic Loads on Cone-Cylinders at Mach Numbers from .7 to 2.0, NASA CR-413, (Washington, D.C., March 1966).
9. R. V. Owens, Aerodynamic Characteristics of Spherically Blunted Cones at Mach Numbers From .5 to 5., NASA TN-D-3088, (Huntsville, Ala., December 1965).
10. J. M. Wu and K. Aoyama, Pressure Distributions for Axisymmetric Bodies with Discontinuous Curvature in Transonic Flow, U.S. Army Missile Command RD-TR-70-25, (Redstone Arsenal, Ala., November 1970).
11. M. D. Van Dyke, "First- and Second-Order Theory of Supersonic Flow Past Bodies of Revolution," Journal of the Aeronautical Sciences, (March 1951), pp. 161-178, 216.
12. C. A. Syvertson and D. H. Dennis, A Second-Order Shock Expansion Method Applicable to Bodies of Revolution Near Zero Lift, NACA TN 3527, (Moffett Field, Calif., January 1956).

13. E. R. Van Driest, "Turbulent Boundary Layer in Compressible Fluids," Journal of the Aeronautical Sciences, (March 1951), pp. 145-160, 216.
14. Bureau of Naval Weapons, Handbook of Supersonic Aerodynamics, NAVWEPS Report 1488, Vol. 3, (Washington, D.C., 1961).
15. J. M. Wu and K. Aoyama, Transonic Flow Field Calculation Around Ogive Cylinders by a Nonlinear Stretching Method, U. S. Army Missile Command Technical Report No. RD-TR-70-12, (Redstone, Ala., April 1970).
16. G. Klopfer and D. Chaussee, Numerical Solution of Three Dimensional Transonic Flows Around Axisymmetric Bodies at Angle of Attack, NEAR TR176, (Mountain View, Calif., February 1979).
17. L. Devan, "An Improved Second-Order Theory of Inviscid Supersonic Flow Past Bodies of Revolution," Paper 80-0030, Presented at the AIAA 18th Aerospace Sciences Meeting, (Pasadena, California, January 1980).
18. J. H. Allen and E. W. Perkins, Characteristics of Flow Over Inclined Bodies of Revolution, NACA RMA50607, (Moffett Field, Calif., 1965).
19. R. L. Bisplinghoff, H. Ashley, and R. L. Halfman, Aeroelasticity, Addison-Wesley Publishing Co., (Reading, Mass., 1955).
20. H. Ashley and M. Landahl, Aerodynamics of Wings and Bodies, Addison-Wesley Publishing Co., (Reading, Mass., 1965).
21. D. E. Davis, Generalized Aerodynamic Forces on a T-Tail Oscillating Harmonically in Subsonic Flow, R and M 3422, Aeronautical Research Council, London, (May 1964).
22. McDonnell Douglas Corp., USAF Stability and Control DATCOM, Revisions by Flight Control Division, AFFDL (Wright-Patterson Air Force Base, Ohio).
23. J. N. Nielsen, Missile Aerodynamics, McGraw Hill Book Co., Inc., (1960) (Available only from University Microfilms International).
24. G. F. Aiello, Aerodynamic Methodology (Bodies with Tails at Arbitrary Roll Angles) Transonic and Supersonic, Martin Marietta Corp., OR 14, 145, (Orlando, Fla., April 1976).
25. L. E. Ericsson, Modification of Aerodynamic Prediction of the Longitudinal Dynamics of Tactical Weapons, LMSC-D646354, (Sunnyvale, Calif., June 1979).
26. L. E. Ericsson and S. R. DeLu, User's Manual for LMSC Generalized Wing-Body Subroutine, LMSC-D646354A, (Sunnyvale, Calif., August 1979).

27. R. Whyte, J. Burnett, and W. Hathaway, Evaluation of the Computation of Pitch Damping by Subroutine LMSC, General Electric Co., Armament Systems Division, (Burlington, Vt., November 1979).
28. V. E. Lockwood, Effects of Sweep on the Damping-in-Roll Characteristics of Three Sweptback Wings Having an Aspect Ratio of 4 at Transonic Speeds, NACA, RM L50519, (Hampton, Va., December 1950).
29. G. J. Adams and D. W. Dugan, Theoretical Damping in Roll and Rolling Moment Due to Differential Wing Incidence for Slender Cruciform Wings and Wing-Body Combinations, NACA TR 1088, (Moffett Field, Calif., 1952).
30. E. J. Ohlmeyer, Dynamic Stability of the Improved 5"/54 Projectile, NWL Technical Report TR-2871, (Dahlgren, Va., December 1972).
31. R. H. Whyte, Effects of Boattail Angle on Aerodynamic Characteristics of 175mm M437 Projectile at Supersonic Mach Numbers, U.S. Army Munitions Command Technical Memorandum 1646, (Dover, N.J., September 1965).
32. John A. Darling, Handbook of Blunt-Body Aerodynamics Volume 1 -- Static Stability, Naval Ordnance Laboratory Technical Report 73-225, (Silver Spring, Md., December 1973).
33. C. M. Jackson, W. C. Sawyer, and R. S. Smith, A Method for Determining Surface Pressure on Blunt Bodies of Revolution at Small Angles-of Attack in Supersonic Flow, NASA TN D-4865, (Hampton, Va., 1968).
34. Engineering Design Handbook -- Design for Control of Projectile Flight Characteristics, Headquarters, U.S. Army Materiel Command Pamphlet 706-242, (Washington, D.C., September 1966).
35. John D. Nicolaides, Missile Flight and Astrodynamics, Bureau of Weapons, Department of the Navy Technical Note No. 100-A, (Washington, D.C., 1959-61).
36. W. B. Baker, Jr., An Aerodynamic Coefficient Prediction Technique for Slender Bodies with Low Aspect Ratio Fins at Mach Numbers from .6 to 3.0 and Angles-of-Attack from 0 to 180 Degrees, AEDC-TR-77-97, (Tullahoma, Tenn., March 1978).
37. James O. Nichols, Analysis and Compilation of Missile Aerodynamic Data, NASA CR-2835, (Washington, D.C., November 1975).
38. Robert L. McCoy, 'McDrag' - A Computer Program for Estimating the Drag Coefficients of Projectiles, BRL Technical Report ARBRL-TR-02293, (Aberdeen, Md., February 1981).

39. W. D. Washington and W. Pettis, Jr., Boattail Effects on Static Stability at Small Angles-of-Attack, U.S. Army Missile Command Report No. RD-TM-68-5, (Redstone Arsenal, Ala., 1968).
40. D. R. Chapman, W. R. Wimbrow, and R. H. Kester, Experimental Investigation of Base Pressure on Blunt-Trailing-Edge Wings at Supersonic Velocities, NACA Report 1109, (Moffett Field, Calif., 1952).
41. J. R. Spahr and R. R. Dickey, Effect of Tail Surfaces on the Base Drag of a Body of Revolution at Mach Numbers of 1.5 and 2.0, NACA TN-2360, (Moffett Field, Calif., 1951).

APPENDIX
LIST OF SYMBOLS

A	Parameter in equation for skin friction
AR	Aspect ratio (b^2/S_T)
a	Speed of sound (ft/sec)
a_m	Missile acceleration during maneuver (g's)
a_T	Target acceleration during maneuver (g's)
B	Parameter in equation for skin friction, lift interference parameter
B_{IA}	Lift interference parameter, infinite afterbody
B_{NA}	Lift interference parameter, no afterbody
B_{SA}	Lift interference parameter, short afterbody
b	Span of two fins (excluding body) (ft)
c	Local chord length (ft)
\bar{c}	Mean aerodynamic chord (ft)
C_A	Axial force coefficient
C_{AB}	Base axial force coefficient
C_{ABA}	Increment in base force coefficient due to angle-of-attack
C_{Af}	Forebody axial force coefficient
C_{AF}	Axial force due to skin friction
C_{AP}	Pressure (or wave) axial force coefficient
C_{APO}	Nose separation drag coefficient
C_{ARB}	Axial force coefficient due to presence of a rotating band
C_{AW}	Wing axial force coefficient
C_D	Drag coefficient in wind axes
C_{D_0}	Zero angle-of-attack drag coefficient

C_{dc}	Infinite cylinder crossflow drag coefficient
C_F, C_f	Friction coefficient
C_{FC}	Friction coefficient at critical Reynolds number
C_l	Roll moment coefficient
C_{lp}	Roll damping coefficient $[\partial C_l / \partial (pD/2V)]$ (rad^{-1})
C_m	Pitching moment coefficient
$C_{mq} + C_{m\dot{\alpha}}$	Pitch damping coefficient $\left\{ (1/q_\infty SD) \left\{ [\partial M_y / \partial (qD/2V)] + [\partial M_y / \partial (\dot{\alpha}D/2V)] \right\} \right\}$ (rad^{-1})
$C_{m\alpha}$	Pitching moment coefficient derivative
$C_{m\delta}$	Pitching moment coefficient derivative due to fin deflection, δ_F
C_N	Normal force coefficient
C_{NB}	Body-alone normal force coefficient
$C_{NB(F)}$	Normal force coefficient correction for interference due to body in presence of a fin
$C_{NF(B)}$	Normal force coefficient correction for interference due to fin in presence of a body
C_{NTi}	Isolated i^{th} fin (in presence of the body) normal force coefficient (cruciform configuration)
$C_{NT(V)}$	Tail normal force coefficient correction for canard shed vortex
$C_{N(TOT)}, C_{N(B+T)}$	Body-tail total normal force coefficient at small α and high α , respectively
$C_{N\alpha}$	Normal force coefficient derivative
$C_{n_{p\alpha}}$	Magnus moment coefficient derivative $\left\{ (1/q_\infty SD) [\partial^2 M_z / \partial (pD/2V) d\alpha] \right\}$ (rad^{-1})
C_p	Pressure coefficient

C_{pL}, C_{pU}	Pressure coefficients for lower and upper surfaces of the wing, respectively
C_{pBA}	Base pressure coefficient
C_r	Fin root chord (ft)
C_{r1}	Distance from wing root leading edge to first surface discontinuity downstream, parallel to freestream (ft)
C_{r2}	Distance from wing root trailing edge to first surface discontinuity upstream, parallel to freestream (ft)
C_t	Fin tip chord (ft)
C_{t1}	Distance from wing tip leading edge to first surface discontinuity downstream, parallel to freestream (ft)
C_{t2}	Distance from wing tip trailing edge to first surface discontinuity upstream, parallel to freestream (ft)
C_1	Parameter in equations for skin friction, transonic nose normal force
C_2	Parameter in equations for skin friction, transonic nose normal force
C_y	Constant in determining pitch damping coefficient
CG	Center of gravity
D	Body reference diameter (ft)
\bar{D}	Mean body diameter
D_c, D_w	Mean body diameter near a canard and tail, respectively
d_1	Parameter in equation for skin friction
d_2	Parameter in equation for skin friction
F	Mach wave angle proportionality factor
f_w	Spanwise location of panel vortex
f^*	Dynamic pressure ratio across a bow shock

g	Acceleration due to gravity (ft/sec ²)
H	Rotating band height above body (cal)
HE_o	Initial heading error (rad)
I_{BT}	Body-tail normal force coefficient interference
I_{SP}	Specific impulse (sec)
I_X	Body polar inertia (slug-ft ²)
I_Y	Body transverse (pitch axis) inertia (slug-ft ²)
i_t	Tail interference factor
K	Hypersonic similarity parameter
$K_B, K_C, K_{B(F)},$ $K_{F(B)}, k_{B(F)}, k_{F(B)}$	Interference parameters
L	Body length (cal)
L_A, L_B, L_N	Lengths of afterbody, boattail, and nose, respectively (cal)
L_{BA}	Body alone lift
$L_{B(F)}, L_{F(B)}$	Interference lift
L_C	Combination lift of wing plus body
L_F	Fin alone lift
L_1	Comparable body length
M	Mach number
M_a, M_b	Intermediate transonic Mach numbers
M_{fb}	Force break Mach number
M_l	Mach number separating low supersonic and high supersonic inviscid body alone and wing wave drag computations
M_{le}	Mach number separating low supersonic and high supersonic inviscid lift and dynamic derivative computations

M^*	Mach number related to nose length used for interpolations
m	Mass
m_{HE}	Miss distance due to heading error (meters)
N	Effective navigation ratio
p	Roll rate (rad/sec)
q	Pitch rate (rad/sec)
q_∞	Dynamic pressure
R	Body radius (cal)
\bar{R}	Mean local body radius (cal)
R_{be}	Radome boresight error
R_N	Body, nose spherical radius (cal)
R_{NC}	Critical Reynolds number
R_{NE}	Effective radius of spherical cap (cal)
R_{NL}	Reynolds number based on body length
R_0	Body radius at base of spherical cap (cal)
R'_0	Body surface slope at $x=0$
R'_s	Body surface slope at nose-afterbody junction
R_X	Range (ft)
S	Area (unit ²)
S_b	Body surface area (cal ²)
S_d	Dynamic stability factor
S_g	Gyroscopic stability factor
S_p	Body longitudinal planform area (cal ²)
S_T	Total planform area (ft ²)

S_W	Planform area for two tail fins (ft ²)
S_w	Wetted area (ft ²)
s	Distance along linear segment
\tilde{s}	Point on body at which perturbation solution begins
\overline{st}	Origin of source or doublet distribution
T	Temperature (°R)
T_R	Thrust (lb)
T_w	Wall temperature (°R)
t	Local thickness of lifting surface (ft)
\tilde{t}	Body surface match point for spherical cap (cal)
t_f	Time of flight (sec)
t_o	Total missile maneuver time constant
t_r	Lifting surface thickness at root (ft)
t_t	Lifting surface thickness at tip (ft)
V	Velocity (ft/sec)
V_c	Closing velocity (ft/sec)
V_m	Missile velocity (ft/sec)
V_0	Initial velocity (ft/sec)
W	Weight (lb)
W_L	Launch weight (Lb)
w	Perturbation velocity (ft/sec)
X	Stretched coordinate at which singularity exists
x	Body coordinate (parallel to body axis) or lifting surface chordwise coordinate for fin only (cal)
\tilde{x}	Body coordinate including spherical cap (cal)

x_{AFT}	Distance from tail trailing edge to base of body (cal)
x_{cg}	Distance from nose to moment reference (cal)
\bar{x}_c, \bar{x}_w	Distances to fin apex for canard and tail, respectively, from nose (cal)
x_{cp}	Distance from moment reference to center of pressure (cal)
x_{cpB}	Body-alone x_{cp} from nose (cal)
$(x_{cp})_{Ti}$	Isolated i^{th} fin (cruciform configuration) x_{cp} from nose (cal)
$(x_{cp})_{TOT}$	Total body-tail x_{cp} from nose (cal)
x_{cpi}	Interference x_{cp} from nose (cal)
x_p	Body planform area center location (cal)
x_{te}	Distance defined in Equation (125)
Y	Stretched coordinate at which singularity exists, functional parameter, radius coordinate
y	Spanwise distance on lifting surface (ft)
y_{cpi}	Spanwise location of center of pressure for isolated i^{th} fin (ft)
α	Angle-of-attack (rad)
$\beta, \bar{\beta}$	Compressibility similarity parameter, $\sqrt{ M_\infty^2 - 1 }$
Γ	Second derivative of C_p with respect to α evaluated at $\alpha=0, \theta=0$
γ	Calorically perfect gas heat capacity ratio
$\dot{\gamma}$	Flight path angle of missile rate-of-change (deg/sec)
γ_G	Streamwise circulation per unit length
$\gamma_1, \gamma_2, \gamma_3, \gamma_4$	Sweep angles for local surface discontinuities on a fin, functional parameter (deg, rad)
γ_{LE}	Leading edge sweep angle of lifting surface ($=\gamma_1$) (deg, rad)
Δ	Incremental value, second derivative of C_p with respect to α evaluated at $\alpha=0, \theta=\pi/2$

δ	Local body angle (rad)
δ^*	Nose slope angle (rad)
δ_F	Fin control deflection angle (deg)
ε	Angle associated with body slope (rad)
ε_s	Angle of nose-afterbody junction (rad)
ε_0	Initial body surface angle following spherical cap (rad)
η	Crossflow drag proportionality factor, functional parameter
θ	Azimuthal angle from the leeside, roll angle (rad)
θ_B	Boattail or flare angle (deg)
θ_c	Cone half angle (deg)
θ^*	Equivalent cone angle for nose of given length (rad)
Λ	Parameter proportional to derivative of C_p with respect to α for $\alpha=0$, $\theta=0$, functional variable
λ	C_t/C_r
μ	Mach wave angle, $\sin^{-1}\left(\frac{1}{M}\right)$
ξ	Functional parameter
ρ	Density (slug/ft ³)
ρ_{lr}	Root leading edge radius (cal)
ρ_{lt}	Tip leading edge radius (cal)
ρ_{tr}	Root trailing edge radius (cal)
ρ_{tt}	Tip trailing edge radius (cal)
σ	Area of influence on lifting surface, stress (psi)
τ	Time (sec)
τ_{AF}	Airframe time constant
τ_F	Guidance filter time lag constant

τ_g	Total missile guidance time constant
τ_1	Tracking loop time constant
Φ, ϕ	Disturbance potential
χ	Functional parameter

Superscripts

Differentiation with respect to x
Span including body

Subscripts

A	Afterbody
a	Asymptotic value
B	Base
b	Body
C	Conical value
ℓ	Local
N	Nose
O	Ogival value
p	Pressure
RB	Rotating band
ref	Reference value
std	Standard value
T	Tail value
W	Wing
w	Wave drag component

Subscripts (Cont'd)

- 0 Stagnation value (when referring to pressure, except on pages 24-25 where it refers to the $M_\infty=0$ case), value at $\alpha=0$ (drag only)
- 1, 2 Values upstream and downstream from a body corner, respectively
- α Partial differential with respect to α ($\alpha \rightarrow 0$)
- ∞ Freestream condition
- * Parameter in determination of $C_{mq} + C_{m\alpha}$ using LMSC method

DISTRIBUTION

Commander
Naval Sea Systems Command
Washington, DC 20360 (2)
Attn: SEA-62R41, Mr. L. Pasiuk
Technical Library

Commander
Naval Materiel Command
Washington, DC 20360 (3)
Attn: Mr. S. Jacobson (MAT-032)
Dr. John Huth
Technical Library

Commander
Naval Air Systems Command
Washington, DC 20360 (4)
Attn: AIR-320, Dr. H. Mueller
AIR-330D, Dr. W. H. Clark
AIR-530, S. Loezos
Technical Library

Commander
Naval Weapons Center
China Lake, CA 93555 (6)
Attn: Mr. R. Van Aken
Mr. R. Meeker
Mr. Lloyd Smith
Mr. R. E. Smith
Mr. H. Schafer
Technical Library

Commander
Pacific Missile Test Center
Point Mugu, CA 93041 (3)
Attn: Mr. J. Rom
Mr. G. Cooper
Technical Library

Commander
Naval Ship Research and Development Center
Washington, DC 20007 (3)
Attn: Dr. T. C. Tai
Mr. M. J. Malia
Technical Library

DISTRIBUTION (Cont'd)

Office of Naval Research
800 N. Quincy Street
Arlington, VA 22217 (3)
Attn: Mr. D. Siegel
Dr. R. Whitehead
Technical Library

Commanding Officer
Naval Air Development Center
Warminster, PA 18974 (3)
Attn: Mr. S. Greenhalgh
Mr. C. Reitz
Technical Library

Superintendent
U.S. Naval Academy
Annapolis, MD 21402 (4)
Attn: Head, Weapons Dept.
Head, Science Dept.
Dr. A. Maddox
Technical Library

Superintendent
U.S. Naval Postgraduate School
Monterey, CA 95076
Attn: Technical Library

Officer in Charge
Naval Intelligence Support Center
4301 Suitland Road
Washington, DC 20390 (2)
Attn: J. B. Chalk
Technical Library

Commanding Officer
Naval Ordnance Station
Indian Head, MD 20640
Attn: Technical Library

Director, Development Center
Marine Corps Development and Education
Command
Quantico, VA 22134

DISTRIBUTION (Cont'd)

Chief of S and R Division
Development Center
Marine Corps Development and Education
Command
Quantico, VA 22134

Commanding General
Ballistic Research Laboratory
Aberdeen Proving Ground, MD 21005
Attn: Dr. C. H. Murphy
Mr. L. McAllister
Mr. A. Platou
Mr. R. McCoy
Dr. R. Sedney
Dr. W. Sturek
Mr. C. Nietubicz
Technical Library

(8)

Commanding General
ARRADCOM
Picatinny Arsenal
Dover, NJ 07801
Attn: Mr. A. Loeb
Mr. H. Hudgins
Mr. G. Friedman
Mr. W. Gadomski
Technical Library

(5)

Commanding General
U.S. Army Missile R and D Command
DROMI-TDK
Redstone Arsenal
Huntsville, AL 35809
Attn: Mr. R. Deep
Dr. D. J. Spring
Technical Library

(3)

Commanding Officer
Harry Diamond Laboratories
Washington, DC 20013
Attn: Technical Library

DISTRIBUTION (Cont'd)

Arnold Engineering Development Center

USAF

Tullahoma, TN 37389

(3)

Attn: Mr. J. Usselton

Mr. W. B. Baker, Jr.

Technical Library

Commanding Officer

Air Force Armament Laboratory

Eglin Air Force Base, FL 32542

(7)

Attn: Dr. D. Daniel

Mr. C. Butler

Mr. K. Cobb

Mr. C. Mathews

Mr. E. Sears

Mr. F. Stevens

Dr. L. E. Lijewski

USAF Academy

Colorado Springs, CO 80912

Attn: Technical Library

Commanding Officer

Air Force Wright Aeronautical Laboratories

(AFSC)

Wright-Patterson Air Force Base, OH 45433

(6)

Attn: Dr. G. Kurylowich

Mr. D. Shereda

Mr. J. Jenkins

Mr. D. Hoak

Mr. G. Fleeman

Mr. M. Pinney

Advanced Research Projects Agency

Department of Defense

Washington, DC 20305

Attn: Technical Library

NASA

Washington, DC 20546

Attn: Technical Library

NASA Ames Research Center

Moffett Field, CA 94035

(3)

Attn: Dr. G. Chapman

Mr. V. L. Peterson

Technical Library

DISTRIBUTION (Cont'd)

NASA Langley Research Center
Langley Station
Hampton, VA 23365

(7)

Attn: Mr. J. South
Mr. L. Spearman
Mr. C. M. Jackson, Jr.
Mr. W. C. Sawyer,
Dr. R. C. Swanson, Jr.
Miss E. J. Landrum
Technical Library

Virginia Polytechnic Institute and State
University

Department of Aerospace Engineering
Blacksburg, VA 24060

(3)

Attn: Dr. J. A. Schetz
Dr. C. H. Lewis
Technical Library

North Carolina State University
Department of Mechanical and Aerospace
Engineering

Box 5246

Raleigh, NC 27607

(2)

Attn: Dr. F. R. De Jarnette
Technical Library

The University of Tennessee Space Institute
Tullahoma, TN 37388

(3)

Attn: Dr. J. M. Wu
Mr. C. Balasubramayan
Technical Library

University of Notre Dame
Department of Aerospace and Mechanical
Engineering

Box 537

Notre Dame, IN 46556

(2)

Attn: Dr. R. Nelson
Technical Library

DISTRIBUTION (Cont'd)

Applied Physics Laboratory
The Johns Hopkins University
Johns Hopkins Road
Laurel, MD 20810

(7)

Attn: Dr. L. L. Cronvich
Mr. E. T. Marley
Mr. J. C. Hagan
Mr. E. Lucero
Mr. L. Tisserand
Mr. G. J. Pietrangeli
Technical Library

Raytheon Company
Missile Systems Division
Hartwell Road
Bedford, MS 01730

(2)

Attn: Mr. D. P. Forsmo
Technical Library

McDonnell-Douglas Astronautics Co. (West)
5301 Bolsa Avenue
Huntington Beach, CA 92647
Attn: Dr. J. Xerikos
Technical Library

(2)

McDonnell-Douglas Astronautics Co. (East)
Box 516
St. Louis, MO 61366
Attn: Mr. J. Williams
Mr. S. Vukelich
Technical Library

(3)

Lockheed Missiles and Space Co., Inc.
P.O. Box 1103
Huntsville, AL 35807
Attn: Dr. D. Andrews
Technical Library

(2)

Lockheed Missiles and Space Co., Inc.
P.O. Box 504
Sunnyvale, CA 94086
Attn: Dr. Lars E. Ericsson
Mr. P. Reding
Mr. H. S. Shen
Technical Library

(4)

DISTRIBUTION (Cont'd)

Nielsen Engineering and Research, Inc.
510 Clyde Avenue
Mountain View, CA 95043

General Electric Co.
Armament Systems Department
Burlington, VT 05401
Attn: Mr. R. Whyte

CAL SPAN Advanced Technology Center
P.O. Box 400
Buffalo, NY 14225
Attn: Mr. B. Omilian

Northrop Services, Inc.
Huntsville, AL 35810
Attn: Mr. W. Boyle

Science Applications Inc.
680 E. Swedesford Rd.
Wayne, PA 19087
Attn: Mr. P. Murad

Vought Corporation
P.O. Box 5907
Dallas, TX 75222
Attn: Mr. F. Prillman
Dr. W. B. Brooks
Mr. R. Stancil

(3)

Hughes Aircraft Corp.
Canoga Park, CA 91304
Attn: Dr. J. Sun
Technical Library

(2)

Sandia Laboratories
Albuquerque, NM 87115
Attn: Mr. R. La Farge
Mr. R. Eisler
Mr. W. Wolfe
Technical Library

(4)

Martin Marietta Aerospace
P.O. Box 5837
Orlando, FL 32805
Attn: Mr. G. F. Aiello
Technical Library

(2)

DISTRIBUTION (Cont'd)

Business and Technology Systems, Inc.
Suite 400 Aerospace Building
10210 Greenbelt Rd.
Seabrook, MD 20801
Attn: Dr. J. B. Eades, Jr.

Lawrence Livermore Laboratory
Earth Sciences Division
University of California
Livermore, CA 94550 (2)
Attn: Mr. D. G. Miller
Technical Library

Honeywell Inc.
600 Second Street
Minneapolis, MN 55343 (2)
Attn: Mr. S. Sopczak
Technical Library

Pacifica Technology
P.O. Box 148
Del Mar, CA 92014
Attn: Dr. H. T. Ponsford

Rockwell International
Missile Systems Division
4300 E. Fifth Avenue
P.O. Box 1259
Columbus, OH 43216 (2)
Attn: Mr. J. E. Rachner
Technical Library

Boeing Computer Services, Inc.
P.O. Box 24346
Seattle, WA 98124
Attn: Mr. R. Wyrick

Motorola Inc.
Missile Systems Operations
8201 East McDowell Rd.
P.O. Box 1417
Scottsdale, AZ 85252
Attn: Mr. G. H. Rapp

DISTRIBUTION (Cont'd)

Raytheon Company
Spencer Laboratory
Box SL7162
Burlington, MS 01805
Attn: Mr. S. Pearlsing
Mr. P. Giragosian

(2)

Defense Technical Information Center
Cameron Station
Alexandria, VA 22314

(12)

Library of Congress
Washington, DC 20540
Attn: Gift and Exchange Division

(4)

GIDEP Operations Office
Corona, CA 91720

Defense Printing Service
Washington Navy Yard
Washington, DC 20374

EG&G, Washington Analytical Services Center, Inc.
P.O. Box 552
Dahlgren, VA 22448
Attn: Technical Library

Local:

E41
G
G20
G30
G40
K
K10
K20
K21
K21 (Devan)
K22
K23
K24
R
R44
U20
U23
X210

(2)

(40)

(2)

(2)

(5)

(6)